

# **Investigations on the Development of Newton Power flow Models of Hybrid AC-DC Systems**

A Thesis Submitted to the  
Delhi Technological University  
For the award of Doctor of Philosophy  
In  
Electrical Engineering

By

**SHAGUFTA KHAN  
(2K12/Ph.D./EE/03)**



Under the Supervision of:


**Dr. Suman Bhowmick**

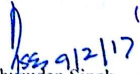
**DEPARTMENT OF ELECTRICAL ENGINEERING  
DELHI TECHNOLOGICAL UNIVERSITY  
DELHI-110042**

**FEBRUARY 2017**

## CERTIFICATE

Certified that the thesis titled "Investigations on the Development of Newton Power flow Models of Hybrid AC-DC Systems" which is being submitted by Shagufta Khan for the award of Doctor of Philosophy in Electrical Engineering, Delhi Technological University, Delhi, is a record of student's own work carried out by her under my supervision and guidance. The matter embodied in this thesis has not been submitted for any other degree.

  
Dr. Suman Bhowmick  
Department of Electrical Engineering  
Delhi Technological University  
Bawana Road  
Delhi-110042, India  
Associate Professor  
Electrical Engineering Department  
Delhi Technological University  
(Formerly Delhi College of Engineering)  
Govt. of NCT of Delhi  
Bawana Road, Delhi-110042

  
Prof. Madhusudan Singh,  
Head, Department of Electrical Engineering  
Delhi Technological University  
Delhi-110042

Professor & Head  
Electrical Engineering Department  
Delhi Technological University  
(Formerly Delhi College of Engineering)  
Govt. of NCT of Delhi  
Bawana Road, Delhi-110042

## ACKNOWLEDGEMENT

I would like to express my deep and sincere gratitude to my supervisor **Dr. Suman Bhowmick**, for his valuable guidance, scholarly input, continual patience and consistent encouragement I received throughout the research work. I also thank him for encouraging me to stay in the lab for long hours. His wide knowledge and logical way of thinking have helped me to complete my research work. Sir, has always made himself available to clarify my doubts despite his busy schedules and I consider it as a great opportunity to do my doctoral programme under his guidance and to learn from his research expertise. Thank you very much Sir, for all your help and support.

I would like to express my deepest thanks to Prof. Madhusudan Singh, HOD, Electrical Engineering, Delhi Technological University (formerly Delhi College of Engineering) for his immense support and valuable guidance during the entire work of this thesis. I also would like to thanks to Prof. Moinuddin, Computer Science, Jamia Hamdard, Delhi for his constant encouragement and support.

I also express my thanks to SRC members mainly Prof. T.S Bhatti who have given me valuable guidance and advice to improve quality of my research work. I would like to express my sincere gratitude to Prof. Narendra Kumar 1, who has taught me relevant course work and his valuable support. I am also very grateful to Dr. M. Rizwan who helped me in numerous ways during various stages of my Ph.D. I also extend my sincere thanks to Prof. Pragati kumar, Prof. Narendra kumar 2, Dr. Rachna Garg, Dr. Priya Mahajan and other faculties of the Electrical Engineering, Delhi Technological University, Delhi, for their encouragement and moral support for the completion of this thesis.

I am also thankful to IIT Delhi for permitting me to access old issues of international journals and reference books related with my research works. I also would like to thank to all the personnel of Senior Machine Lab for their enormous support and help during my research work. I also thank the office staff of Central Library and Central Computer Centre for their valuable co-operation and support.

I extend my personal thanks to my friends and colleagues specially, Nikita Gupta, Md. Tausif Ahmad, Priyanka Chaudhry, Imran Ahmad Quadri and Shruti Jaiswal for their valuable support and reminding me to complete my work at earliest.

A special thank to my father Mohd. Iqbal Khan and mother Gulzar Begum. Words can not express how grateful I am to my parents for all the sacrifices that they have made for me.

Finally, I would like to thank the Almighty Allah, for granting me the ability and patience to complete my thesis successfully.

I will keep on trusting You for my future. Thank you, Allah.

Date: 09/02/17

Place: Delhi



Shagufta Khan

(2k12/Ph.D/EE/03)

## List of abbreviations

BTB	Back to back
CT	Computational time in seconds taken by the algorithm to converge to a specified tolerance
FACTS	Flexible AC transmission systems
HVDC	High voltage direct current
IDCPFC	Interline direct current power flow controller
IGBT	Insulated gate bipolar transistor
IPFC	Interline power flow controller
LCC	Line commutated converter
MLDC	Multi-terminal LCC-based HVDC
MTDC	Multi-terminal Direct Current
MVDC	Multi-terminal VSC-based HVDC
NI	Number of iterations taken by the algorithm to converge to a specified tolerance
NR	Newton Raphson
OWF	Offshore wind farm
PTP	Point to point
PWM	Pulse width modulation
RoW	Right of way
VSC	Voltage source converter
XLPE	Cross linked poly ethylene

# List of symbols

## 1. CAPITALS

<b>E</b>	Vector for mismatch error
<b>E<sub>AC</sub></b>	Vector for mismatch error in AC network
<b>E<sub>DC</sub></b>	Vector for mismatch error in DC network
<b>I<sub>AC base</sub></b>	AC base current
<b>I<sub>DC base</sub></b>	DC base current
<b>I<sub>DC</sub></b>	DC current
<b>I<sub>sha</sub></b>	Current through the converter transformer of the a <sup>th</sup> VSC
<b>I<sub>DCa</sub><sup>*</sup></b>	DC current reference for linear V-I droop line of the a <sup>th</sup> VSC
<b>J</b>	Jacobian matrix
<b>J<sub>old</sub></b>	Conventional power flow Jacobian sub-block
<b>P<sub>Di</sub></b>	Active power demand at bus 'i'
<b>P<sub>i</sub></b>	Net active power injection at bus 'i'
<b>P</b>	Bus active power injection vector
<b>P<sub>i</sub><sup>SP</sup></b>	Specified active power injection at bus 'i'
<b>P<sub>DCR</sub></b>	Active power associated with the rectifier
<b>P<sub>DCI</sub></b>	Active power associated with the inverter
<b>P<sub>sha</sub></b>	Active power flow in the line connecting the a <sup>th</sup> VSC to its AC bus
<b>P<sub>sha</sub><sup>SP</sup></b>	Specified active power flow in the line connecting the a <sup>th</sup> VSC to its AC bus
<b>P<sub>sha</sub><sup>cal</sup></b>	Calculated active power flow in the line connecting the a <sup>th</sup> VSC to its AC bus

$P_{\text{loss}a}$	Losses of the $a^{\text{th}}$ VSC
$P_{\text{DC}a}^*$	DC power reference for linear V-P droop line of the $a^{\text{th}}$ VSC
$P_{\text{IDCPFC}}$	Power delivered by the IDCPFC
$P_{\text{DCWF}}$	Rectifying power of wind farm injected into the DC grid
$\mathbf{P}_{\text{DCWF}}$	Vector of rectifying powers of wind farms
$\mathbf{Q}$	Bus reactive power injection vector
$Q_{\text{DCR}}$	Reactive power associated with the rectifier
$Q_{\text{DCI}}$	Reactive power associated with the inverter
$Q_{\text{Di}}$	Reactive power demand at bus 'i'
$Q_i$	Net reactive power injection at bus 'i'
$Q_i^{\text{SP}}$	Specified reactive power injection at bus 'i'
$Q_{\text{sha}}$	Reactive power flow in the line connecting the $a^{\text{th}}$ VSC to its AC bus
$Q_{\text{sha}}^{\text{SP}}$	Specified reactive power flow in the line connecting the $a^{\text{th}}$ VSC to its AC bus
$Q_{\text{sha}}^{\text{cal}}$	Calculated reactive power flow in the line connecting the $a^{\text{th}}$ VSC to its AC bus
$R_{\text{DC}}$	Resistance of DC link
$R_a$	droop control gain of the $a^{\text{th}}$ VSC
$R_{\text{sha}}$	Resistance of the $a^{\text{th}}$ VSC transformer
$R_{\text{DC base}}$	DC base resistance
$\mathbf{R}$	Mismatch vector of control specifications
$R_{\text{max}}$	Maximum droop control gain
$S_{\text{base}}$	Base MVA
$\mathbf{S}_{\text{sha}}$	Complex line power flow at the terminal end of the line

	connecting the $a^{\text{th}}$ VSC to its AC bus
$\mathbf{V}$	AC bus voltage vector
$V_{\text{AC base}}$	AC base voltage
$V_{\text{DC}}$	DC bus voltage
$V_{\text{DC base}}$	DC base voltage
$V_{\text{DCI}}$	DC bus voltage at the inverter side
$V_{\text{DCI1}}$	DC bus voltage at the inverter-1 side
$V_{\text{DCI2}}$	DC bus voltage at the inverter-2 side
$V_{\text{DCR}}$	DC bus voltage at the rectifier side
$V_i$	AC bus voltage magnitude (rms) at $i^{\text{th}}$ bus
$\mathbf{V}_{\text{sha}}$	Voltage phasor representing the output of the $a^{\text{th}}$ VSC
$V_{\text{doR}}$	No load direct voltage at the rectifier side
$V_{\text{DCa}}^*$	DC voltage reference for the droop line of the $a^{\text{th}}$ VSC
$V_{\text{doI}}$	No load direct voltage at the inverter side
$V_{\text{DCav}}^*$	Average value of DC voltage references in a DC grid
$V_{\text{DCav}}$	Average value of the DC voltages in a DC grid
$V_{\text{Bus}}$	Specified AC bus voltage
$V_{\text{DCs}}$	Variable DC voltage source of IDCPFC
$V_{\text{DChigh}}^*$	Upper DC voltage threshold for constant DC power operation in nonlinear voltage droop characteristics
$V_{\text{DClow}}^*$	Lower DC voltage threshold for constant DC power operation in nonlinear voltage droop characteristics
$V_{\text{DC max}}$	Maximum DC voltage threshold in nonlinear voltage droop characteristics
$V_{\text{DC min}}$	Minimum DC voltage threshold in nonlinear voltage droop



	characteristics
$X_c$	Commutating reactance
$X_{c \text{ base}}$	Base value of the commutating reactance
$X_{\text{sha}}$	Leakage reactance of the $a^{\text{th}}$ converter transformer
$Y_{ik}$	Magnitude of the element in the $i^{\text{th}}$ row and $k^{\text{th}}$ column of the bus admittance matrix
$Y_{\text{dc}}$	Admittance matrix of DC grid
$Z_{\text{AC base}}$	AC base Impedance
$Z_{\text{sha}}$	Leakage impedance of the $a^{\text{th}}$ converter transformer
$Z_{\text{DC base}}$	DC base Impedance

## 2. LOWERCASE

$a_1$	Constant representing no load VSC losses
$a_I$	Converter transformer tap ratio at the inverter side
$a_R$	Converter transformer tap ratio at the rectifier side
$b_1$	Constant representative of the linear dependency of the VSC losses on the converter current magnitude
$c$	Constant representative of the VSC architecture
$c_1$	Constant representative of the quadratic dependency of the VSC losses on the converter current magnitude
$\mathbf{f}$	Vector of control functions
$g$	Number of generators in the AC system
$k$	Constant which depends on the type of converter in the LCC-HVDC system

$m$	Modulation index of the VSC
$n$	Total number of buses in the AC system
$n_b$	Number of bridges in the LCC-HVDC system
p.u	Per unit
$p$	Total number of DC terminals
$q$	Total number of VSCs
$y_{sha}$	Admittance of the converter transformer of the $a^{\text{th}}$ VSC
$z$	Total number of variable DC voltage sources in IDCPFC

### 3. UPPERCASE GREEK

$\Sigma$	Summation symbol
$\Delta$	Mismatch in electrical quantity of interest; mismatch vector

### 4. LOWERCASE GREEK

$\alpha_R$	Firing angle of the rectifier in the LCC-HVDC system
$\gamma_I$	Extinction angle of the inverter in the LCC-HVDC system
$\theta_i$	Phase angle of voltage at AC bus 'i'
$\theta$	Vector comprising phase angles of bus voltages
$\theta_{sh}$	Vector of phase angles of output voltage phasors of the VSC
$\theta_{sha}$	Phase angle of the output voltage phasor of the $a^{\text{th}}$ VSC
$\phi_R$	Power factor angle at the rectifier end of the LCC-HVDC system
$\phi_I$	Power factor angle at the inverter end of the LCC-HVDC system
$\phi_{sha}$	Phase angle of $y_{sha}$

## 5. SUBSCRIPTS

i	Bus 'i' quantity
AC	AC side quantity
DC	DC side quantity
DCR	DC quantity at rectifier end
DCI	DC quantity at inverter end
AC base	AC base values
DC base	DC base values
b	Number of bridges
R	Rectifier
I	Inverter
Sha	Shunt connected quantity of a <sup>th</sup> VSC
DCs	DC voltage source
IDCPFC	IDCPFC quantities
Loss	VSC loss quantity
DCmin	Minimum DC quantity
DCmax	Maximum DC quantity
DCavg	Average value of DC voltage

## 6. SUPERSCRIPTS

$( )^T$	Transpose of a matrix
$( )^{cal}$	Calculated or unknown quantity
$( )^*$	Conjugate of a complex quantity
$( )^{sp}$	Specified or known quantity
$( )^{old}$	Quantity in the original network without any HVDC link

## List of figures

Fig. no.	Title	Page no.
2.1	Three terminal HVDC link between buses 'i', 'j' and 'k' of an existing AC power system network	19
2.2	Flow chart of unified method corresponding to control strategy 1	28
2.3	Flow chart of sequential method corresponding to control strategy 1	29
2.4	Convergence characteristic for the base case power flow in the IEEE-300 bus system	31
2.5	Convergence characteristic of Table 2.6 for model-1 employing control strategy-1	32
2.6	Convergence characteristic of Table 2.6 for model-2 employing control strategy-1	32
2.7	Bus voltage profile of Table 2.6 for model-1 employing control strategy-1	33
2.8	Bus voltage profile of Table 2.6 for model-2 employing control strategy-1	33
2.9	Convergence characteristic of Table 2.6 for model-1 employing control strategy-2	34
2.10	Convergence characteristic of Table 2.6 for model-2 employing control strategy-2	35
2.11	Bus voltage profile of Table 2.6 for model-1 employing control strategy-2	35
2.12	Bus voltage profile of Table 2.6 for model-2 employing	36

	control strategy-2	
2.13	Convergence characteristic of Table 2.6 for model-1 employing control strategy-3	37
2.14	Convergence characteristic of Table 2.6 for model-2 employing control strategy-3	37
2.15	Bus voltage profile of Table 2.6 for model-1 employing control strategy-3	38
2.16	Bus voltage profile of Table 2.6 for model-2 employing control strategy-3	38
2.17	Convergence characteristic of Table 2.7 for model-1 employing control strategy-4	40
2.18	Convergence characteristic of Table 2.7 for model-2 employing control strategy-4	41
2.19	Bus voltage profile of Table 2.7 for model-1 employing control strategy-4	41
2.20	Bus voltage profile of Table 2.7 for model-2 employing control strategy-4	42
2.21	Convergence characteristic of Table 2.7 for model-1 employing control strategy-5	43
2.22	Convergence characteristic of Table 2.7 for model-2 employing control strategy-5	43
2.23	Bus voltage profile of Table 2.7 for model-1 employing control strategy-5	44
2.24	Bus voltage profile of Table 2.7 for model-2 employing control strategy-5	44
2.25	Convergence characteristic of Table 2.7 for model-1 employing control strategy-6	45

2.26	Convergence characteristic of Table 2.7 for model-2 employing control strategy-6	46
2.27	Bus voltage profile of Table 2.7 for model-1 employing control strategy-6	46
2.28	Bus voltage profile of Table 2.7 for model-2 employing control strategy-6	47
2.29	Convergence characteristic of Table 2.8 for model-1 employing control strategy-7	49
2.30	Convergence characteristic of Table 2.8 for model-2 employing control strategy-7	49
2.31	Bus voltage profile of Table 2.8 for model-1 employing control strategy-7	50
2.32	Bus voltage profile of Table 2.8 for model-2 employing control strategy-7	50
2.33	Convergence characteristic of Table 2.8 for model-1 employing control strategy-8	51
2.34	Convergence characteristic of Table 2.8 for model-2 employing control strategy-8	52
2.35	Bus voltage profile of Table 2.8 for model-1 employing control strategy-8	52
2.36	Bus voltage profile of Table 2.8 for model-2 employing control strategy-8	53
2.37	Convergence characteristic of Table 2.8 for model-1 employing control strategy-9	55
2.38	Convergence characteristic of Table 2.8 for model-2 employing control strategy-9	55
2.39	Bus voltage profile of Table 2.8 for model-1 employing control strategy-9	56

2.40	Bus voltage profile of Table 2.8 for model-2 employing control strategy-9	56
2.41	Convergence characteristic of Table 2.9 for model-1 employing control strategy-1	58
2.42	Convergence characteristic of Table 2.9 for model-2 employing control strategy-1	58
2.43	Bus voltage profile of Table 2.9 for model-1 employing control strategy-1	59
2.44	Bus voltage profile of Table 2.9 for model-2 employing control strategy-1	59
2.45	Convergence characteristic of Table 2.9 for model-1 employing control strategy-2	60
2.46	Convergence characteristic of Table 2.9 for model-2 employing control strategy-2	61
2.47	Bus voltage profile of Table 2.9 for model-1 employing control strategy-2	61
2.48	Bus voltage profile of Table 2.9 for model-2 employing control strategy-2	62
2.49	Convergence characteristic of Table 2.9 for model-1 employing control strategy-3	64
2.50	Convergence characteristic of Table 2.9 for model-2 employing control strategy-3	64
2.51	Bus voltage profile of Table 2.9 for model-1 employing control strategy-3	65
2.52	Bus voltage profile of Table 2.9 for model-2 employing control strategy-3	65



	control strategy-3	
2.53	Convergence characteristic of Table 2.10 for model-1 employing control strategy-4	66
2.54	Convergence characteristic of Table 2.10 for model-2 employing control strategy-4	67
2.55	Bus voltage profile of Table 2.10 for model-1 employing control strategy-4	67
2.56	Bus voltage profile of Table 2.10 for model-2 employing control strategy-4	68
2.57	Convergence characteristic of Table 2.10 for model-1 employing control strategy-5	70
2.58	Convergence characteristic of Table 2.10 for model-2 employing control strategy-5	70
2.59	Bus voltage profile of Table 2.10 for model-1 employing control strategy-5	71
2.60	Bus voltage profile of Table 2.10 for model-2 employing control strategy-5	71
2.61	Convergence characteristic of Table 2.10 for model-1 employing control strategy-6	72
2.62	Convergence characteristic of Table 2.10 for model-2 employing control strategy-6	72
2.63	Bus voltage profile of Table 2.10 for model-1 employing control strategy-6	73
2.64	Bus voltage profile of Table 2.10 for model-2 employing control strategy-6	73

2.65	Convergence characteristic of Table 2.11 for model-1 employing control strategy-7	76
2.66	Convergence characteristic of Table 2.11 for model-2 employing control strategy-7	76
2.67	Bus voltage profile of Table 2.11 for model-1 employing control strategy-7	77
2.68	Bus voltage profile of Table 2.11 for model-2 employing control strategy-7	77
2.69	Convergence characteristic of Table 2.11 for model-1 employing control strategy-8	78
2.70	Convergence characteristic of Table 2.11 for model-2 employing control strategy-8	79
2.71	Bus voltage profile of Table 2.11 for model-1 employing control strategy-8	79
2.72	Bus voltage profile of Table 2.11 for model-2 employing control strategy-8	80
2.73	Convergence characteristic of Table 2.11 for model-1 employing control strategy-9	81
2.74	Convergence characteristic of Table 2.10 for model-2 employing control strategy-9	81
2.75	Bus voltage profile of Table 2.11 for model-1 employing control strategy-9	82
2.76	Bus voltage profile of Table 2.11 for model-2 employing control strategy-9	82
3.1	Schematic diagram of a 'q' terminal PTP VSC-HVDC	89

	system	
3.2	Equivalent circuit of the ‘q’ terminal PTP VSC-HVDC system	90
3.3	Schematic diagram of a ‘q’ terminal BTB VSC-HVDC system	96
3.4	Equivalent circuit of a ‘q’ terminal BTB VSC-HVDC system	97
3.5	Flow Chart of the Unified NR AC-MVDC power-flow algorithm for the PTP connection	101
3.6	Flow Chart of the Unified NR AC-MVDC power-flow algorithm for the BTB connection	103
3.7	Representation of VSCs as equivalent complex load powers	105
3.8	Flow Chart of the Sequential AC-MVDC power-flow algorithm for the PTP connection	108
3.9	Convergence characteristic for the base case power flow in the IEEE-300 bus	111
3.10	Convergence characteristic for the study of Table 3.1	111
3.11	Bus voltage profile for the study of Table 3.1	112
3.12	Convergence characteristic for the first study of Table 3.2	114
3.13	Convergence characteristic for the second study of Table 3.2	114
3.14	Bus voltage profile for the first study of Table 3.2	116
3.15	Bus voltage profile for the second study of Table 3.2	116
3.16	Convergence characteristic for the study of Table 3.3	118
3.17	Bus voltage profile for the study of Table 3.3	119
3.18	Convergence characteristic for the study of Table 3.4	121
3.19	Bus voltage profile for the study of Table 3.4	121

3.20	Convergence characteristic for the first study of Table 3.5	124
3.21	Convergence characteristic for the second study of Table 3.5	124
3.22	Bus voltage profile for the first study of Table 3.5	125
3.23	Bus voltage profile for the second study of Table 3.5	125
3.24	Convergence characteristic for the study of Table 3.6	127
3.25	Bus voltage profile for the study of Table 3.6	127
3.26	Convergence characteristic for the study of Table 3.7	129
3.27	Bus voltage profile for the study of Table 3.7	129
4.1	Schematic diagram of an integrated AC-MTDC system	136
4.2	Equivalent circuit of Fig. 4.1	136
4.3	Linear Voltage Droop Characteristic of the $a^{\text{th}}$ VSC	140
4.4	Nonlinear Voltage Droop Characteristic of the $a^{\text{th}}$ VSC	142
4.5	Voltage Margin Characteristic of the $a^{\text{th}}$ VSC	142
4.6	Power flows for the $a^{\text{th}}$ VSC connected to its AC bus ' $(i+a-1)$ '	144
4.7	Flow chart of the proposed approach (Model A)	147
4.8	Flow chart of the proposed approach (Model B)	148
4.9	Convergence characteristic for the base case power flow in IEEE-300 bus system	154
4.10	Convergence characteristic for the case study of Table 4.1	154
4.11	Convergence characteristic for the case study of Table 4.2	155
4.12	Bus voltage profile for the study of Table 4.1	155

4.13	Bus voltage profile for the study of Table 4.2	156
4.14	Convergence characteristic for the case study of Table 4.3	159
4.15	Convergence characteristic for the case study of Table 4.4	159
4.16	Bus voltage profile for the study of Table 4.3	160
4.17	Bus voltage profile for the study of Table 4.4	160
4.18	Convergence characteristic for the study of Table 4.5	164
4.19	Convergence characteristic for the study of Table 4.6	165
4.20	Bus voltage profile for the study of Table 4.5	165
4.21	Bus voltage profile for the study of Table 4.6	166
4.22	Convergence characteristic for the study of Table 4.7	170
4.23	Convergence characteristic for the study of Table 4.8	170
4.24	Bus voltage profile for the study of Table 4.7	171
4.25	Bus voltage profile for the study of Table 4.8	171
5.1	Schematic diagram of an AC-MTDC system incorporating an IDCPFC	175
5.2	Equivalent circuit of AC-MTDC system incorporating an IDCPFC	176
5.3	Flow chart of the proposed approach with IDCPFC	184
5.4	Convergence characteristic for the base case power flow in IEEE-300 bus system	187
5.5	Convergence characteristic for the case study of row 1 in Table 5.1	188
5.6	Convergence characteristic for the case study of rows 3-11 in Table 5.1	188
5.7	Convergence characteristic for the case study of row 1	189

	in Table 5.2	
5.8	Convergence characteristic for the case study of rows 3-11 in Table 5.2	189
5.9	Bus voltage profile for the study of Table 5.1	190
5.10	Bus voltage profile for the study of Table 5.2	190
5.11	Convergence characteristic for the case study of rows 3-11 in Table 5.3	193
5.12	Convergence characteristic for the case study of rows 3-11 in Table 5.4	194
5.13	Bus voltage profile for the study of Table 5.3	194
5.14	Bus voltage profile for the study of Table 5.4	195
5.15	Convergence characteristic for the case study of row1 in Table 5.5	197
5.16	Convergence characteristic for the case study of rows 3-15 in Table 5.5	197
5.17	Bus voltage profile for the study of Table 5.5	198
5.18	Convergence characteristic for the case study of rows 3-15 in Table 5.6	200
5.19	Bus voltage profile for the study of Table 5.6	200
6.1	Schematic diagram of hybrid AC-MVDC system with offshore wind farms	203
6.2	Equivalent circuit of hybrid AC-MVDC system with offshore wind farms	204
6.3	Nonlinear Voltage Droop Characteristic of the a <sup>th</sup> VSC	210
6.4	Voltage Margin Characteristic of the a <sup>th</sup> VSC	211
6.5	Flow chart of the proposed approach (Model A)	216
6.6	Flow chart of the proposed approach (Model B)	217
6.7	Convergence characteristic of row in Table 6.1	220

6.8	Convergence characteristic of rows 2-6 in Table 6.1	220
6.9	Bus voltage profile for the study of Table 6.1	221
6.10	Convergence characteristic of rows 8-10 in Table 6.2	224
6.11	Bus voltage profile for the study of Table 6.2	224
6.12	Variation of the power generation of the OWF connected at bus 5 and the DC voltage	225
6.13	Variation of NI with the variation of $P_{DCWF2}$	225
6.14	Convergence characteristic of rows 2-10 in Table 6.3	227
6.15	Bus voltage profile for the study of Table 6.3	227
6.16	Convergence characteristic of rows 5-13 in Table 6.4	230
6.17	Bus voltage profile for the study of Table 6.4	230
6.18	Convergence characteristic of rows 5-13 in Table 6.5	232
6.19	Bus voltage profile for the study of Table 6.5	232

## List of tables

Table no.	Title	Page no.
2.1	Different base values for DC system	19
2.2	Basic converter equations for a 3 terminal DC network in per unit system	20
2.3	Some Control Strategies for a 3-Terminal DC link	22
2.4	Individual functions comprising 'f' for Control Strategy 1	26
2.5	Steps to compute active and reactive power injections in control strategies 1 and 5	27
2.6	Study with three different control strategies 1, 2 and 3 of unified method	39
2.7	Study with three different control strategies 4, 5 and 6 of unified method	48
2.8	Study with three different control strategies 7, 8 and 9 of unified method	54
2.9	Study with three different control strategies 1, 2 and 3 of sequential method	63
2.10	Study with three different control strategies 4, 5 and 6 of sequential method	74
2.11	Study with three different control strategies 7, 8 and 9 of sequential method	83
3.1	Study of IEEE 300 bus system with BTB VSC HVDC network	110
3.2	Study of IEEE 300 bus system with three terminal PTP VSC HVDC network	115
3.3	Study of IEEE 300 bus system with four terminal VSC HVDC network	117
3.4	Study of IEEE 300 bus system with five terminal VSC HVDC network	120



3.5	Study of IEEE 300 bus system with three terminal VSC HVDC network	123
3.6	Study of IEEE 300 bus system with four terminal VSC HVDC network	126
3.7	Study of IEEE 300 bus system with five terminal VSC HVDC network	128
3.8	A comparison of the convergence characteristics of the unified and the sequential AC-DC power-flow algorithms	130
3.9	A comparison of convergence features with existing models	131
4.1	Study of IEEE 300 bus system with three terminal VSC HVDC network incorporating linear DC voltage droop characteristics (Model A)	151
4.2	Study of IEEE 300 bus system with three terminal VSC HVDC network incorporating linear DC voltage droop characteristics (Model B)	153
4.3	Study of IEEE 300 bus system with three terminal VSC HVDC network incorporating nonlinear DC voltage droop characteristics with dead-band	157
4.4	Study of IEEE 300 bus system with three terminal VSC HVDC network employing voltage margin control	158
4.5	Study of IEEE 300 bus system with five terminal VSC HVDC network employing linear DC voltage droop characteristics (Model A)	162
4.6	Study of IEEE 300 bus system with five terminal VSC HVDC network incorporating linear DC voltage droop characteristics (Model B)	163
4.7	Study of IEEE 300 bus system with five terminal VSC	167

	HVDC network incorporating non-linear voltage droop characteristics with Dead Band	
4.8	Study of IEEE 300 bus system with five terminal VSC HVDC network incorporating non-linear DC voltage droop characteristics (Voltage Margin)	169
5.1	Study of IEEE 300 bus system with three terminal VSC HVDC network incorporating IDCPFC in DC current control mode	185
5.2	Study of IEEE 300 bus system with three terminal VSC HVDC network incorporating IDCPFC in DC current control mode	186
5.3	Study of IEEE 300 bus system with three terminal VSC HVDC network incorporating IDCPFC in DC power control mode	192
5.4	Study of IEEE 300 bus system with three terminal VSC HVDC network incorporating IDCPFC in DC power control mode	192
5.5	Study of IEEE 300 bus system with five terminal VSC HVDC network incorporating IDCPFC in DC current control mode	196
5.6	Study of IEEE 300 bus system with five terminal VSC HVDC network incorporating IDCPFC in DC power control mode	199
6.1	Study of IEEE 300 bus system with five terminal VSC HVDC network incorporating OWFs (Slack control)	219
6.2	Study of IEEE 300 bus system with five terminal VSC HVDC network incorporating OWFs (Model A)	223
6.3	Study of IEEE 300 bus system with five terminal VSC HVDC network incorporating OWFs (Model B)	226

6.4	Study of IEEE 300 bus system with five terminal VSC HVDC network incorporating OWFs with Droop Control and Dead-band at Operating Point A	228
6.5	Different operating points for nonlinear V-P droop with dead band	229
6.6	Study of IEEE 300 bus system with five terminal VSC HVDC network incorporating OWFs with Droop Control and Voltage Margin	231
6.7	A comparison of convergence features with existing models	233

## ABSTRACT

For the past few decades, the construction of generation facilities and new transmission lines have been delayed in light of rising energy cost, environmental concerns, rights-of-way (RoW) restrictions and other legislative and cost problems. In addition, system stability issues may render long distance AC transmission infeasible. In this respect, High-Voltage DC (HVDC) transmission requires a smaller RoW, simpler and cheaper transmission towers, reduced conductor and insulator costs, reduced losses and is not limited by stability considerations. A HVDC link can augment system reliability by interconnecting two asynchronous AC grids and can integrate offshore wind farms with onshore AC grids.

The first commercial application of HVDC transmission took place between the Swedish mainland and the island of Gotland in 1954, using mercury arc valves. Subsequently, the first 320 MW thyristor based HVDC system was commissioned in 1972 between the Canadian provinces of New Brunswick and Quebec. Continuous development in conversion equipment led to reduced size and cost which resulted in more widespread use of HVDC transmission. The thyristor based line commutated converter (LCC) based HVDC (LCC-HVDC) technology now constitutes the bulk of the installed HVDC transmission corridors over the world.

With LCC-HVDC, for controlling the active power, both the rectification and inversion processes consume reactive power. This necessitates the use of reactive power sources to match the reactive power demand at both ends. To reduce the effects of harmonic voltages and currents generated by the converters, harmonic filters are used on both the AC and the DC sides. Also, a minimum short circuit level is required to avoid voltage instability. However, despite its limitations, LCC-HVDC possesses

high reliability, good overload capability and lower converter losses. It requires low maintenance and capital cost and is robust to DC fault currents due to its current regulating nature.

Subsequently, the development of the Insulated Gate Bipolar Transistor (IGBT) paved the way for the Voltage Sourced Converter (VSC) based HVDC (VSC-HVDC) technology, which offered significant advantages over the LCC-HVDC. VSC-HVDC facilitates independent active and reactive power control, along with reduction in filter size [8] - [18]. VSC-HVDC also enables the integration of offshore wind farms with AC grids. Compact, modular designs of the VSCs enable rapid installation, commissioning and relocation. Unlike LCC-HVDC, fixed DC voltage polarity in the VSC-HVDC enables the use of stronger and lighter XLPE cables, suitable for under-sea environment and attractive for offshore transmission. In addition, VSC-HVDC systems can be integrated with AC systems having low short circuit ratios.

The first 3-MW, VSC-HVDC link was commissioned at Hellsjon in Sweden in 1997. Subsequently, rapid development in the VSC technology has now resulted in the availability of higher rated (up to 2000 MW) VSC-HVDC links. This has resulted in the installation and commissioning of a large number of VSC-HVDC systems worldwide.

Now, in both LCC-HVDC and VSC-HVDC systems, the converter stations can be connected in two ways - back-to-back (BTB) and point-to-point (PTP). Most of the MTDC systems installed worldwide are in PTP configurations, their DC sides being interconnected through DC links or cables.

Unlike a two-terminal HVDC interconnection, a multi-terminal HVDC (MTDC) system is more versatile and better capable of utilizing the economic and technical advantages of HVDC technology. Moreover, sources of renewable energy can be easily integrated with a MTDC system, as and when the need arises.

For proper MTDC operation, DC voltage control is an essential requirement. In this respect, several control techniques have been envisaged. These include DC slack bus control (also known as DC master-slave control), distributed DC voltage droop control, power synchronization control, hierarchical power control and transient management control.

However, among all the DC voltage control techniques, the DC slack bus control and distributed DC voltage droop control have been the more popular and widely employed ones.

In DC slack bus control, the voltage of one DC terminal, known as the DC slack bus, is maintained constant by the master converter. The main disadvantage of this control scheme is the DC grid instability following a failure of the master converter.

The above problem can be tackled by ensuring that individual converters contribute to the DC voltage regulation scheme by adjusting their active power flow in response to changes in the DC voltage with the operating point, known as DC voltage droop control. For MTDC control, both linear and nonlinear types of DC voltage droop characteristics have been envisaged to ensure proper sharing based on the converter ratings. Voltage-Power (V-P), Voltage-Current (V-I), Voltage Margin (VM), V-P droop with power Dead-Band (DB) and V-P droop with voltage limits are some of the more widely used characteristics.

To manage power-flows within the DC grids, DC power-flow control devices have been conceptualized and developed. They include the use of DC transformers, variable resistors, current flow controllers (CFCs), thyristor power flow controllers (TPFCs), DC series voltage sources and Interline DC Power Flow Controllers (IDCPFCs) for power-flow control in meshed DC grids. The IDCPFC is a DC power-flow controller without an external AC or DC source and is used for power-flow management of DC grids, similar to its AC counterpart - the flexible AC transmission systems (FACTS) based Interline Power Flow Controller (IPFC).

Now, for proper planning, design and operation of AC power systems integrated with multi-terminal DC grids, the development of suitable power-flow models of both LCC and VSC based hybrid AC-DC systems is a fundamental requirement.

Because of the need of suitable power-flow models of both LCC and VSC based hybrid AC-DC systems and the adoption of the Newton-Raphson algorithm as the de-facto standard for industrial power-flow solutions, a lot of attention is being paid towards the development of Newton-Raphson power-flow models of such hybrid AC-DC systems.

The development of Newton-Raphson power-flow models of both LCC and VSC based integrated AC-DC systems has resulted in two distinctly different approaches known as the unified and the sequential Newton algorithms, respectively. In the former, the AC and the DC quantities are solved simultaneously, while in the latter, the AC and the DC systems are solved separately in each iteration. Unlike the unified method, the sequential method is easier to implement and poses lesser computational burden due to the smaller size of the Jacobian matrix. Many

comprehensive research works have been carried out for the development of unified and sequential Newton power-flow models of both LCC and VSC based hybrid AC-DC systems.

However, from the research works existing in the literature, it is observed that the following issues have not been addressed.

1. For the Newton power-flow modelling of LCC based hybrid AC-DC systems, the base values of the various DC quantities can be defined in several ways, giving rise to different per-unit AC-DC system models, each model comprising separate set of system equations in per-unit. Although different per-unit system models affect the convergence of the AC-DC power-flow algorithm in different ways, the aspect has not been investigated in detail.
2. A comprehensive comparison of the unified and sequential Newton power-flow algorithms vis-à-vis standard and non-standard control strategies for LCC based hybrid AC-DC systems is yet to be carried out.
3. Most of the existing Newton power-flow models of VSC based hybrid AC-DC systems do not take into account the modulation index of a converter. The modulation index 'm' is an important parameter for VSC operation. Operational considerations limit the minimum and the maximum value of the modulation index. Thus, a power-flow model should yield the value of 'm' and ' $V_{DC}$ ' directly, for a given operating condition, so that it can be checked whether 'm' lies within its specified limits (with sufficient margin for a dynamic response), along with ' $V_{DC}$ '.



4. Development of a unified Newton power-flow model of VSC based hybrid AC-DC systems incorporating both linear and nonlinear DC voltage droop control.
5. Incorporation of DC power flow controllers like IDCPFC in an existing Newton power-flow model of a VSC based hybrid AC-DC system.
6. Integration of renewable energy resources like offshore wind farms (OWFs) with existing power-flow models of VSC based hybrid AC-DC systems.

To address the above limitations, in the present thesis, an attempt has been made to investigate systematically the development of unified and sequential Newton power-flow models of both LCC based and VSC based hybrid AC-DC systems.

For LCC based hybrid AC-DC power systems, both the unified and the sequential Newton power-flow models are developed to investigate the effects of different per-unit AC-DC system models and different DC link control strategies on their convergence. Subsequently, both the unified and sequential Newton power-flow models of VSC based hybrid AC-DC systems are developed in this thesis to include MTDC grid control strategies like master-slave control and DC voltage droop control (both linear and nonlinear). Thereafter, DC grid power-flow controllers like IDCPFC and multiple offshore wind farms are also included in these power-flow models. In all the models developed, the modulation indices of the pulse-width modulation scheme pertaining to the VSCs appear as unknowns, along with the converter DC side voltages and the phase angles of the fundamental converter AC side voltages.

The outline of the contributing chapters of the thesis is as follows:

Chapter 2 presents the development of unified and sequential Newton power-flow models of LCC based hybrid AC-DC systems, in light of different per-unit AC-DC system models and diverse DC link control strategies employed.

Chapter 3 addresses the development of unified and sequential Newton power-flow models of VSC based hybrid AC-DC systems for both the back-to-back (BTB) and the point-to-point (PTP) VSC-HVDC configurations, employing DC slack-bus (master-slave) control for the MTDC grid.

Chapter 4 addresses the development of unified Newton power-flow models of VSC based hybrid AC-DC systems employing DC voltage droop control. The DC voltage droop control comprises both linear {voltage-power (V-P) and voltage-current (V-I)} as well as non-linear {power dead-band and voltage limits} droop characteristics. Based on the terminal end line active and reactive power specifications of the VSCs, two different droop control models have been developed.

Chapter 5 addresses the development of a unified Newton power-flow model of VSC based hybrid AC-DC systems incorporating IDCPFC(s) for the power-flow management of the DC grid. The IDCPFC(s) employs both DC link current and DC link power controls.

Chapter 6 addresses the development of a Newton power-flow model of VSC based hybrid AC-DC systems integrated with multiple offshore wind farms (OWFs). The VSCs employ both linear and nonlinear DC voltage droop control. The effects of the OWFs on the DC grid voltage profile and the power-flow convergence are investigated, vis-à-vis varying wind farm powers.

VSC losses are included in all the power-flow models.

Validity of all the models investigated is demonstrated on the IEEE 300 bus test system to test their convergence characteristics.

Finally, Chapter 7 presents the conclusions of the work reported in the thesis and makes some suggestions for further work in the areas covered by the thesis.

# TABLE OF CONTENTS

	Page no.
Certificate	i
Acknowledgement	ii
List of abbreviations	iv
List of symbols	v
List of figures	xii
List of tables	xxiii
Abstract	xxvii
<b>Chapter 1</b>	
Introduction and literature review	1-15
1.1 Introduction	1
1.2 Scope of the present work	13
<b>Chapter 2</b>	
Newton Power-Flow Modelling of Line Commutated Converter (LCC) Based Integrated AC-DC Systems	16-85
2.1 Introduction	16
2.2 Modelling of Integrated AC-MLDC Systems	18
2.3 Control strategies for MLDC grids	20
2.4 Power Flow Equations of Integrated AC-MLDC Systems	23
2.5 Implementation in Newton Power Flow Analysis	25
2.6 Case studied and results	29
2.6.1 Unified AC-DC power-flow studies of IEEE 300 bus test system	30

	incorporating 3-terminal LCC-HVDC network	
	2.6.2 Sequential AC-DC power-flow studies of IEEE 300 bus test system incorporating 3-terminal LCC-HVDC network	57
	2.7 Conclusions	84
<b>Chapter 3</b>	Newton Power Flow Modelling of Voltage Source Converter (VSC) Based Integrated AC-DC Systems Employing DC Slack-Bus Control	86-132
	3.1 Introduction	86
	3.2 Modelling of Integrated AC-MVDC Systems Employing DC Slack Bus Control	88
	3.2.1 Modelling of Integrated AC-MVDC Systems in the PTP Configuration	88
	3.2.2 Power Flow Equations of Integrated AC-MVDC system in the PTP Configuration	91
	3.2.3 Modelling of Integrated AC-MVDC Systems in the BTB Configuration	96
	3.2.4 Power Flow Equations of Integrated AC-MVDC systems in the BTB Configuration	97
	3.3 Implementation in Newton Power Flow Analysis	98
	3.3.1 Unified AC-DC Power Flow Method	98
	3.3.1.1 Unified AC-DC Power-Flow Method for PTP Configuration	98
	3.3.1.2 Unified AC-DC Power-Flow Method for BTB Configuration	101
	3.3.2 Sequential AC-DC Power Flow Method	103
	3.3.2.1 Sequential AC-DC Power-Flow Method for the PTP Configuration	103

	3.3.2.2 Sequential AC-DC Power-Flow Method for the BTB Configuration	108
	3.4 Case Studies and Results	109
	3.4.1 Studies with unified power-flow model of integrated AC-MVDC systems	109
	3.4.2 Studies with sequential power-flow model of integrated AC MVDC systems	122
	3.5 Conclusions	131
<b>Chapter 4</b>	Newton Power Flow Modelling of Voltage Source Converter (VSC) Based Integrated AC-DC Systems Employing DC Voltage Droop Control	133-172
	4.1 Introduction	133
	4.2 Modelling of Integrated AC-MVDC Systems Employing DC Voltage Droop Control	134
	4.3 Power Flow Equations of Integrated AC- MVDC systems with DC Voltage Droop Control	137
	4.4 DC Voltage droop control in MVDC Systems	139
	4.5 Modeling of AC-MTDC Systems with DC Voltage Droop Control	143
	4.6 Case Studies and Results	149
	4.6.1 Studies of three terminal VSC-HVDC network incorporated in the IEEE 300 bus system	150
	4.6.2 Studies of five terminal VSC-HVDC network incorporated in the IEEE 300 bus system	161
	4.7 Conclusions	172
<b>Chapter 5</b>	Newton Power Flow Modelling of Voltage Source Converter (VSC) Based Integrated AC-DC Systems Incorporated with Interline DC Power Flow Controller (IDCPFC)	173-201
	5.1 Introduction	173

	5.2 Modeling of AC-MVDC Systems incorporating IDCPFCs	174
	5.3 Power Flow Equations of Integrated AC- MVDC systems incorporating IDCPFC	178
	5.4 Implementation in Newton Power Flow Analysis	182
	5.5 Case studied and results	183
	5.5.1 Study of three terminal VSC-HVDC network incorporating IDCPFC	184
	5.5.2 Study of five terminal VSC-MTDC network incorporating IDCPFC	195
	5.6 Conclusions	200
<b>Chapter 6</b>	Newton Power Flow Modelling of Voltage Source Converter (VSC) Based Integrated AC-DC Systems with Renewable Energy Sources	202-233
	6.1 Introduction	202
	6.2 Modeling of AC-MVDC systems incorporating renewable energy sources	202
	6.3 Power flow equations in the proposed model of integrated VSC HVDC System with Renewable Energy Sources	205
	6.4 Modeling of AC-MTDC Systems employing DC slack bus Control	207
	6.5 Modeling of AC-MTDC Systems with DC Voltage Droop Control	208
	6.5.1 Types of DC voltage droop control	209
	6.5.2 Implementation of DC voltage droop control in AC-MTDC systems integrated with offshore wind farms	211
	6.6 Case Studies and Results	217

	6.6.1 Study of five terminal MVDC network with offshore wind farms employing DC slack bus control	218
	6.6.2 Study of five terminal MVDC network with offshore wind farms employing DC voltage droop control	221
	6.7 Conclusions	233
<b>Chapter 7</b>	Conclusions and scope of further work	234-236
	7.1 Conclusions	234
	7.2 Some suggestions for further work	235
<b>Bibliography</b>		237-249
<b>Appendix A</b>	Derivations of expressions	250-256
<b>Appendix B</b>	Author's brief biography	257
<b>Appendix C</b>	List of publications	258



# Chapter 1

## Introduction and Literature Review

### 1.1 Introduction

For the past few decades, the construction of generation facilities and new transmission lines have been delayed in light of rising energy cost, environmental concerns, rights-of-way (RoW) restrictions and other legislative and cost problems. In addition, system stability issues may render long distance AC transmission infeasible. In this respect, High-Voltage DC (HVDC) transmission has proved to be a viable option. For a given power level, a DC link requires a smaller RoW, simpler and cheaper transmission towers, reduced conductor and insulator costs along with reduced losses. Unlike AC, the length of a DC transmission link is not limited by stability considerations. A HVDC link can be used to augment system reliability by interconnecting two asynchronous AC grids [1]-[16]. For lengths exceeding about 500 km, HVDC transmission is proving to be more economical than AC. In recent years, the harnessing of renewable energy sources has become a necessary and attractive option. In this respect, HVDC links can be used to integrate offshore wind farms with onshore AC grids [4], [12], [15] and [16].

The first commercial application of HVDC transmission took place between the Swedish mainland and the island of Gotland in 1954, using mercury arc valves. Subsequently, the first 320 MW thyristor based HVDC system was commissioned in 1972 between the Canadian provinces of New Brunswick and Quebec [2] – [4]. Over the years, development in conversion equipment reduced their size and cost which

resulted in more widespread use of HVDC transmission. This so called line commutated converter (LCC) based HVDC (LCC-HVDC) technology now constitutes the bulk of the installed HVDC transmission corridors over the world.

With LCC-HVDC, commutation is achieved using the source voltage and the leakage reactance of the converter transformer. Thus, for controlling the active power, both the rectification and inversion processes consume reactive power, the reactive power consumption varying with load. This necessitates the use of reactive power sources to match the reactive power demand at both ends [1], [6], [7]. To reduce the effects of harmonic voltages and currents generated by the converters, harmonic filters are used on both the AC and the DC sides. Also, in LCC-HVDC systems, a minimum short circuit level is required to avoid voltage instability. In LCC-HVDC transmission, the reversal of power is carried out by reversing the polarity of the DC voltage. Hence, stronger and lighter Cross Linked Poly-Ethylene (XLPE) cables cannot be used, which are suited for harsh environmental conditions as encountered in the ocean beds [4], [12]. However, despite its limitations, LCC-HVDC possesses high reliability, good overload capability and lower converter losses. It requires low maintenance and capital cost and is robust to DC fault currents due to its current regulating nature [1], [6], [7].

Subsequently, the advancement of power electronics led to the development of the Insulated Gate Bipolar Transistor (IGBT), which paved the way for the Voltage Sourced Converter (VSC) based HVDC (VSC-HVDC) technology. The VSC-HVDC offered significant advantages over the LCC-HVDC. VSC-HVDC facilitates independent active and reactive power control, along with reduction in filter size [8] - [18]. Compact, modular designs of the VSCs enable rapid installation, commissioning and relocation. In addition, due to the secure energy supply and environmental

changes, the demand of renewable energy has been increasing. This has necessitated the integration of offshore renewable power resources with the onshore AC grid. In order to achieve this, VSC based HVDC transmission has been proposed over conventional HVDC [4], [12], [16], [19]-[20]. Unlike LCC-HVDC, fixed DC voltage polarity in VSC-HVDC enables the use of stronger and lighter XLPE cables, suitable for under-sea environment, making VSC based HVDC systems particularly attractive for offshore transmission [4], [12]. This enables the integration of offshore wind farms with AC grids. Due to the use of self commutated devices in VSC-HVDC technology, ac system voltage for commutation is not required and therefore VSC-HVDC systems can be integrated with AC systems having low short circuit ratios.

The first 3-MW, VSC-HVDC link was commissioned at Hellsjon in Sweden in 1997. Subsequently, rapid development in the VSC technology has now resulted in the availability of higher rated (up to 2000 MW) VSC-HVDC links. Notable among other VSC-HVDC projects are BorWin 1 and 2, HelWin 1 and 2, INELFE, the South-West link, DolWin 1 and 2 etc [4], [12]. A meshed multi-terminal DC (MTDC) grid linking offshore wind farms and three asynchronous AC grids of the European Network of Transmission System Operators for Electricity (ENTSO-E) is also being envisaged in the North Sea region [19], [20].

Now, in both the LCC-HVDC and the VSC-HVDC systems, the converter stations can be located closely, in the same sub-station or remotely, at different locations. The corresponding configurations are known as back-to-back (BTB) and point-to-point (PTP), respectively. Most of the MTDC systems installed worldwide are in PTP configurations, their DC sides being interconnected through DC links or cables [4], [10], [12].

Unlike a two-terminal HVDC interconnection, a multi-terminal HVDC (MTDC) system is more versatile and better capable of utilizing the economic and technical advantages of the HVDC technology. Moreover, sources of renewable energy can be easily integrated with a MTDC system, as and when the need arises [19] - [21].

For proper MTDC operation in DC grids, DC voltage control is an essential requirement. In this respect, several control techniques have been envisaged. An extensive review of these control techniques has been presented in [22]. [23] – [36] detail some of the comprehensive research works carried out in the area of DC voltage control. [23] has employed DC slack bus control on two and six terminal DC systems. In a similar manner, [24] –[29] have applied DC voltage droop control to diverse topologies of VSC based hybrid AC-DC networks and have provided a design methodology to select the droop gains. [30] - [31] have employed DC voltage droop control for grid side VSCs to transmit wind farm generated power to AC grids. Application of power synchronization control for integrating offshore wind farms (OWFs) and island systems to an AC grid using a VSC-HVDC link have been reported in [32] - [34]. Further, [35] and [36] have employed hierarchical power control and transient management control, respectively, in VSC-MTDC grids.

However, among all the DC voltage control techniques, DC slack bus control (also known as master-slave control) and distributed voltage droop control have been the more popular and widely employed ones [10]-[12], [23]-[31], [37].

In DC slack bus control [10]-[12], [23], the voltage of one DC terminal is maintained constant. It is known as the DC slack bus and it sustains the power balance of the DC grid. The VSC which controls its DC side voltage is known as the master

VSC. The rest of the VSCs regulate their active power flow. The main disadvantage of this control scheme is the DC grid instability following a failure of the master converter.

The above problem can be tackled by ensuring that individual VSCs contribute to the DC voltage regulation scheme by adjusting their active power flow in response to changes in the DC voltage with the operating point, known as DC voltage droop control [12], [24]-[31], [37]. In this scheme, in case of outage of the master converter, the remaining ones can share the DC grid power imbalance to maintain its reliability. For MTDC control, different types of DC voltage droop control have been envisaged to ensure proper sharing based on the converter ratings. These include both linear and nonlinear voltage droop characteristics. Among the linear ones, Voltage-Power (V-P) and Voltage-Current (V-I) droops have been the two most popular strategies for DC voltage droop control. Nonlinear voltage droop control characteristics include dead-bands and limits. Among the nonlinear ones, Voltage Margin (VM), V-P droop with power Dead-Band (DB) and V-P droop with voltage limits are some of the more widely used characteristics [12], [24]-[31], [37].

One of the main challenges in VSC based integrated AC-DC systems is the issue of managing power-flows within the DC grids. Although the converters control the power injections into the DC grid, the power-flows within the DC grid depend upon the resistances of the DC lines or cables [37]-[38]. In this respect, DC power-flow control devices [39]-[44] have been conceptualized and developed. These DC power-flow control devices can be either DC/DC transformer based or auxiliary variable voltage source based. [39] has reported the use of DC transformers to regulate power-flows in DC networks. [40] has proposed the use of DC transformers, variable resistors and series voltage sources for power-flow control in meshed DC

grids. [41] has proposed a current flow controller (CFC) for enhancing the control of around a DC grid. [42] has considered a thyristor power flow controller (TPFC) for four-quadrant control in a MTDC grid. The Interline DC Power Flow Controller (IDCPFC) reported in [43]-[44] is a DC power-flow controller without an external AC or DC source which can be used for power-flow management of MTDC grids. It is similar to the Interline Power Flow Controller (IPFC), which is a VSC based flexible AC transmission systems (FACTS) device developed for AC grids [45]-[47].

Now, for proper planning, design and operation of AC power systems integrated with multi-terminal DC grids, power-flow solution of such hybrid AC-DC systems are required. These comprise both line commutated converter (LCC) and voltage sourced converter (VSC) based hybrid AC-DC systems. Therefore, the development of suitable power-flow models of such systems is a fundamental requirement.

The earliest power-flow algorithms were based on the Gauss-Siedel method. However, they exhibited poor convergence characteristics. Subsequently, the Newton-Raphson Power-Flow method was developed. With development of sparse matrix techniques, the Newton-Raphson method emerged as the method of choice in commercial power-flow packages [48]. To reduce the computational burden, a simplification of the Newton-Raphson method – the fast-decoupled power-flow, was also developed [49].

For the power flow solution of both LCC and VSC based integrated AC-DC systems using the Newton Raphson method, two different algorithms have generally been reported in the literature. These are known as the unified and the sequential method, respectively. In the unified method, the AC and the DC quantities are solved

simultaneously, which increases the size of the Jacobian matrix. In the sequential AC–DC power-flow algorithm, the AC and the DC systems are solved separately in each iteration and are coupled by injecting an equivalent amount of real and reactive power at the terminal AC buses [1], [6] and [7]. Unlike the unified method, the sequential method is easier to implement and poses lesser computational burden due to the smaller size of the Jacobian matrix.

Some comprehensive power-flow and optimal power-flow (OPF) models of LCC based hybrid AC-DC systems have been presented in [50]-[75]. [50] has presented a simple LCC based AC-DC power flow formulation for a two terminal DC network. A fast decoupled algorithm to compute the power-flow solution of a hybrid AC-DC network has been reported in [51], which can be used to investigate nonstandard control strategies to maintain overall system stability. [52] has proposed a novel unified power-flow model of hybrid AC-DC systems by using the PI bus formulation to model the nonlinear load bus. An efficient and versatile optimal power flow algorithm for hybrid AC-DC systems has been described in [53]. [54] has presented a sequential AC-DC power flow algorithm using the modified Gauss and Gauss-Seidel methods. [55] has presented an optimal reactive power-flow (ORPF) model with generator capability limits using a heuristic approach. [56], [57] have implemented optimal power-flow models of integrated AC-DC systems using genetic algorithm and artificial bee colony algorithm, respectively. [58] has presented an ORPF model using genetic algorithms. An ORPF model of offshore wind farms connected to the AC grid using LCC-HVDC link has been presented in [59]. [60] has presented a second order AC-DC power flow algorithm based on the Cartesian coordinate formulation of ac-dc system equations. [61] - [64] have presented unified power-flow models of LCC based integrated AC-DC systems. [61] has implemented a

unified, fast decoupled, AC-DC power-flow model in the New Zealand system. It comprises multiple AC systems interconnected by a DC link. [62] has presented a unified AC-DC power-flow model in which the equations pertaining to the DC system can be included directly in the Newton power-flow model of the AC system. [63] has presented a fast decoupled power-flow technique for integrated AC-DC systems, using Zollenkof's bifactorization. [64] has presented a novel, unified power-flow method to include DC networks in power-flow calculations by treating the converters as voltage dependent loads. [65] has presented a sequential AC-DC power-flow model of hybrid AC-DC systems with an ability to handle discrete tap-step and tap limits of the converter transformer. [66] has also presented a sequential AC-DC power-flow model without considering the effect of the converter transformer reactance. [67] has presented a sequential power-flow model of parallel multi-terminal DC networks with an ability to handle a large variety of converter controls and modify them to respect angle, transformer tap and converter voltage and current limits. In [68], an improved sequential AC-DC power-flow model has been presented for state estimation of hybrid AC-DC systems. An improved sequential approach for multi-infeed DC systems has been presented in [69] to enhance the robustness of the AC-DC power-flow calculation. A novel sequential power-flow model of hybrid AC-DC systems is presented in [70] which can handle the constraints on the DC currents, converter control angles and off nominal tap ratios. [71] has shown that the solvability of the HVDC system depends on the non-singularity of the linearised co-efficient matrix which integrates the network and control modes. [72] has presented a sequential AC-DC power-flow model which replaces the DC network by voltage dependent loads. [73] has described a sequential algorithm to solve hybrid AC-DC networks by representing the converters by Norton's equivalent current sources in parallel with the



commutation resistances. An economical and fast power-flow algorithm for hybrid AC-DC systems has been presented in [74]. [75] has presented a power-flow model of hybrid AC-DC systems to extend the formulation of [74] by including the converter transformer reactance and decoupling the AC system variables from the DC network.

Similar to LCC based hybrid AC-DC systems, [76]-[103] present some comprehensive research works carried out in the area of power-flow and optimal power-flow (OPF) modeling of VSC based hybrid AC-DC systems. One of the earliest power-flow models for VSC based hybrid AC-DC systems was proposed by [76]. However, the analysis of [76] was limited to a two-terminal network only. [77] has presented a unified power-flow model of multi-terminal VSC based integrated AC-DC systems for both the back-to-back (BTB) and the point-to-point (PTP) configurations. [78] has introduced a unified AC-DC unit (ADU) which has been applied to two different AC-DC analyses. [79] has proposed a unified power-flow algorithm for VSC based AC-DC networks able to deal with different DC voltage control schemes. A sequential AC-DC power-flow model using the equivalent power injection method has been presented in [80]. A sequential power-flow model for multi-terminal VSC-HVDC systems employing DC voltage droop control has been presented in [81]. [82] presents a comprehensive, sequential power-flow model of VSC based integrated AC-DC systems employing various nonlinear DC voltage droop control. [83] presents an OPF model of a VSC based hybrid AC-DC network with two different VSC control strategies to minimize the transmission loss. An improved analytical model of VSC based hybrid AC-DC power systems employing DC voltage droop control has been presented in [84], which estimates the result of power distributions, DC voltage deviations and power loss variations, taking converter outage and overload into account. [85] has presented a unified power-flow

model of VSC-HVDC systems where the VSCs have been modeled as compound transformer devices to account for the phase-shifting and scaling nature of the pulse-width modulation (PWM) control. An OPF model of an AC system integrated with a VSC based HVDC network has been proposed in [86]. However, the analysis is limited to a two-terminal HVDC network. [87] extends the method of DC OPF to AC grids for use in combined AC-DC networks. [88] has presented a unified power-flow model of VSC based hybrid AC-DC systems applicable for any number of converters, network configurations and control methodologies. [89] presents a unified power-flow model of VSC based hybrid AC-DC systems in augmented rectangular coordinates. [90] has proposed a general frame-of-reference for true unified, iterative solutions of AC/DC power flows which accommodates any number of AC/DC sub-networks. [91] has proposed a highly convergent algorithm which employs the power-flow analysis of AC grids for analyzing power-flows in DC networks. [92] - [94] have presented comprehensive, sequential power-flow model of multi-terminal, VSC based hybrid AC-DC networks employing DC slack bus control. However, the analysis of [93] does not take into account VSC losses. [95] has reported that incorporation of VSC-HVDC in meshed networks reduces overall system losses and that the reduction increases with increased system loading. [96] has implemented a sequential power-flow model of a multi-terminal, VSC based hybrid AC-DC network using MATPOWER libraries. A comparative analysis of the unified and sequential power-flow models of multi-terminal, VSC based hybrid AC-DC networks is presented in [97]. [98] has investigated the speed and the robustness of unified and sequential VSC-MTDC models employing DC master slave and voltage droop controls, inclusive of converter station losses. A mixed AC-DC OPF model has been employed in [99] for the cost-benefit analysis of VSC-MTDC installations. [99] has reported

that VSC-MTDC systems lead to a reduction in the total operation cost. [100] has implemented a VSC-HVDC model in an existing OPF algorithm, with the various inequality constraints handled by the multipliers method. An improved corrective security constrained optimal power flow (CSCOPF) for a meshed AC/DC power transmission network with VSC-MTDC grids has been presented in [101]. [102] has presented an effective dc voltage and power-sharing control structure for multi-terminal dc (MTDC) grids based on an optimal power flow (OPF) procedure and voltage-droop control structure in order that the optimally-tuned voltage-droop controllers lead to the optimal operation of the MTDC grid. [103] has presented an OPF model for MTDC grids with offshore wind farms and storage devices. The optimization scheme includes real weather conditions and operational constraints are included to achieve the best scheduling of the system and minimum losses.

However, in most of these models, the following issues have not been addressed.

1. For the Newton power-flow modeling of LCC based hybrid AC-DC systems, the base values of the various DC quantities can be defined in several ways, giving rise to different per-unit AC-DC system models, each model comprising separate set of system equations in per-unit. Although different per-unit system models affect the convergence of the AC-DC power-flow algorithm in different ways, the aspect has not been investigated in detail.
2. A comprehensive comparison of the unified and sequential Newton power-flow algorithms vis-à-vis standard and non-standard control strategies for LCC based hybrid AC-DC systems is yet to be carried out.

3. Most of the existing Newton power-flow models of VSC based hybrid AC-DC systems do not take into account the modulation index of a converter. The modulation index 'm' is an important parameter for VSC operation. Operational considerations limit the minimum and maximum value of the modulation index. While a low 'm' limits the maximum fundamental AC side voltage of the VSC, over-modulation ( $m > 1$ ) may result in low-order harmonics in the AC system [11]. Thus, a power-flow model should yield the value of 'm' and ' $V_{DC}$ ' directly, for a given operating condition, so that it can be checked whether 'm' lies within its specified limits (with sufficient margin for a dynamic response), along with ' $V_{DC}$ '.
4. Development of a unified Newton power-flow model of VSC based AC-DC systems incorporating DC voltage droop control.
5. Incorporation of interline DC/DC current flow or power flow controllers like IDCPFCs in existing Newton power-flow models of VSC based hybrid AC-DC systems.
6. Integration of renewable energy resources like offshore wind farms (OWFs) with existing power-flow models of VSC based hybrid AC-DC systems.

To address the above limitations, in the present thesis, an attempt has been made to investigate systematically the development of unified and sequential Newton power-flow models of both LCC based and VSC based hybrid AC-DC systems and their convergence characteristics vis-à-vis different HVDC control strategies.

## 1.2 Scope of the present work

In this thesis, unified and sequential Newton power-flow models of both LCC and VSC based hybrid AC-DC networks have been developed. For LCC based hybrid AC-DC networks, the effects of the different per-unit system models and different DC link control strategies on the convergence of the AC-DC power-flow algorithm are investigated. Subsequently, unified and sequential Newton power-flow models of VSC based hybrid AC-DC systems are developed, which can employ DC grid control strategies like master-slave control and voltage droop control. Thereafter, the Newton power-flow modeling of VSC based hybrid AC-DC systems incorporating IDCPFC(s) for the power-flow management of the DC grid(s) has been carried out. Finally, the Newton power-flow models of VSC based hybrid AC-DC systems incorporating multiple offshore wind farms have been developed and their effects on the DC grid voltage profile and their convergence characteristics vis-à-vis varying wind powers have been investigated. In all the models developed, the modulation indices of the pulse-width modulation scheme pertaining to the VSCs appear as unknowns, along with the converter DC side voltages and the phase angles of the fundamental converter AC side voltages.

The outline of the remaining chapters of the thesis is as follows:

Chapter 2 presents the development of Newton power-flow models of LCC based hybrid AC-DC systems. Both unified and sequential power-flow models of such systems are developed in this chapter. The effects of the different per-unit AC-DC system models on the convergence of the unified and sequential AC-DC power-flow algorithms are investigated in light of diverse DC link control strategies employed. The convergence characteristics validate the model.

Chapter 3 addresses the development of unified and sequential Newton power-flow models of VSC based hybrid AC-DC systems. DC slack-bus (master-slave) control is employed for the multi-terminal DC (MTDC) grid. The proposed model is applicable for both the back-to-back (BTB) and the point-to-point (PTP) VSC-HVDC configurations. Both the MTDC grid topology and the number of VSCs can be arbitrarily chosen in the proposed model. Several case studies were carried out with diverse topologies of MTDC networks, employing different DC grid control strategies.

Chapter 4 addresses the development of Newton power-flow models of VSC based hybrid AC-DC systems employing DC voltage droop control. The DC voltage droop control comprises both linear {voltage-power (V-P) and voltage-current (V-I)} as well as non-linear {power dead-band and voltage limits} droop characteristics. Voltage margin control is also employed in the proposed model, as a specific case of the voltage droop with a power dead-band. Based on the terminal end line active and reactive power specifications of the VSCs, two different droop control models have been developed. Multiple case studies have been carried out with diverse topologies of MTDC networks, employing different types (linear and nonlinear) of DC voltage droop controls.

Chapter 5 addresses the development of a unified Newton power-flow model of a VSC based hybrid AC-DC system incorporating an IDCPFC for the power-flow management of the DC grid. The IDCPFC comprises variable DC voltage sources which are incorporated in series with the DC links and regulates their power flow by controlling the power exchanged with these links. The IDCPFC considered in the model is a generalized one, with an arbitrary number of DC voltage sources. The IDCPFC employs both DC link current and DC link power controls.

Chapter 6 addresses the development of power-flow models of VSC based hybrid AC-DC systems integrated with multiple offshore wind farms (OWFs). The VSCs employ DC voltage droop control. Both linear and nonlinear voltage droop characteristics are incorporated. The effects of the OWFs on the DC grid voltage profile and the power-flow convergence are investigated, vis-à-vis varying wind farm powers.

In all the power-flow models developed, VSC losses have been included.

Feasibility studies of all the models proposed in chapters 2-6 have been carried out on the IEEE 300 bus test system [104] to validate their convergence characteristics.

Finally, Chapter 7 presents the conclusions of the work reported in the thesis and makes some suggestions for further work in the areas covered by the thesis.

# Chapter 2

## Newton Power-Flow Modeling of Line Commutated Converter (LCC) Based Hybrid AC-DC Systems

### 2.1 Introduction

As already mentioned in Chapter 1, the LCC-Based HVDC technology constitutes the bulk of the installed DC transmission capacity over the world. A multi-terminal LCC-based HVDC (MLDC) interconnection is more versatile and better capable of utilising the economic and technical advantages of the LCC-HVDC technology than a two-terminal one.

For planning, operation and control of AC power systems incorporating MLDC networks, the power-flow solution of hybrid AC-MLDC systems is required. This necessitates suitable Newton power-flow models of such systems. Now, for developing such models, the base values of the various DC quantities can be defined in several ways, each comprising separate sets of system equations in per-unit. It is observed that different per-unit system models affect the convergence of the AC-DC power flow algorithm in different ways. Although several choices are feasible, only two different per-unit system models are considered in this thesis.

Now, to solve the power flow equations in hybrid AC-MLDC systems, two different algorithms are available in the literature. These are known as the unified and the sequential Newton method, respectively [1], [6]. In the unified method, the AC and the DC quantities are solved simultaneously, which increases the size of the



Jacobian matrix. [52], [61]-[64] present some comprehensive research works on the unified method.

In the sequential AC-DC Newton power flow algorithm, the AC and the DC systems are solved separately in each iteration and are coupled by injecting an equivalent amount of real and reactive power at the AC terminal buses [1], [6]. Unlike the unified method, the sequential method is easier to implement and poses lesser computational burden due to the smaller size of the Jacobian matrix. [54], [65]-[75] present some comprehensive research works on the sequential method.

For power-flow solution of hybrid AC-MLDC systems, five quantities are required to be solved per converter [1], [6]. These include the DC voltage, the DC current, the control angle, the converter transformer tap ratio and the converter power factor. On the other hand, only three independent equations comprising two basic converter equations and one DC network equation exist per converter. Thus, for solution, two additional equations are usually required. These two equations are derived from the control specifications adopted for the DC links. Thus, mathematically, the control specifications are used to bridge the gap between the number of independent equations and the number of unknown quantities. Control specifications usually include specified values of converter transformer tap ratio, converter control angle, DC voltage, DC current or DC power. Depending on the application, several combinations of valid control specifications are possible. Each combination of a set of valid control specifications is known as a control strategy [1], [6]. The number of possible control strategies increase drastically with increase in the number of the DC terminals or converters. Out of a myriad of combinations, only some control strategies are practically adopted in practice. In this thesis, nine control strategies have been considered for a three-terminal DC network.

It is to be noted that in this chapter as well as in the subsequent chapters, bold quantities represent complex variables and equivalent-pi models are used to represent the transmission lines.

## 2.2 Modeling of Hybrid AC-MLDC Systems

Fig. 2.1 depicts a typical AC power system incorporating a three terminal DC network. The DC network contains two HVDC links. The first link is connected in the branch “i - j” between any two system buses “i” and “j” of the AC network while the second one is connected in the branch “i - k” between system buses “i” and “k”. The three converters representing one rectifier and two inverters are connected to the AC system at buses “i”, “j” and “k” respectively, through their respective converter transformers. The complex load powers at the AC buses ‘i’, ‘j’ and ‘k’ are represented as  $\mathbf{S}_{Di} = P_{Di} + j Q_{Di}$ ,  $\mathbf{S}_{Dj} = P_{Dj} + j Q_{Dj}$  and  $\mathbf{S}_{Dk} = P_{Dk} + j Q_{Dk}$ , respectively. The effects of the DC links are accounted for as equivalent amount of real and reactive power injections  $P_{DCR}$ ,  $Q_{DCR}$ ,  $P_{DCI1}$ ,  $Q_{DCI1}$ ,  $P_{DCI2}$  and  $Q_{DCI2}$  at the converters’ AC terminal buses “i”, “j” and “k”, respectively. These power injections are included in the analysis by appropriate modifications of the power flow equations, as detailed later.

Prior to the selection of variables and formulation of the equations, several basic assumptions are made for the analysis of steady state DC converter operation [1]-[3], [6]. These are

1. The three AC voltages at the terminal bus bars are balanced and sinusoidal.
2. The operation of the converters is perfectly balanced.
3. The direct currents and voltages are smooth.

4. The converter transformers are lossless and their magnetizing admittances are ignored.

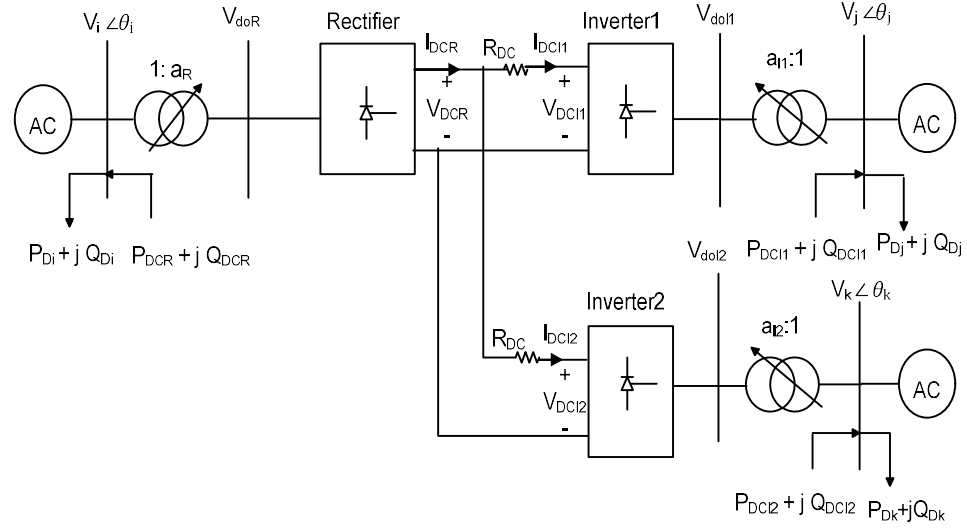


Fig. 2.1: Three terminal HVDC link between buses ‘i’, ‘j’ and ‘k’ of an existing AC power system network

Subsequently, for analysis of the integrated AC-DC system, the DC and AC equations are combined together which requires the translation of the converter equations into the per-unit system in order to use them with AC system per-unit equations. The base values for the DC system are defined in Table 2.1 which culminate in the per-unit AC-DC system equations as given in Table 2.2.

Table 2.1

Different base values for DC system

Convention 1 (Model-1)	Convention 2 (Model-2)
$V_{DC \text{ base}} = k V_{AC \text{ base}} ; \text{ where } k = \frac{3\sqrt{2}}{\pi} n_b$	$V_{DC \text{ base}} = V_{DC \text{ base}}$
$I_{DC \text{ base}} = \frac{\sqrt{3}}{k} I_{AC \text{ base}}$	$I_{DC \text{ base}} = \sqrt{3} I_{DC \text{ base}}$
$Z_{DC \text{ base}} = k^2 Z_{AC \text{ base}}$	$Z_{DC \text{ base}} = Z_{DC \text{ base}}$
$R_{DC \text{ base}} = \frac{3}{\pi} n_b X_{c \text{ base}}$	$R_{DC \text{ base}} = X_{c \text{ base}}$

Table 2.2

Basic converter equations for a 3 terminal DC network in per unit system

Per unit system 1 (Model-1)	Per unit system 2 (Model-2)	eqn. no.
$V_{\text{DCR}} = a_R V_i \cos\alpha_R - X_c I_{\text{DCR}}$	$V_{\text{DCR}} = \frac{3\sqrt{2}}{\pi} a_R n_b V_i \cos\alpha_R - \frac{3X_c}{\pi} n_b I_{\text{DCR}}$	(2.1)
$V_{\text{DCI1}} = a_{i1} V_j \cos\gamma_{i1} - X_c I_{\text{DCI1}}$	$V_{\text{DCI1}} = \frac{3\sqrt{2}}{\pi} a_{i1} n_b V_j \cos\gamma_{i1} - \frac{3X_c}{\pi} n_b I_{\text{DCI1}}$	(2.2)
$V_{\text{DCI2}} = a_{i2} V_k \cos\gamma_{i2} - X_c I_{\text{DCI2}}$	$V_{\text{DCI2}} = \frac{3\sqrt{2}}{\pi} a_{i2} n_b V_k \cos\gamma_{i2} - \frac{3X_c}{\pi} n_b I_{\text{DCI2}}$	(2.3)
$V_{\text{DCR}} = a_R V_i \cos\phi_R$	$V_{\text{DCR}} = \frac{3\sqrt{2}}{\pi} a_R n_b V_i \cos\phi_R$	(2.4)
$V_{\text{DCI1}} = a_{i1} V_j \cos\phi_{i1}$	$V_{\text{DCI1}} = \frac{3\sqrt{2}}{\pi} a_{i1} n_b V_j \cos\phi_{i1}$	(2.5)
$V_{\text{DCI2}} = a_{i2} V_k \cos\phi_{i2}$	$V_{\text{DCI2}} = \frac{3\sqrt{2}}{\pi} a_{i2} n_b V_k \cos\phi_{i2}$	(2.6)
	$I_{\text{DCI1}} = \frac{V_{\text{DCR}} - V_{\text{DCI1}}}{R_{\text{DC}}}$	(2.7)
	$I_{\text{DCI2}} = \frac{V_{\text{DCR}} - V_{\text{DCI2}}}{R_{\text{DC}}}$	(2.8)
	$I_{\text{DCR}} = I_{\text{DCI1}} + I_{\text{DCI2}}$	(2.9)
	$P_{\text{DCR}} = V_{\text{DCR}} I_{\text{DCR}}$	(2.10)
	$P_{\text{DCI1}} = V_{\text{DCI1}} * \left[ \frac{V_{\text{DCR}} - V_{\text{DCI1}}}{R_{\text{DC}}} \right]$	(2.11)
	$P_{\text{DCI2}} = V_{\text{DCI2}} * \left[ \frac{V_{\text{DCR}} - V_{\text{DCI2}}}{R_{\text{DC}}} \right]$	(2.12)

From Table 2.2, it can be observed that twelve independent equations exist against a total of eighteen unknowns. Thus, for a complete solution, six quantities (two per converter) are needed to be specified. These are derived from the control specifications adopted for the DC links. Each combination of a set of valid control specifications is known as a control strategy. Theoretically, the number of possible control strategies increase rapidly with increase in the number of the DC terminals or converters. However, only a few of the possible control strategies are practically adopted in practice. This is explained in the next section.

### 2.3 Control strategies for MLDC grids

For a three terminal DC network, several control strategies are possible [1]. However, due to a lack of space, only nine typical control strategies are considered in this paper. These are detailed in Table 2.3.

*A. Control Strategy-1*

In this control strategy, the DC voltage and the firing angle are specified for the rectifier. On the other hand, the active powers for both the inverters are specified along with their extinction angles.

*B. Control Strategy-2*

In this control strategy, the DC voltage and the firing angle are specified for the rectifier. For inverter-1, the active power is specified while the DC current is specified for inverter-2. In addition, the extinction angles of both the inverters are specified.

*C. Control Strategy-3*

In this control strategy, at the rectifier terminal, the DC voltage and the firing angle are specified. The DC current is specified at inverter-1 while the active power is specified at inverter-2. Also, the extinction angles of both the inverters are specified.

*D. Control Strategy-4*

In this control strategy, the DC voltage and the firing angle are specified at the rectifier end while the DC currents and the extinction angles are specified for both the inverters.

*E. Control Strategy-5*

In this control strategy, the DC voltage is specified for the rectifier while the active powers are specified for both the inverters. In addition, the tap settings for all the three converter transformers are specified.

### F. Control Strategy-6

In this control strategy, the DC voltage is specified for the rectifier while the DC currents are specified for both the inverters. The tap settings for all the three converter transformers are also specified.

### G. Control Strategy-7

In this control strategy, at the rectifier terminal, the DC voltage is specified. The active power is specified at inverter-1 while the DC current is specified at inverter-2. In addition, the tap settings are specified for all the three converter transformers.

Table 2.3

Some Control Strategies for a 3-Terminal DC link

Control Strategies	Specified Quantities	Unknown Quantities
1	$P_{DC1}, P_{DC2}, V_{DCR}, \alpha_R, \gamma_{11}, \gamma_{12}$	$V_{DC1}, V_{DC2}, P_{DCR}, I_{DC1}, I_{DC2}, I_{DCR}, a_R, a_{11}, a_{12}, \cos\phi_R, \cos\phi_{11}, \cos\phi_{12}$
2	$P_{DC1}, I_{DC2}, V_{DCR}, \alpha_R, \gamma_{11}, \gamma_{12}$	$V_{DC1}, V_{DC2}, P_{DC2}, P_{DCR}, I_{DC1}, I_{DCR}, a_R, a_{11}, a_{12}, \cos\phi_R, \cos\phi_{11}, \cos\phi_{12}$
3	$P_{DC2}, I_{DC1}, V_{DCR}, \alpha_R, \gamma_{11}, \gamma_{12}$	$V_{DC1}, V_{DC2}, P_{DC1}, P_{DCR}, I_{DC2}, I_{DCR}, a_R, a_{11}, a_{12}, \cos\phi_R, \cos\phi_{11}, \cos\phi_{12}$
4	$I_{DC1}, I_{DC2}, V_{DCR}, \alpha_R, \gamma_{11}, \gamma_{12}$	$V_{DC1}, V_{DC2}, P_{DC1}, P_{DC2}, P_{DCR}, I_{DCR}, a_R, a_{11}, a_{12}, \cos\phi_R, \cos\phi_{11}, \cos\phi_{12}$
5	$P_{DC1}, P_{DC2}, V_{DCR}, a_R, a_{11}, a_{12}$	$V_{DC1}, V_{DC2}, P_{DCR}, I_{DC1}, I_{DC2}, I_{DCR}, \alpha_R, \gamma_{11}, \gamma_{12}, \cos\phi_R, \cos\phi_{11}, \cos\phi_{12}$
6	$I_{DC1}, I_{DC2}, V_{DCR}, a_R, a_{11}, a_{12}$	$V_{DC1}, V_{DC2}, P_{DC1}, P_{DC2}, P_{DCR}, I_{DCR}, \alpha_R, \gamma_{11}, \gamma_{12}, \cos\phi_R, \cos\phi_{11}, \cos\phi_{12}$
7	$P_{DC1}, I_{DC2}, V_{DCR}, a_R, a_{11}, a_{12}$	$V_{DC1}, V_{DC2}, P_{DC2}, P_{DCR}, I_{DC1}, I_{DCR}, \alpha_R, \gamma_{11}, \gamma_{12}, \cos\phi_R, \cos\phi_{11}, \cos\phi_{12}$
8	$I_{DC1}, P_{DC2}, V_{DCR}, a_R, a_{11}, a_{12}$	$V_{DC1}, V_{DC2}, P_{DC1}, P_{DCR}, I_{DC2}, I_{DCR}, \alpha_R, \gamma_{11}, \gamma_{12}, \cos\phi_R, \cos\phi_{11}, \cos\phi_{12}$
9	$P_{DC1}, P_{DC2}, V_{DC1}, \alpha_R, \gamma_{11}, \gamma_{12}$	$V_{DCR}, V_{DC2}, P_{DCR}, I_{DC1}, I_{DC2}, I_{DCR}, a_R, a_{11}, a_{12}, \cos\phi_R, \cos\phi_{11}, \cos\phi_{12}$

### H. Control Strategy- 8

In this control strategy, the DC voltage is specified at the rectifier terminal. For inverter-1, the DC current is specified while for inverter-2, the active power is specified. The tap settings for all the three converter transformers are also specified.

### I. Control Strategy-9

In this control strategy, the firing angle is specified for the rectifier while the DC voltage is specified for inverter-1. In addition, the values of the active powers and the extinction angles are specified for both the inverters.

## 2.4 Power Flow Equations of Integrated AC-MLDC Systems

Let us consider the integrated AC-DC system shown in Fig. 2.1. From Fig. 2.1, it can be observed that for any AC bus ‘i’, which is not connected to any DC link, the mismatches in the active and reactive power injections are given respectively, by

$$\Delta P_i = P_i^{sp} - \sum_{p=1}^n V_i V_p Y_{ip} \cos(\theta_i - \theta_p - \phi_{ip}) \quad (2.13)$$

$$\Delta Q_i = Q_i^{sp} - \sum_{p=1}^n V_i V_p Y_{ip} \sin(\theta_i - \theta_p - \phi_{ip}) \quad (2.14)$$

Now, in the DC network shown in Fig. 2.1, the three converters representing one rectifier and two inverters are connected to the AC system at buses “i”, “j” and “k” respectively, through their respective converter transformers. The DC network contains two HVDC links. The first link is connected in the branch ‘i’ and ‘j’ between any two AC buses ‘i’ and ‘j’ while the second one is connected in the branch “i-k” between AC buses “i” and “k”. For solving the AC power flow, the effects of the DC links are included in the power flow equations by injecting an equivalent amount of real and reactive power at the terminal AC buses connected to the converters. This results in appropriate modifications of the mismatch equations at the converter terminal AC buses. At the rectifier bus ‘i’, the effect of the DC link is incorporated in the AC power flow as equivalent active and reactive power injections ‘P<sub>DCR</sub>’ and ‘Q<sub>DCR</sub>’. Similarly, at

the inverter buses ‘j’ and ‘k’, the active and reactive power injections representing the effect of the DC network are ‘ $P_{DCI1}$ ’, ‘ $Q_{DCI1}$ ’, ‘ $P_{DCI2}$ ’ and ‘ $Q_{DCI2}$ ’ respectively.

Thus, for the AC buses ‘i’, ‘j’ and ‘k’, the mismatches in the active and reactive power injections can be written as

$$\Delta P_i = P_i^{sp} - \sum_{p=1}^n V_i V_p Y_{ip} \cos(\theta_i - \theta_p - \phi_{ip}) - P_{DCR} \quad (2.15)$$

$$\Delta Q_i = Q_i^{sp} - \sum_{p=1}^n V_i V_p Y_{ip} \sin(\theta_i - \theta_p - \phi_{ip}) - Q_{DCR} \quad (2.16)$$

$$\Delta P_j = P_j^{sp} - \sum_{p=1}^n V_j V_p Y_{jp} \cos(\theta_j - \theta_p - \phi_{jp}) + P_{DCI1} \quad (2.17)$$

$$\Delta Q_j = Q_j^{sp} - \sum_{p=1}^n V_j V_p Y_{jp} \sin(\theta_j - \theta_p - \phi_{jp}) - Q_{DCI1} \quad (2.18)$$

$$\Delta P_k = P_k^{sp} - \sum_{p=1}^n V_k V_p Y_{kp} \cos(\theta_k - \theta_p - \phi_{kp}) + P_{DCI2} \quad (2.19)$$

$$\Delta Q_k = Q_k^{sp} - \sum_{p=1}^n V_k V_p Y_{kp} \sin(\theta_k - \theta_p - \phi_{kp}) - Q_{DC} \quad (2.20)$$

where

$$P_{DCR} = V_{DCR} I_{DCR}, \quad Q_{DCR} = P_{DCR} \tan \phi_R, \quad P_{DCI1} = V_{DCI1} I_{DCI1}, \quad Q_{DCI1} = P_{DCI1} \tan \phi_{I1},$$

$$P_{DCI2} = V_{DCI2} I_{DCI2}, \quad Q_{DCI2} = P_{DCI2} \tan \phi_{I2}.$$

In the above equations, the equivalent active power injections ‘ $P_{DCR}$ ’, ‘ $P_{DCI1}$ ’ and ‘ $P_{DCI2}$ ’ are usually specified or can be very easily computed by manipulation of the specified variables. However, for the equivalent reactive power injections  $Q_{DCR}$ ,  $Q_{DCI1}$  and  $Q_{DCI2}$ , the case is different, depending on the control strategy adopted for the DC links. For control strategies 1, 2, 3, 4 and 9,  $\phi_R$ ,  $\phi_{I1}$  and  $\phi_{I2}$  (and hence  $Q_{DCR}$ ,  $Q_{DCI1}$  and  $Q_{DCI2}$ ) can be computed by manipulation of the specified variables. However, for control strategies 5, 6, 7 and 8,  $\phi_R$ ,  $\phi_{I1}$  and  $\phi_{I2}$  (and hence  $Q_{DCR}$ ,  $Q_{DCI1}$  and  $Q_{DCI2}$ ) are dependent on both the specified variables as well as the AC state variables.



It is important to note the conventions of the signs of the equivalent real and reactive power injections representing the DC link. It is assumed that the rectifier consumes both real and reactive powers from the AC grid while the inverters supply real power and consume reactive power [6].

## 2.5 Implementation in Newton Power Flow Analysis

### a) Unified Method

If the number of voltage controlled buses is (g-1), the unified AC-DC power-flow problem for a ‘n’ bus AC power system incorporating a 3-terminal HVDC network employing Control strategy 1 (Table 2.3) can be formulated as,

Solve:

$$\boldsymbol{\theta} = [\theta_2 \dots \theta_n]^T, \mathbf{V} = [V_{g+1} \dots V_n]^T, \mathbf{X} = [V_{DC11} V_{DC12} a_R a_{11} a_{12} \phi_R \phi_{11} \phi_{12}]^T$$

$$\text{Specified: } \mathbf{P} = [P_2 \dots P_n]^T, \mathbf{Q} = [Q_{g+1} \dots Q_n]^T, \mathbf{f} = [f_{11} \dots f_{18}]^T$$

where the individual functions ‘ $f_{1q}$ ’ ( $q = 1, 2 \dots 8$ ) comprising ‘ $\mathbf{f}$ ’ are derived from the basic converter equations, the DC network equations and the control specifications (corresponding to Control strategy 1) and are detailed in Table 2.4.

For the above formulation, it has been assumed that the ‘g’ generators are connected at the first ‘g’ buses of the system with bus 1 being the slack bus. Thus the Newton power-flow equation can be written as,

$$\begin{bmatrix} \frac{\partial \mathbf{P}}{\partial \boldsymbol{\theta}} & \frac{\partial \mathbf{P}}{\partial \mathbf{V}} & \frac{\partial \mathbf{P}}{\partial \mathbf{X}} \\ \frac{\partial \mathbf{Q}}{\partial \boldsymbol{\theta}} & \frac{\partial \mathbf{Q}}{\partial \mathbf{V}} & \frac{\partial \mathbf{Q}}{\partial \mathbf{X}} \\ \frac{\partial \mathbf{f}}{\partial \boldsymbol{\theta}} & \frac{\partial \mathbf{f}}{\partial \mathbf{V}} & \frac{\partial \mathbf{f}}{\partial \mathbf{X}} \end{bmatrix} \begin{bmatrix} \Delta \boldsymbol{\theta} \\ \Delta \mathbf{V} \\ \Delta \mathbf{X} \end{bmatrix} = \begin{bmatrix} \Delta \mathbf{P} \\ \Delta \mathbf{Q} \\ \Delta \mathbf{f} \end{bmatrix} \quad (2.21)$$

The different Jacobian sub matrices can be identified easily from eqn. (2.21). The details are given in Appendix A.

In a similar manner, the Newton Raphson power flow formulations can be developed very easily for other control strategies.

Table 2.4

Individual functions comprising ‘f’ for Control Strategy 1

Per unit system 1	Per unit system 2	Con. func.
$V_{DCR} - a_R V_i \cos\alpha_R + X_c \left( \frac{2V_{DCR} - V_{DCI1} - V_{DCI2}}{R_{DC}} \right) = 0$	$V_{DCR} - \frac{3\sqrt{2}}{\pi} a_R n_b V_i \cos\alpha_R + \frac{3X_c}{\pi} n_b \left( \frac{2V_{DCR} - V_{DCI1} - V_{DCI2}}{R_{DC}} \right) = 0$	$f_{11}$
$V_{DCI1} - a_{i1} V_j \cos\gamma_{i1} + X_c \left( \frac{V_{DCR} - V_{DCI1}}{R_{DC}} \right) = 0$	$V_{DCI1} - \frac{3\sqrt{2}}{\pi} a_{i1} n_b V_j \cos\gamma_{i1} + \frac{3X_c}{\pi} n_b \left( \frac{V_{DCR} - V_{DCI1}}{R_d} \right) = 0$	$f_{12}$
$V_{DCI2} - a_{i2} V_k \cos\gamma_{i2} + X_c \left( \frac{V_{DCR} - V_{DCI2}}{R_{DC}} \right) = 0$	$V_{DCI2} - \frac{3\sqrt{2}}{\pi} a_{i2} n_b V_k \cos\gamma_{i2} + \frac{3X_c}{\pi} n_b \left( \frac{V_{DCR} - V_{DCI2}}{R_{DC}} \right) = 0$	$f_{13}$
$V_{DCR} - a_R V_i \cos\phi_R = 0$	$V_{DCR} - \frac{3\sqrt{2}}{\pi} a_R n_b V_i \cos\phi_R = 0$	$f_{14}$
$V_{DCI1} - a_{i1} V_j \cos\phi_{i1} = 0$	$V_{DCI1} - \frac{3\sqrt{2}}{\pi} a_{i1} n_b V_j \cos\phi_{i1} = 0$	$f_{15}$
$V_{DCI2} - a_{i2} V_k \cos\phi_{i2} = 0$	$V_{DCI2} - \frac{3\sqrt{2}}{\pi} a_{i2} n_b V_k \cos\phi_{i2} = 0$	$f_{16}$
$P_{DCI1} R_{DC} - V_{DCI1} V_{DCR} + V_{DCI1}^2 = 0$		$f_{17}$
$P_{DCI2} R_{DC} - V_{DCI2} V_{DCR} + V_{DCI2}^2 = 0$		$f_{18}$

### b) Sequential Method

In this method, the AC and DC variables are calculated separately. First the DC network equations are solved to compute the DC voltages and / or currents. This is followed by the computation of the other DC variables (converter power factors, converter control angles or converter transformer tap ratios) from the basic converter equations. Subsequently, the equivalent active (‘P<sub>DCR</sub>’, ‘P<sub>DCI1</sub>’ and ‘P<sub>DCI2</sub>’) and reactive (Q<sub>DCR</sub>, Q<sub>DCI1</sub> and Q<sub>DCI2</sub>) power injections are computed for solving the AC power-flow equations. It is important to note that the computation of the reactive power injections is dependent on the control strategy employed for the DC link. For Control Strategies-5, 6, 7 and 8, the computation of the reactive power injections are dependent on the AC power-flow iterative process and are updated every iteration, unlike Control Strategies-1, 2, 3, 4 and 9. The steps involved in the computation of the active and

reactive power injections for only two typical control strategies 1 and 5 are detailed in Table 2.5. In control strategy 5 the reactive power injections are dependent on the AC power flow iterative process while in control strategy 1 they are independent of it. Although the steps involved in the computation of the power injections pertaining to the rest of the control strategies are not shown, they can be computed in ways similar to control strategies 1 and 5.

Table 2.5

Steps to compute active and reactive power injections in control strategies 1 and 5

Control Strategy-1		Control Strategy-5	
Specified quantities	Unknown quantities	Specified quantities	Unknown quantities
$P_{DC11}, P_{DC12}, V_{DCR}, \alpha_R, \gamma_{11}, \gamma_{12}$	$V_{DC11}, V_{DC12}, P_{DCR}, I_{DC11}, I_{DC12}, I_{DCR}, a_R, a_{11}, a_{12}, \cos\phi_R, \cos\phi_{11}, \cos\phi_{12}$	$P_{DC11}, P_{DC12}, V_{DCR}, a_R, a_{11}, a_{12}$	$V_{DC11}, V_{DC12}, P_{DCR}, I_{DC11}, I_{DC12}, I_{DCR}, \alpha_R, \gamma_{11}, \gamma_{12}, \cos\phi_R, \cos\phi_{11}, \cos\phi_{12}$
<p>Step 1: compute <math>V_{DC11}</math> and <math>V_{DC12}</math> using DC load flow</p> <p>Step 2: compute <math>I_{DC11} = \frac{V_{DCR} - V_{DC11}}{R_{DC}}</math></p> <p>Step 3: compute <math>I_{DC12} = \frac{V_{DCR} - V_{DC12}}{R_{DC}}</math></p> <p>Step 4: compute <math>I_{DCR} = I_{DC11} + I_{DC12}</math></p> <p>Step 5: compute <math>P_{DCR} = V_{DCR} I_{DCR}</math></p> <p>Step 6: Compute <math>\cos\phi_R = \frac{V_{DCR} \cos\alpha_R}{V_{DCR} + X_c I_{DCR}}</math></p> <p>Step 7: Compute <math>Q_{DCR} = P_{DCR} \tan\phi_R</math></p> <p>Step 8: Compute <math>\cos\phi_{11} = \frac{V_{DC11} \cos\gamma_{11}}{V_{DC11} + X_c I_{DC11}}</math></p> <p>Step 9: Compute <math>\cos\phi_{12} = \frac{V_{DC12} \cos\gamma_{12}}{V_{DC12} + X_c I_{DC12}}</math></p> <p>Step 10: Compute <math>Q_{DC11} = P_{DC11} \tan\phi_{11}</math></p> <p>Step 11: Compute <math>Q_{DC12} = P_{DC12} \tan\phi_{12}</math></p> <p><b>Note:</b> <math>P_{DC11}</math> and <math>P_{DC12}</math> are specified. <math>P_{DCR}</math>, <math>Q_{DCR}</math>, <math>Q_{DC11}</math> and <math>Q_{DC12}</math> can be computed prior to the AC power flow and hence, are independent of the iterative loop.</p>	<p>Step 1: compute <math>V_{DC11}</math> and <math>V_{DC12}</math> using DC load flow</p> <p>Step 2: compute <math>I_{DC11} = \frac{V_{DCR} - V_{DC11}}{R_{DC}}</math></p> <p>Step 3: compute <math>I_{DC12} = \frac{V_{DCR} - V_{DC12}}{R_{DC}}</math></p> <p>Step 4: compute <math>I_{DCR} = I_{DC11} + I_{DC12}</math></p> <p>Step 5: compute <math>P_{DCR} = V_{DCR} I_{DCR}</math></p> <p>Step 6: Compute <math>\cos\phi_R = \frac{V_{DCR}}{a_R V_i}</math></p> <p><b>Note 1:</b> <math>V_i</math> is an AC power flow variable and is updated every iteration. Hence, <math>\cos\phi_R</math> changes in every iteration.</p> <p>Step 7: Compute <math>Q_{DCR} = P_{DCR} \tan\phi_R</math></p> <p>Step 8: Compute <math>\cos\phi_{11} = \frac{V_{DC11}}{a_{11} V_j}</math></p> <p>Step 9: Compute <math>\cos\phi_{12} = \frac{V_{DC12}}{a_{12} V_k}</math></p> <p><b>Note 2:</b> <math>V_j</math> and <math>V_k</math> are also AC power flow variables and are updated every iteration, along with <math>\cos\phi_{11}</math> and <math>\cos\phi_{12}</math>.</p> <p>Step 10: Compute <math>Q_{DC11} = P_{DC11} \tan\phi_{11}</math></p> <p>Step 11: Compute <math>Q_{DC12} = P_{DC12} \tan\phi_{12}</math></p> <p><b>Note 3:</b> <math>P_{DC11}</math> and <math>P_{DC12}</math> are specified. <math>P_{DCR}</math> can be computed prior to the AC power flow. However, <math>Q_{DCR}</math>, <math>Q_{DC11}</math> and <math>Q_{DC12}</math> depend upon <math>\phi_R</math>, <math>\phi_{11}</math> and <math>\phi_{12}</math> respectively, and need to be updated every iteration.</p>		

If the number of voltage controlled buses is (g-1), the sequential AC-DC power-flow problem for a 'n' bus AC power system incorporating a 3-terminal HVDC network can be formulated as,

Solve:

$$\boldsymbol{\theta} = [\theta_2 \dots \theta_n]^T, \mathbf{V} = [V_{g+1} \dots V_n]^T \quad (2.22)$$

Specified:

$$\mathbf{P} = [P_2 \dots P_n]^T, \mathbf{Q} = [Q_{g+1} \dots Q_n]^T \quad (2.23)$$

The Newton Power Flow equation would be represented as,

$$\begin{bmatrix} \frac{\partial \mathbf{P}}{\partial \boldsymbol{\theta}} & \frac{\partial \mathbf{P}}{\partial \mathbf{V}} \\ \frac{\partial \mathbf{Q}}{\partial \boldsymbol{\theta}} & \frac{\partial \mathbf{Q}}{\partial \mathbf{V}} \end{bmatrix} \begin{bmatrix} \Delta \boldsymbol{\theta} \\ \Delta \mathbf{V} \end{bmatrix} = \begin{bmatrix} \Delta \mathbf{P} \\ \Delta \mathbf{Q} \end{bmatrix} \quad (2.24)$$

Flow charts for unified and sequential methods corresponding to control strategy-1 are shown in Figures 2.2 and 2.3, respectively.

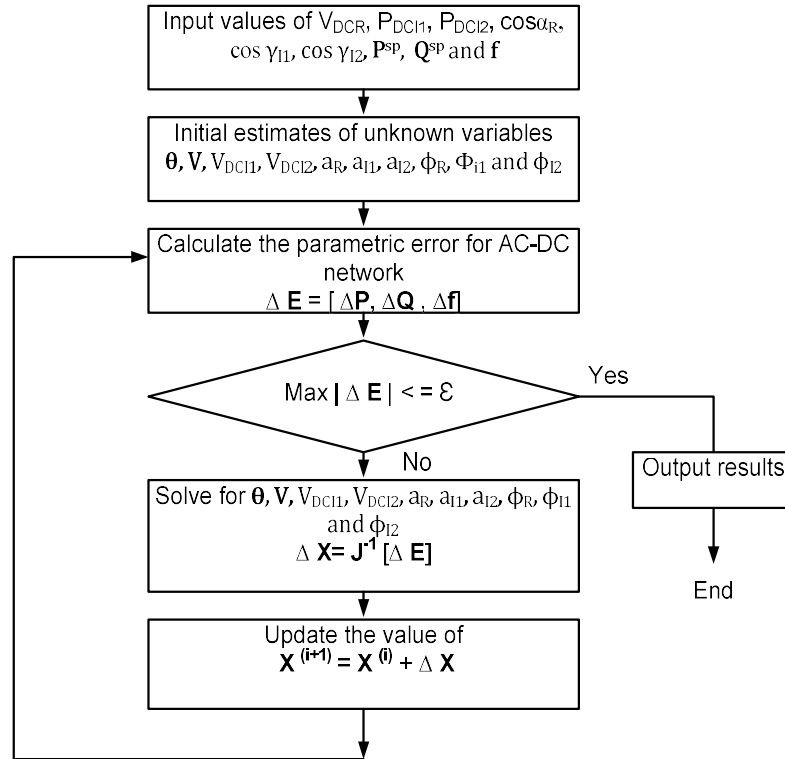


Fig. 2.2: Flow chart of unified method corresponding to control strategy 1

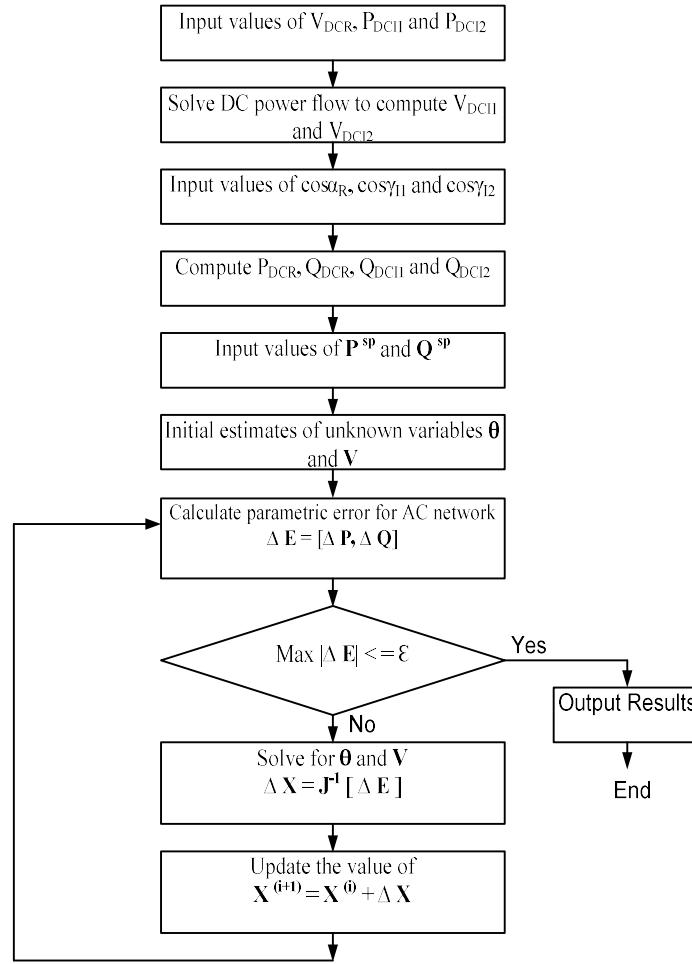


Fig. 2.3: Flow chart of sequential method corresponding to control strategy 1

## 2.6 Case Studies and Results

Numerous case studies were carried out on a three-terminal DC network incorporated in the IEEE 300-bus test system [104]. All the three converters are connected to their respective AC buses by converter transformers. Nine typical control strategies are considered for the three-terminal DC network. The effect of the different control strategies on the AC-DC power flow convergence was studied. In addition, the base values chosen for the various DC quantities can be defined in several ways, giving rise to multiple per-unit HVDC system models. In this context, two different per-unit system models are considered in this chapter. It is observed that the adoption of

different per-unit system models (depending on the selection of the base values chosen for the various DC quantities) affects the AC-DC power flow convergence differently. For all the case studies, the commutating reactance and the DC link resistance were chosen as 0.1p.u. and 0.01p.u., respectively. The number of bridges “ $n_b$ ” for all the converters was taken to be equal to 2. The initial values of variables corresponding to LCC based HVDC system were shown in Appendix A. A convergence tolerance of  $10^{-10}$  p.u. was uniformly adopted for all the case studies. In each of the case studies, ‘NI’ and ‘CT’ denote the number of iterations and the computational time in seconds {on a Intel® Core (TM) 2 Duo CPU T6400, 2GHz, 2GB RAM processor} for the algorithm to converge to the specified tolerance. All the case studies were implemented in MATLAB. Although a large number of case studies were conducted to validate the proposed model, a few sets of representative results are presented in this chapter.

### **2.6.1 Unified AC-DC power-flow studies of IEEE 300 bus test system incorporating 3-terminal LCC-HVDC network**

#### **Case I: Control strategy-1**

In this case study, two HVDC links are considered. The first HVDC link is incorporated between AC buses “25-26” and the second one between buses “25-232”. The converter connected to bus no. 25 is made to operate as a rectifier. On the other hand, both the converters connected to buses 26 and 232 are operated as inverters. As detailed in columns 1-5 of Table 2.6, the active power flows on the DC links 25-26 and 25-232 are set to values of 0.15 p.u and 0.1 p.u., respectively. The DC voltages on the rectifier side for model-1 and model-2 are set to values of 1 p.u and 2.3 p.u respectively. It may be noted that these values are different on account of the different constants being associated with the two models in p.u (Table 2.2). The firing

angle for the rectifier and the extinction angles for both the inverters are set to  $5^\circ$  and  $15^\circ$ , respectively. The power flow solution is shown in columns 6-11 of Table 2.6. From Table 2.6, it is observed that although the final power-flow solutions corresponding to the two models are different, the power-flow convergence patterns are similar. Both the models require the same number of iterations to converge, with Model 1 taking slightly less computational time than Model-2. The convergence characteristics corresponding to the base case power-flow and the unified AC-DC power-flow corresponding to model-1 and model-2 are shown in Figures 2.4, 2.5 and 2.6, respectively. From Figures 2.4-2.6, it is observed that for Control Strategy-1, the proposed unified AC-DC power-flow algorithm does not demonstrate quadratic convergence characteristics, as in the base case power flow. The bus voltage profiles for model-1 and model-2 are depicted in Figures 2.7 and 2.8, respectively. From Figures 2.7 and 2.8, it is observed that the bus voltage profile hardly changes except for the AC terminal buses at which the LCC HVDC links are incorporated.

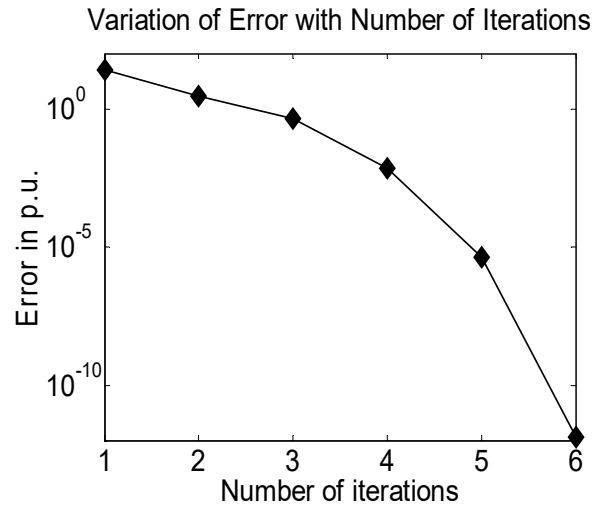


Fig. 2.4: Convergence characteristic for the base case power flow in the IEEE-300 bus system

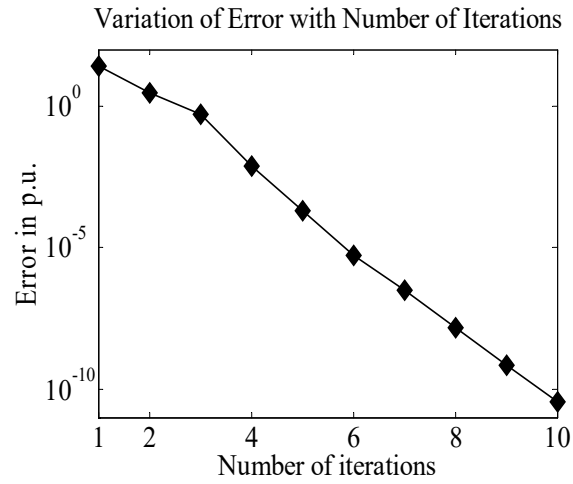


Fig. 2.5: Convergence characteristic of Table 2.6 for model-1 employing control strategy-1

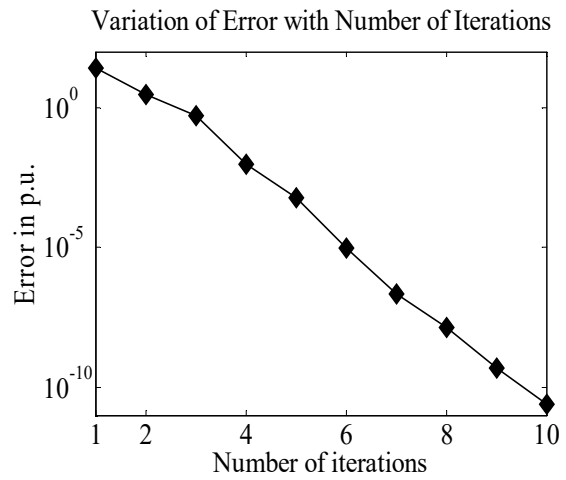


Fig. 2.6: Convergence characteristic of Table 2.6 for model-2 employing control strategy-1



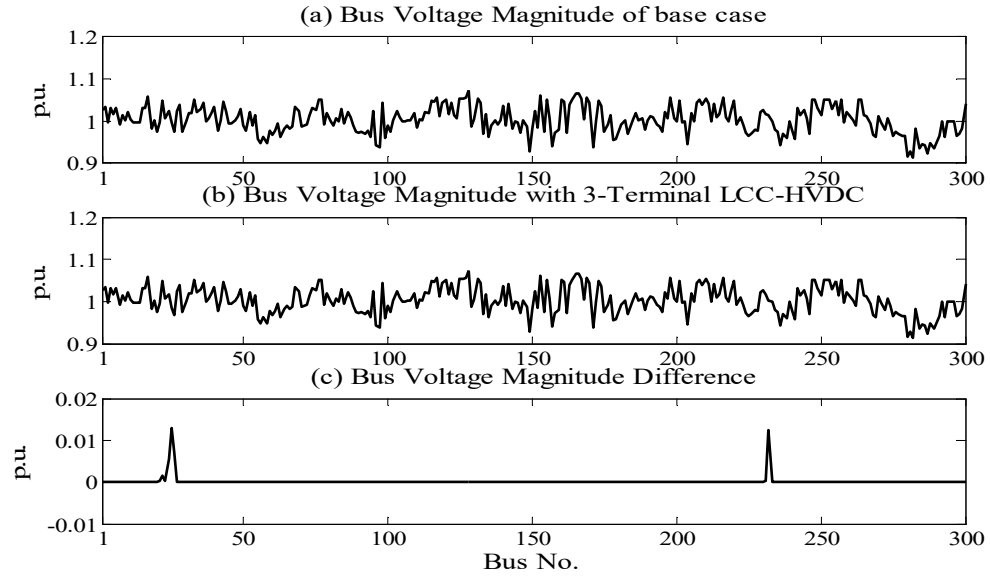


Fig. 2.7: Bus voltage profile of Table 2.6 for model-1 employing control strategy-1

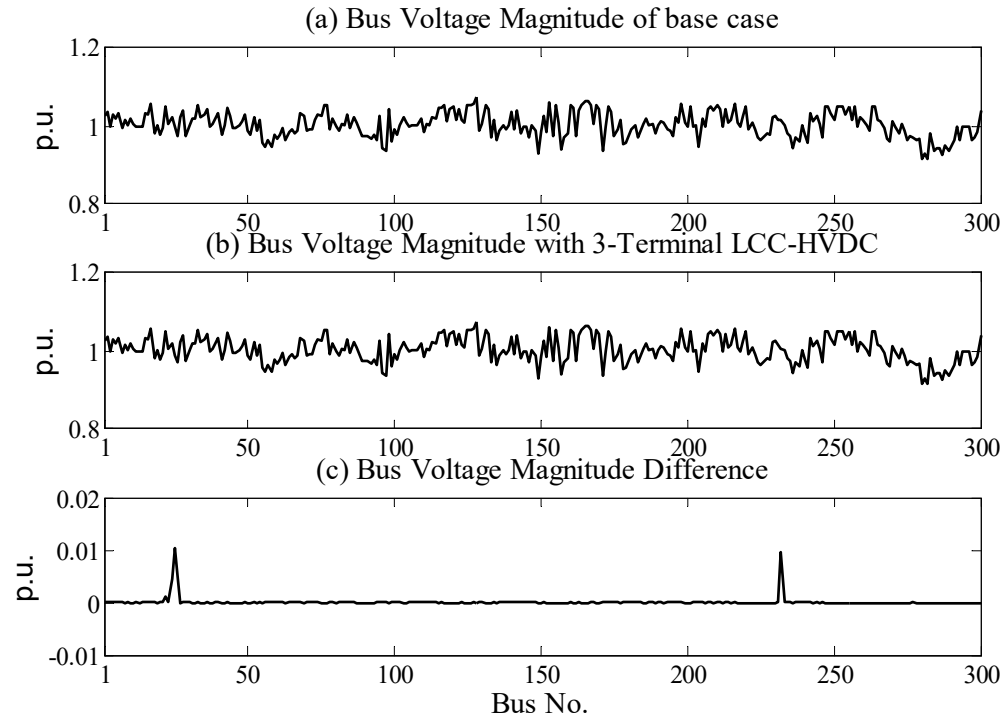


Fig. 2.8: Bus voltage profile of Table 2.6 for model-2 employing control strategy-1

## Case II: Control strategy-2

In this case study, two HVDC links are connected between AC buses “213-214” and “213-216”. The converter connected to bus no. 213 operates as a rectifier while both the converters connected to buses 214 and 216 operate as inverters. The rectifier end DC voltage is specified along with the firing angle. While the first inverter is operated in constant power mode, the second one is operated in the constant current mode. In addition, the extinction angles for both the inverters are specified. These values are detailed in columns 1-5 of Table 2.6. The power flow solution is detailed in columns 6-11 of Table 2.6. From Table 2.6, it is observed that Model-2 exhibits better convergence characteristics. Also, ‘CT’ for Model-2 is lesser than that for Model-1. The convergence characteristics of model 1 and model 2, corresponding to control strategy 2, are shown in Figures 2.9 and 2.10, respectively. The bus voltage profiles with model 1 and model 2 for control strategy 2 are shown in Figures 2.11 and 2.12, respectively.

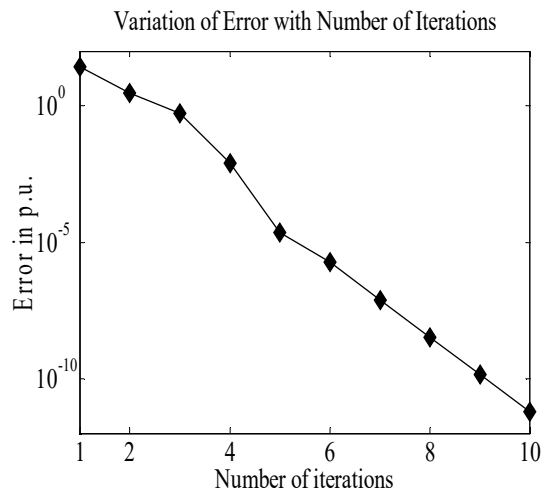


Fig. 2.9: Convergence characteristic of Table 2.6 for model-1 employing control strategy-2

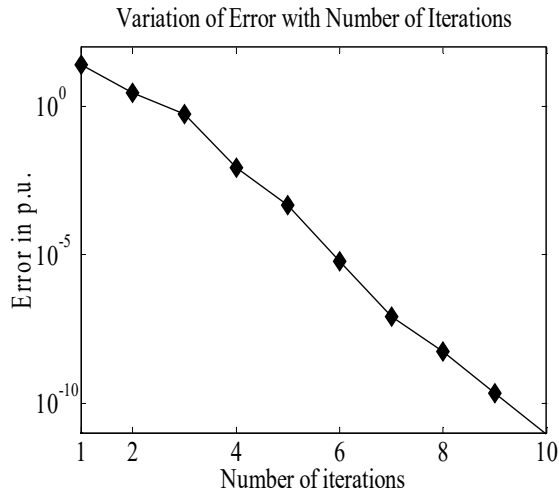


Fig. 2.10: Convergence characteristic of Table 2.6 for model-2 employing control strategy-2

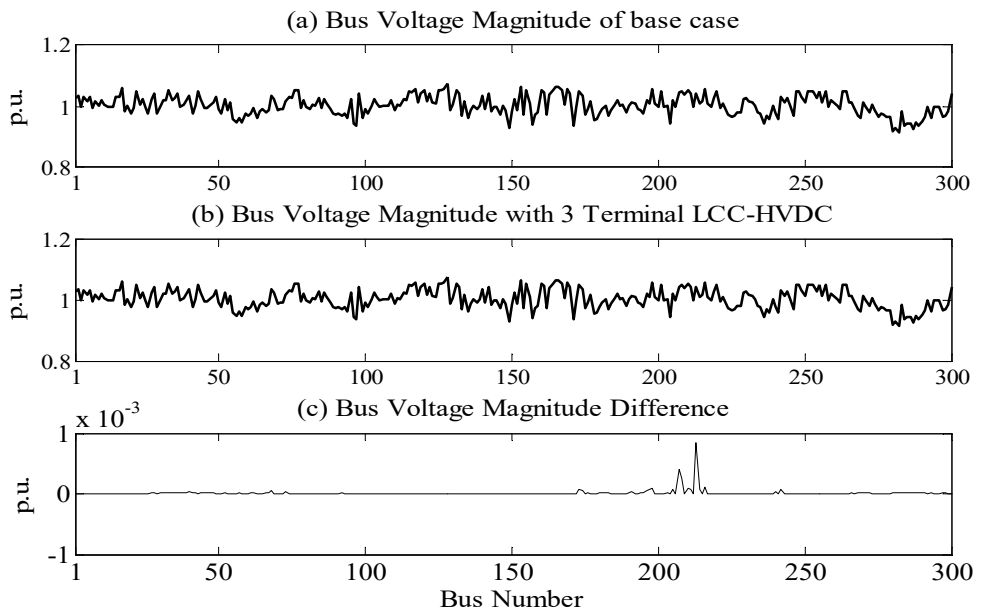


Fig. 2.11: Bus voltage profile of Table 2.6 for model-1 employing control strategy-2

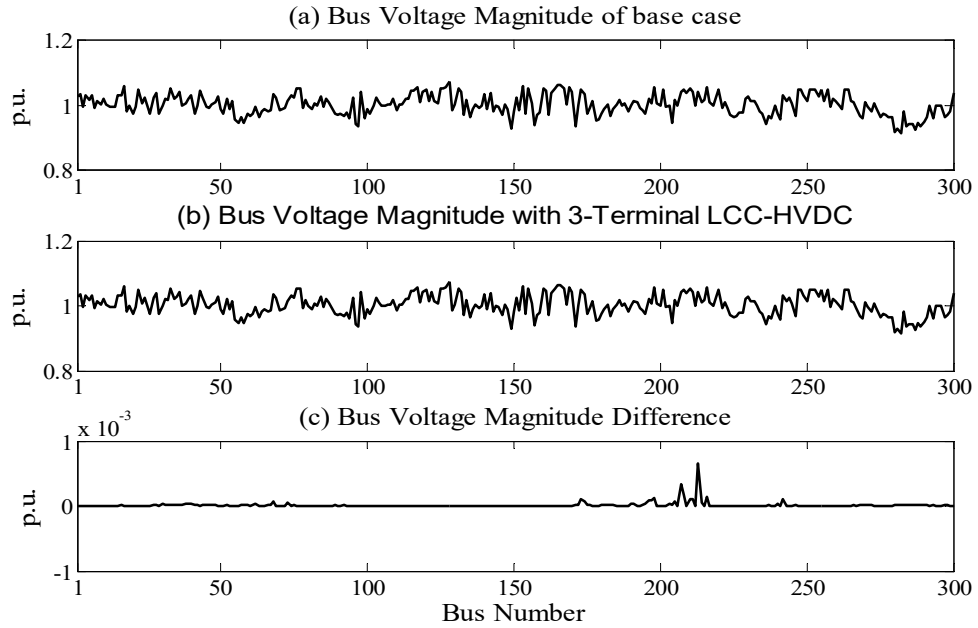


Fig. 2.12: Bus voltage profile of Table 2.6 for model-2 employing control strategy-2

### Case III: Control strategy-3

In this case study, two HVDC links are connected between AC buses “109-146” and “109-147”. The converter connected to bus no. 109 operates as a rectifier while those connected to buses 146 and 147 operate as inverters. The rectifier end DC voltage is specified along with the firing angle. While the first inverter acts on constant current mode, the second one operates on constant power mode. In addition, the extinction angles for both the inverters are specified. These values are detailed in columns 1-5 of Table 2.6. The power flow solution is detailed in columns 6-11 of Table 2.6. It is observed from the power-flow solution that both the models demonstrate almost similar convergence characteristics. However, ‘CT’ for Model-1 is slightly less than that in Model-2. The convergence characteristics of model 1 and model 2 corresponding to control strategy 3 are shown in Figures 2.13 and 2.14, respectively.

The bus voltage profiles with model 1 and model 2 for control strategy 3 are shown in Figures 2.15 and 2.16, respectively.

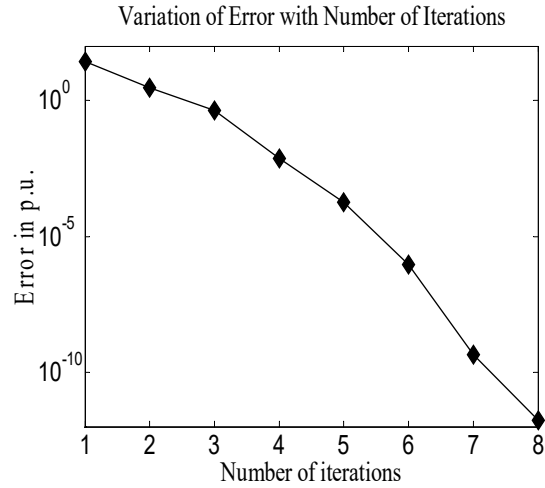


Fig. 2.13: Convergence characteristic of Table 2.6 for model-1 employing control strategy-3

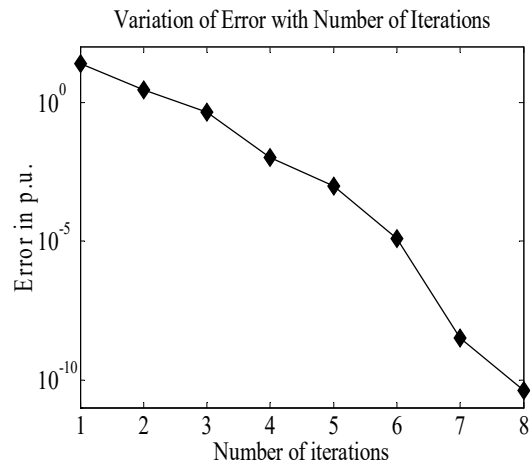


Fig. 2.14: Convergence characteristic of Table 2.6 for model-2 employing control strategy-3

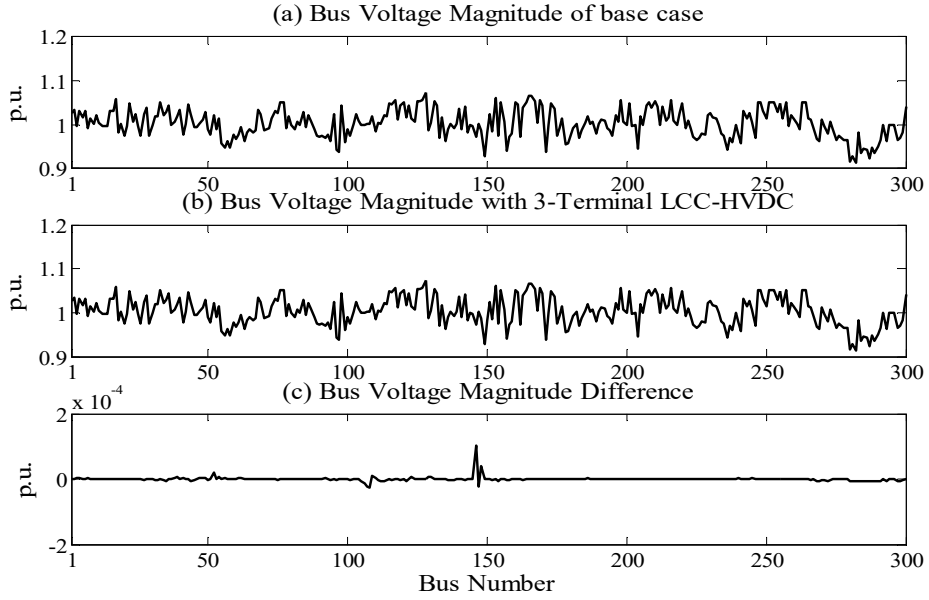


Fig. 2.15: Bus voltage profile of Table 2.6 for model-1 employing control strategy-3

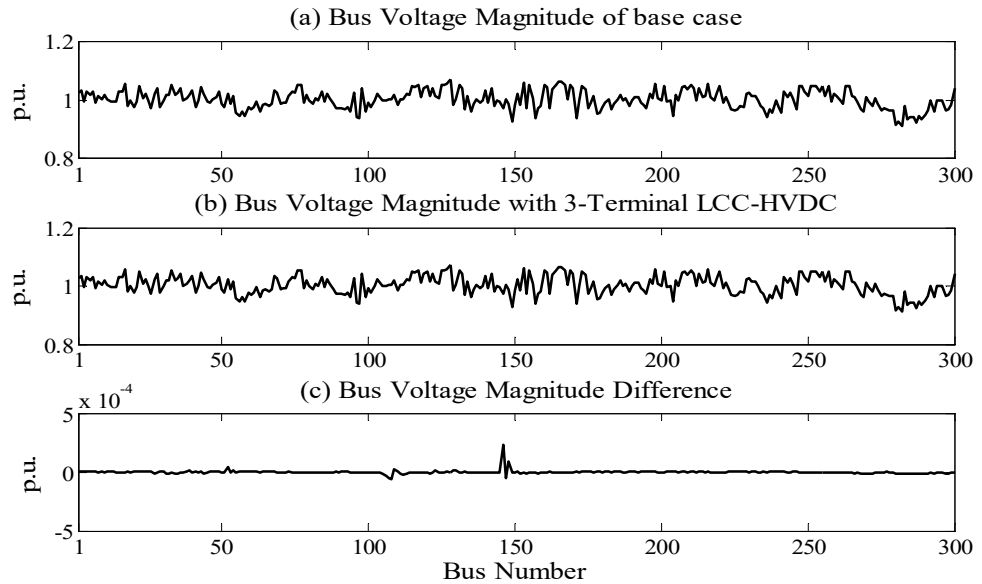


Fig. 2.16: Bus voltage profile of Table 2.6 for model-2 employing control strategy-3

Table 2.6

Study with three different control strategies 1, 2 and 3 of unified method

HVDC links		HVDC link specification			Power flow solution											
Rectifier bus	Inverter buses	Control strategy-1			AC terminal buses			HVDC variables								
		Spec. Values	Model 1	Model 2	ACSV	Model 1	Model 2	DCSV	Model 1	Model 2						
25	26	$P_{DC11}$ (p.u)	0.15	0.15	$V_{25}$	0.9854	0.9879	$V_{DC11}$	0.9985	2.2993						
								$V_{DC12}$	0.999	2.2996						
								$P_{DCR}$	0.2503	0.2501						
		$P_{DC12}$ (p.u)	0.1	0.1	$\theta_{25}$	-2.1018	-2.1461	$I_{DC11}$	0.1502	0.0652						
								$I_{DC12}$	0.1001	0.0435						
								$I_{DCR}$	0.2503	0.1087						
	$V_{DCR}$ (p.u)	1	2.3	$V_{26}$	0.9679	0.9698	$a_R$	1.0442	0.8731							
							$a_{11}$	1.0841	0.9137							
							$a_{12}$	1.0425	0.8805							
							$\cos\phi_R$	0.9719	0.9873							
							$\cos\phi_{11}$	0.9516	0.9607							
							$\cos\phi_{12}$	0.9563	0.9624							
232		$\alpha_R$ (deg.)	5	5	$\theta_{26}$	-4.5343	-4.5598	NI	10	10						
								$Y_{11}$ (deg.)	15	15	$V_{232}$	1.002	1.0047	CT	2.3135	2.3935
								$Y_{12}$ (deg.)	15	15	$\theta_{232}$	-1.7842	-1.836			
213	214	Spec. Values	Model 1	Model 2	ACSV	Model 1	Model 2	DC SV	Model 1	Model 2						
								$V_{DC11}$	0.997	2.2987						
								$V_{DC12}$	0.9901	2.2772						
		$P_{DC11}$ (p.u)	0.3	0.3	$V_{213}$	1.0409	1.0410	$P_{DC12}$	0.099	0.2277						
								$P_{DCR}$	0.4009	0.5302						
								$I_{DC11}$	0.3009	0.1305						
	$V_{DCR}$ (p.u)	1	2.3	$V_{214}$	1.0095	1.0095	$I_{DCR}$	0.4009	0.2305							
							$a_R$	1.0031	0.829							
							$a_{11}$	1.0533	0.8775							
							$a_{12}$	0.9801	0.8298							
							$\cos\phi_R$	0.9578	0.9867							
							$\cos\phi_{11}$	0.9376	0.9607							
216		$\alpha_R$ (deg.)	5	5	$\theta_{214}$	-20.7274	-20.7806	$\cos\phi_{12}$	0.9563	0.9619						
								$Y_{11}$ (deg.)	15	15	$V_{216}$	1.0564	1.0564	NI	10	10
								$Y_{12}$ (deg.)	15	15	$\theta_{216}$	-20.9194	-20.9184	CT	2.37714	2.352065
109	146	Spec. Values	Model 1	Model 2	ACSV	Model 1	Model 2	DC SV	Model 1	Model 2						
								$V_{DC11}$	0.9995	2.2995						
								$V_{DC12}$	1	2.3						
		$P_{DC12}$ (p.u)	0.1	0.1	$V_{109}$	1.0195	1.0195	$P_{DCR}$	0.05	0.115						
								$P_{DC11}$	0.05	0.115						
								$I_{DC11}$	0	0						
	$V_{DCR}$ (p.u)	1	2.3	$V_{146}$	0.9717	0.9716	$I_{DCR}$	0.05	0.05							
							$a_R$	0.9896	0.8419							
							$a_{11}$	1.0702	0.9109							
							$a_{12}$	1.0325	0.8792							
							$\cos\phi_R$	0.9912	0.9921							
							$\cos\phi_{11}$	0.9611	0.9619							
147		$\alpha_R$ (deg.)	5	5	$\theta_{146}$	-6.3944	-5.885	$\cos\phi_{12}$	0.9659	0.9659						
								$Y_{11}$ (deg.)	15	15	$V_{147}$	1.0027	1.0028	NI	8	8
								$Y_{12}$ (deg.)	15	15	$\theta_{147}$	-4.3604	-3.9388	CT	1.9757	2.012735

#### Case IV: Control strategy-4

In this case study, the converter connected to AC bus no. 101 acts as a rectifier while those connected to AC buses 102 and 105 act as inverters. The rectifier end DC voltage is specified along with the firing angle. Both the inverters are operated at constant current and constant extinction angle. The values of the specified quantities are detailed in columns 1-5 of Table 2.7. The power flow solution is detailed in columns 6-11 of Table 2.7. The convergence characteristics of model 1 and model 2 corresponding to control strategy 4 are shown in Figures 2.17 and 2.18, respectively. It is again observed that both the models demonstrate similar convergence characteristics, with Model-1 taking slightly less ‘CT’ and less ‘NI’ to converge. The bus voltage profiles with model 1 and model 2 for control strategy 4 are shown in Figures 2.19 and 2.20, respectively.

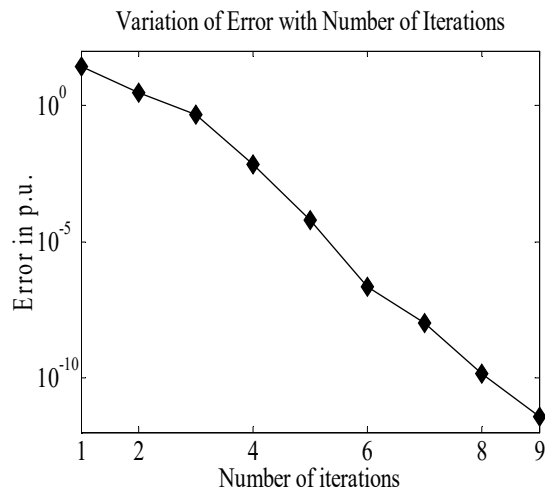


Fig. 2.17: Convergence characteristic of Table 2.7 for model-1 employing control strategy-4



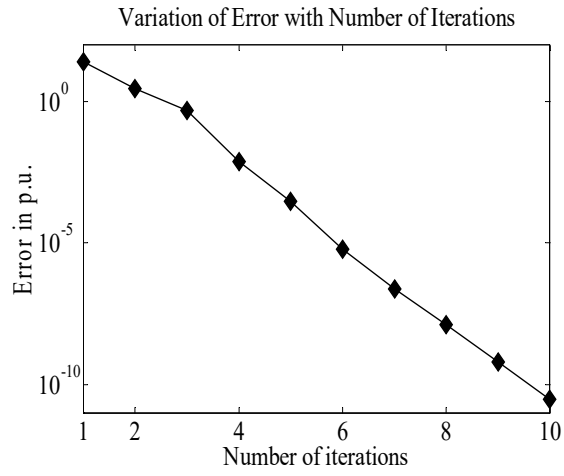


Fig. 2.18: Convergence characteristic of Table 2.7 for model-2 employing control strategy-4

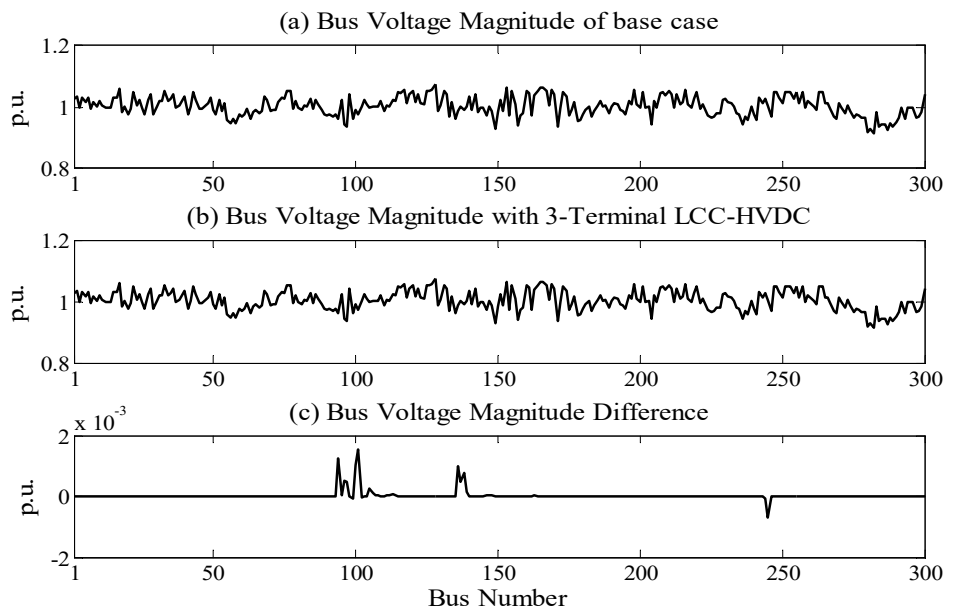


Fig. 2.19: Bus voltage profile of Table 2.7 for model-1 employing control strategy-4

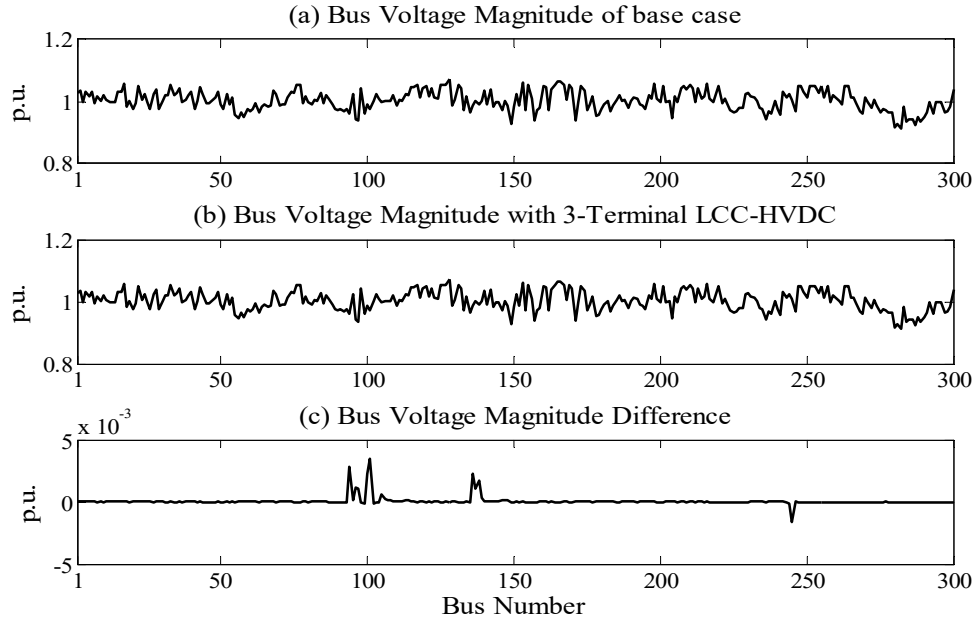


Fig. 2.20: Bus voltage profile of Table 2.7 for model-2 employing control strategy-4

### Case V: Control strategy-5

In this case, two HVDC links are incorporated between AC buses “86-87” and “86-90”. The converter connected to bus no. 86 operates as a rectifier while both the converters connected to buses 87 and 90 operate as inverters. In this control strategy, the rectifier end DC voltage is specified and both the inverters are operated in the constant power mode. In addition, the tap ratios of all the three converter transformers are specified. Columns 1-5 of Table 2.7 show these specified values. The power flow solution is shown in columns 6-11 of Table 2.7. It is also observed that Model-1 fares slightly better than Model-2 in terms of ‘CT’. The convergence characteristics of model 1 and model 2 corresponding to control strategy 5 are shown in Figures 2.21 and 2.22, respectively. The bus voltage profiles with model 1 and model 2 corresponding to control strategy 5 are shown in Figures 2.23 and 2.24, respectively.

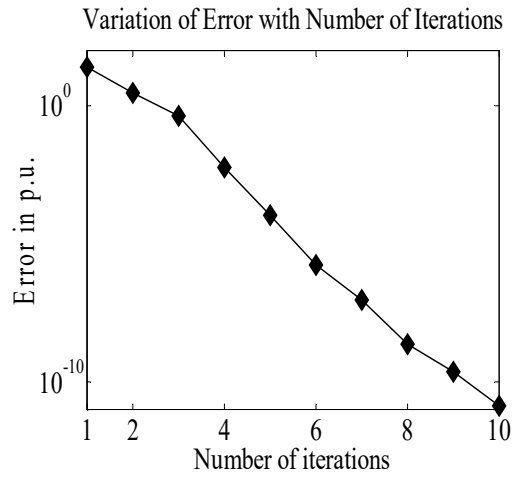


Fig. 2.21: Convergence characteristic of Table 2.7 for model-1 employing control strategy-5

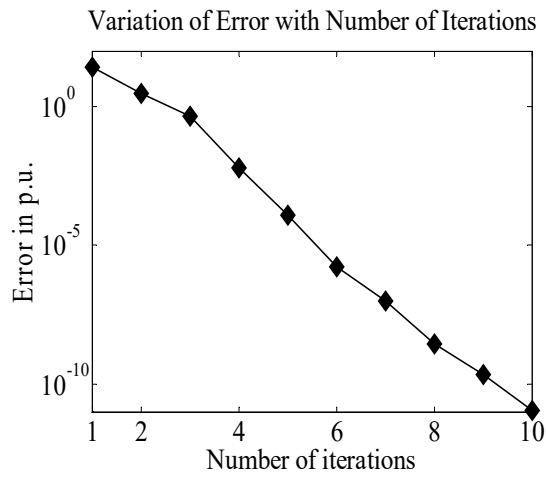


Fig. 2.22: Convergence characteristic of Table 2.7 for model-2 employing control strategy-5

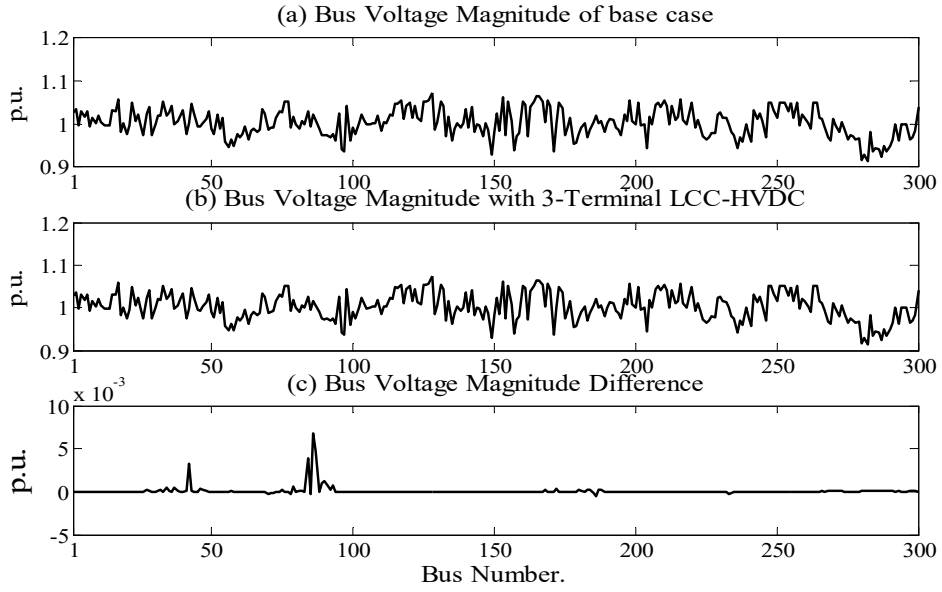


Fig. 2.23: Bus voltage profile of Table 2.7 for model-1 employing control strategy-5

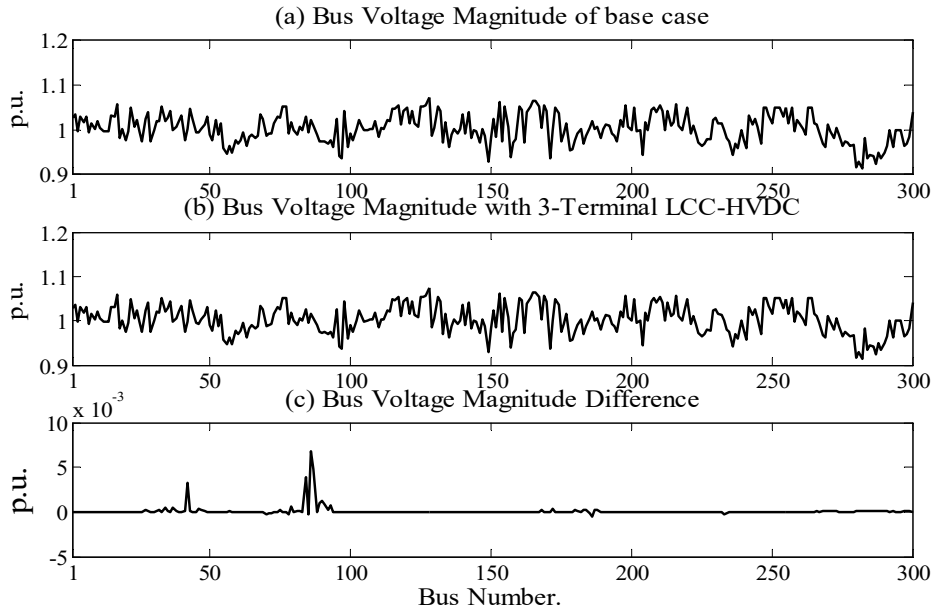


Fig. 2.24: Bus voltage profile of Table 2.7 for model-2 employing control strategy-5

### Case VI: Control strategy-6

In this case, the two HVDC links are connected between AC buses “78-84” and “78-86”. While the converter connected to bus no. 78 operates as a rectifier, the converters connected to buses 84 and 86 operate as inverters. In this control strategy, the rectifier end DC voltage is specified. On the other hand, both the inverters are operated in the constant current mode. Also, the tap ratios of all the three converter transformers are specified. While columns ‘1-5’ of Table 2.7 shows the values of the specified quantities, columns 6-11 details the power-flow solution. Again, from the values of ‘CT’ and ‘NI’, it is observed that Model-1 fares better than Model-2. The convergence characteristics of model 1 and model 2 corresponding to control strategy 6 are shown in Figures 2.25 and 2.26, respectively. The bus voltage profiles with model 1 and model 2 corresponding to control strategy 6 are shown in Figures 2.27 and 2.28, respectively.

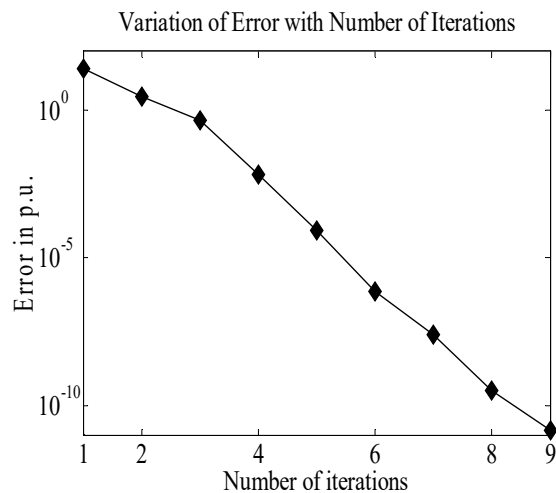


Fig. 2.25: Convergence characteristic of Table 2.7 for model-1 employing control strategy-6

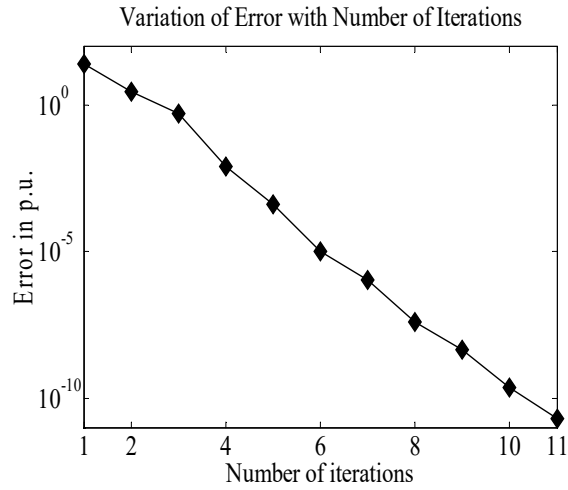


Fig. 2.26: Convergence characteristic of Table 2.7 for model-2 employing control strategy-6

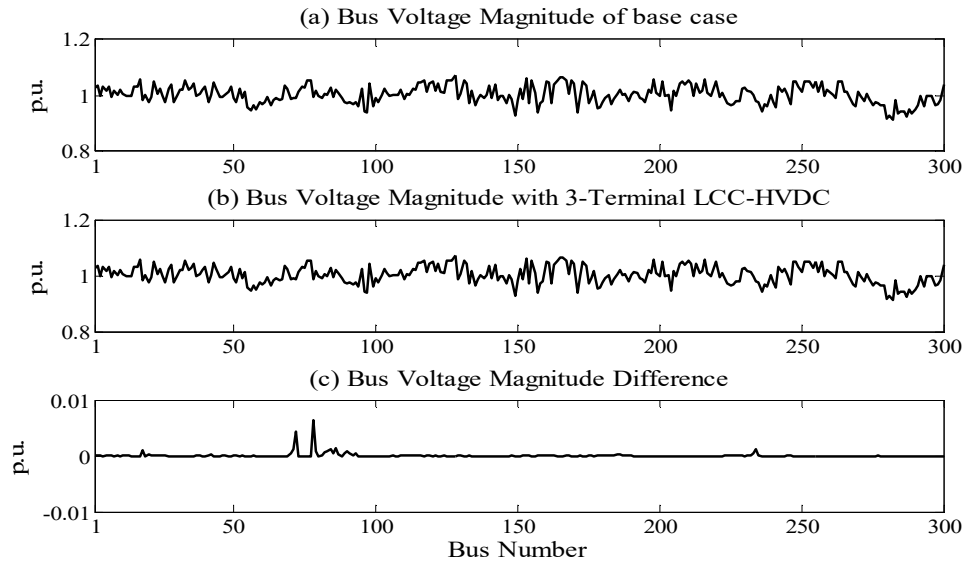


Fig. 2.27: Bus voltage profile of Table 2.7 for model-1 employing control strategy-6

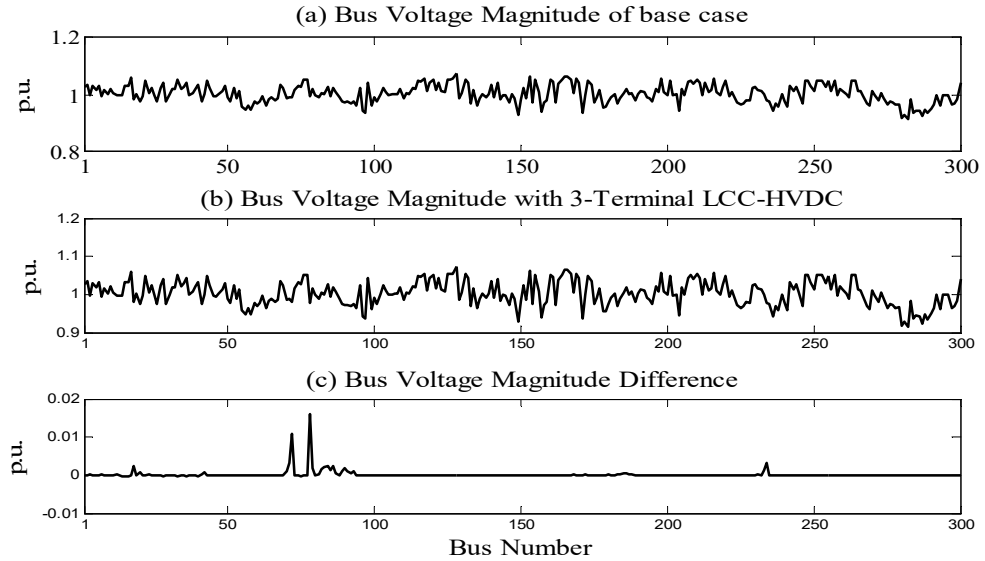


Fig. 2.28: Bus voltage profile of Table 2.7 for model-2 employing control strategy-6

### Case VII: Control strategy-7

In this case study, two HVDC links are incorporated between AC buses “68-173” and “68-174”. The converter connected to bus no. 68 acts as a rectifier while both the converters connected to buses 173 and 174 act as inverters. In this control strategy, the rectifier end DC voltage is specified. The first inverter is operated in the constant power mode while the second one is operated in the constant current mode. In addition, the tap ratios of all the three converter transformers are specified. The specified values are given in columns 1-5 of Table 2.8. The power flow solution is shown in columns 6-11 of Table 2.8. From the power-flow solution, it is again observed that the values of ‘NI’ and ‘CT’ for Model-2 are more than that for Model-1. The convergence characteristics of models 1 and 2 corresponding to control strategy 7 are shown in Figures 2.29 and 2.30, respectively. The bus voltage profiles with models 1 and 2 corresponding to control strategy 7 are shown in Figures 2.31 and 2.32, respectively.

Table 2.7

Study with three different control strategies 4, 5 and 6 of unified method

HVDC link		HVDC link specification			Power flow solution										
Rectifier bus	Inverter buses	Control strategy-4			AC terminal buses			HVDC variables							
		Spec. Val.	Model 1	Model 2	AC SV	Model 1	Model 2	DC SV	Model 1	Model 2					
101	102	$I_{DCI1}$ (p.u)	0.1	0.1	$V_{101}$	0.9745	0.9726	$V_{DCI1}$	0.9985	2.2985					
								$V_{DCI2}$	0.999	2.299					
								$P_{DCI1}$	0.0999	0.2299					
		$I_{DCI2}$ (p.u)	0.05	0.05	$\theta_{101}$	-14.5011	-14.7822	$P_{DCI2}$	0.05	0.115					
								$P_{DCR}$	0.15	0.345					
								$I_{DCR}$	0.15	0.15					
	105	$V_{DCR}$ (p.u)	1	2.3	$V_{102}$	1.0014	1.0015	$a_R$	1.0455	0.8898					
								$a_{11}$	1.0427	0.887					
								$a_{12}$	1.0408	0.8863					
		$\alpha_R$ (deg.)	5	5	$\theta_{102}$	-17.271	-16.8811	$\cos\phi_R$	0.9815	0.9839					
								$\cos\phi_{11}$	0.9563	0.958					
								$\cos\phi_{12}$	0.9611	0.9619					
$\gamma_{11}$ (deg.)	15	15	$V_{105}$	0.9987	0.9984	NI	9	10							
$\gamma_{12}$ (deg.)	15	15	$\theta_{105}$	-12.7184	-12.6926	CT	2.071	2.3187							
Control strategy-5			AC terminal buses			HVDC variables									
86	87	Spec. Values	Model 1	Model 2	AC SV	Model 1	Model 2	$V_{DCI1}$	0.998	2.991					
								$V_{DCI2}$	0.998	2.991					
								$P_{DCR}$	0.4008	0.4002					
		$P_{DCI1}$ (p.u)	0.2	0.2	$\theta_{86}$	-13.6274	-13.6275	$I_{DCI1}$	0.2004	0.087					
								$I_{DCI2}$	0.2004	0.087					
								$I_{DCR}$	0.4008	0.174					
	$V_{DCR}$ (p.u)	1	2.3	$V_{87}$	1.0025	1.0026	$\alpha_R$	12.0888	8.405						
							$\gamma_{11}$	21.0307	18.4729						
							$\gamma_{12}$	17.7966	21.7883						
	90	$a_R$	1.05	0.86	$\theta_{87}$	-15.6906	-15.6907	$\cos\phi_R$	0.9401	0.9725					
								$\cos\phi_{11}$	0.9133	0.9417					
								$\cos\phi_{12}$	0.9334	0.9219					
$a_{11}$		1.09	0.9	$V_{90}$	0.972	0.972	NI	10	10						
							$a_{12}$	1.1	0.95	$\theta_{90}$	-23.6159	-23.6159	CT	2.21679	2.2872
													Control strategy-6		
78	84	Spec. Values	Model 1	Model 2	AC SV	Model 1	Model 2	$V_{DCI1}$	0.999	2.299					
								$V_{DCI2}$	0.999	2.299					
								$P_{DCI1}$	0.0999	0.2299					
		$I_{DCI1}$ (p.u)	0.1	0.1	$V_{78}$	0.9769	0.9769	$P_{DCI2}$	0.0999	0.2299					
								$P_{DCR}$	0.2	0.46					
								$I_{DCR}$	0.2	0.2					
	86	$V_{DCR}$ (p.u)	1	2.3	$V_{84}$	1.0262	1.0263	$\alpha_R$	6.2257	10.0717					
								$\gamma_{11}$	22.1221	21.6945					
								$\gamma_{12}$	22.5174	18.9575					
		$a_R$	1.04	0.9	$\theta_{84}$	-10.77	-10.7698	$\cos\phi_R$	0.9746	0.9685					
								$\cos\phi_{11}$	0.9172	0.9215					
								$\cos\phi_{12}$	0.9146	0.938					
$a_{11}$	1.06	0.9	$V_{86}$	1.0195	1.0195	NI	9	11							
						$a_{12}$	1.07	0.89	$\theta_{86}$	-11.6496	-11.6497	CT	1.95103	2.372151	



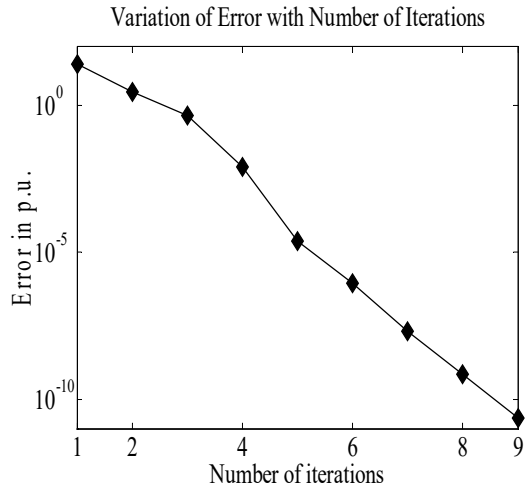


Fig. 2.29: Convergence characteristic of Table 2.8 for model-1 employing control strategy-7

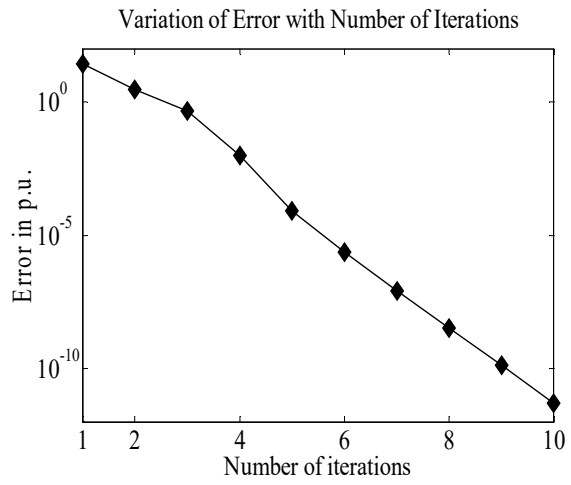


Fig. 2.30: Convergence characteristic of Table 2.8 for model-2 employing control strategy-7

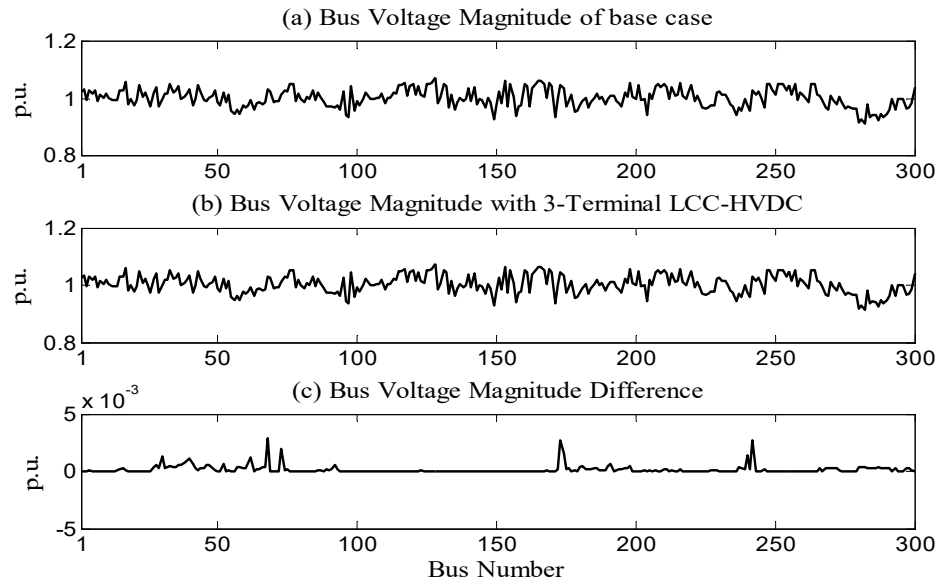


Fig. 2.31: Bus voltage profile of Table 2.8 for model-1 employing control strategy-7

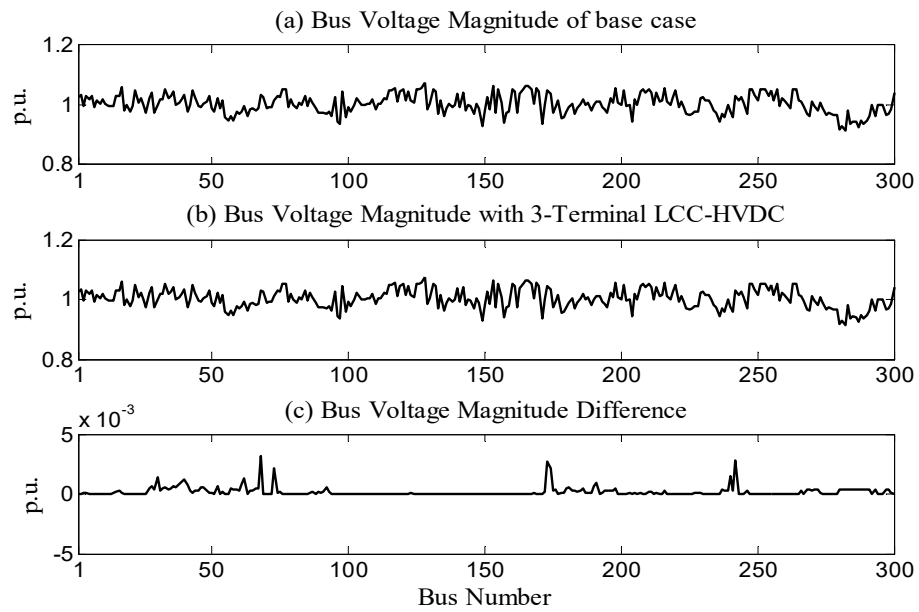


Fig. 2.32: Bus voltage profile of Table 2.8 for model-2 employing control strategy-7

### Case VIII: Control strategy-8

In this case, two HVDC links are incorporated between AC buses “15-31” and “15-74”. The converter connected to bus no. 15 operates as a rectifier while both the converters connected to buses 31 and 74 operate as inverters. In this control strategy, the rectifier end DC voltage is specified. The first and the second inverters are operated in the constant current and constant power modes, respectively. In addition, the tap ratios of all the three converter transformers are specified. Columns 1-5 of Table 2.8 shows these specified values. The power flow solution is shown in columns 6-11 of Table 2.8. From the power-flow solution, it is again observed that Model-1 fares slightly better than Model-2 in respect of ‘CT’. The convergence characteristics with models 1 and 2 corresponding to control strategy 8 are shown in Figures 2.33 and 2.34, respectively. The bus voltage profiles with models 1 and model 2 corresponding to control strategy 8 are shown in Figures 2.35 and 2.36, respectively.

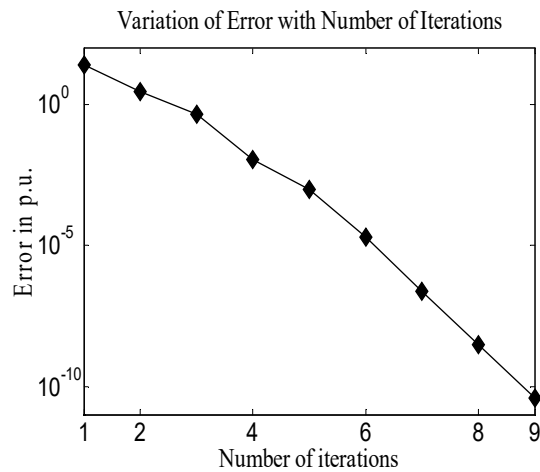


Fig. 2.33: Convergence characteristic of Table 2.8 for model-1 employing control strategy-8

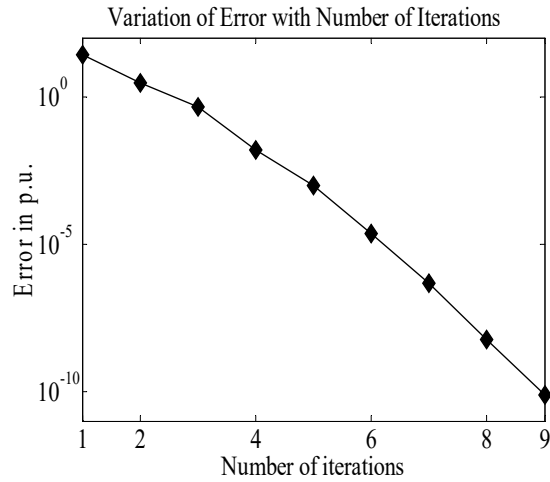


Fig. 2.34: Convergence characteristic of Table 2.8 for model-2 employing control strategy-8

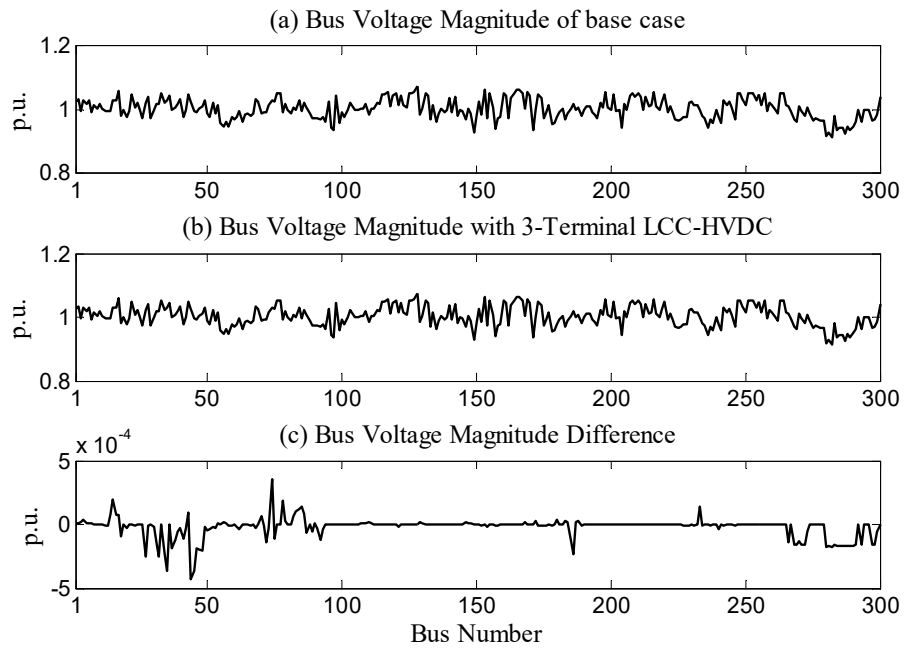


Fig. 2.35: Bus voltage profile of Table 2.8 for model-1 employing control strategy-8

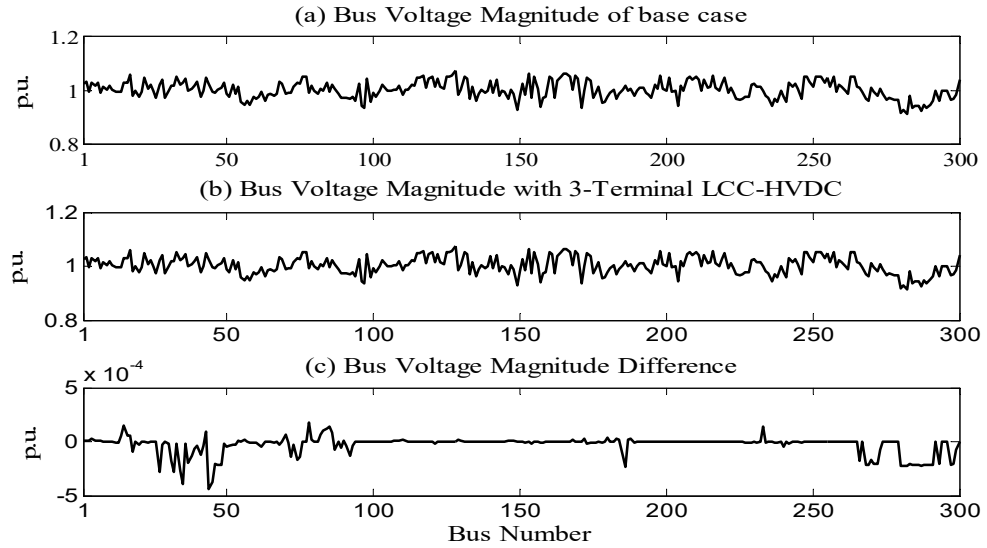


Fig. 2.36: Bus voltage profile of Table 2.8 for model-2 employing control strategy-8

#### Case IX: Control strategy-9

In this case, two HVDC links are incorporated between AC buses “266-270” and “266-271”. The converter connected to bus no. 266 acts as a rectifier while both the converters connected to buses 270 and 271 operate as inverters. While the rectifier operates in the constant firing angle mode, the inverters are operated in the constant power and constant extinction angle mode. Columns 1-5 of Table 2.8 show these specified values. The power flow solution is shown in columns 6-11 of Table 2.8. Model-2 is observed to have slightly lesser ‘CT’ than Model-1. The convergence characteristics with model 1 and model 2 corresponding to control strategy 9 are shown in Figures 2.37 and 2.38, respectively. The bus voltage profiles with model 1 and model 2 corresponding to control strategy 9 are depicted in Figures 2.39 and 2.40, respectively.

Table 2.8

Study with three different control strategies 7, 8 and 9 of unified method

HVDC link		HVDC link specification			Power flow solution									
Rectifier Bus	Inverter Buses	Control strategy-7			AC terminal buses			HVDC variables						
		Spec. values	Model 1	Model 2	AC SV	Model 1	Model 2	DC SV	Model 1	Model 2				
68	173	$P_{DC11}$ (p.u)	0.2	0.2	$V_{68}$	1.0309	1.0306	$V_{DC11}$	1	2.3				
								$V_{DC12}$	0.999	2.299				
								$P_{DC12}$	0.999	0.2299				
		$I_{DC12}$ (p.u)	0.1	0.1	$\theta_{68}$	-18.7703	-18.7794	$P_{DCR}$	0.3	0.43				
								$I_{DC11}$	0.2	0.087				
								$I_{DCR}$	0.3	0.187				
	174	$V_{DCR}$ (p.u)	1	2.3	$V_{173}$	1.0465	1.0465	$\alpha_R$	14.0617	9.1939				
								$\gamma_{11}$	21.8305	21.3478				
								$\gamma_{12}$	21.7536	21.1622				
		$a_R$	1.03	0.85	$\theta_{173}$	-18.7687	-18.7227	$\cos\phi_R$	0.9418	0.9721				
								$\cos\phi_{11}$	0.9101	0.9247				
								$\cos\phi_{12}$	0.9196	0.9249				
$a_{11}$	1.05	0.88	$V_{174}$	1.0346	1.0341	NI	9	10						
						$a_{12}$	1.05	0.89	$\theta_{174}$	-20.4037	-20.2606	CT	2.1869	2.44519
												Control strategy-8		
Spec. values	Model 1	Model 2	AC SV	Model 1	Model 2							DC SV	Model 1	Model 2
15	31	$I_{DC11}$ (p.u)	0.04	0.04	$V_{15}$	1.0311	1.0312	$V_{DC11}$	0.9996	2.2996				
								$V_{DC12}$	0.9998	2.2991				
								$P_{DC11}$	0.04	0.092				
		$P_{DC12}$ (p.u)	0.2	0.2	$\theta_{15}$	-7.9123	-7.9121	$P_{DCR}$	0.2404	0.2921				
								$I_{DC12}$	0.2004	0.087				
								$I_{DCR}$	0.2404	0.127				
	74	$V_{DCR}$ (p.u)	1	2.3	$V_{31}$	1.0199	1.0199	$\alpha_R$	10.4853	13.9799				
								$\gamma_{11}$	20.4163	21.4698				
								$\gamma_{12}$	21.560	20.8776				
		$a_R$	1.01	0.86	$\theta_{31}$	-10.5732	-10.5731	$\cos\phi_R$	0.9602	0.9603				
								$\cos\phi_{11}$	0.9334	0.9275				
								$\cos\phi_{12}$	0.9136	0.9276				
$a_{11}$	1.05	0.9	$V_{74}$	1.0305	1.031	NI	9	9						
						$a_{12}$	1.06	0.89	$\theta_{74}$	-9.3778	-9.3882	CT	2.196934	2.226688
												Control strategy-9		
Spec. values	Model 1	Model 2	AC SV	Model 1	Model 2							DC SV	Model 1	Model 2
266	270	$P_{DC11}$ (p.u)	0.3	0.3	$V_{266}$	1.0071	1.0082	$V_{DCR}$	1.003	2.3013				
								$V_{DC12}$	1.002	2.3009				
								$P_{DCR}$	0.4010	0.4002				
		$P_{DC12}$ (p.u)	0.1	0.1	$\theta_{266}$	-11.2395	-11.2379	$I_{DC11}$	0.3	0.1304				
								$I_{DC12}$	0.0998	0.0435				
								$I_{DCR}$	0.3998	0.1739				
	271	$V_{DC11}$ (p.u)	1	2.3	$V_{270}$	1.0072	1.0083	$a_R$	1.0396	0.8606				
								$a_{11}$	1.0587	0.8838				
								$a_{12}$	1.064	0.8966				
		$\alpha_R$ (deg.)	5	5	$\theta_{270}$	-11.2534	-11.2519	$\cos\phi_R$	0.958	0.982				
								$\cos\phi_{11}$	0.9378	0.9552				
								$\cos\phi_{12}$	0.9564	0.9624				
$\gamma_{11}$ (deg.)	15	15	$V_{271}$	0.9847	0.9872	NI	10	10						
						$\gamma_{12}$ (deg.)	15	15	$\theta_{271}$	-15.1206	-15.1079	CT	2.305518	2.287

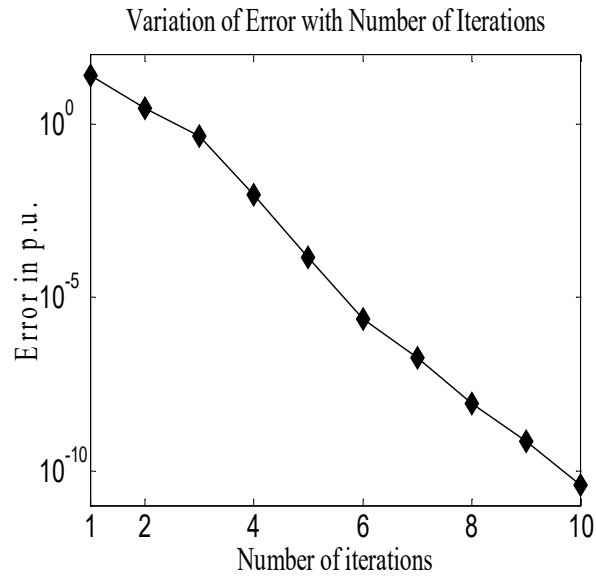


Fig. 2.37: Convergence characteristic of Table 2.8 for model-1 employing control

strategy-9

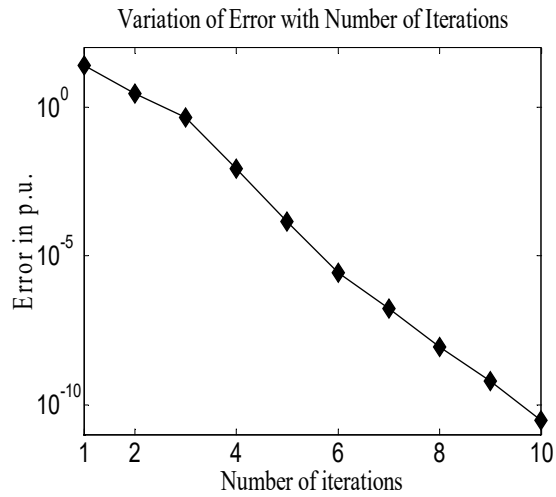


Fig. 2.38: Convergence characteristic of Table 2.8 for model-2 employing control

strategy-9

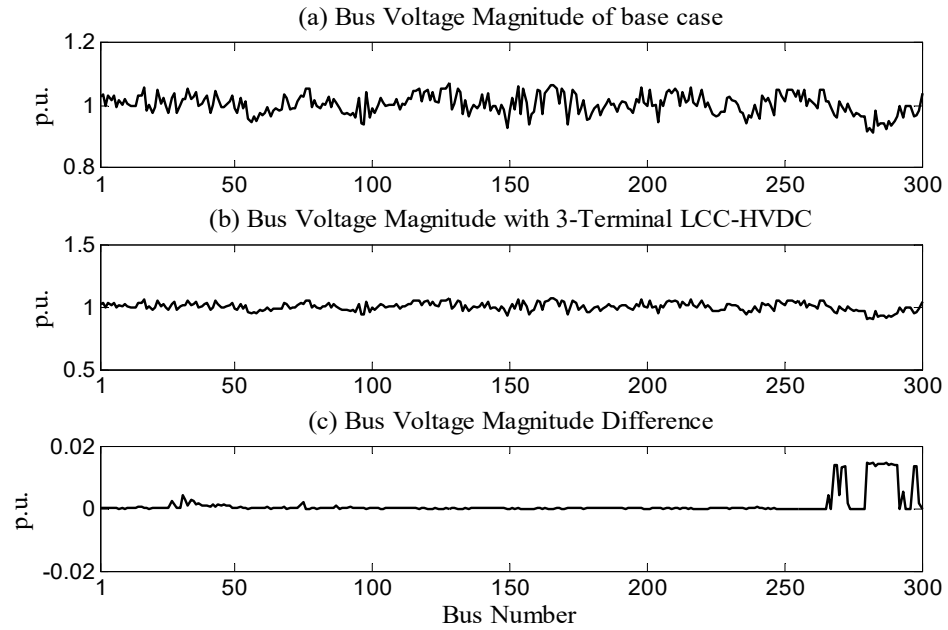


Fig. 2.39: Bus voltage profile of Table 2.8 for model-1 employing control strategy-9

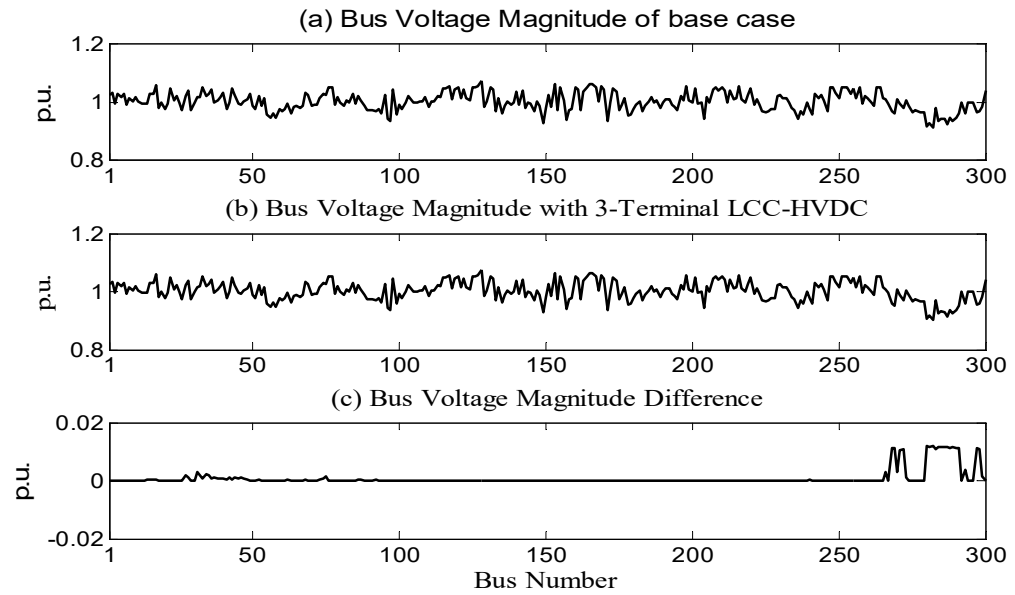


Fig. 2.40: Bus voltage profile of Table 2.8 for model-2 employing control strategy-9



From the above studies of unified method, it is observed that, the convergence characteristics corresponding to all the presented control strategies do not possess the quadratic convergence characteristics as in base case.

### **2.6.2 Sequential AC-DC power-flow studies of IEEE 300 bus test system incorporating 3-terminal LCC-HVDC network**

#### **Case I: Control strategy-1**

In this case study, two HVDC links are considered. The first link is incorporated between AC buses “25-26” and the second one between buses “25-232”. The converter connected to bus no. 25 operates as a rectifier. On the other hand, both the converters connected to buses 26 and 232 operate as inverters. The active power flows on the links 25-26 and 25-232 are set to 0.15 p.u and 0.1 p.u, respectively. The DC voltages on the rectifier side for model-1 and model-2 are set to values of 1 p.u and 2.3 p.u, respectively. It may be noted that these values are different on account of the different constants being associated with the two models (Table 2.2). The firing angle for the rectifier and the extinction angles for both the inverters are set to  $5^\circ$  and  $15^\circ$ , respectively. The power flow solution is shown in columns 6-11 of Table 2.9. From Table 2.9, it is observed that although the final power-flow solutions corresponding to two models are different, the power-flow convergence patterns are similar. Although both the models require the same ‘NI’ to converge, Model-1 takes slightly less ‘CT’ than Model-2. The convergence characteristics with model 1 and model 2 corresponding to control strategy 1 are shown in Figures 2.41 and 2.42, respectively. The bus voltage profiles with model 1 and model 2 for control strategy 1 are shown in Figures 2.43 and 2.44, respectively.

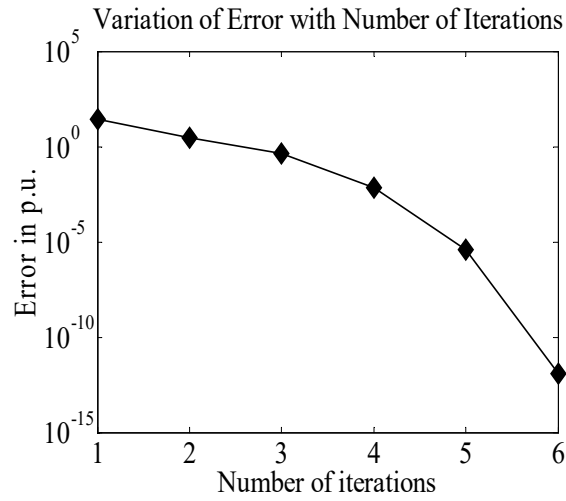


Fig. 2.41: Convergence characteristic of Table 2.9 for model-1 employing control strategy-1

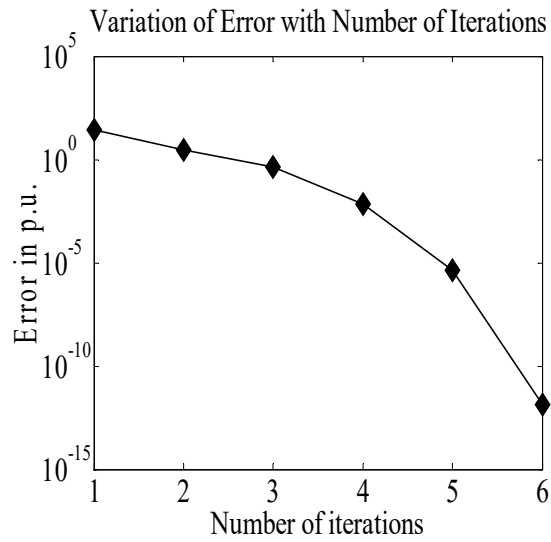


Fig. 2.42: Convergence characteristic of Table 2.9 for model-2 employing control strategy-1

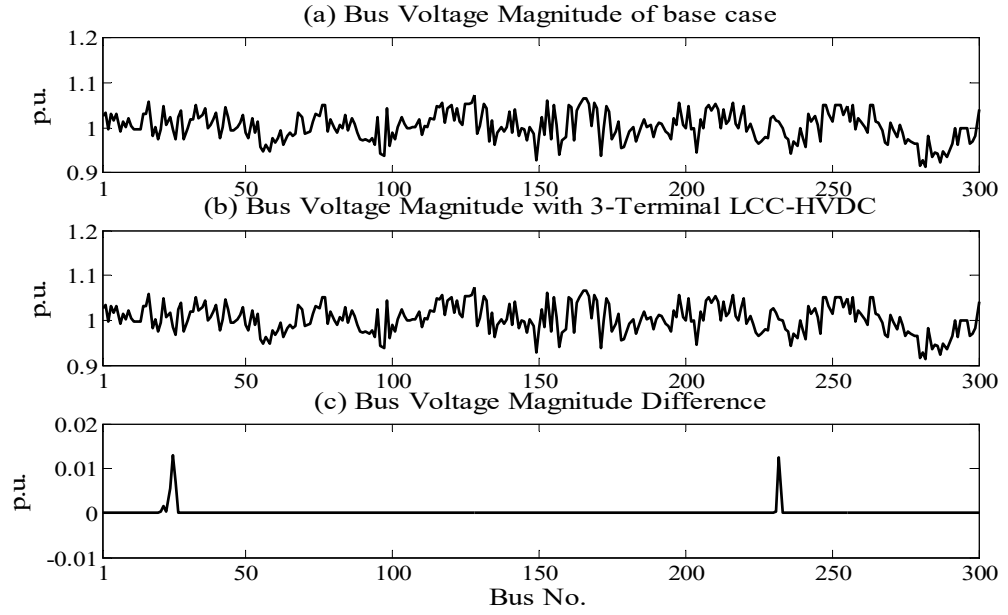


Fig. 2.43: Bus voltage profile of Table 2.9 for model-1 employing control strategy-1

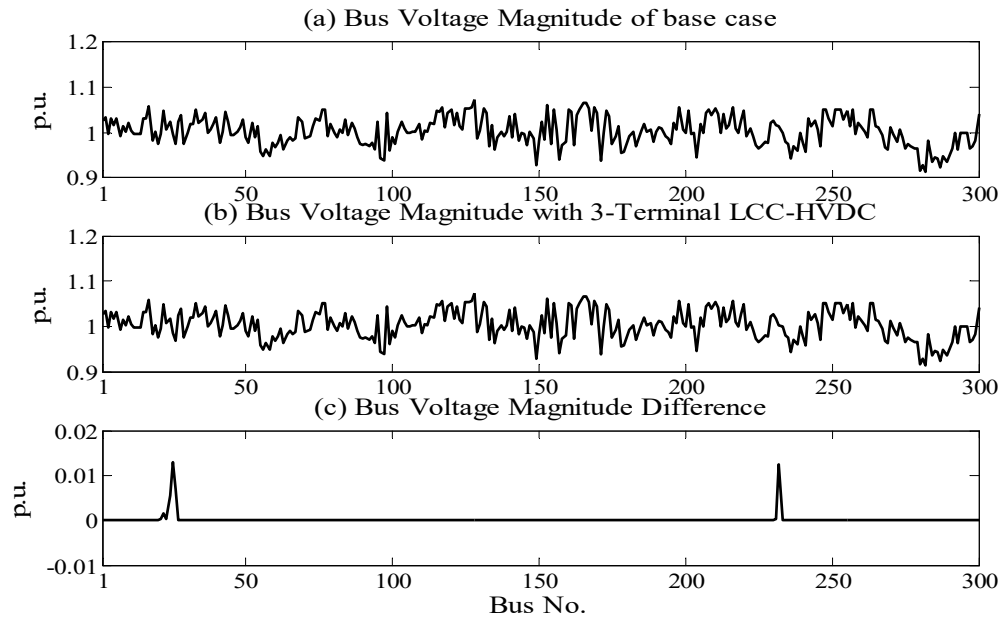


Fig. 2.44: Bus voltage profile of Table 2.9 for model-2 employing control strategy-1

## Case II: Control strategy-2

In this case study, two HVDC links are connected between AC buses “213-214” and “213-216”. The converter connected to bus no. 213 operates as a rectifier while both the converters connected to buses 214 and 216 operate as inverters. The rectifier end DC voltage is specified along with the firing angle. While the first inverter acts on constant power mode, the second one acts on constant current mode. In addition, the extinction angles for both the inverters are specified. These values are detailed in columns 1-5 of Table 2.9. The power flow solution is detailed in columns 6-11 of Table 2.9. From Table 2.9, it is observed that Model-2 demonstrates slightly better convergence than Model-1, in terms of lower ‘CT’. The convergence characteristics with model 1 and model 2 corresponding to control strategy 2 are shown in Figures 2.45 and 2.46, respectively. The bus voltage profiles of model 1 and model 2 for control strategy 2 are shown in Figures 2.47 and 2.48, respectively.

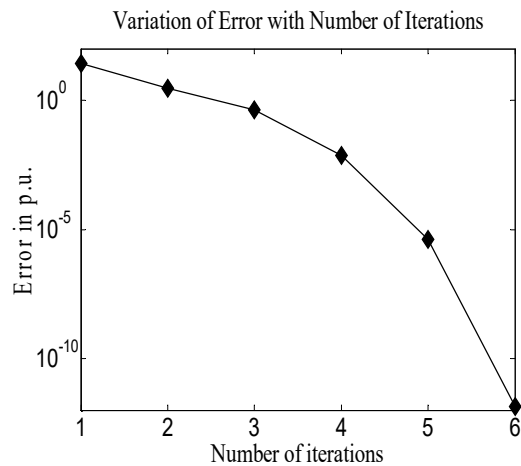


Fig. 2.45: Convergence characteristic of Table 2.9 for model-1 employing control strategy-2

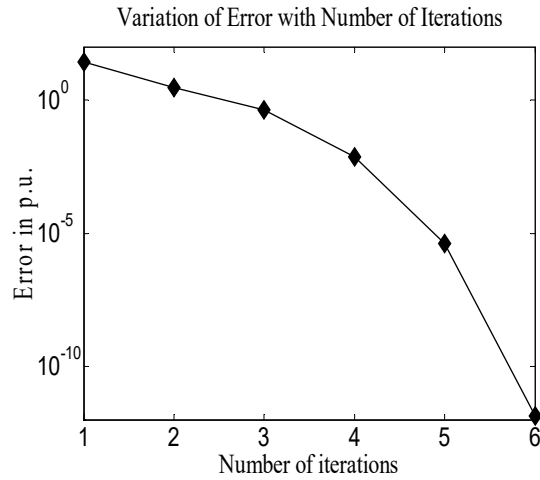


Fig. 2.46: Convergence characteristic of Table 2.9 for model-2 employing control strategy-2

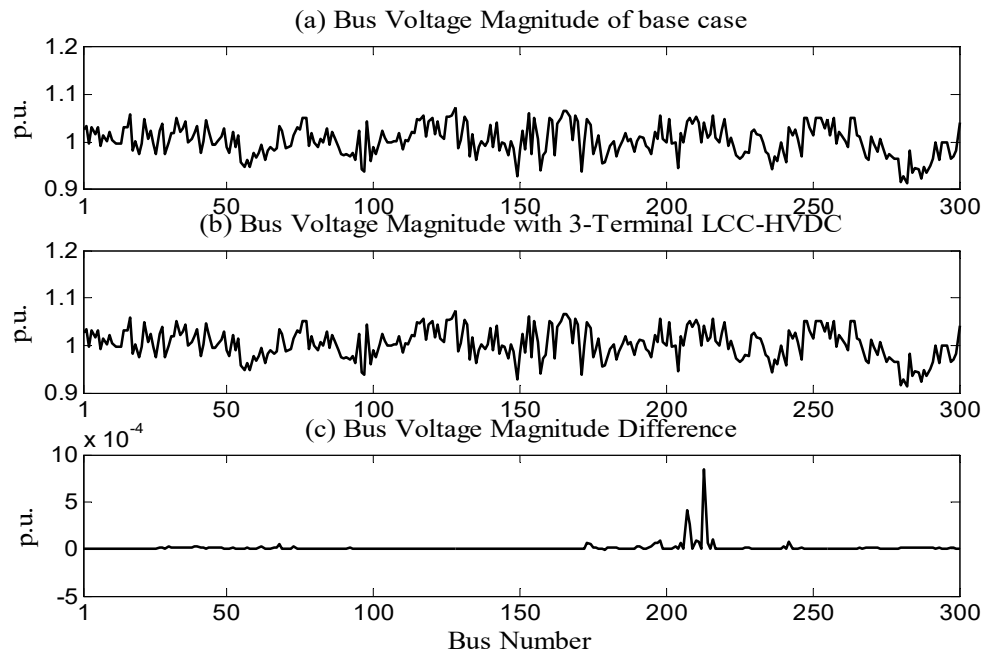


Fig. 2.47: Bus voltage profile of Table 2.9 for model-1 employing control strategy-2

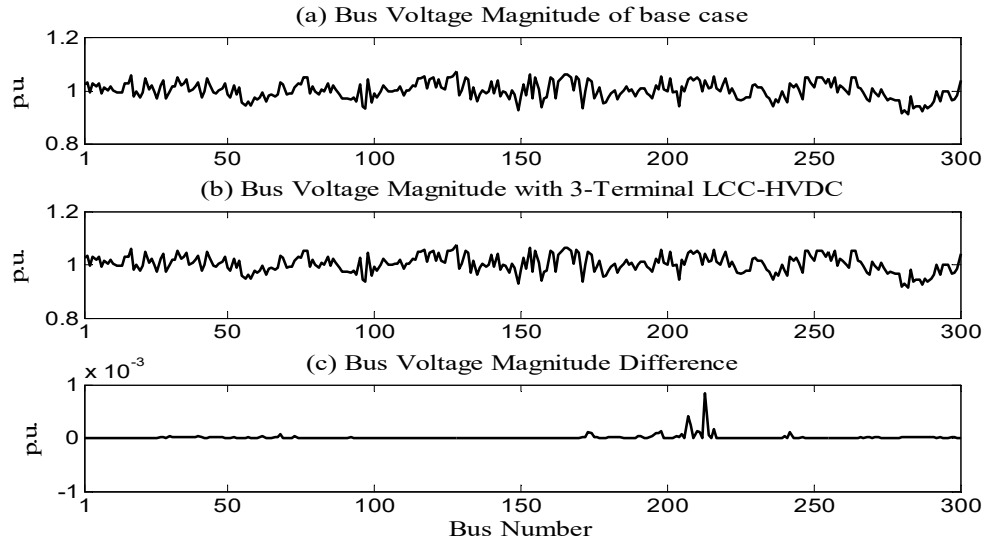


Fig. 2.48: Bus voltage profile of Table 2.9 for model-2 employing control strategy-2

### Case III: Control strategy-3

In this case, two HVDC links are connected between AC buses “109-146” and “109-147”. While the converter connected to bus no. 109 acts as a rectifier, both the converters connected to buses 146 and 147 operate as inverters. The rectifier end DC voltage is specified along with the firing angle. While the first inverter operates in constant current mode, the second one operates in the constant power mode. In addition, the extinction angles for both the inverters are specified. These values are detailed in columns 1-5 of Table 2.9. The power flow solution is detailed in columns 6-11 of Table 2.9. It is observed from the power-flow solution, that both the models demonstrate almost similar convergence characteristics. However, model-2 takes slightly less CT to converge. The convergence characteristics with model 1 and model 2 corresponding to control strategy 3 are shown in Figures 2.49 and 2.50, respectively. The bus voltage profiles with model 1 and model 2 for control strategy 3 are shown in Figures 2.51 and 2.52, respectively.

Table 2.9

Study with three different control strategies 1, 2 and 3 of sequential method

HVDC links		HVDC link specification			Power flow solution														
Rectifier bus	Inverter buses	Control strategy-1			AC terminal buses			HVDC variables											
		Spec. Values	Model 1	Model 2	AC SV	Model 1	Model 2	DC SV	Model 1	Model 2									
25	26	$P_{DC11}$ (p.u)	0.15	0.15	$V_{25}$	0.9938	0.9879	$V_{DC11}$	0.9985	2.2993									
								$V_{DC12}$	0.999	2.2996									
								$P_{DCR}$	0.2503	0.2501									
		$P_{DC12}$ (p.u)	0.1	0.1	$\theta_{25}$	0.2585	-2.1461	$I_{DC11}$	0.1502	0.0652									
								$I_{DC12}$	0.1001	0.0435									
								$I_{DCR}$	0.2503	0.1087									
	$V_{DCR}$ (p.u)	1	2.3	$V_{26}$	0.9732	0.9698	$a_R$	1.0237	0.8731										
							$a_{11}$	1.0904	0.9137										
							$a_{12}$	1.034	0.8805										
	232		$\alpha_R$ (deg.)	5	5	$\theta_{26}$	-2.0488	-4.5599	$\cos\phi_R$	0.9814	0.9873								
									$\cos\phi_{11}$	0.9423	0.9607								
									$\cos\phi_{12}$	0.9563	0.9624								
$\gamma_{11}$ (deg.)			15	15	$V_{232}$	1.0103	1.0047	NI	6	6									
$\gamma_{12}$ (deg.)	15	15	$\theta_{232}$	0.5706	-1.836	CT	1.33934	1.360377											
213	214	Spec. Values	Model 1	Model 2	AC SV	Model 1	Model 2	DC SV	Model 1	Model 2									
											$P_{DC11}$ (p.u)	0.3	0.3	$V_{213}$	1.0409	1.0409	$V_{DC11}$	0.997	2.2987
																	$V_{DC12}$	0.999	2.299
		$P_{DC12}$	0.0999	0.2299															
		$I_{DC12}$ (p.u)	0.1	0.1	$\theta_{213}$	-20.8941	-20.9826	$P_{DCR}$	0.4009	0.5302									
								$I_{DC11}$	0.3009	0.1305									
	$I_{DCR}$							0.4009	0.2305										
	216		$V_{DCR}$ (p.u)	1	2.3	$V_{214}$	1.0095	1.0095	$a_R$	1.0031	0.837								
									$a_{11}$	1.0533	0.8822								
									$a_{12}$	0.9888	0.8411								
			$\alpha_R$ (deg.)	5	5	$\theta_{214}$	-20.7203	-20.7635	$\cos\phi_R$	0.9578	0.9775								
									$\cos\phi_{11}$	0.9376	0.9556								
									$\cos\phi_{12}$	0.9564	0.958								
			$\gamma_{11}$ (deg.)	15	15	$V_{216}$	1.0564	1.0563	NI	6	6								
$\gamma_{12}$ (deg.)			15	15	$\theta_{216}$	-20.9123	-20.9012	CT	1.37153	1.360508									
109	146	Spec. Values	Model 1	Model 2	AC SV	Model 1	Model 2	DC SV	Model 1	Model 2									
											$P_{DC12}$ (p.u)	0.1	0.1	$V_{109}$	1.0190	1.0194	$V_{DC11}$	0.9995	2.995
																	$V_{DC12}$	0.999	2.996
		$P_{DCR}$	0.1501	0.215															
		$I_{DC11}$ (p.u)	0.05	0.05	$\theta_{109}$	5.6989	5.7082	$P_{DC11}$	0.05	0.115									
								$I_{DC12}$	0.1001	0.0435									
	$I_{DCR}$							0.1501	0.0935										
	147		$V_{DCR}$ (p.u)	1	2.3	$V_{146}$	0.9713	0.9716	$a_R$	1.133	0.8451								
									$a_{11}$	1.1186	0.9109								
									$a_{12}$	1.1356	0.8823								
			$\alpha_R$ (deg.)	5	5	$\theta_{146}$	-6.6123	-6.4623	$\cos\phi_R$	0.8662	0.9885								
									$\cos\phi_{11}$	0.9199	0.9619								
$\cos\phi_{12}$									0.878	0.9624									
$\gamma_{11}$ (deg.)	15	15	$V_{147}$	1.002	1.0026	NI	6	6											
$\gamma_{12}$ (deg.)	15	15	$\theta_{147}$	-4.4854	-4.4246	CT	1.49552	1.392965											

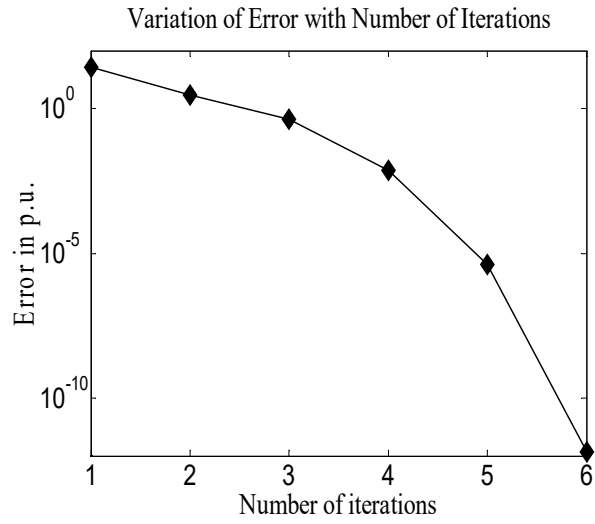


Fig. 2.49: Convergence characteristic of Table 2.9 for model-1 employing control strategy-3

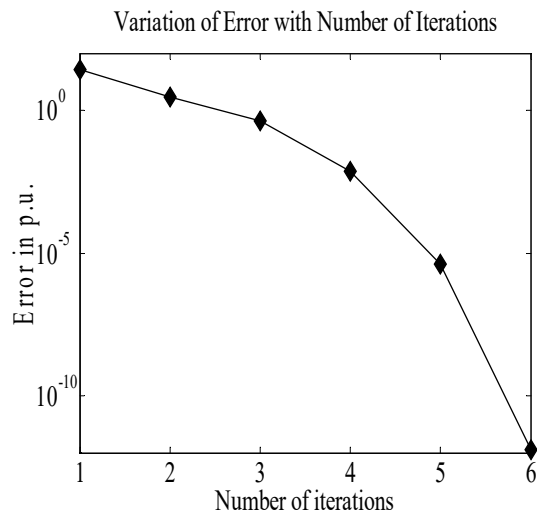


Fig. 2.50: Convergence characteristic of Table 2.9 for model-2 employing control strategy-3



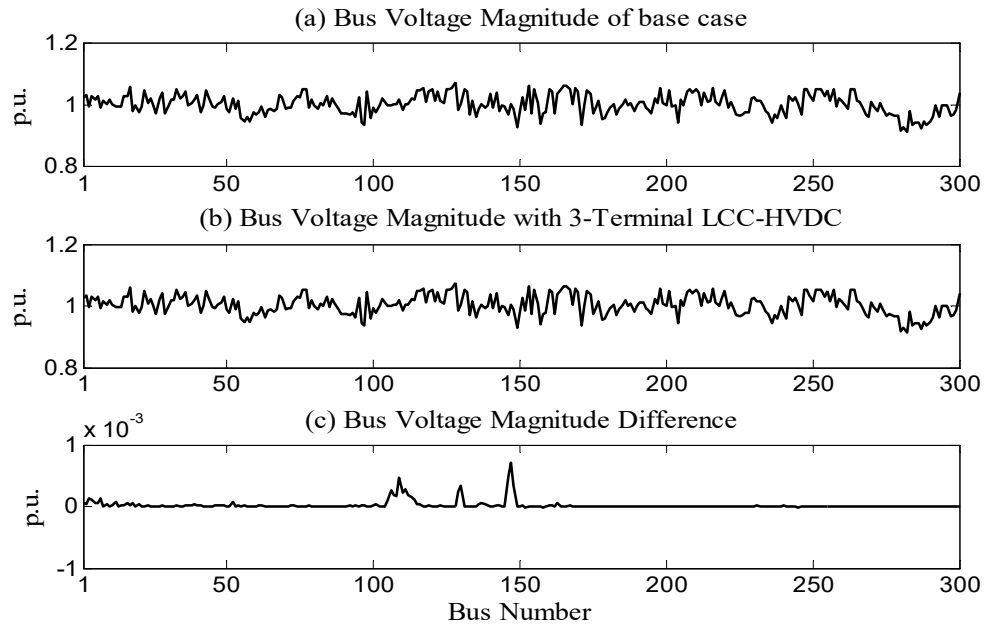


Fig. 2.51: Bus voltage profile of Table 2.9 for model-1 employing control strategy-3

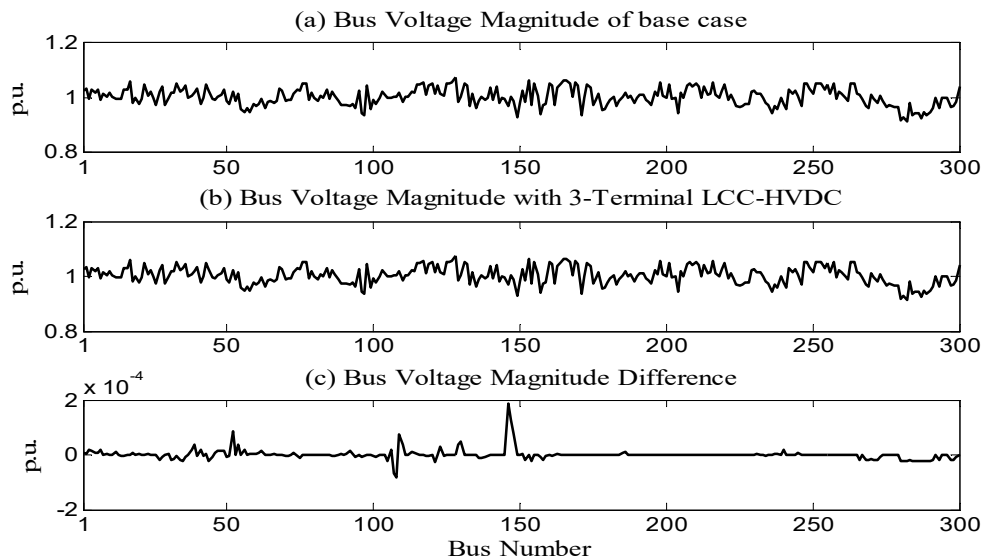


Fig. 2.52: Bus voltage profile of Table 2.9 for model-2 employing control strategy-3

#### Case IV: Control strategy-4

In this case study, the rectifier is connected to AC bus no. 101 while the inverters are connected to buses 102 and 105, respectively. The rectifier end DC voltage is specified along with the firing angle. Both the inverters are operated at constant current and constant extinction angle mode. The values of the specified quantities are detailed in columns 1-5 of Table 2.10. The power flow solution is detailed in columns 6-11 of Table 2.10. It is again observed that both the models demonstrate similar convergence characteristics, with Model-2 taking slightly less CT to converge. The convergence characteristics with model 1 and model 2 corresponding to control strategy 4 are shown in Figures 2.53 and 2.54, respectively. The bus voltage profiles with model 1 and model 2 for control strategy 4 are shown in Figures 2.55 and 2.56, respectively.

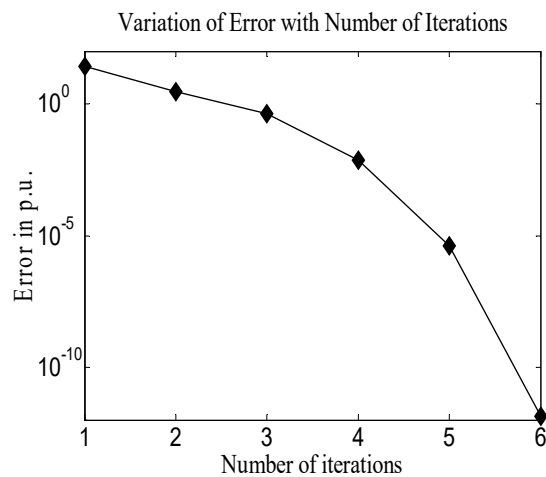


Fig. 2.53: Convergence characteristic of Table 2.10 for model-1 employing control strategy-4

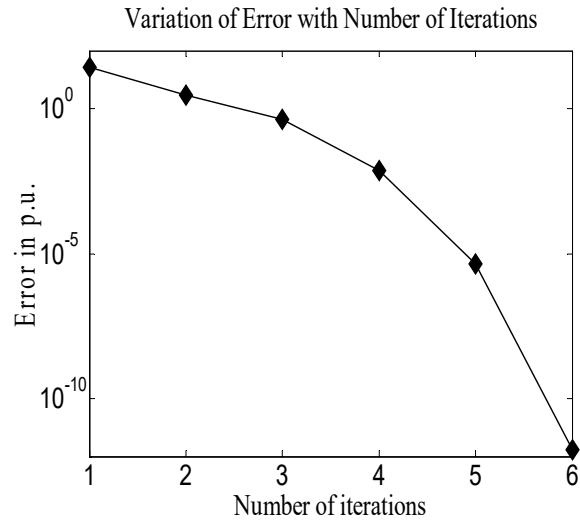


Fig. 2.54: Convergence characteristic of Table 2.10 for model-2 employing control strategy-4

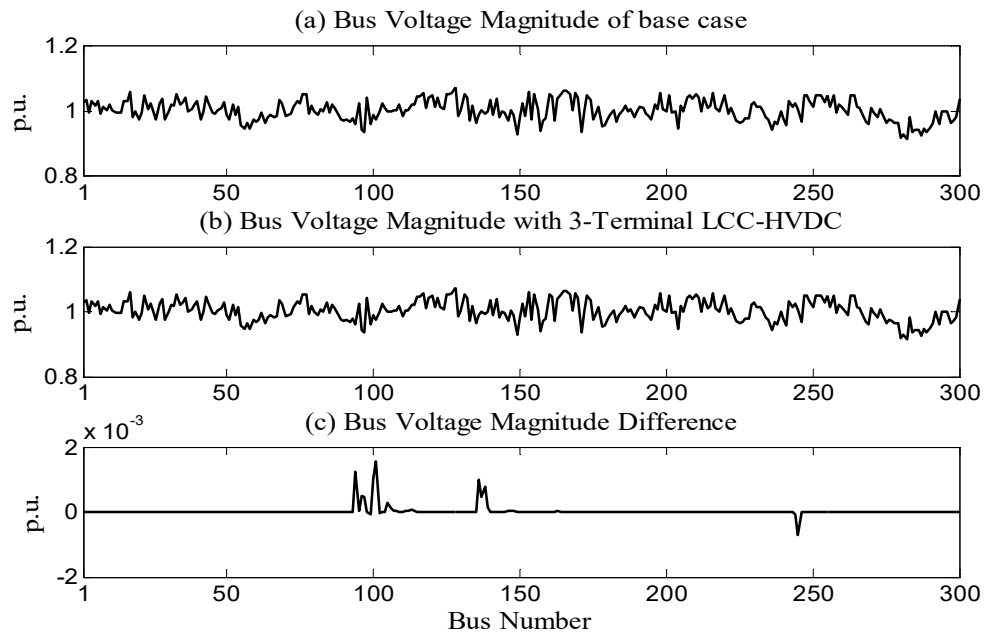


Fig. 2.55: Bus voltage profile of Table 2.10 for model-1 employing control strategy-4

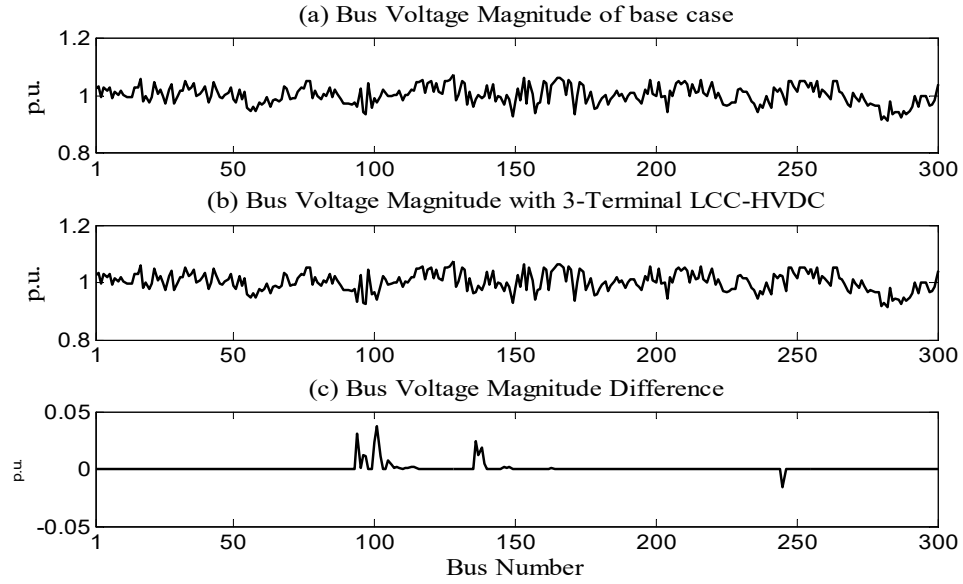


Fig. 2.56: Bus voltage profile of Table 2.10 for model-2 employing control strategy-4

#### Case V: Control strategy-5

In this case, two HVDC links are incorporated between AC buses “86-87” and “86-90”. The converter connected to bus no. 86 operates as a rectifier while both the converters connected to buses 87 and 90 operate as inverters. In this strategy, the rectifier end DC voltage is specified. Both the inverters are operated in the constant power mode. In addition, the tap ratios of all the three converter transformers are specified. Columns 1-5 of Table 2.10 show these specified values. The power flow solution is shown in columns 6-11 of Table 2.10. From the power-flow solution, it is observed that the number of iterations ‘NI’ taken to converge has increased for both the models along with increased values of computational time ‘CT’. This is because for this control strategy, the equivalent reactive power injections (at the converter terminal buses) cannot be computed a-priori and need to be updated in every iteration. This affects the convergence pattern adversely. It is also observed from the values of

‘CT’ that Model-2 fares slightly better than Model-1. The convergence characteristics with model 1 and model 2 corresponding to control strategy 5 are shown in Figures 2.57 and 2.58, respectively. The bus voltage profiles of model 1 and model 2 for control strategy 5 are shown in Figures 2.59 and 2.60, respectively.

#### **Case VI: Control strategy-6**

In this case, the two HVDC links are connected between AC buses “78-84” and “78-86”. While the converter connected to bus no. 78 operates as a rectifier, the converters connected to buses 84 and 86 operate as inverters. In this control strategy, the rectifier end DC voltage is specified. On the other hand, both the inverters are operated in the constant current mode. Also, the tap ratios of all the three converter transformers are specified. While columns ‘1-5’ of Table 2.10 show the values of the specified quantities, columns 6-11 detail the power-flow solution. From the power flow solution, it is observed that again the convergence pattern is adversely affected by this control strategy, as the converter equivalent reactive power injections are updated in each iteration. Again, from the values of ‘CT’ and ‘NI’, it is observed that Model-1 fares better than Model-2. The convergence characteristics with model 1 and model 2 corresponding to control strategy 6 are shown in Figures 2.61 and 2.62, respectively. The bus voltage profiles with model 1 and model 2 for control strategy 6 are shown in Figures 2.63 and 2.64, respectively.

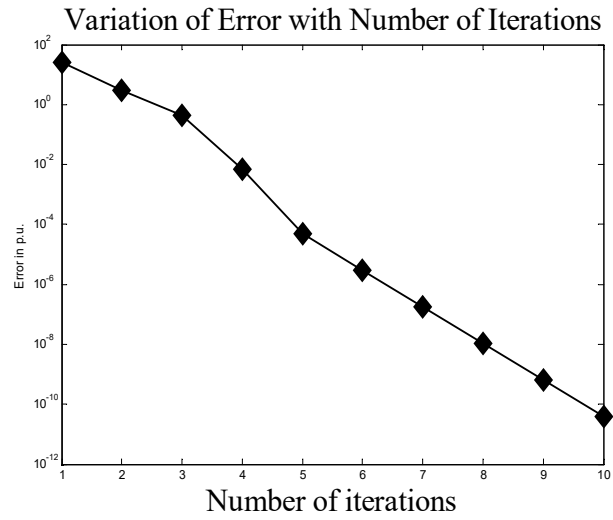


Fig. 2.57: Convergence characteristic of Table 2.10 for model-1 employing control strategy-5

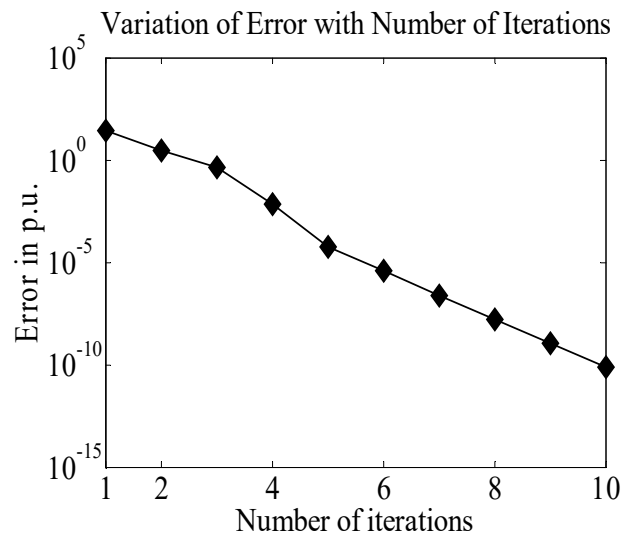


Fig. 2.58: Convergence characteristic of Table 2.10 for model-2 employing control strategy-5

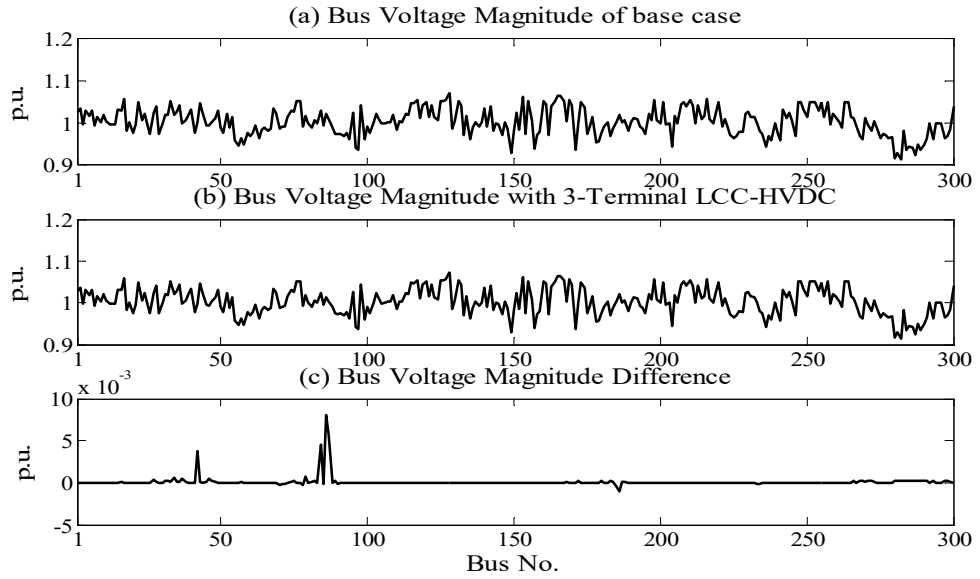


Fig. 2.59: Bus voltage profile of Table 2.10 for model-1 employing control strategy-5

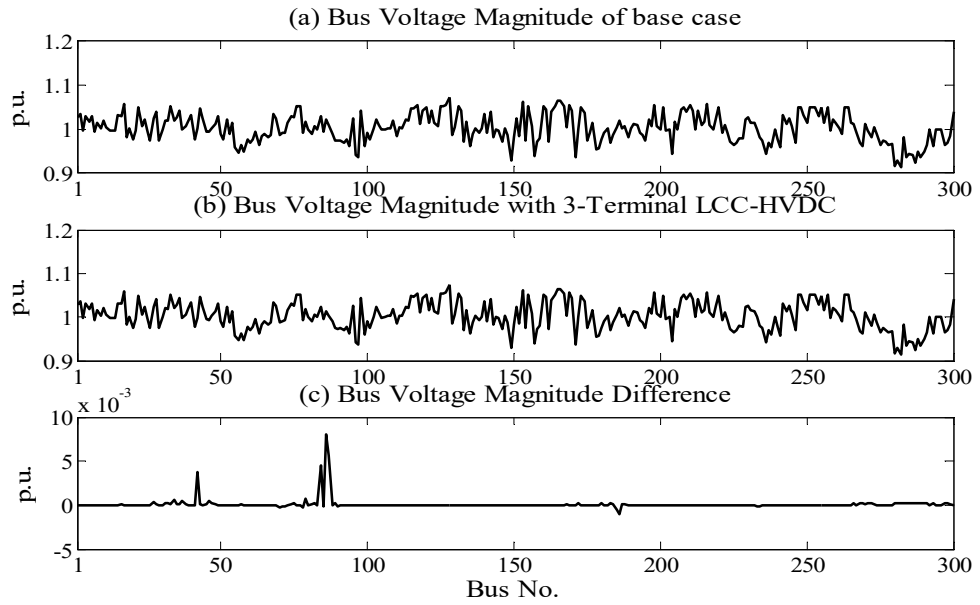


Fig. 2.60: Bus voltage profile of Table 2.10 for model-2 employing control strategy-5

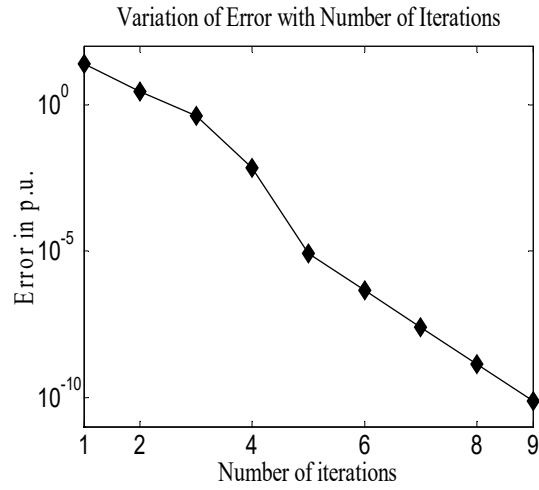


Fig. 2.61: Convergence characteristic of Table 2.10 for model-1 employing control

strategy-6

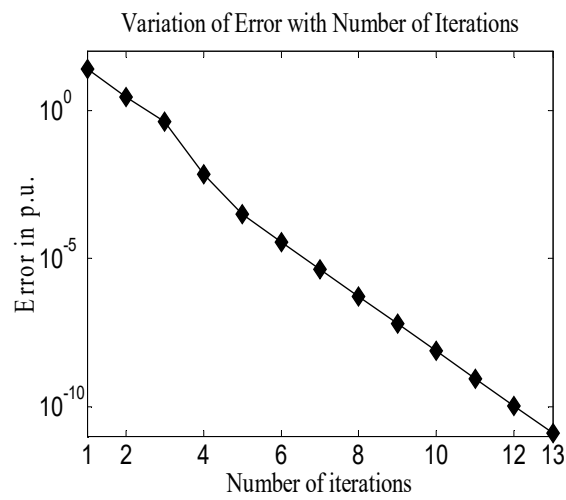


Fig. 2.62: Convergence characteristic of Table 2.10 for model-2 employing control

strategy-6



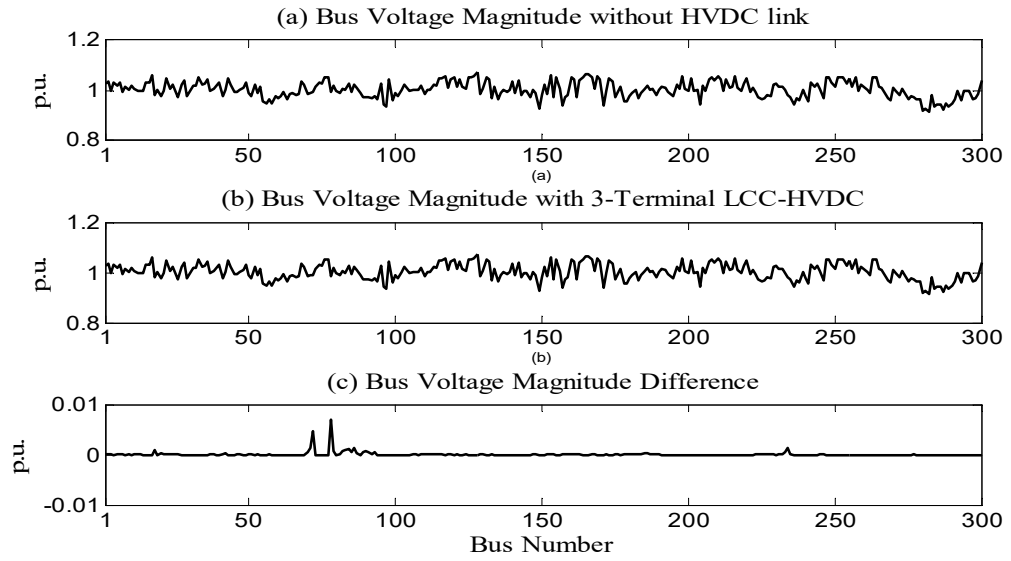


Fig. 2.63: Bus voltage profile of Table 2.10 for model-1 employing control strategy-6

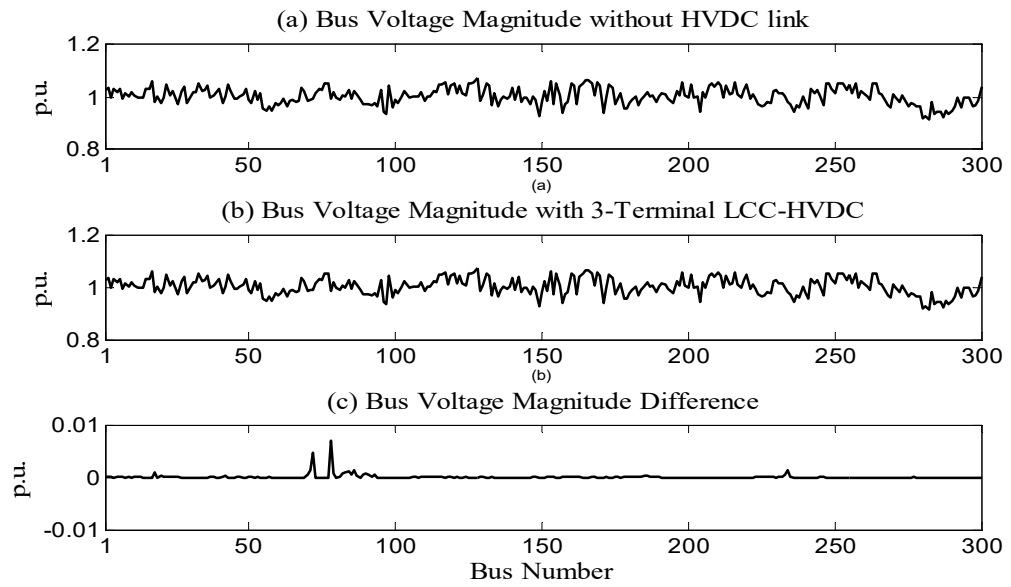


Fig. 2.64: Bus voltage profile of Table 2.10 for model-2 employing control strategy-6

Table 2.10

Study with three different control strategies 4, 5 and 6 of sequential method

HVDC link		HVDC link specification			Power flow solution											
Rectifier bus	Inverter buses	Control strategy-4			AC terminal buses			HVDC variables								
		Spec. Vals.	Model 1	Model 2	AC SV	Model 1	Model 2	DC SV	Model 1	Model 2						
101	102	$I_{DC11}$ (p.u.)	0.1	0.1	$V_{101}$	0.9745	0.9384	$V_{DC11}$	0.999	2.295						
								$V_{DC12}$	0.9995	2.296						
								$P_{DC11}$	0.0999	1.1475						
		$I_{DC12}$ (p.u.)	0.05	0.05	$\theta_{101}$	-14.5005	-18.0564	$P_{DC12}$	0.05	0.9184						
								$P_{DCR}$	0.15	2.07						
								$I_{DCR}$	0.15	0.9						
	105	$V_{DCR}$ (p.u.)	1	2.3	$V_{102}$	1.0014	0.9901	$a_R$	1.0455	0.979						
								$a_{11}$	1.0432	0.9255						
								$a_{12}$	1.0413	0.9174						
		$\alpha_R$ (deg.)	5	5	$\theta_{102}$	-17.2702	-14.7398	$\cos\phi_R$	0.9815	0.9269						
								$\cos\phi_{11}$	0.9564	0.9273						
								$\cos\phi_{12}$	0.9611	0.9348						
	$Y_{11}$ (deg.)	15	15	$V_{105}$	0.9987	0.9912	NI	6	6							
	$Y_{12}$ (deg.)	15	15	$\theta_{105}$	-12.7177	-12.8546	CT	1.51186	1.41018							
Control strategy-5			AC terminal buses			HVDC variables										
86	87	Spec. Val.	Model 1	Model 2	AC SV	Model 1	Model 2	DC SV	Model 1	Model 2						
								$P_{DC11}$ (p.u.)	0.2	0.2	$V_{86}$	1.013	1.0141	$V_{DC11}$	0.998	2.991
								$P_{DC12}$ (p.u.)	0.2	0.2	$\theta_{86}$	-13.6274	-13.6383	$V_{DC12}$	0.998	2.991
		$V_{DCR}$ (p.u.)	1	2.3	$V_{87}$	1.0025	1.0035	$P_{DCR}$	0.4008	0.4002						
								$I_{DC11}$	0.2004	0.087						
								$I_{DC12}$	0.2004	0.087						
	90	$a_R$	1.05	0.88	$\theta_{87}$	-15.6906	-15.7001	$I_{DCR}$	0.4008	0.174						
								$\alpha_R$	12.0888	14.5339						
								$Y_{11}$	21.037	20.1385						
		$a_{11}$	1.09	0.91	$V_{90}$	0.972	0.9733	$Y_{12}$	17.7966	16.703						
								$\cos\phi_R$	0.9401	0.9542						
								$\cos\phi_{11}$	0.9133	0.9321						
	$a_{12}$	1.1	0.92	$\theta_{90}$	-23.6159	-23.6212	$\cos\phi_{12}$	0.9334	0.9506							
							NI	10	10							
CT							2.02501	2.0171								
Control strategy-6			AC terminal buses			HVDC variables										
78	84	Spec. Val.	Model 1	Model 2	AC SV	Model 1	Model 2	DC SV	Model 1	Model 2						
								$I_{DC11}$ (p.u.)	0.1	0.1	$V_{78}$	0.9861	0.9757	$V_{DC11}$	0.999	2.299
								$I_{DC12}$ (p.u.)	0.1	0.1	$\theta_{78}$	-10.2544	-11.4187	$V_{DC12}$	0.999	2.299
		$V_{DCR}$ (p.u.)	1	2.3	$V_{84}$	1.0276	1.0263	$P_{DC11}$	0.0999	0.2299						
								$P_{DC12}$	0.0999	0.2299						
								$P_{DCR}$	0.2	0.46						
	86	$a_R$	1.05	0.91	$\theta_{84}$	-11.5247	-10.776	$I_{DCR}$	0.2	0.2						
								$\alpha_R$	9.8874	12.8457						
								$Y_{11}$	20.7534	21.6895						
		$a_{11}$	1.05	0.9	$V_{86}$	1.0209	1.0196	$Y_{12}$	22.5238	18.8897						
								$\cos\phi_R$	0.9658	0.959						
								$\cos\phi_{11}$	0.9258	0.9215						
	$a_{12}$	1.07	0.89	$\theta_{86}$	-12.4037	-11.6552	$\cos\phi_{12}$	0.9146	0.938							
							NI	9	13							
CT							1.84502	2.531736								

### **Case VII: Control strategy-7**

In this case study, two HVDC links are incorporated between AC buses “68-173” and “68-174”. The converter connected to bus no. 68 acts as a rectifier while both the converters connected to buses 173 and 174 act as inverters. In this control strategy, the rectifier end DC voltage is specified. The first inverter is operated in the constant power mode while the second one operates in the constant current mode. In addition, the tap ratios of all the three converter transformers are specified. The specified values are given in columns 1-5 of Table 2.11. The power flow solution is shown in columns 6-11 of Table 2.11.

From the power-flow solution, it is again observed that the convergence pattern is adversely affected by this particular control strategy as seen from the increased values of ‘NI’ and ‘CT’. This is because for this control strategy too, the converter equivalent reactive power injections need to be updated in every iteration. Also, Model-1 is observed to have slightly better convergence than Model-2 in respect of both ‘CT’ and ‘NI’. The convergence characteristics with model 1 and model 2 corresponding to control strategy 7 are shown in Figures 2.65 and 2.66, respectively. The bus voltage profiles with model 1 and model 2 for control strategy 7 are shown in Figures 2.67 and 2.68, respectively.

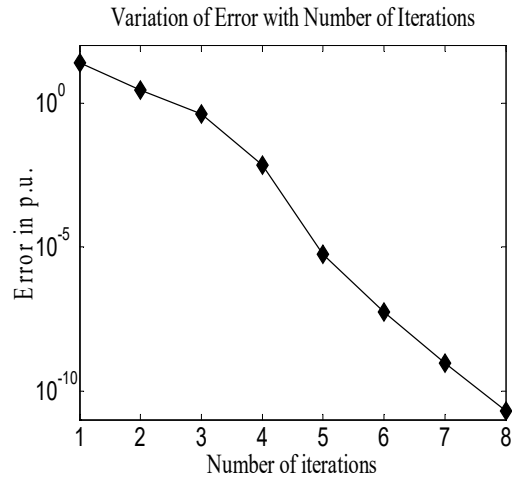


Fig. 2.65: Convergence characteristic of Table 2.11 for model-1 employing control strategy-7

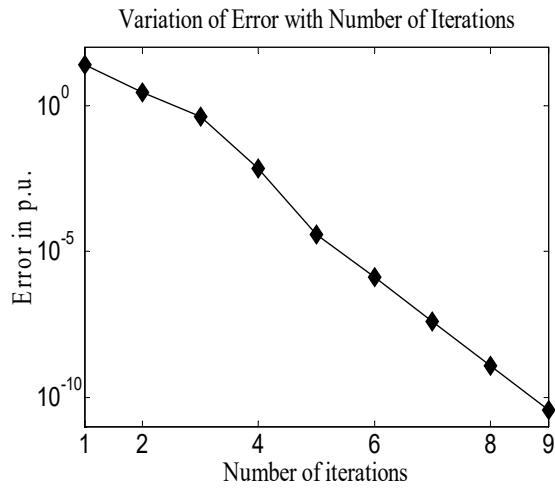


Fig. 2.66: Convergence characteristic of Table 2.11 for model-2 employing control strategy-7

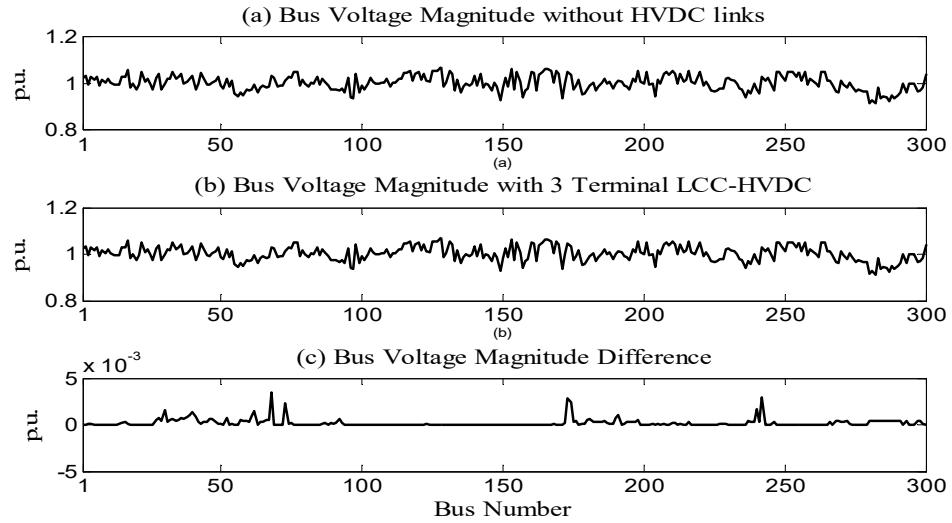


Fig. 2.67: Bus voltage profile of Table 2.11 for model-1 employing control strategy-7

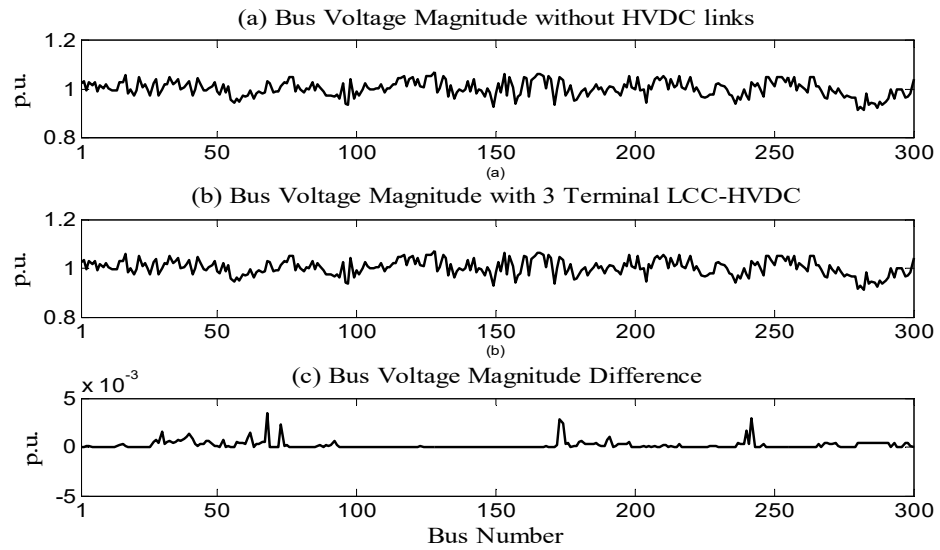


Fig. 2.68: Bus voltage profile of Table 2.11 for model-2 employing control strategy-7

### Case VIII: Control strategy-8

In this case, two HVDC links are incorporated between AC buses “15-31” and “15-74”. The converter connected to bus no. 15 operates as a rectifier while both the converters connected to buses 31 and 74 operate as inverters. Control Strategy-8 is

selected for the control of the DC links. In this control strategy, the rectifier end DC voltage is specified. The first and the second inverters are operated in the constant current and constant power modes, respectively. In addition, the tap ratios of all the three converter transformers are specified. Columns 1-5 of Table 2.11 show these specified values. The power flow solution is shown in columns 6-11 of Table 2.11. From the power-flow solution, it is again observed from the increased values of ‘CT’ and ‘NI’ that in this control strategy, the updating of the equivalent reactive power injections at the converter terminal buses in every iteration affect the convergence pattern adversely. Model-1 is observed to demonstrate slightly better convergence than Model-2 in respect of ‘CT’. The convergence characteristics with model 1 and model 2 corresponding to control strategy 8 are shown in Figures 2.69 and 2.70, respectively. The bus voltage profiles with model 1 and model 2 for control strategy 8 are shown in Figures 2.71 and 2.72, respectively.

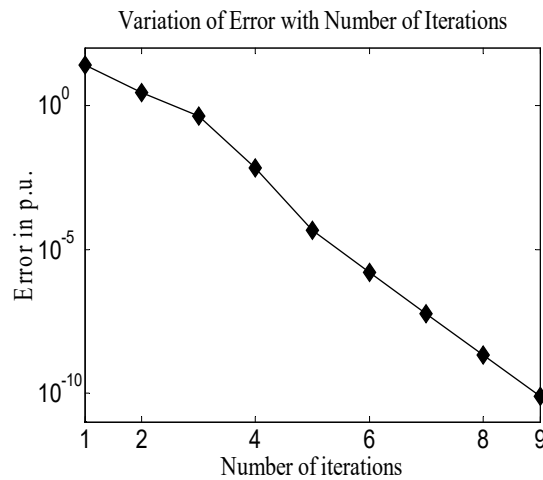


Fig. 2.69: Convergence characteristic of Table 2.11 for model-1 employing control strategy-8

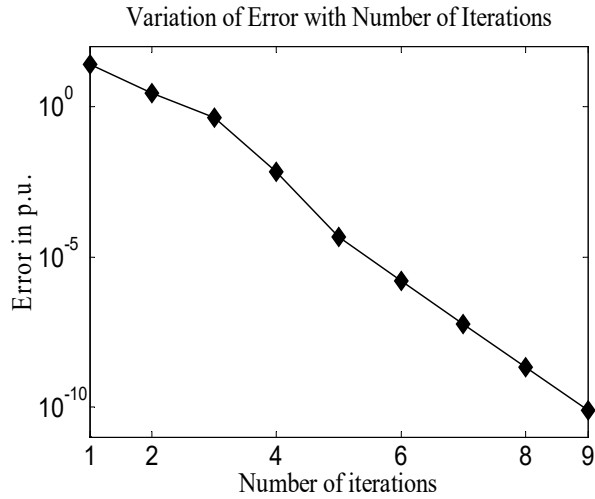


Fig. 2.70: Convergence characteristic of Table 2.11 for model-2 employing control strategy-8

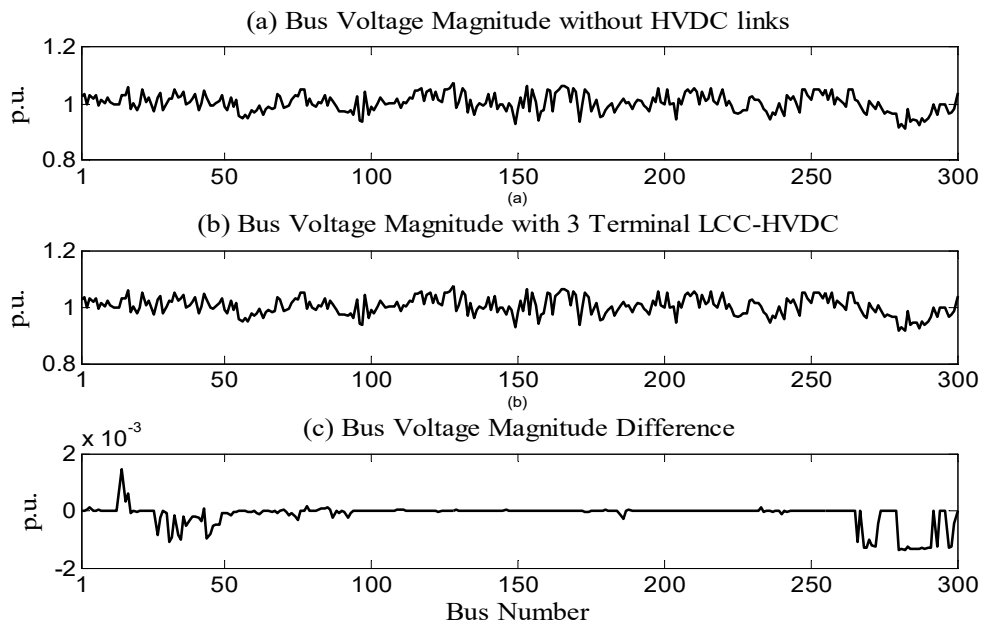


Fig. 2.71: Bus voltage profile of Table 2.11 for model-1 employing control strategy-8

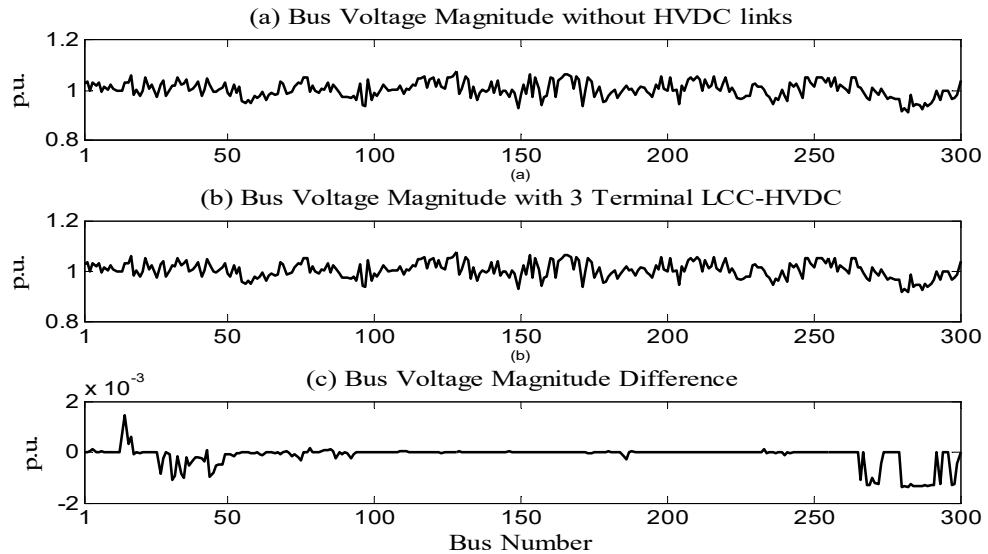


Fig. 2.72: Bus voltage profile of Table 2.11 for model-2 employing control strategy-8

### Case IX: Control strategy-9

In this case, two HVDC links are incorporated between AC buses “266-270” and “266-271”. The converter connected to bus no. 266 acts as a rectifier while both the converters connected to buses 270 and 271 act as inverters. In this control strategy, the rectifier is operated in the constant firing angle mode while the two inverters are operated in constant power and constant extinction angle modes. Columns 1-5 of Table 2.11 shows these specified values. The power flow solution is shown in columns 6-11 of Table 2.11. From the reduced values of ‘CT’ and ‘NI’ it is observed that as compared to the case studies with Control Strategies-5, 6, 7 and 8, with Control Strategy-9, the convergence pattern is better because the equivalent reactive power injections at the converter terminal buses can be computed a-priori and are independent of the iterative loop. Model-1 fares slightly better than Model-2 in terms of ‘CT’. The convergence characteristics with model 1 and model 2 corresponding to control strategy 9 are shown in Figures 2.73 and 2.74, respectively. The bus voltage



profiles with model 1 and model 2 for control strategy 9 are shown in Figures 2.75 and 2.76, respectively.

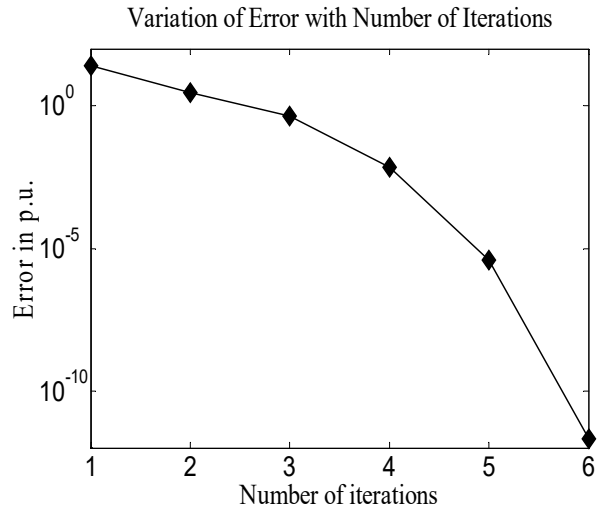


Fig. 2.73: Convergence characteristic of Table 2.11 for model-1 employing control strategy-9

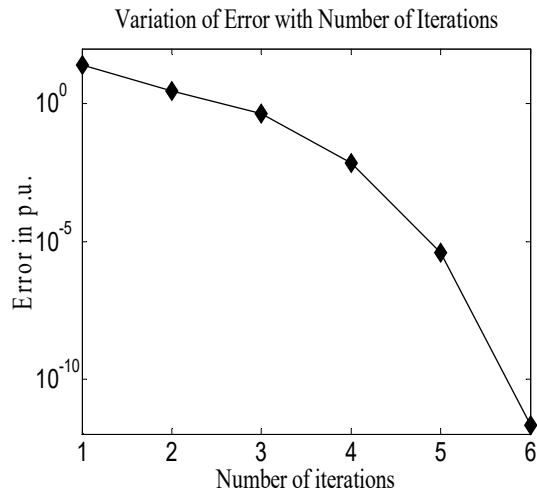


Fig. 2.74: Convergence characteristic of Table 2.10 for model-2 employing control strategy-9

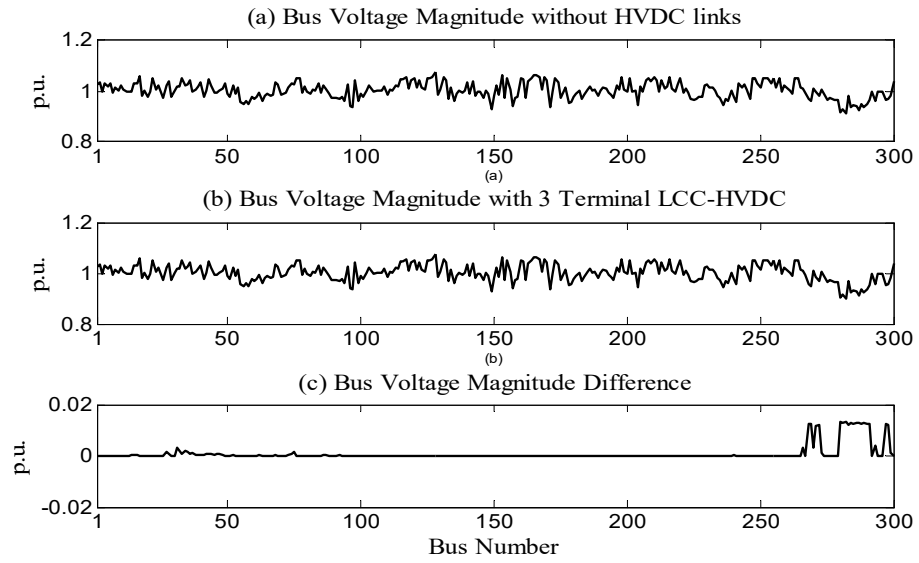


Fig. 2.75: Bus voltage profile of Table 2.11 for model-1 employing control strategy-9

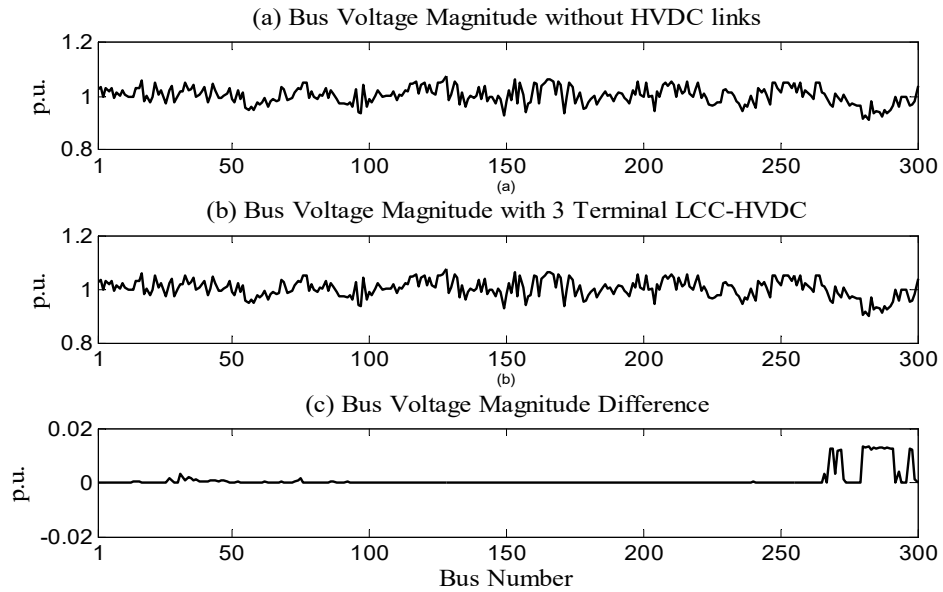


Fig. 2.76: Bus voltage profile of Table 2.11 for model-2 employing control strategy-9

Table 2.11

Study with three different control strategies 7, 8 and 9 of sequential method

HVDC link		HVDC link specification			Power flow solution					
Rectifier Bus	Inverter Buses	Control strategy-7			AC terminal buses			HVDC variables		
		Spec. Vals.	Model 1	Model 2	AC SV	Model 1	Model 2	DC SV	Model 1	Model 2
68	173	$P_{DC11}$ (p.u)	0.2	0.2	$V_{68}$	1.0309	1.0306	$V_{DC11}$	0.998	2.2991
								$V_{DC12}$	0.999	2.299
								$P_{DC12}$	0.0999	0.2299
		$I_{DC12}$ (p.u)	0.1	0.1	$\theta_{68}$	-18.7713	-18.7794	$P_{DCR}$	0.3004	0.4301
								$I_{DC11}$	0.2004	0.087
								$I_{DCR}$	0.3004	0.187
	174	$V_{DCR}$ (p.u)	1	2.3	$V_{173}$	1.0464	1.0465	$\alpha_R$	14.05	12.5736
								$\gamma_{11}$	22.1011	21.3748
								$\gamma_{12}$	21.7528	22.6652
								$\cos\phi_R$	0.9418	0.9611
		$a_R$	1.03	0.86	$\theta_{173}$	-18.7713	-18.7227	$\cos\phi_{11}$	0.9083	0.9248
								$\cos\phi_{12}$	0.9196	0.9148
								NI	8	9
								CT	1.82981	1.982946
Control strategy-8			AC terminal buses			HVDC variables				
15	31	Spec. Vals.	Model 1	Model 2	AC SV	Model 1	Model 2	DC SV	Model 1	Model 2
								$V_{DC11}$	0.9996	2.2996
								$V_{DC12}$	0.9998	2.2991
		$I_{DC11}$ (p.u)	0.04	0.04	$V_{15}$	1.0298	1.0284	$P_{DC11}$	0.04	0.092
								$P_{DCR}$	0.2404	0.2921
								$I_{DC12}$	0.2004	0.087
	74	$P_{DC12}$ (p.u)	0.2	0.2	$\theta_{15}$	-7.3763	-9.2746	$I_{DCR}$	0.2404	0.127
								$\alpha_R$	12.874	13.3493
								$\gamma_{11}$	20.5593	21.3213
								$\gamma_{12}$	18.3072	22.2765
		$V_{DCR}$ (p.u)	1	2.3	$V_{31}$	1.0208	1.0189	$\cos\phi_R$	0.952	0.9628
								$\cos\phi_{11}$	0.9326	0.9285
								$\cos\phi_{12}$	0.9307	0.9184
								NI	9	9
$a_R$	1.02	0.86	$\theta_{31}$	-9.8835	-11.1852	CT	1.97939	1.995565		
						$a_{11}$	1.05	0.9		
$a_{12}$	1.04	0.9	$\theta_{74}$	-8.7861	-10.3608	Control strategy-9				
						AC terminal buses			HVDC variables	
266	270	Spec. Values	Model 1	Model 2	AC SV	Model 1	Model 2	DC SV	Model 1	Model 2
								$V_{DCR}$	0.997	2.2987
								$V_{DC12}$	0.999	2.2996
		$P_{DC11}$ (p.u)	0.3	0.3	$V_{266}$	1.0082	1.0092	$P_{DCR}$	0.4010	0.4002
								$I_{DC11}$	0.3009	0.1305
								$I_{DC12}$	0.1001	0.0435
	271	$P_{DC12}$ (p.u)	0.1	0.1	$\theta_{266}$	-10.5314	-10.5448	$I_{DCR}$	0.401	0.174
								$a_R$	1.0226	0.8556
								$a_{11}$	1.068	0.8861
								$a_{12}$	1.0594	0.895
		$V_{DC11}$ (p.u)	1	2.3	$V_{270}$	1.0082	1.0093	$\cos\phi_R$	0.967	0.9855
								$\cos\phi_{11}$	0.9287	0.9522
								$\cos\phi_{12}$	0.9563	0.9624
								NI	6	6
$\alpha_R$ (deg.)	5	5	$\theta_{270}$	-10.5314	-10.537	$\cos\phi_{12}$	0.9563	0.9624		
						$\gamma_{11}$ (deg.)	15	15		
$\gamma_{12}$ (deg.)	15	15	$\theta_{271}$	-14.4112	-14.4049	CT	1.38442	1.397773		
						Control strategy-9			HVDC variables	

The convergence characteristics corresponding to some of the control strategies in the sequential method retain the quadratic convergence characteristics similar to the base case. However, for other control strategies, the quadratic convergence characteristics are not retained. In addition, the bus voltage profiles for these studies do not change except the terminal AC buses at which the LCC HVDC converters are placed.

## **2.7 Conclusions**

In this chapter, both unified and sequential Newton power-flow models of LCC based hybrid AC-DC systems have been presented. Based on the selection of the base values of the various DC quantities, two different per-unit AC-DC system models have been considered. The convergence characteristics of both the unified and the sequential Newton power-flow algorithms have been investigated in light of these two per-unit AC-DC system models and diverse DC link control strategies employed. All the power-flow models were implemented on a 3-terminal MLDC network incorporated in the IEEE 300-bus test system [104]. Nine different control strategies have been considered for control of the HVDC links.

It is observed that corresponding to the unified Newton power-flow model, the convergence characteristics with both the per-unit system models (Models 1 and 2) are similar, independent of the control strategy adopted. However, the convergence characteristics vary slightly with the location of the MLDC network i.e. the AC system buses between which the link is incorporated and the values of the electrical quantities specified in the control strategy adopted for the DC links.

Corresponding to the sequential Newton power-flow model, it is observed that the convergence characteristics are strongly dependent on the control strategy employed for the DC links. For some of the control strategies, the converter

equivalent reactive power injections need to be computed in every NR iteration. This affects the convergence of the algorithm. Similar to the unified model, the convergence characteristics is also observed to be affected by the location of the MLDC network in the AC system and the values of the electrical quantities specified in the DC link control strategy. It is also observed that in most of the cases, the convergence characteristics are almost similar for both the per-unit models.

In the next chapter, the Newton power flow modeling of VSC based hybrid AC-DC systems is presented.

# Chapter 3

## Newton Power Flow Modeling of Voltage Source Converter (VSC) Based Hybrid AC-DC Systems Employing DC Slack-Bus Control

### 3.1 Introduction

The advancement of power-electronics led to the development of Insulated Gate Bipolar Transistor (IGBT), which paved the way for VSC-based HVDC technology. VSC-HVDC based on PWM scheme has the advantage of independent active and reactive power control, reversible power flow without the change of voltage polarity along with reduction in filter size [8] – [18].

Unlike a two-terminal VSC HVDC interconnection, a multi-terminal VSC-based HVDC (MVDC) interconnection is able to exploit the economic and technical advantages of the VSC HVDC technology in a superior way. It is also better suited if futuristic integration of renewable energy sources are planned [19] – [21]. In a MVDC system, the converters stations can be located closely, in the same sub-station or remotely, at different locations. The corresponding configurations are known as Back-to-Back (BTB) or Point-to-Point (PTP), respectively. Most of the MVDC systems installed worldwide are in the PTP configuration, their DC sides being interconnected through DC links or cables [4], [10] and [12].

In a MVDC system, one of the VSCs acts as a master converter while the rest act as slave converters [10], [12]. The master converter controls the voltage magnitude of its AC terminal bus while the slave converters control the active and

reactive powers at the terminal end of the lines connecting them to the AC system buses [10], [12]. [23]-[36] present some comprehensive research works on the control of VSC-based HVDC systems.

For planning, operation and control of AC power systems incorporating VSC HVDC networks, power flow solution of the integrated AC-DC systems is an essential requirement. In this respect, [76] – [80], [85], [88]-[94], present some comprehensive research works on the development of efficient Newton power-flow algorithms for VSC based hybrid AC-DC systems.

However, it is observed that in none of the above works, the modulation index of the converter has been considered as an unknown. The converter modulation index ‘ $m$ ’ is an important parameter for VSC operation. Operational considerations limit the minimum and maximum value of the modulation index ‘ $m$ ’. It has been reported that [11] while a low ‘ $m$ ’ limits the maximum fundamental AC side voltage of the VSC, over-modulation ( $m > 1$ ) may result in low-order harmonics in the AC voltage spectrum. Practical ranges of ‘ $m$ ’ have been reported in [18].

Thus, a power-flow model should yield the value of ‘ $m$ ’ and ‘ $V_{DC}$ ’ directly, for a given operating condition, so that it can be checked whether ‘ $m$ ’ lies within its specified limits (with sufficient margin for a dynamic response), along with ‘ $V_{DC}$ ’.

This chapter presents the development of unified and sequential Newton power-flow models of hybrid AC-MVDC systems. For control of the MVDC grid, DC slack-bus control has been employed. In all the models, the converter modulation indices appear as unknowns along with the DC side voltages and the phase angles of the AC side voltage phasors of the VSCs. In addition, both the number of VSCs and

the MVDC network topology can be arbitrarily chosen in the model. All the models account for the converter losses.

## **3.2 Modeling of Hybrid AC-MVDC Systems Employing DC Slack**

### **Bus Control**

For the power flow modeling of an integrated AC-MVDC system, the following assumptions have been adopted [4], [8] [10] and [12].

- The supply voltages are sinusoidal and balanced (contain only fundamental frequency and positive sequence components).
- All the transmission lines are represented by their equivalent-pi models.
- The harmonics generated by the VSCs are neglected.
- The switches are assumed to be ideal.

Now, based on the locations of the VSCs, a MVDC system can have a Back to Back (BTB) or a Point to Point (PTP) configuration. In the Back to Back (BTB) scheme, the converters usually exist at the same location. On the other hand, in a Point to Point (PTP) scheme, the DC links are used to transmit the bulk power between converters which are at different locations. Depending upon the MVDC configuration (PTP or BTB), the power-flow equations and their implementation by the Newton's method are slightly different. These are elaborated below.

### **3.2.1 Modeling of Hybrid AC-MVDC Systems in the PTP Configuration**

Figure 3.1 shows a 'n' bus AC power system network incorporating a MVDC grid, which is interconnected in the PTP configuration. The MVDC grid comprises 'q' VSCs which are connected to 'q' AC buses through their respective coupling



transformers. Without loss of generality, it is assumed that the ‘q’ VSC converters are connected to AC buses ‘i’, ‘(i+1)’, and so on, up to bus ‘(i+q-1)’. The equivalent circuit of Figure 3.1 is shown in Figure 3.2.

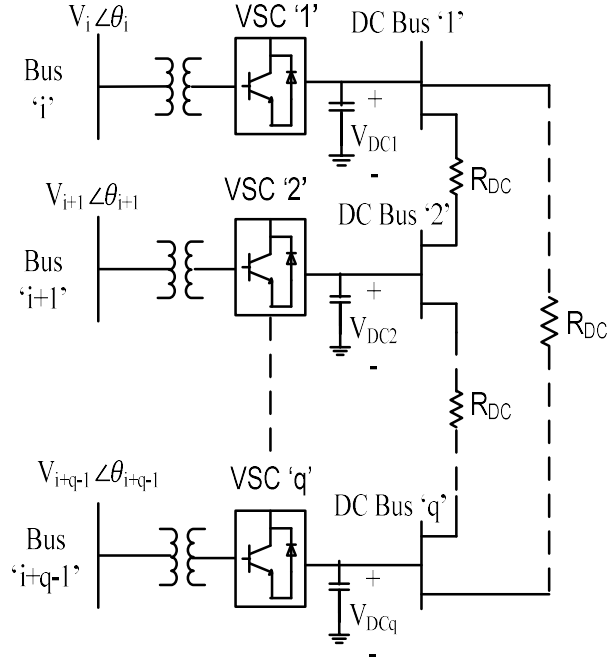


Fig. 3.1: Schematic diagram of a ‘q’ terminal PTP VSC-HVDC system

In Figure 3.2, the ‘q’ VSCs are represented by ‘q’ fundamental frequency, positive sequence voltage sources. The  $a^{\text{th}}$  ( $1 \leq a \leq q$ ) voltage source  $\mathbf{V}_{\text{sha}}$  (not shown) is connected to AC bus ‘(i+a-1)’ through the leakage impedance  $\mathbf{Z}_{\text{sha}} = R_{\text{sha}} + j X_{\text{sha}}$  of the  $a^{\text{th}}$  coupling transformer.

Now, let  $\mathbf{y}_{\text{sha}} = 1/\mathbf{Z}_{\text{sha}}$ . Then, from Figure 3.2, the current through the  $a^{\text{th}}$  ( $1 \leq a \leq q$ ) coupling transformer can be written as

$$\mathbf{I}_{\text{sha}} = \mathbf{y}_{\text{sha}} (\mathbf{V}_{\text{sha}} - \mathbf{V}_{i+a-1}) \quad (3.1)$$

where  $V_{sha}$  is the voltage phasor representing the output of the  $a^{\text{th}}$  VSC and is given by  $V_{sha} = V_{sha} \angle \theta_{sha} = m_a c V_{DCa} \angle \theta_{sha}$ , where ' $m_a$ ' and ' $V_{DCa}$ ' are the modulation index and the DC side voltage of the  $a^{\text{th}}$  ( $1 \leq a \leq q$ ) VSC, with ' $c$ ' being a constant which depends on the type of converter [11], [12]. The  $a^{\text{th}}$  VSC is connected to the AC terminal bus ' $(i+a-1)$ ' whose voltage is represented by the phasor  $V_{i+a-1} = V_{i+a-1} \angle \theta_{i+a-1}$ .

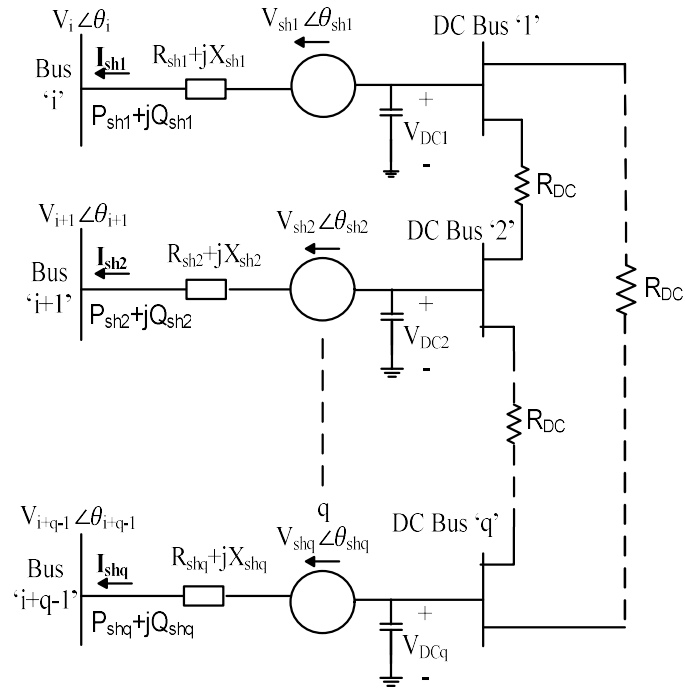


Fig. 3.2: Equivalent circuit of the ' $q$ ' terminal PTP VSC-HVDC system

Hence from Figure 3.2, the net current injection at the AC bus ' $(i+a-1)$ ' connected to the  $a^{\text{th}}$  ( $1 \leq a \leq q$ ) VSC can be written as

$$\mathbf{I}_{i+a-1} = [\mathbf{Y}_{(i+a-1)(i+a-1)}^{\text{old}} + \mathbf{y}_{sha}] \mathbf{V}_{i+a-1} + \sum_{k=1, k \neq i+a-1}^n \mathbf{Y}_{(i+a-1)k} \mathbf{V}_k - \mathbf{y}_{sha} \mathbf{V}_{sha} \quad (3.2)$$

$$\text{or, } \mathbf{I}_{i+a-1} = \sum_{k=1}^n \mathbf{Y}_{(i+a-1)k} \mathbf{V}_k - \mathbf{y}_{sha} \mathbf{V}_{sha} \quad (3.3)$$

where,  $Y_{(i+a-1)(i+a-1)}^{\text{old}} = y_{(i+a-1)0} + \sum_{k=1, k \neq i+a-1}^n y_{(i+a-1)k}$  and  $Y_{(i+a-1)(i+a-1)} = Y_{(i+a-1)(i+a-1)}^{\text{old}} + y_{\text{sha}}$  are the self admittances of bus ‘(i+a-1)’ for the original ‘n’ bus AC system without any VSC and with the a<sup>th</sup> VSC connected, respectively. ‘ $y_{(i+a-1)0}$ ’ accounts for the shunt capacitances of all the transmission lines connected to bus ‘(i+a-1)’.

### 3.2.2 Power Flow Equations of Hybrid AC-MVDC system in the PTP Configuration

With the a<sup>th</sup> ( $1 \leq a \leq q$ ) VSC connected, the net injected active power at the corresponding AC terminal bus ‘(i+a-1)’ can be written as

$$P_{i+a-1} = \text{Re} \{ V_{i+a-1} I_{i+a-1}^* \}$$

$$= \sum_{k=1}^n V_{i+a-1} V_k Y_{(i+a-1)k} \cos [\theta_{i+a-1} - \theta_k - \phi_{(i+a-1)k}] - m_a c V_{\text{DCa}} V_{i+a-1} y_{\text{sha}} \cos(\theta_{i+a-1} - \theta_{\text{sha}} - \phi_{\text{sha}}) \quad (3.4)$$

since  $V_{\text{sha}} = m_a c V_{\text{DCa}}$ , as already discussed.

In a similar manner, the net injected reactive power at bus ‘(i+a-1)’ can be written as

$$Q_{i+a-1} = \sum_{k=1}^n V_{i+a-1} V_k Y_{(i+a-1)k} \sin[\theta_{i+a-1} - \theta_k - \phi_{(i+a-1)k}] - m_a c V_{\text{DCa}} V_{i+a-1} y_{\text{sha}} \sin(\theta_{i+a-1} - \theta_{\text{sha}} - \phi_{\text{sha}}) \quad (3.5)$$

Also, from Figure 3.2, the active and reactive power flows at the terminal end of the line connecting the a<sup>th</sup> VSC to AC bus ‘(i+a-1)’ can be written as

$$P_{\text{sha}} = \text{Re} [ V_{i+a-1} I_{\text{sha}}^* ] = m_a c V_{\text{DCa}} V_{i+a-1} y_{\text{sha}} \cos(\theta_{i+a-1} - \theta_{\text{sha}} - \phi_{\text{sha}}) - V_{i+a-1}^2 y_{\text{sha}} \cos \phi_{\text{sha}} \quad (3.6)$$

$$Q_{\text{sha}} = m_a c V_{\text{DCa}} V_{i+a-1} y_{\text{sha}} \sin(\theta_{i+a-1} - \theta_{\text{sha}} - \phi_{\text{sha}}) + V_{i+a-1}^2 y_{\text{sha}} \sin \phi_{\text{sha}} \quad (3.7)$$

From eqns. (3.6) and (3.7), the apparent power flow at the terminal end of the line connecting the  $a^{\text{th}}$  VSC to AC bus ‘(i+a-1)’ can be calculated as

$$S_{\text{sha}} = V_{i+a-1} I_{\text{sha}} = \sqrt{P_{\text{sha}}^2 + Q_{\text{sha}}^2}$$

$$= y_{\text{sha}} [V_{i+a-1}^4 + m_a^2 c^2 V_{\text{DCa}}^2 V_{i+a-1}^2 - 2m_a c V_{\text{DCa}} V_{i+a-1}^3 \cos(\theta_{i+a-1} - \theta_{\text{sha}})]^{1/2} \quad (3.8)$$

The derivation of eqn. (3.8) is given in Appendix A.

Now, for the ‘q’ terminal DC system shown in Figure 3.2, the net current injection at the  $u^{\text{th}}$  ( $1 \leq u \leq q$ ) DC bus i.e. at the DC terminal of the  $u^{\text{th}}$  VSC, is given as

$$I_{\text{DCu}} = \sum_{v=1}^q Y_{\text{DCuv}} V_{\text{DCv}} \quad (3.9)$$

where  $Y_{\text{DCuv}} = -\frac{1}{R_{\text{DCuv}}}$ , ‘ $R_{\text{DCuv}}$ ’ being the DC link resistance between the DC buses ‘u’ and ‘v’.

Now, from Figure 3.2, the active power delivered by the  $a^{\text{th}}$  ( $1 \leq a \leq q$ ) VSC at its AC terminal can be written as  $P_{\text{ACa}} = \text{Re}(\mathbf{V}_{\text{sha}} \mathbf{I}_{\text{sha}}^*)$ . In a similar manner, the net power injection at the  $a^{\text{th}}$  DC terminal is given by  $P_{\text{DCa}} = V_{\text{DCa}} I_{\text{DCa}} = \sum_{v=1}^q V_{\text{DCa}} V_{\text{DCv}} Y_{\text{DCav}}$ .

Now, for the  $a^{\text{th}}$  VSC, the converter losses [18], [92] are

$$P_{\text{lossa}} = a_1 + b_1 I_{\text{sha}} + c_1 I_{\text{sha}}^2 \quad (3.10)$$

Where, ‘ $a_1$ ’ indicates the VSC losses no load, ‘ $b_1$ ’ and ‘ $c_1$ ’ are constants representative of the linear and quadratic dependency of the VSC losses on the converter current magnitude ( $I_{\text{sha}}$ ), respectively. The derivation of the converter current magnitude ( $I_{\text{sha}}$ ) is given in Appendix A.

As already discussed earlier, for the master converter, the line active and reactive powers are not specified. Hence, Eq. (3.10) can be written as

$$P_{\text{lossa}} = a_1 + b_1 \frac{S_{\text{sha}}^{\text{cal}}}{V_{i+a-1}} + c_1 \left( \frac{S_{\text{sha}}^{\text{cal}}}{V_{i+a-1}} \right)^2 \quad (3.11)$$

where,  $S_{\text{sha}}^{\text{cal}}$  is the calculated value of apparent power.

For any slave converter, Eq. (3.10) can be written as

$$P_{\text{lossa}} = a_1 + b_1 \frac{\sqrt{P_{\text{sha}}^{\text{sp}2} + Q_{\text{sha}}^{\text{sp}2}}}{V_{i+a-1}} + c_1 \left( \frac{\sqrt{P_{\text{sha}}^{\text{sp}2} + Q_{\text{sha}}^{\text{sp}2}}}{V_{i+a-1}} \right)^2 \quad (3.12)$$

where,  $P_{\text{sha}}^{\text{sp}}$  and  $Q_{\text{sha}}^{\text{sp}}$  are the specified values of the active and reactive powers at the terminal end of the line connecting the  $a^{\text{th}}$  VSC to the AC bus '(i+a-1)' respectively.

Thus, from Fig. 3.2, for the  $a^{\text{th}}$  VSC,

$$\text{Re}(\mathbf{V}_{\text{sha}} \mathbf{I}_{\text{sha}}^*) + \sum_{v=1}^q V_{\text{DCa}} V_{\text{DCv}} Y_{\text{DCav}} = -P_{\text{lossa}} \quad (3.13)$$

Substituting eqns. (3.1) and (3.9) in eqn. (3.13) and manipulating, we get,

$$(m_a c V_{\text{DCa}})^2 y_{\text{sha}} \cos \phi_{\text{sha}} - m_a c V_{\text{DCa}} V_{i+a-1} y_{\text{sha}} \cos(\theta_{\text{sha}} - \theta_{i+a-1} - \phi_{\text{sha}}) + \sum_{v=1}^q V_{\text{DCa}} V_{\text{DCv}} Y_{\text{DCav}} + P_{\text{lossa}} = 0$$

or,  $f_{1a} = 0$  (3.14)

where,  $1 \leq a \leq q$ .

Thus, 'q' independent equations are obtained. The derivation of eqn. (3.14) are shown in Appendix A.

Again from Fig. 3.2, for the ‘q’ terminal VSC-HVDC system, there are one master VSC and ‘(q-1)’ slave VSCs. The master VSC is used to control the voltage magnitude of its AC terminal bus while the slave VSCs operate in the PQ or PV control modes. The slave VSCs control the active and reactive power flows  $P_{sh}$  and  $Q_{sh}$  {as given by eqns. (3.6) and (3.7), respectively} at the terminal end of the lines connecting the VSCs to their respective AC system buses. Again, without loss of generality, if the  $r^{\text{th}}$  ( $1 \leq r \leq q$ ) VSC is chosen to be the master VSC, the additional equations obtained for the slave VSCs can be expressed as

$$P_{sha}^{\text{sp}} - P_{sha}^{\text{cal}} = 0 \quad (3.15)$$

$$Q_{sha}^{\text{sp}} - Q_{sha}^{\text{cal}} = 0 \quad (3.16)$$

$$\forall a, 1 \leq a \leq q, a \neq r$$

In the above equations,  $P_{sha}^{\text{sp}}$  and  $Q_{sha}^{\text{sp}}$  are the specified active and the reactive powers respectively, in the line connecting the  $a^{\text{th}}$  slave VSC  $\{1 \leq a \leq q, a \neq r\}$  to its AC terminal bus ‘(i+a-1)’ while  $P_{sha}^{\text{cal}}$  and  $Q_{sha}^{\text{cal}}$  are their calculated values which can be obtained using eqns. (3.6) and (3.7).

Thus, we get ‘(2q-2)’ independent equations corresponding to the ‘(q-1)’ slave VSCs.

Now, the master VSC ‘r’ controls the voltage magnitude at its AC terminal bus. Thus, for the AC terminal bus corresponding to the  $a^{\text{th}}$  VSC, if  $V_{i+a-1}^{\text{sp}}$  is the bus voltage control reference and  $V_{i+a-1}^{\text{cal}}$  is the calculated value of the voltage magnitude at bus ‘(i+a-1)’, this can be expressed as

$$V_{i+a-1}^{\text{sp}} - V_{i+a-1}^{\text{cal}} = 0 \quad (3.17)$$

$\forall a, 1 \leq a \leq q, a = r, \{ \text{as the } r^{\text{th}} (1 \leq r \leq q) \text{ VSC is chosen to be the master VSC} \}.$

It may be noted that a slave converter may be used to control the AC bus voltage magnitude rather than the line reactive power, in which case eqn. (3.16) becomes

$$V_{i+a-1}^{\text{sp}} - V_{i+a-1}^{\text{cal}} = 0 \quad (3.18)$$

$\forall a, 1 \leq a \leq q, a \neq r.$

Now, similar to the AC power flow, a slack bus is chosen for the DC power flow and its voltage is pre specified. It serves the dual role of providing the DC voltage control and balancing the active power exchange among the VSCs. From Fig. 3.2, in the ‘q’ terminal DC system, the first terminal is chosen as the DC slack bus, by convention.

This is represented as

$$V_{\text{DC1}}^{\text{sp}} - V_{\text{DC1}}^{\text{cal}} = 0 \quad (3.19)$$

At this stage, it is worthwhile to take stock of the unknown and the specified quantities. Corresponding to each VSC, three new variables enter into the picture. These include the modulation index ‘m’, the DC side voltage ‘ $V_{\text{DC}}$ ’ and the phase angle ‘ $\theta_{\text{sh}}$ ’ of the AC side output voltage (phasor) of the VSC. Also, as discussed earlier, the DC side voltage ‘ $V_{\text{DC1}}$ ’ of the first VSC is chosen as the slack bus. Thus, due to incorporation of the ‘q’ terminal VSC-HVDC network, ‘(3q-1)’ additional variables need to be solved.

Against this, we have ‘q’ independent equations corresponding to the function ‘ $f_1$ ’ {eqn. (3.14)} along with ‘(2q-2)’ independent equations for the line active and reactive powers {eqns. (3.6) and (3.7)} corresponding to the ‘(q-1)’ slave VSCs. This gives as (3q-2) independent equations. Now as the master VSC ‘r’ controls the

voltage magnitude of its AC terminal bus, the net reactive power injection at that bus is available as a specified quantity. This can be expressed as

$$Q_{i+a-1}^{sp} - Q_{i+a-1}^{cal} = 0 \quad (3.20)$$

$\forall a, 1 \leq a \leq q, a = r$ . This completes the formulation.

### 3.2.3 Modeling of Hybrid AC-MVDC Systems in the BTB Configuration

Figure 3.3 shows the AC-MVDC network shown in Fig. 3.1, now connected in the BTB configuration. The equivalent circuit of Figure 3.3 is shown in Figure 3.4.

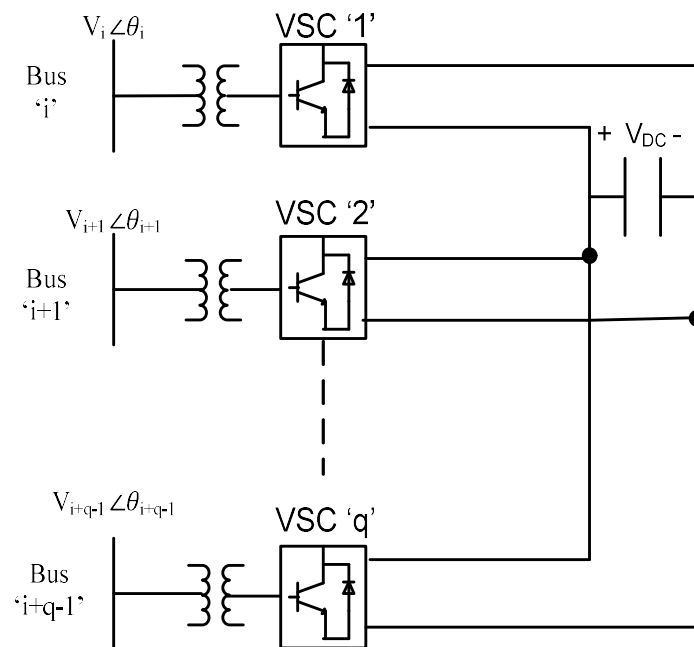


Fig. 3.3: Schematic diagram of a 'q' terminal BTB VSC-HVDC system



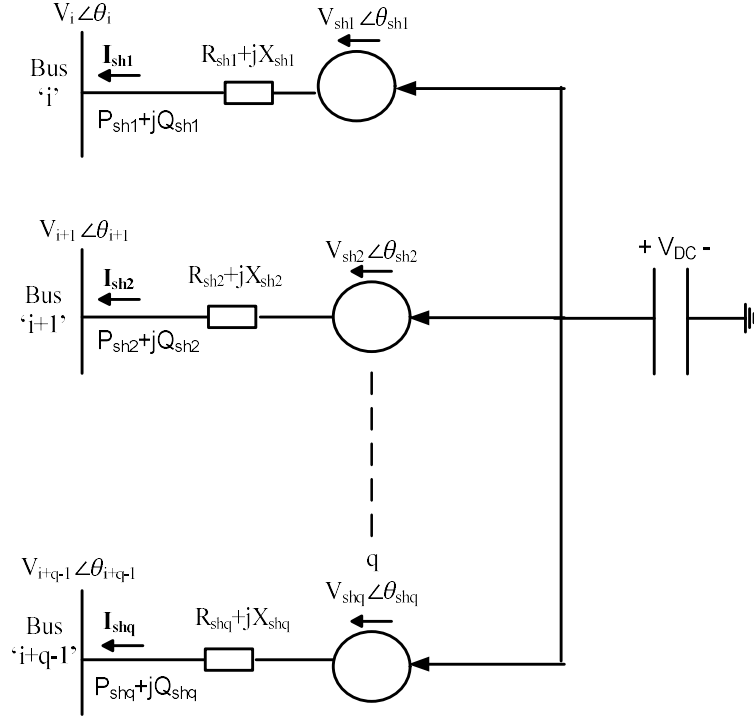


Fig. 3.4: Equivalent circuit of a ‘q’ terminal BTB VSC-HVDC system

### 3.2.4 Power Flow Equations of Integrated AC-MVDC systems in the BTB Configuration

The equations for the AC-MVDC system with the VSC-HVDC network connected in the BTB configuration would be similar to those in Section 3.2.2, except some minor modifications. These are elaborated below.

It may be noted that in the BTB configuration of Fig. 3.3, the DC side voltage ‘ $V_{DC}$ ’ is common to all the ‘q’ VSCs. Thus,  $V_{DCa} = V_{DC} \quad \forall a, 1 \leq a \leq q$ . As a consequence, eqns. (3.6) and (3.7) are retained with appropriate modifications (‘ $V_{DCa}$ ’ replaced by ‘ $V_{DC}$ ’). However, as the DC network is now rendered lossless, the ‘q’ independent equations represented by eqn. (3.14) are now replaced by a single independent equation as shown below.

From Fig. 3.3 and 3.4, it can be observed that,

$$\sum_{a=1}^q \operatorname{Re}(\mathbf{V}_{\text{sha}} \mathbf{I}_{\text{sha}}^*) + \sum_{a=1}^q P_{\text{lossa}} = 0 \quad (3.21)$$

Substituting eqns. (3.1) and (3.9) in eqn. (3.21) and manipulating, we get,

$$\sum_{a=1}^q [(m_a c V_{\text{DC}})^2 y_{\text{sha}} \cos \phi_{\text{sha}} - m_a c V_{\text{DC}} V_{i+a-1} y_{\text{sha}} \cos(\theta_{\text{sha}} - \theta_{i+a-1} - \phi_{\text{sha}})] + P_{\text{lossa}} = 0$$

$$f_1 = 0 \quad (3.22)$$

Thus, we get a single independent equation.

It may also be noted that eqn. (3.22) will be retained, without any modification.

### 3.3 Implementation in Newton Power Flow Analysis

In this section, the unified and the sequential AC-DC power-flow algorithms are used for solving the power-flow equations developed in section 3.2. The unified method is implemented first for both the PTP and the BTB configurations, followed by the sequential method.

#### 3.3.1 Unified AC-DC Power Flow Method

This method deals with the simultaneous solution of the AC and DC variables. The unified method is used to solve the AC-DC power-flow equations with the MVDC system connected in the PTP and the BTB configurations. The PTP configuration is discussed first.

##### 3.3.1.1 Unified AC-DC Power-Flow Method for PTP Configuration

In Fig. 3.1, without any loss of generality, if it is assumed that there are ‘g’ generators connected at the first ‘g’ buses of the ‘n’ bus AC system with bus 1 being the slack bus, then the Newton power-flow equation for the AC power system incorporated with the ‘q’ terminal VSC-HVDC network connected in the PTP configuration can be written as

Solve:  $\boldsymbol{\theta}$ ,  $\mathbf{V}$ ,  $\mathbf{X}$

Specified:  $\mathbf{P}$ ,  $\mathbf{Q}$ ,  $\mathbf{R}$

Where,

$$\boldsymbol{\theta} = [\theta_2 \dots \theta_n]^T, \mathbf{V} = [V_{g+1} \dots V_n]^T, \boldsymbol{\theta}_{sh} = [\theta_{sh1} \dots \theta_q]^T, \mathbf{m} = [m_1 \dots m_q]^T$$

$$\mathbf{V}_{DC} = [V_{DC2} \dots V_{DCq}]^T \text{ and } \mathbf{X} = [\boldsymbol{\theta}_{sh}^T \mathbf{m}^T \mathbf{V}_{DC}^T]^T$$

$$\mathbf{P} = [P_2 \dots P_n]^T, \mathbf{Q} = [Q_{g+1} \dots Q_n]^T, \mathbf{P}_{sh} = [P_{sh2}, \dots P_{shq}], \mathbf{Q}_{sh} = [Q_{sh} , \dots Q_{shq}],$$

$$\mathbf{f}_1 = [f_{11} \dots f_{1q}] \text{ and } \mathbf{R} = [\mathbf{P}_{sh}, \mathbf{Q}_{sh}, V_{i+r-1}, \mathbf{f}_1]^T$$

Thus the basic equation for the Newton power flow analysis is given below

$$\begin{bmatrix} \mathbf{J}_{old} & \frac{\partial \mathbf{P}}{\partial \boldsymbol{\theta}_{sh}} & \frac{\partial \mathbf{P}}{\partial \mathbf{m}} & \frac{\partial \mathbf{P}}{\partial \mathbf{V}_{DC}} \\ \frac{\partial \mathbf{R}}{\partial \boldsymbol{\theta}} & \frac{\partial \mathbf{R}}{\partial \mathbf{V}} & \frac{\partial \mathbf{R}}{\partial \boldsymbol{\theta}_{sh}} & \frac{\partial \mathbf{R}}{\partial \mathbf{m}} & \frac{\partial \mathbf{R}}{\partial \mathbf{V}_{DC}} \end{bmatrix} \begin{bmatrix} \Delta \boldsymbol{\theta} \\ \Delta \mathbf{V} \\ \Delta \boldsymbol{\theta}_{sh} \\ \Delta \mathbf{m} \\ \Delta \mathbf{V}_{DC} \end{bmatrix} = \begin{bmatrix} \Delta \mathbf{P} \\ \Delta \mathbf{Q} \\ \Delta \mathbf{R} \end{bmatrix} \quad (3.23)$$

In eqn. (3.23),  $\mathbf{J}_{old}$  is the conventional load flow (without incorporating HVDC link)

Jacobian sub-block given as follows

$$\mathbf{J}_{old} = \begin{bmatrix} \frac{\partial \mathbf{P}}{\partial \boldsymbol{\theta}} & \frac{\partial \mathbf{P}}{\partial \mathbf{V}} \\ \frac{\partial \mathbf{Q}}{\partial \boldsymbol{\theta}} & \frac{\partial \mathbf{Q}}{\partial \mathbf{V}} \end{bmatrix}$$

Also, in eqn. (3.23), ' $\Delta \mathbf{P}$ ', ' $\Delta \mathbf{Q}$ ' and ' $\Delta \mathbf{R}$ ' represent the mismatch vectors. In addition,  $\Delta \boldsymbol{\theta}$ ,  $\Delta \mathbf{V}$ ,  $\Delta \boldsymbol{\theta}_{sh}$ ,  $\Delta \mathbf{m}$  and  $\Delta \mathbf{V}_{DC}$  represent correction vectors. In the above formulation, it is assumed that all the slave converters operate in the PQ control mode. However, it may be noted that if they are made to operate in the PV control mode, the corresponding elements of the correction and mismatch vectors have to be modified accordingly. Some typical elements of eqn. (3.23) are given in Appendix A.

Fig 3.5 depicts the flow chart of the unified AC-MVDC Newton-Raphson power flow algorithm with the MVDC network configured in the PTP fashion.

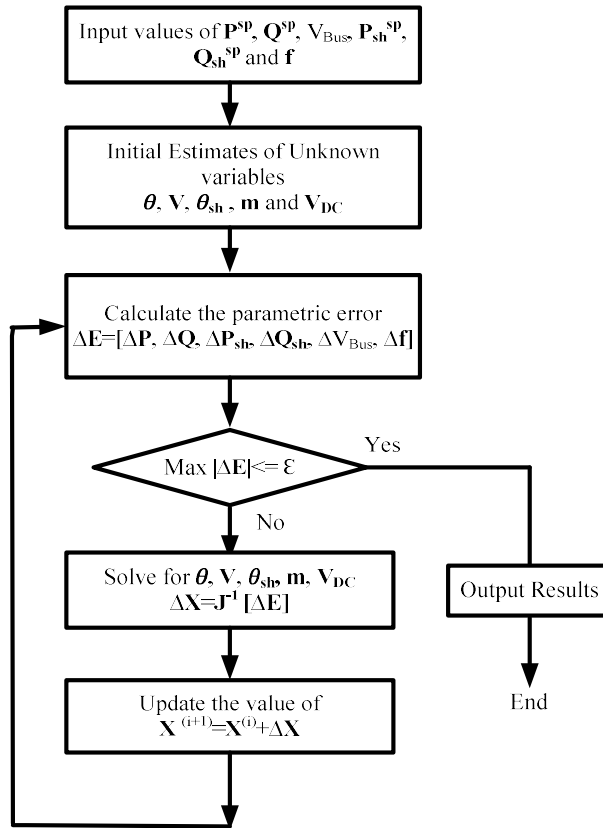


Fig. 3.5: Flow Chart of the Unified NR AC-MVDC power-flow algorithm for the PTP connection

### 3.3.1.2 Unified AC-DC Power-Flow Method for BTB Configuration

In Fig. 3.3, again, without any loss of generality, if it is assumed that there are ‘g’ generators connected at the first ‘g’ buses of the ‘n’ bus AC system with bus 1 being the slack bus, then the Newton power-flow equation for the AC power system network incorporated with the ‘q’ terminal HVDC network connected in the BTB configuration can be written as

Solve:  $\theta, V, X$

Specified:  $P, Q, R$

Where,

$$\boldsymbol{\theta} = [\theta_2 \dots \theta_n]^T, \mathbf{V} = [V_{g+1} \dots V_n]^T, \boldsymbol{\theta}_{sh} = [\theta_{sh} \dots \theta_{shq}]^T, \mathbf{m} = [m_1 \dots m_q]^T$$

$$\text{and } \mathbf{X} = [\boldsymbol{\theta}_{sh}^T \mathbf{m}^T]^T$$

$$\mathbf{P} = [P_2 \dots P_n]^T, \mathbf{Q} = [Q_{g+1} \dots Q_n]^T, \mathbf{P}_{sh} = [P_{sh2} \dots P_{shq}], \mathbf{Q}_{sh} = [Q_{sh2} \dots Q_{shq}],$$

$$\text{and } \mathbf{R} = [\mathbf{P}_{sh} \ \mathbf{Q}_{sh} \ V_{i+r-1} \ f_1]^T$$

Thus, the basic equation for the Newton power flow analysis is

$$\mathbf{J} \begin{bmatrix} \Delta \boldsymbol{\theta} \\ \Delta \mathbf{V} \\ \Delta \boldsymbol{\theta}_{sh} \\ \Delta \mathbf{m} \end{bmatrix} = \begin{bmatrix} \Delta \mathbf{P} \\ \Delta \mathbf{Q} \\ \Delta \mathbf{R} \end{bmatrix} \quad (3.24)$$

where,  $\mathbf{J} = \begin{bmatrix} \mathbf{J}_{old} & \frac{\partial \mathbf{P}}{\partial \boldsymbol{\theta}_{sh}} & \frac{\partial \mathbf{P}}{\partial \mathbf{m}} \\ \frac{\partial \mathbf{Q}}{\partial \boldsymbol{\theta}_{sh}} & \frac{\partial \mathbf{Q}}{\partial \mathbf{m}} \\ \frac{\partial \mathbf{R}}{\partial \boldsymbol{\theta}} & \frac{\partial \mathbf{R}}{\partial \mathbf{V}} & \frac{\partial \mathbf{R}}{\partial \boldsymbol{\theta}_{sh}} & \frac{\partial \mathbf{R}}{\partial \mathbf{m}} \end{bmatrix}$  is the Jacobian matrix. In eqn. (3.24), ' $\mathbf{J}_{old}$ ' is the

conventional power flow Jacobian sub-block corresponding to the 'n' bus AC system.

Also, in eqn. (3.24), ' $\Delta \mathbf{R}$ ' is the vector comprising the mismatches of the control specifications of the VSC-HVDC. In the above formulation, it is assumed that all the slave converters operate in the PQ control mode. However, it may be noted that if they are made to operate in the PV control mode, the corresponding elements of the correction and mismatch vectors have to be modified accordingly.

Fig 3.6 depicts the flow chart of the unified AC-MVDC Newton-Raphson power flow algorithm with the MVDC network configured in the BTB fashion.

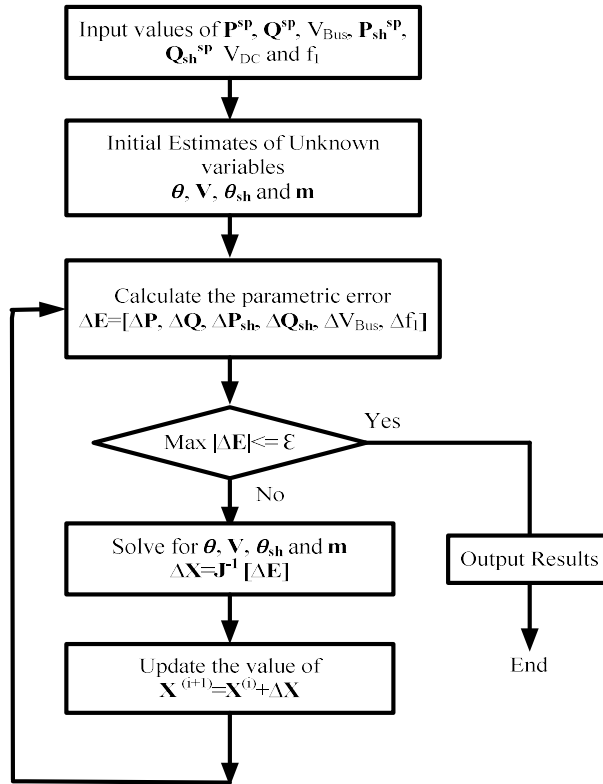


Fig. 3.6: Flow Chart of the Unified NR AC-MVDC power-flow algorithm for the BTB connection

### 3.3.2 Sequential AC-DC Power Flow Method

In this method, the AC and the DC equations are solved separately. The sequential method is used to solve the AC-DC power-flow equations with the MVDC system connected in the PTP and the BTB configurations. The PTP configuration is discussed below.

#### 3.3.2.1 Sequential AC-DC Power-Flow Method for the PTP Configuration

In the sequential method, the effect of the ‘q’ VSCs represented as ‘q’ equivalent loads on the secondary sides of the converter transformers. This is shown in Fig. 3.7.

The secondaries of the ‘q’ converter transformers are shown connected to ‘q’ fictitious AC buses ‘j’, ‘(j+1)’, and so on, up to bus ‘(j+q-1)’, as shown in the figure. The effect of the ‘q’ VSCs are represented as ‘q’ equivalent complex loads at these fictitious AC buses ‘j’ to ‘(j+q-1)’. In this respect, it may be noted from Fig. 3.7 that ‘(q-1)’ complex powers (‘S<sub>sh2</sub>’ to ‘S<sub>shq</sub>’) are specified only in the terminal ends of the lines connected to their AC terminal buses {buses ‘(i+1)’ to ‘(i+q-1)’}. Let  $\mathbf{S}_{sha} = P_{sha} + jQ_{sha}$  ( $2 \leq a \leq q$ ) be the complex power specified in the terminal end of the line connected to the AC bus ‘(i+a-1)’ through the a<sup>th</sup> coupling transformer. Then, from Fig. 3.7, the active component of the equivalent complex load power at the fictitious AC bus ‘(j+a-1)’ {which represents the effect of the a<sup>th</sup> VSC} can be expressed as

$$P_{sha}' = P_{sha} + I_{sha}^2 R_{sha} = P_{sha}^{sp} + \left( \frac{P_{sha}^{sp 2} + Q_{sha}^{sp 2}}{V_{i+a-1}^2} \right) R_{sha} \quad (3.25)$$

where  $P_{sha}^{sp}$  is the specified active power in the terminal end of the line connected to the AC bus ‘(i+a-1)’.

But from Fig. 3.2, the active power delivered by the a<sup>th</sup> ( $1 \leq a \leq q$ ) VSC at its AC terminal is

$$P_{sha}' = \text{Re}(\mathbf{V}_{sha} \mathbf{I}_{sha}^*) = m_a^2 c^2 V_{DCa}^2 y_{sha} \cos \phi_{sha} - m_a c V_{DCa} V_{i+a-1} y_{sha} \cos(\theta_{sha} - \theta_{i+a-1} - \phi_{sha}) \quad (3.26)$$

Substituting eqn. (3.25) in (3.26), we get

$$m_a^2 c^2 V_{DCa}^2 y_{sha} \cos \phi_{sha} - m_a c V_{DCa} V_{i+a-1} y_{sha} \cos(\theta_{sha} - \theta_{i+a-1} - \phi_{sha}) - P_{sha}^{sp} - \left( \frac{P_{sha}^{sp 2} + Q_{sha}^{sp 2}}{V_{i+a-1}^2} \right) R_{sha} = 0$$

$$\text{or, } f_{2a} = 0 \quad (3.27)$$



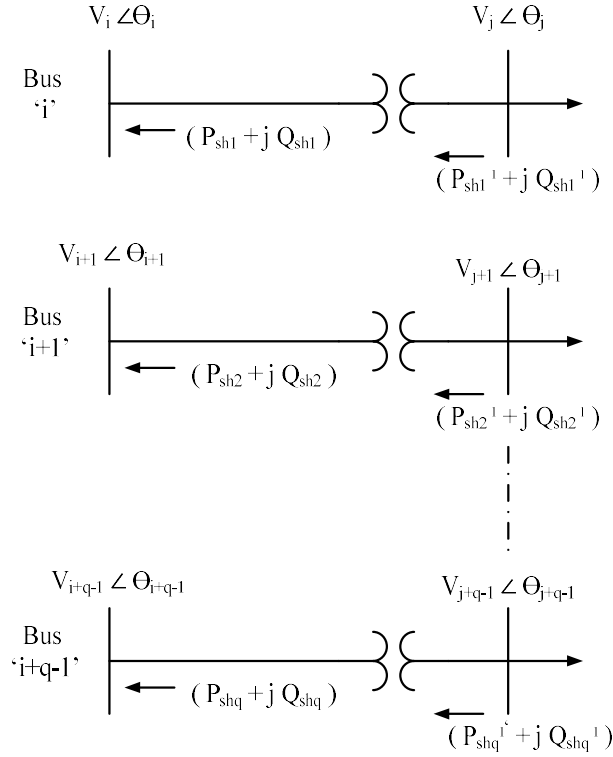


Fig. 3.7: Representation of VSCs as equivalent complex load powers

In a similar manner, the reactive component of the equivalent complex load power at the fictitious AC bus ‘(j+a-1)’ {which represents the effect of the a<sup>th</sup> VSC} can be expressed as

$$-m_a^2 c^2 V_{DCa}^2 y_{sha} \sin \phi_{sha} - m_a c V_{DCa} V_{i+a-1} y_{sha} \sin(\theta_{sha} - \theta_{i+a-1} - \phi_{sha}) - Q_{sha}^{sp} - \left( \frac{P_{sha}^{sp\ 2} + Q_{sha}^{sp\ 2}}{V_{i+a-1}^2} \right) X_{sha} = 0$$

$$\text{or, } f_{3a} = 0 \quad (3.28)$$

If the a<sup>th</sup> ( $1 \leq a \leq q$ ) VSC operates in the PV control mode, ‘ $Q_{sha}$ ’ is not specified and hence, eqn. (3.26) is modified to {using Eq. (A.8) of Appendix A}

$$P'_{sha} - P_{sha}^{sp} - I_{sha}^2 R_{sha} = 0$$

$$\begin{aligned}
& \text{or, } m_a^2 c^2 V_{DCa}^2 y_{sha} \cos\phi_{sha} - m_a c V_{DCa} V_{i+a-1} y_{sha} \cos(\theta_{sha} - \theta_{i+a-1} - \phi_{sha}) - P_{sha}^{SP} \\
& - [V_{i+a-1}^2 y_{sha}^2 + m_a^2 c^2 V_{DCa}^2 y_{sha}^2 - 2m_a c V_{DCa} V_{i+a-1} \cos(\theta_{i+a-1} - \theta_{sha})] R_{sha} = 0 \\
& \text{or, } f_{4a} = 0 \tag{3.29}
\end{aligned}$$

### AC Network Solution

Corresponding to Fig. 3.1, the Newton power-flow equation for the sequential solution of the AC power system variables can be written as

Solve:  $\boldsymbol{\theta}$ ,  $\mathbf{V}$ ,  $\mathbf{X}$

Specified:  $\mathbf{P}$ ,  $\mathbf{Q}$ ,  $\mathbf{R}$

Where,

$$\boldsymbol{\theta} = [\theta_2 \dots \theta_n]^T, \mathbf{V} = [V_{g+1} \dots V_n]^T, \boldsymbol{\theta}_{sh} = [\theta_{sh1} \dots \theta_q]^T, \mathbf{m} = [m_1 \dots m_q]^T$$

$$\text{and } \mathbf{X} = [\boldsymbol{\theta}_{sh}^T, \mathbf{m}^T]^T$$

$$\mathbf{P} = [P_2 \dots P_n]^T, \mathbf{Q} = [Q_{g+1} \dots Q_n]^T,$$

$$\mathbf{f}_2 = [f_{22} \dots f_{2q}], \mathbf{f}_3 = [f_{32} \dots f_{3q}] \text{ and } \mathbf{R} = [V_{i+r-1}, \mathbf{f}_2, \mathbf{f}_3, f_{11}]^T$$

Thus the basic Newton power flow equation is given below

$$\begin{bmatrix}
\mathbf{J}_{old} & \frac{\partial \mathbf{P}}{\partial \boldsymbol{\theta}_{sh}} & \frac{\partial \mathbf{P}}{\partial \mathbf{m}} \\
\frac{\partial \mathbf{Q}}{\partial \boldsymbol{\theta}_{sh}} & \frac{\partial \mathbf{Q}}{\partial \mathbf{m}} \\
\frac{\partial \mathbf{R}}{\partial \boldsymbol{\theta}_{sh}} & \frac{\partial \mathbf{R}}{\partial \mathbf{m}}
\end{bmatrix}
\begin{bmatrix}
\Delta \boldsymbol{\theta} \\
\Delta \mathbf{V} \\
\Delta \boldsymbol{\theta}_{sh} \\
\Delta \mathbf{m}
\end{bmatrix}
=
\begin{bmatrix}
\Delta \mathbf{P} \\
\Delta \mathbf{Q} \\
\Delta \mathbf{R}
\end{bmatrix} \tag{3.30}$$

In eqn. (3.30),  $\mathbf{J}_{old}$  is the conventional load flow (without incorporating HVDC link)

Jacobian sub-block given as follows

$$\mathbf{J}_{old} = \begin{bmatrix} \frac{\partial \mathbf{P}}{\partial \boldsymbol{\theta}} & \frac{\partial \mathbf{P}}{\partial \mathbf{V}} \\ \frac{\partial \mathbf{Q}}{\partial \boldsymbol{\theta}} & \frac{\partial \mathbf{Q}}{\partial \mathbf{V}} \end{bmatrix}$$

Also, in eqn. (3.30), ‘ $\Delta \mathbf{P}$ ’, ‘ $\Delta \mathbf{Q}$ ’ and ‘ $\Delta \mathbf{R}$ ’ represent the mismatch vectors. In addition,  $\Delta \boldsymbol{\theta}$ ,  $\Delta \mathbf{V}$ ,  $\Delta \boldsymbol{\theta}_{sh}$  and  $\Delta \mathbf{m}$  represent correction vectors. In the above formulation, it is assumed that all the slave converters operate in the PQ control mode. However, it may be noted that if they are made to operate in the PV control mode, the corresponding elements of the correction and mismatch vectors have to be modified accordingly. Some typical elements of eqn. (3.30) are given in Appendix A.

### DC network solution

Again, corresponding to Fig. 3.1, the Newton power-flow equation for the sequential solution of the DC variables of the ‘q’ bus MVDC system can be written as

Solve:  $\mathbf{V}_{DC}$

Specified:  $\mathbf{f}_5$

Where,

$$\mathbf{V}_{DC} = [V_{DC} \dots V_{DCq}] \quad \text{and} \quad \mathbf{f}_5 = [f_{12} \dots f_{1q}]$$

Thus the basic Newton power flow equation is given below

$$\begin{bmatrix} \frac{\partial \mathbf{f}_5}{\partial \mathbf{V}_{DC}} \end{bmatrix} [\Delta \mathbf{V}_{DC}] = [\Delta \mathbf{f}_5] \quad (3.31)$$

Also, in eqn. (3.31), ‘ $\Delta \mathbf{f}_5$ ’ is the mismatch vector whereas  $\Delta \mathbf{V}_{DC}$  represents the correction vector comprising the DC voltages of all DC buses except the DC slack bus.

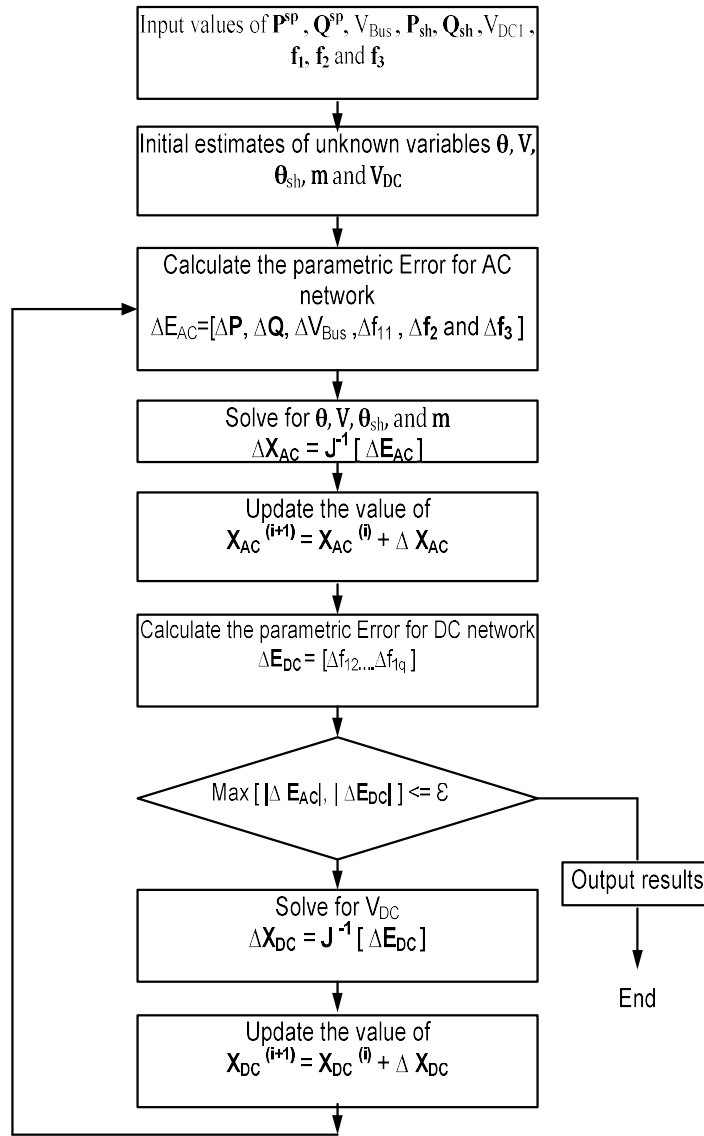


Fig. 3.8: Flow Chart of the Sequential AC-MVDC power-flow algorithm for the PTP connection

### 3.3.2.2 Sequential AC-DC Power-Flow Method for the BTB Configuration

In the BTB configuration, the converters are at the same location and interconnected through a common DC link. Since this DC voltage is specified, the sequential method is not applicable for such AC-DC networks.

### **3.4 Case Studies and Results**

Several case studies were implemented to justify the results. For all successive studies, a M-VSC-HVDC network was integrated in the IEEE 300-bus test system [104]. The resistances and the leakage reactances of all the converter transformers were taken as 0.001 p.u and 0.1 p.u respectively, for the case studies. For all the case studies, the resistance of each DC link was chosen as 0.01 p.u. The converter loss constants ‘a<sub>1</sub>’, ‘b<sub>1</sub>’ and ‘c<sub>1</sub>’ were selected as 0.011, 0.003 and 0.0043, respectively [18], [95]. In addition, the value of ‘c’ for the VSC based converters was uniformly adopted as  $\frac{1}{2\sqrt{2}}$  [100]. The initial values of variables corresponding to VSC based HVDC system were shown in Appendix A. A convergence tolerance of 10<sup>-10</sup> p.u. was uniformly adopted for all the case studies. For all the case studies, ‘NI’ and ‘CT’ denote the number of iterations and the computational time in seconds {on a Intel® Core(TM) 2 Duo CPU T6400, 2GHz, 2GB RAM processor} for the algorithm to converge.

#### **3.4.1 Studies with unified power-flow model of hybrid AC-MVDC systems**

##### **Case I: Three-terminal MVDC network connected in the BTB configuration**

In this study, a three-terminal BTB connected VSC-HVDC network is incorporated in the IEEE-300 bus system between buses 266, 270 and 271. The VSC connected to bus no. 266 is made to operate as the master converter. On the other hand, both the slave

VSCs are connected to buses 270 and 271 and operate in the PQ control mode. The specified values are given in columns 1-3 of Table 3.1. The power flow solution is shown in columns 4-5 of Table 3.1. From Table 3.1, it is observed that the power flow converges in six iterations, similar to the base case power flow (without any HVDC network). Also, the power-flow solution directly yields the VSC modulation indices, unlike existing models. The convergence characteristic plots for the power flows of the base case and BTB VSC-HVDC system are shown in Fig. 3.9 and 3.10, respectively. From Figures 3.9 and 3.10, it is observed that similar to the base case, the proposed unified AC-DC Newton-Raphson algorithm also demonstrates quadratic convergence.

The bus voltage profile for this study is shown in Fig. 3.11. From Fig. 3.11, it is observed that the bus voltage profile hardly changes except for the AC terminal buses at which the VSCs are installed.

Table 3.1

Study of IEEE 300 bus system with BTB VSC HVDC network

HVDC link Connection details		HVDC link Specifications	Power flow solution	
			Base case power flow converged in six iterations (NI=6) with CT=0.56 sec; $V_i = 1.011\angle - 11.24$ ; $V_j = 1.011\angle - 11.32$ ; $V_k = 0.998\angle - 17.67$ ;	
Master Converter	Slave Converters		AC terminal buses	HVDC variables
i	j, k	Master Converter $V_{DC} = 3$ ; $V_i = 1.02$ ; Slave Converters $P_{shj} = 0.5$ ; $Q_{shj} = 0.2$ ; $P_{shk} = 0.3$ ; $Q_{shk} = 0.1$ ;	$V_j = 1.0207\angle - 11.3819$ ; $V_k = 1.0689\angle - 10.3345$ ; $\theta_i = -11.4007$ ;	Master Converter $V_{shi} = 1.0410\angle - 15.9687$ ; $m_i = 0.9815$ ; $P_{lossi}(\%) = 1.66$ ;
				Slave Converters $V_{shj} = 1.0420\angle - 8.6981$ ; $V_{shk} = 1.0789\angle - 8.8489$ ; $m_j = 0.9824$ ; $m_k = 1.0172$ ; $P_{lossj}(\%) = 1.38$ ; $P_{lossk}(\%) = 1.23$ ; NI=6; CT= 1.77;
Note: For the above case study, i=266, j=270, k=271; Values of voltage magnitudes, active and reactive powers are in p.u. Phase angles of voltages are in degrees.				

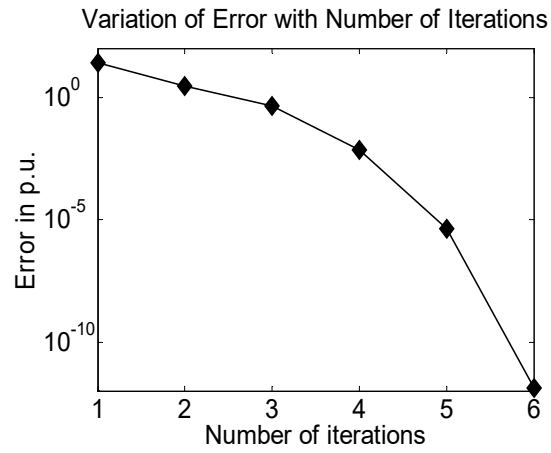


Fig. 3.9: Convergence characteristic of the base case power flow in the IEEE-300 bus system

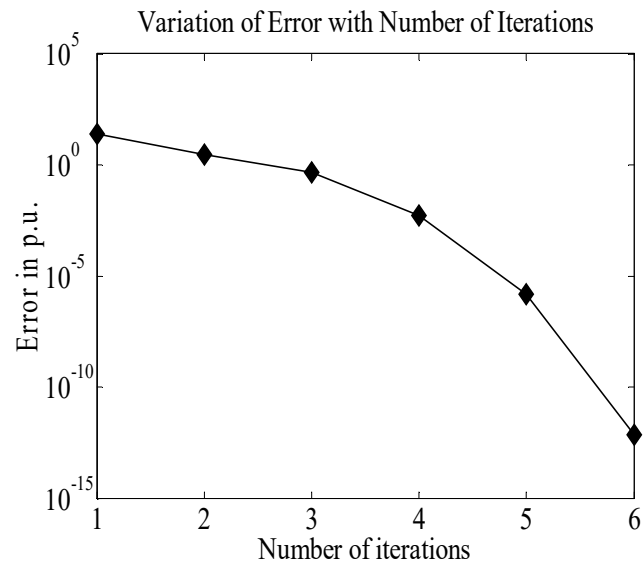


Fig. 3.10: Convergence characteristic for the study of Table 3.1

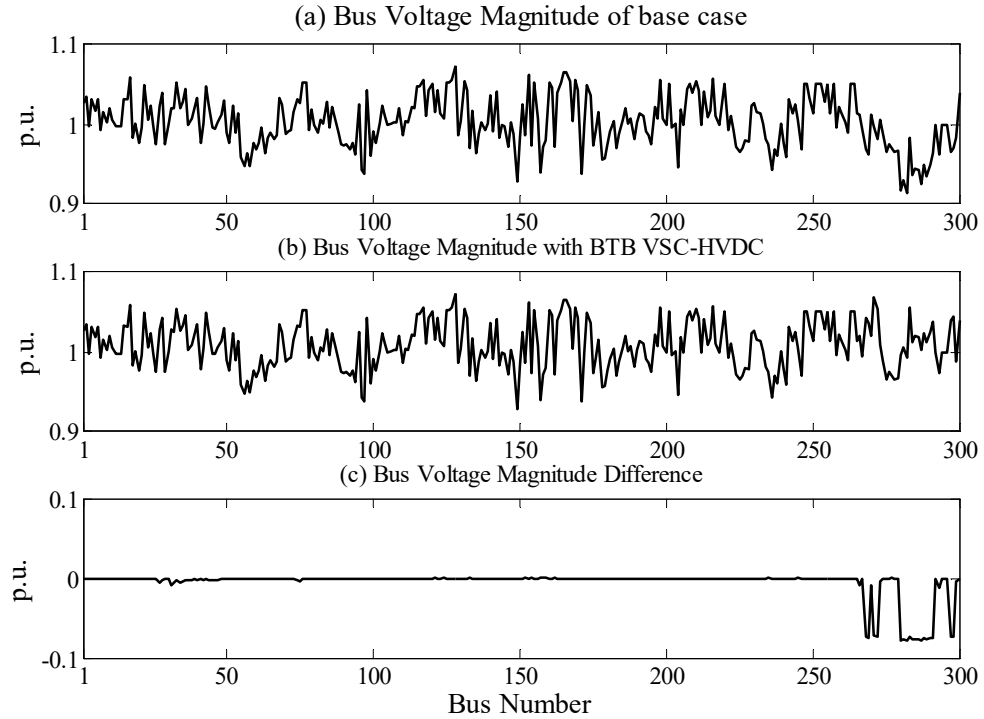


Fig. 3.11: Bus voltage profile for the study of Table 3.1

**Case II: Three-terminal MVDC network connected in the PTP configuration**

In this case study, two separate studies are conducted with a three terminal, PTP connected VSC-HVDC network incorporated in the IEEE-300 bus test system to demonstrate the versatility of the proposed model. In both the studies, the VSC-HVDC network is connected between AC buses 266, 270 and 271.

In the first study, the converter connected to AC bus no. ‘266’ acts as the master converter while those connected to AC buses ‘270’ and ‘271’ act as slave converters. Both the slave converters operate in the PQ control mode. The master converter maintains the voltage magnitude of AC bus no. 266 at a value of 1.02 p.u. The active powers at the terminal end of the lines connecting the converters to the AC



buses '270' and '271' are specified as 0.7 and 0.5 p.u, respectively. In a similar manner, the corresponding line reactive powers are specified as 0.2 and 0.06 p.u., respectively. These specified values are shown in the third row and columns 1-3 of Table 3.2. The power flow solution is shown in the third row and columns 4-5 of Table 3.2.

Subsequently a study is again conducted on the same AC-DC system but with both the slave converters (connected to AC buses '270' and '271') operated in the PV control mode. Their terminal end line active powers are specified as 0.4 and 0.5 p.u, respectively. The voltages of the AC buses '270' and '271' connected to the slave converters are specified as 1.02 and 1.0 p.u, respectively. The specified quantities are detailed in the fourth row and columns 1-3 of Table 3.2. The power flow results are shown in the fourth row and columns 4-5 of Table 3.2.

From Table 3.2, it can be observed that for all the case studies, 'NI' is identical to that in the base case. However, due to increase in the number of unknowns involved, 'CT' increases than that in the base case. It is also observed that 'NI' is independent of the control strategies employed as well as the operating points specified. This demonstrates the robustness of the proposed algorithm.

The convergence characteristic plots for both the studies of Table 3.2 are shown in Figures 3.12 and 3.13, respectively. From Figures 3.12 and 3.13, again, it can be observed that the proposed model possesses quadratic convergence characteristics, similar to the base case power-flow.

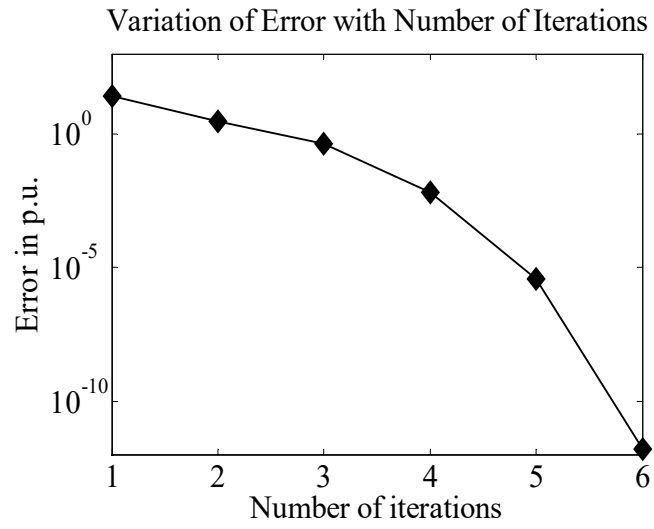


Fig. 3.12: Convergence characteristic for the first study of Table 3.2

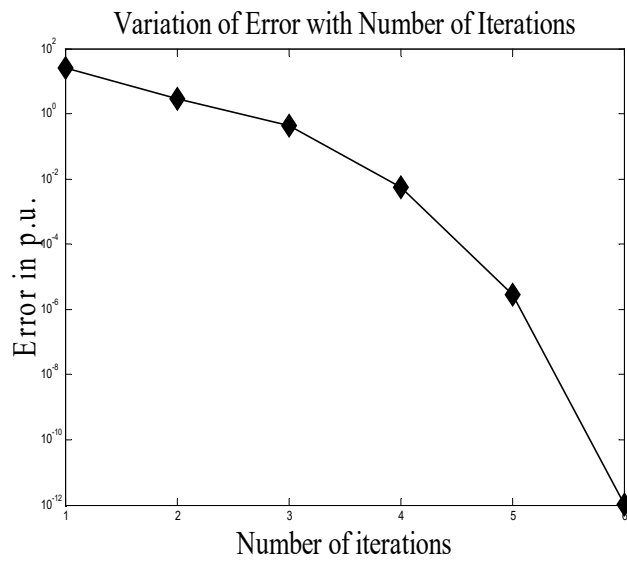


Fig. 3.13: Convergence characteristic for the second study of Table 3.2

Table 3.2

Study of IEEE 300 bus system with three terminal PTP VSC HVDC network

HVDC link Connection details		HVDC link Specifications	Power flow solution	
			Base case power flow converged in six iterations (NI=6) with CT=0.56 sec; $V_i = 1.011\angle -11.24$ ; $V_j = 1.011\angle -11.32$ ; $V_k = 0.998\angle -17.67$ ;	
Master Converter	Slave Converters		AC terminal buses	HVDC variables
i	j, k	Master Converter $V_{DCi} = 3$ ; $V_i = 1.02$ ; Slave Converters $P_{shj} = 0.7$ ; $Q_{shj} = 0.2$ ; $P_{shk} = 0.5$ ; $Q_{shk} = 0.06$ ;	$\theta_i = -11.4398$ ; $\theta_j = -11.3827$ ; $\theta_k = -5.4606$ ; $V_j = 1.0209$ ; $V_k = 1.0503$ ;	Master Converter $V_{shi} = 1.0516\angle -18.1648$ ; $m_i = 0.9914$ ; $P_{DCi} = 1.23$ ; $P_{lossi}(\%) = 2.15$ ;
				Slave Converters $V_{shj} = 1.0434\angle -7.6254$ ; $V_{shk} = 1.0576\angle -2.8837$ ; $V_{DCj} = 2.9978$ ; $V_{DCk} = 2.9981$ ; $m_j = 0.9844$ ; $m_k = 0.9977$ ; $P_{DCj} = -0.7158$ ; $P_{DCk} = -0.5137$ ; $P_{lossj}(\%) = 1.53$ ; $P_{lossk}(\%) = 1.34$ ; NI=6; CT= 1.75
i	j, k	Master Converter $V_{DCi} = 3$ ; $V_i = 1.02$ ; Master Converter $P_{shj} = 0.4$ ; $V_j = 1.02$ ; $P_{shk} = 0.5$ ; $V_k = 1$ ;	$\theta_i = -11.4236$ ; $\theta_j = -11.4157$ ; $\theta_k = -5.0076$ ;	Master Converter $V_{shi} = 1.0781\angle -16.3970$ ; $m_i = 1.0165$ ; $P_{DCi} = 0.9273$ ; $P_{lossi}(\%) = 1.93$ ;
				Slave Converters $V_{shj} = 1.0213\angle -9.2151$ ; $V_{shk} = 0.9975\angle -2.1320$ ; $V_{DCj} = 2.9985$ ; $V_{DCk} = 2.9984$ ; $m_j = 0.9633$ ; $m_k = 0.9410$ ; $P_{DCj} = -0.4130$ ; $P_{DCk} = -0.5138$ ; $P_{lossj}(\%) = 1.28$ ; $P_{lossk}(\%) = 1.36$ ; NI=6; CT= 1.88;

Note: For the above case study,  $i=266$ ,  $j=270$ ,  $k=271$ ; Values of voltage magnitudes, active and reactive powers are in p.u. Phase angles of voltages are in degrees.

The bus voltage profiles for the first and second studies of Table 3.2 are shown in Figures 3.14 and 3.15, respectively. From Figures 3.14 and 3.15, it is observed that the bus voltage profile hardly changes except for the AC terminal buses at which the VSCs are installed.

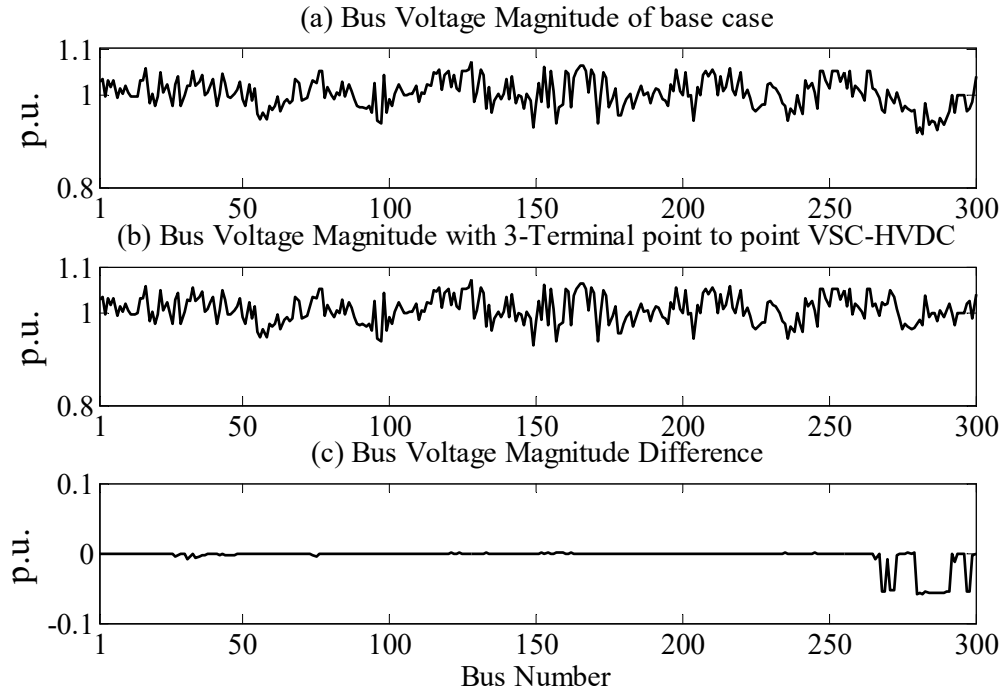


Fig. 3.14: Bus voltage profile for the first study of Table 3.2

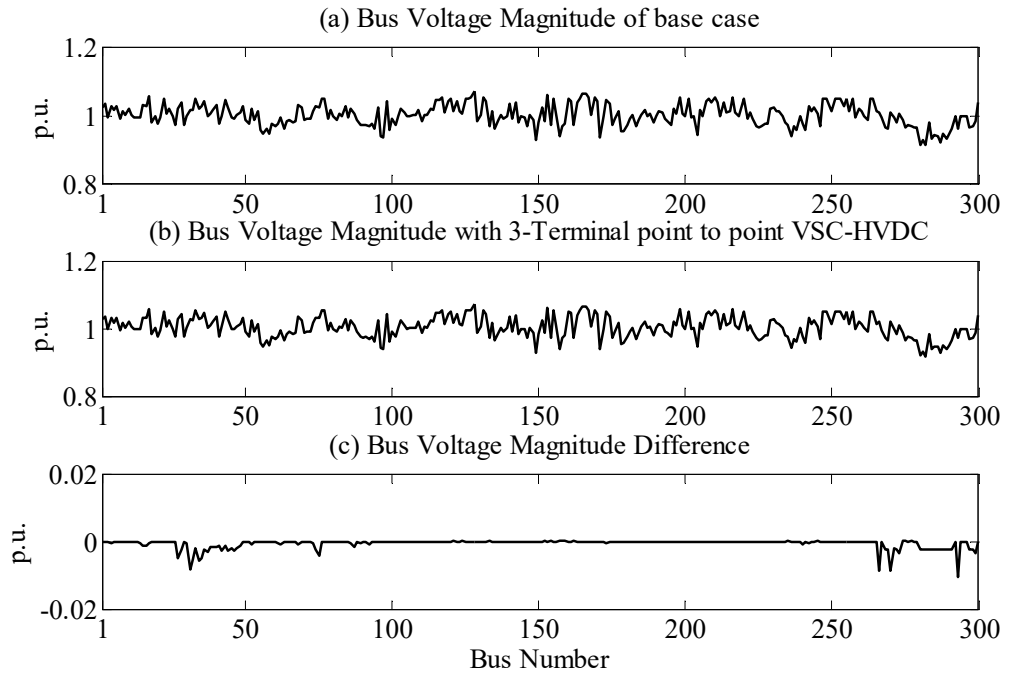


Fig. 3.15: Bus voltage profile for the second study of Table 3.2

### Case III: Four terminal MVDC network connected in the PTP configuration

In this case study, a four-terminal VSC-HVDC network is incorporated in the IEEE 300-bus system between buses 266, 270, 271 and 272. The VSC connected to AC bus no. 266 acts as the master converter while the VSCs connected to AC buses 270, 271 and 272 act as slave converters. The master converter maintains the bus voltage magnitude of the AC bus 266 to a value of 1.02 p.u. All the slave converters operate in the PQ control mode. The specified quantities are shown in the third row and columns 1-3 of Table 3.3. The power flow solution is shown in columns 4-5 of Table 3.3.

Table 3.3

Study of IEEE 300 bus system with four terminal VSC HVDC network

HVDC link: Connection details		HVDC link Specifications	Power flow solution	
Master Converter	Slave Converters		AC terminal buses	HVDC variables
			Base case power flow converged in six iterations (NI=6) with CT=0.56 sec; $V_i = 1.011\angle -11.24$ ; $V_j = 1.011\angle -11.32$ ; $V_k = 0.998\angle -17.67$ ; $V_l = 0.981\angle -19.46$ ;	
i	j, k, l	Master Converter $V_{DCi} = 3$ ; $V_i = 1.02$ ; Slave Converters $P_{shj} = 0.5$ ; $Q_{shj} = 0.1$ ; $P_{shk} = 0.4$ ; $Q_{shk} = 0.05$ ; $P_{shl} = 0.2$ ; $Q_{shl} = 0.03$ ;	$\theta_i = -11.4658$ ; $\theta_j = -11.4428$ ; $\theta_k = -3.1223$ ; $\theta_l = -2.8498$ ; $V_j = 1.0204$ ; $V_k = 1.0590$ ; $V_l = 1.0571$ ;	Master Converter $V_{shi} = 1.0599\angle -17.6502$ ; $m_i = 0.9993$ ; $P_{DCi} = 1.139$ ; $P_{lossi}(\%) = 2.07$ ; Slave Converters $V_{shj} = 1.0318\angle -8.7264$ ; $V_{shk} = 1.0647\angle -1.0918$ ; $V_{shl} = 1.0603\angle -1.8290$ ; $m_j = 0.9733$ ; $m_k = 1.0043$ ; $m_l = 1.0001$ ; $V_{DCj} = 2.9986$ ; $V_{DCk} = 2.9987$ ; $V_{DCl} = 2.9989$ ; $P_{DCj} = -0.5138$ ; $P_{DCk} = -0.4128$ ; $P_{DCl} = -0.2118$ ; $P_{lossj}(\%) = 1.36$ ; $P_{lossk}(\%) = 1.28$ ; $P_{lossl}(\%) = 1.17$ ; NI=6; CT= 1.77;
Note: For the above study, i=266, j=270, k=271 and l=272 Values of voltage magnitudes, active and reactive powers are in p.u. Phase angles of voltages are in degrees.				

The convergence characteristic of this case study is shown in Fig. 3.16. From Fig. 3.16, it can be observed that the proposed algorithm demonstrates a quadratic convergence characteristic, similar to the base case power-flow. Although ‘CT’ increases than that in the base case due to an increase in the number of the unknowns, ‘NI’ remains same. The bus voltage profile for the above study is shown in Fig. 3.17. From Fig. 3.17, it is observed that the bus voltage profile does not change much except the AC terminal buses at which the converters are connected.

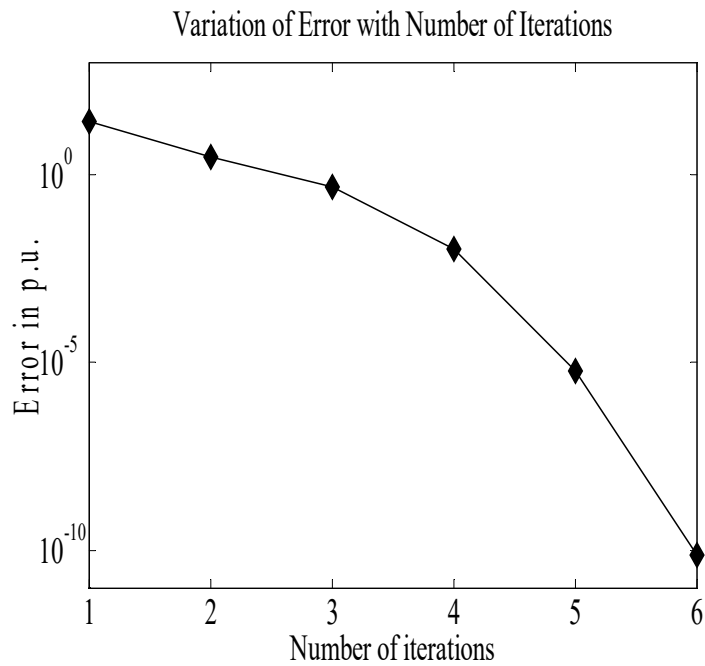


Fig. 3.16: Convergence characteristic for the study of Table 3.3

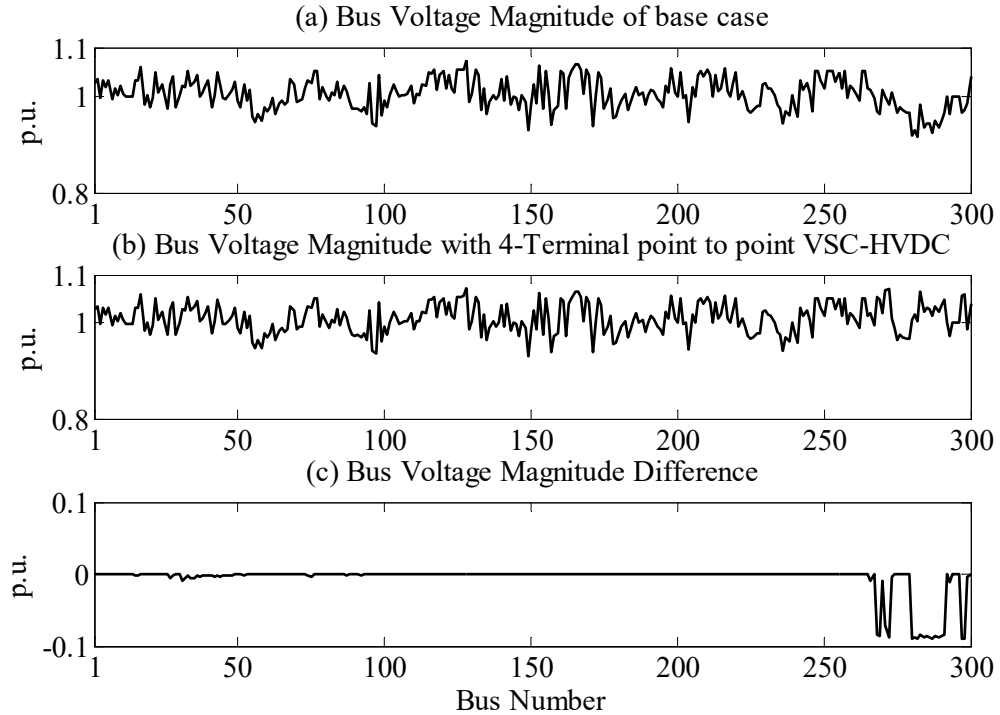


Fig. 3.17: Bus voltage profile for the study of Table 3.3

#### Case IV: Five terminal MVDC network connected in the PTP configuration

In this case study, a five terminal VSC-HVDC network is incorporated in the test system between buses 266, 270, 271, 272 and 273. The converter connected to bus no. 266 acts as the master converter while the converters connected to buses 270, 271, 272 and 273 act as slave converters. The master converter controls the voltage magnitude of AC bus no. 266 to a value of 1.02 p.u. The slave converters connected to buses 272 and 273 operate in the PV control mode while those connected to buses 270 and 271 operate in the PQ control mode. The specified quantities are shown in the third row and columns 1-3 of Table 3.4. The power flow solution is shown in columns 4-5 of Table 3.4. The convergence characteristic for this study is shown in Fig. 3.18. From Fig. 3.18, it is again observed that the proposed model retains the quadratic convergence characteristics of the unified AC-DC Newton-Raphson algorithm. It is

also observed that even though ‘CT’ increases than that of the four-terminal AC-MVDC system of Table 3.3, ‘NI’ remains independent of the size of the MVDC network, the control strategies employed and the quantities specified (operating point). The bus voltage profile for the study of Table 3.4 is shown in Fig. 3.19. From Fig. 3.19, it is again observed that the bus voltage profile does not change much except the AC terminal buses at which the converters are connected.

Table 3.4

Study of IEEE 300 bus system with five terminal VSC HVDC network

HVDC link		HVDC link specifications	Power flow solution	
Master Converter	Slave Converters		AC terminal buses	HVDC variables
			Base case power flow converged in six iterations (NI=6) with CT=0.56 sec; $V_i = 1.011\angle - 11.24$ ; $V_j = 1.011\angle - 11.32$ ; $V_k = 0.998\angle - 17.67$ ; $V_l = 0.981\angle - 19.46$ ; $V_m = 1.006\angle - 17.47$ ;	
i	j, k, l, m	Master Converter $V_{DCi} = 3$ ; $V_i = 1.02$ ; Slave Converters $P_{shj} = 0.3$ ; $V_l = 0.99$ ; $P_{shk} = 0.2$ ; $V_m = 1.01$ ; $P_{shl} = 0.3$ ; $P_{shm} = 0.3$ ; $Q_{shj} = 0.2$ ; $Q_{shk} = 0.05$ ;	$\theta_i = -11.5055$ ; $\theta_j = -11.5252$ ; $\theta_k = -5.1646$ ; $\theta_l = -3.5273$ ; $\theta_m = -6.5236$ ; $V_j = 1.0206$ ; $V_k = 1.0085$ ;	Master Converter $V_{shi} = 1.0616\angle - 17.7394$ ; $m_i = 1.0158$ ; $P_{DCi} = 1.1497$ ; $P_{lossi}(\%) = 2.09$ ; Slave Converters $V_{shj} = 1.0409\angle - 9.9176$ ; $V_{shk} = 1.0139\angle - 4.0466$ ; $V_{shl} = 0.9831\angle - 1.7564$ ; $V_{shm} = 1.0090\angle - 4.8358$ ; $V_{DCj} = 2.9989$ ; $V_{DCk} = 2.9988$ ; $V_{DCl} = 2.9989$ ; $V_{DCm} = 2.9988$ ; $m_j = 0.9722$ ; $m_k = 0.9545$ ; $m_l = 0.9285$ ; $m_m = 0.9527$ ; $P_{DCj} = -0.3127$ ; $P_{DCk} = -0.2118$ ; $P_{DCl} = -0.3125$ ; $P_{DCm} = -0.3124$ ; $P_{lossj}(\%) = 1.26$ ; $P_{lossk}(\%) = 1.18$ ; $P_{lossl}(\%) = 1.24$ ; $P_{lossm}(\%) = 1.23$ ; NI=6; CT= 2.33;
Note: For the above study, i=266, j=270, k=271, l=272 and m=273; Values of voltage magnitudes, active and reactive powers are in p.u. Phase angles of voltages are in degrees.				



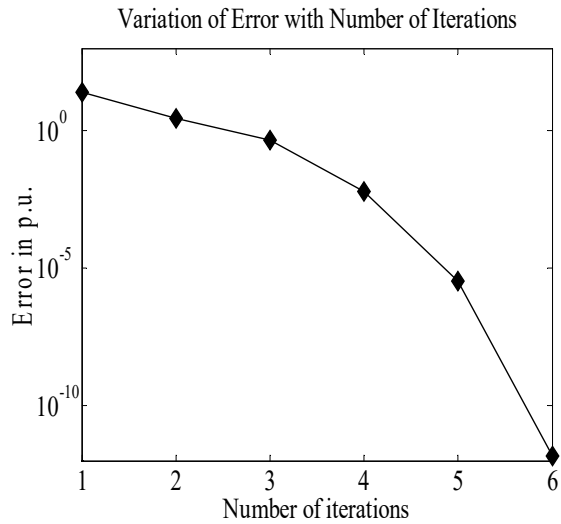


Fig. 3.18: Convergence characteristic for the study of Table 3.4

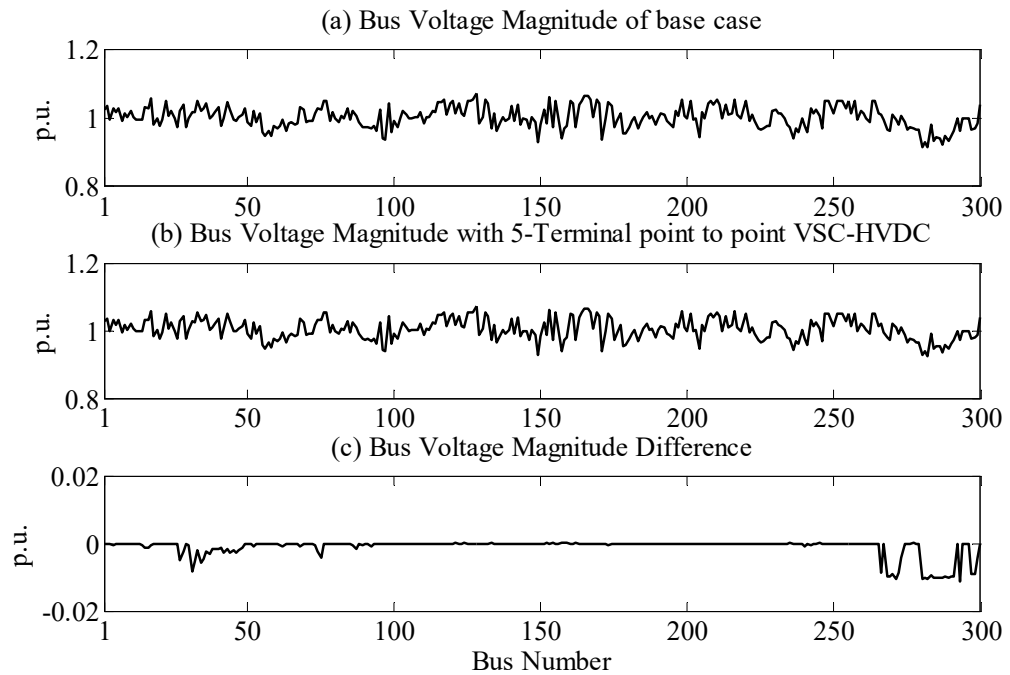


Fig. 3.19: Bus voltage profile for the study of Table 3.4

From Tables 3.1, 3.2, 3.3 and 3.4, it is observed that ‘CT’ increases slightly with increase in the number of DC terminals due to an increase in the number of unknowns.

However, ‘NI’ remains identical to the base case, which shows the robustness of the proposed algorithm. The proposed algorithm is able to accommodate diverse VSC control strategies and operating point specifications. This shows the versatility of the model.

### **3.4.2 Studies with sequential power-flow model of hybrid AC-MVDC systems**

#### **Case I: Three terminal MVDC network connected in the PTP configuration**

In this case study, again two separate, sequential power-flow studies are conducted with a three terminal, PTP connected VSC-HVDC network incorporated in the IEEE-300 bus test system to demonstrate the versatility of the proposed model. In both the studies, the VSC-HVDC network is connected between AC buses 266, 270 and 271. The specified quantities for these studies are identical to those in the case study shown in Table 3.2 and are detailed in rows 3-4 and columns 1-3 of Table 3.5. Rows 3 and 4 correspond to the ‘PQ’ and ‘PV’ control modes of the slave VSCs, respectively. The corresponding power flow solutions are shown in row 3 and row 4 (columns 4-5) of Table 3.5, respectively.

From Table 3.5, it can be observed that for both the studies, ‘NI’ and CT are increased than that of the studies of Table 3.2 carried out using the unified AC-DC Newton-Raphson algorithm. The convergence characteristic plots (variation of mismatch error in p.u. with number of iterations) for first and second studies of Table 3.5 are shown in Figures 3.20 and 3.21, respectively. From Figures 3.20 and 3.21, it can be observed that the quadratic convergence characteristics of the Newton-Raphson method are lost due to the adoption of the sequential Newton-Raphson power-flow algorithm. The values of both ‘NI’ and ‘CT’ have increased than those of Table 3.2. Also, the values of ‘NI’ are dependent on the VSC control strategy employed.

The bus voltage profiles for the first and second studies of Table 3.5 are shown in Figures 3.22 and 3.23, respectively. From Figures 3.22 and 3.23, it is observed that the bus voltage profile hardly changes except for the AC terminal buses at which the VSCs are connected.

Table 3.5

Study of IEEE 300 bus system with three terminal VSC HVDC network

HVDC link Connection details		HVDC link Specifications	Power flow solution	
			Base case power flow converged in six iterations (NI=6) with CT=0.56 sec; $V_i = 1.011\angle -11.24$ ; $V_j = 1.011\angle -11.32$ ; $V_k = 0.998\angle -17.67$ ;	
Master Converter	Slave Converters		AC terminal buses	HVDC variables
i	j, k	Master Converter $V_{DCi} = 3$ ; $V_i = 1.02$ ;  Slave Converters $P_{shj} = 0.7$ ; $Q_{shj} = 0.2$ ; $P_{shk} = 0.5$ ; $Q_{shk} = 0.06$ ;	$\theta_i = -11.4398$ ; $\theta_j = -11.3827$ ; $\theta_k = -5.4606$ ; $V_j = 1.0209$ ; $V_k = 1.0503$ ;	Master Converter $V_{shi} = 1.0516\angle -18.1648$ ; $m_i = 0.9914$ ; $P_{DCi} = 1.2303$ ; $P_{lossi}(\%) = 2.15$ ;
				Slave Converters $V_{shj} = 1.0434\angle -7.6254$ ; $V_{shk} = 1.0576\angle -2.8837$ ; $V_{DCj} = 2.9978$ ; $V_{DCk} = 2.9981$ ; $m_j = 0.9844$ ; $m_k = 0.9977$ ; $P_{DCj} = -0.7158$ ; $P_{DCk} = -0.5137$ ; $P_{lossj}(\%) = 1.53$ ; $P_{lossk}(\%) = 1.34$ ; NI=11; CT= 2.05;
i	j, k	Master Converter $V_{DCi} = 3$ ; $V_i = 1.02$ ;  Slave Converters $P_{shj} = 0.4$ ; $V_j = 1.02$ ; $P_{shk} = 0.5$ ; $V_k = 1$ ;	$\theta_i = -11.4236$ ; $\theta_j = -11.4157$ ; $\theta_k = -5.0076$ ;	Master Converter $V_{shi} = 1.0781\angle -16.397$ ; $m_i = 1.0165$ ; $P_{DCi} = 0.9273$ ; $P_{lossi}(\%) = 1.9251$ ;
				Slave Converters $V_{shj} = 1.0213\angle -9.2151$ ; $V_{shk} = 0.9975\angle -2.1320$ ; $V_{DCj} = 2.9985$ ; $V_{DCk} = 2.9984$ ; $m_j = 0.9633$ ; $m_k = 0.9410$ ; $P_{DCj} = -0.413$ ; $P_{DCk} = -0.5138$ ; $P_{lossj}(\%) = 1.28$ ; $P_{lossk}(\%) = 1.36$ ; NI=10; CT= 1.91;

Note: For the above case study, i=266, j=270, k=271; Values of voltage magnitudes, active and reactive powers are in p.u. Phase angles of voltages are in degrees.

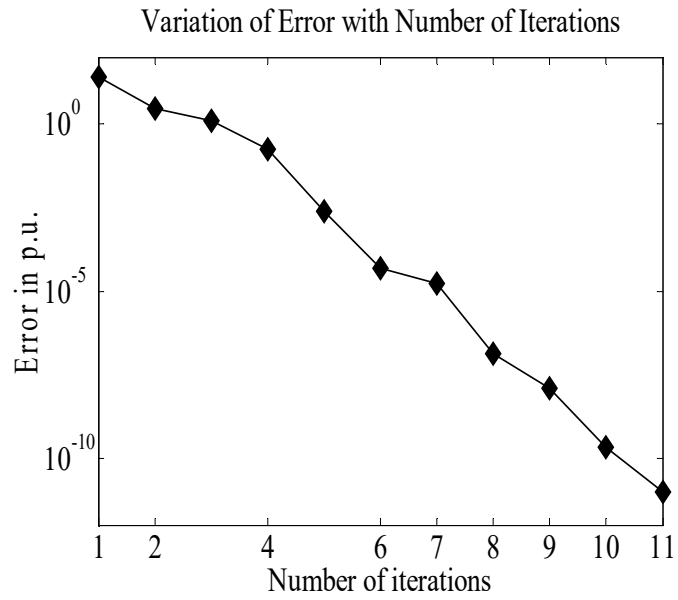


Fig. 3.20: Convergence characteristic for the first study of Table 3.5

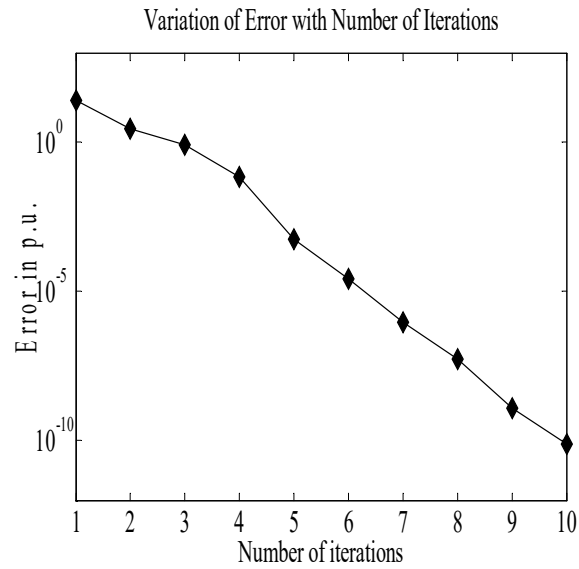


Fig. 3.21: Convergence characteristic for the second study of Table 3.5

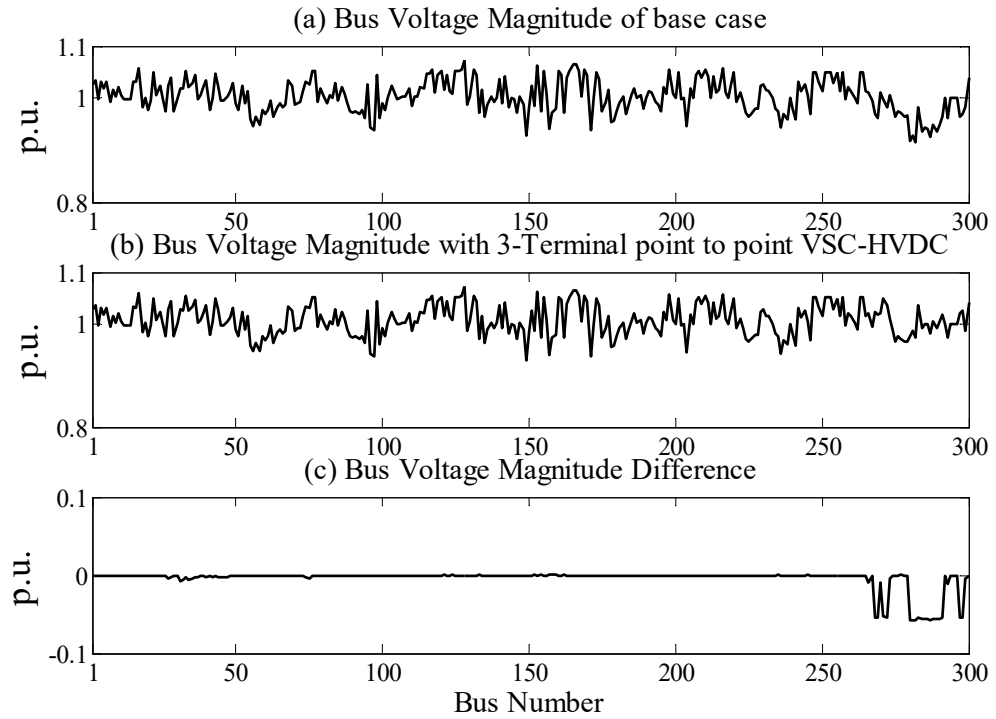


Fig. 3.22: Bus voltage profile for the first study of Table 3.5

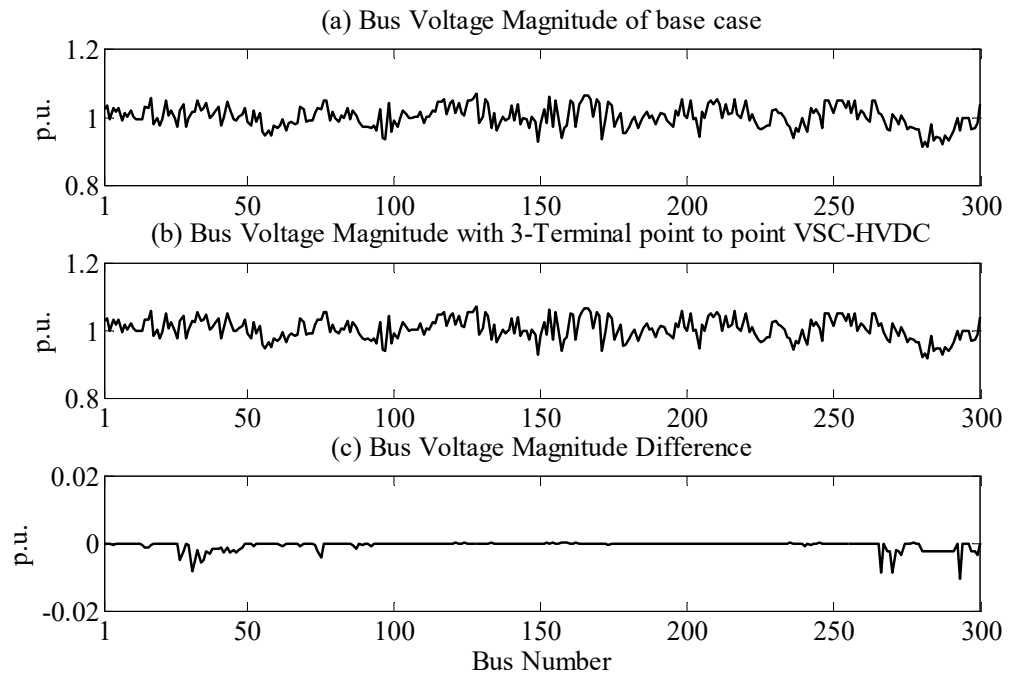


Fig. 3.23: Bus voltage profile for the second study of Table 3.5

## Case II: Four terminal PTP configuration of VSC-HVDC system

In this case study, a four terminal VSC-HVDC network is incorporated in the IEEE 300-bus test system. The specified quantities are identical to those in columns 1-3 of Table 3.3 and are again detailed in columns 1-3 of Table 3.6. The power flow solution is shown in columns 4-5 of Table 3.6. The convergence characteristic corresponding to this case study is shown in Fig. 3.24. Again, it is observed that the quadratic convergence characteristic of the unified Newton-Raphson power-flow algorithm is lost due to the adoption of the sequential power-flow method. The bus voltage profile for this study is shown in Fig. 3.25. From Fig. 3.25, it can be observed that the bus voltage profile does not change much except at the AC terminal buses to which the converters are connected.

Table 3.6

Study of IEEE 300 bus system with four terminal VSC HVDC network

HVDC link: Connection details		HVDC link Specifications	Power flow solution	
Master Converter	Slave Converters		AC terminal buses	HVDC variables
			Base case power flow converged in six iterations (NI=6) with CT=0.56 sec; $V_i = 1.011\angle - 11.24$ ; $V_j = 1.011\angle - 11.32$ ; $V_k = 0.998\angle - 17.67$ ; $V_l = 0.981\angle - 19.46$ ;	
		Master Converter $V_{DCi} = 3$ ; $V_i = 1.02$ ;		Master Converter $V_{shi} = 1.0578\angle - 17.6597$ ; $m_i = 0.9973$ ; $P_{DCi} = 1.139$ ; $P_{lossi}(\%) = 2.06$ ;
i	j, k, l	Slave Converters $P_{shj} = 0.5$ ; $Q_{shj} = 0.1$ ; $P_{shk} = 0.4$ ; $Q_{shk} = 0.05$ ; $P_{shl} = 0.2$ ; $Q_{shl} = 0.05$ ;	$\theta_i = -11.4650$ ; $\theta_j = -11.4420$ ; $\theta_k = -3.2183$ ; $\theta_l = -2.9950$ ; $V_j = 1.0204$ ; $V_k = 1.0681$ ; $V_l = 1.0698$ ;	Slave Converters $V_{shj} = 1.0318\angle - 8.7256$ ; $V_{shk} = 1.0738\angle - 1.2221$ ; $V_{shl} = 1.0748\angle - 2.0008$ ; $m_j = 0.9733$ ; $m_k = 1.0128$ ; $m_l = 1.0137$ ; $V_{DCj} = 2.9986$ ; $V_{DCk} = 2.9987$ ; $V_{DCl} = 2.9989$ ; $P_{DCj} = -0.5138$ ; $P_{DCk} = -0.4129$ ; $P_{DCl} = -0.2118$ ; $P_{lossj}(\%) = 1.36$ ; $P_{lossk}(\%) = 1.27$ ; $P_{lossl}(\%) = 1.17$ ; NI=11; CT= 2.04;
Note: For the above study, i=266, j=270, k=271 and l=272; Values of voltage magnitudes, active and reactive powers are in p.u. Phase angles of voltages are in degrees.				

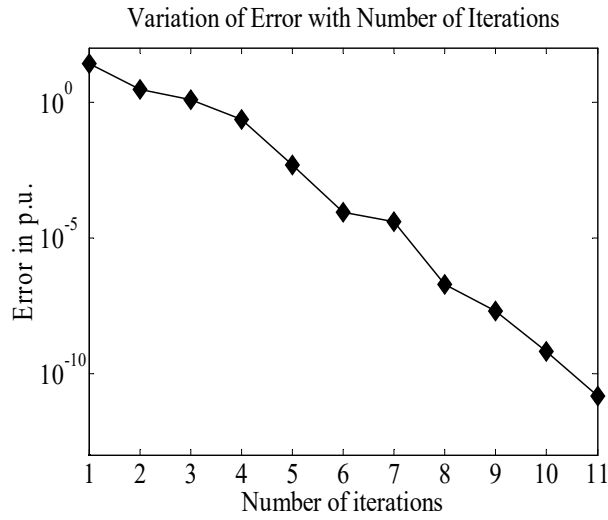


Fig. 3.24: Convergence characteristic for the study of Table 3.6

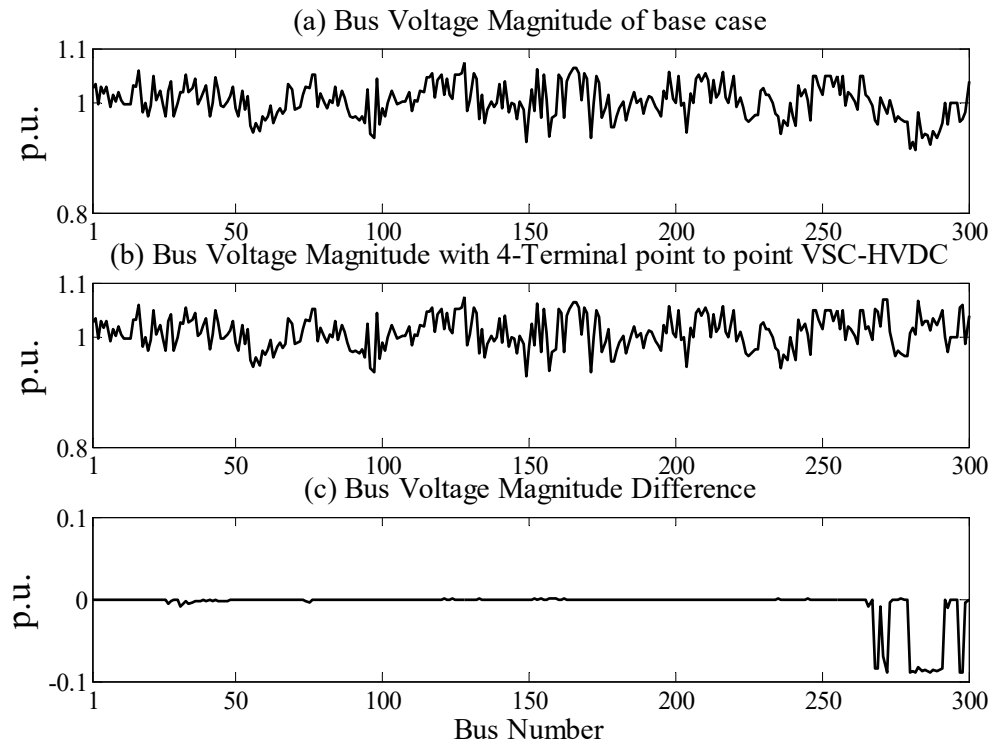


Fig. 3.25: Bus voltage profile for the study of Table 3.6

### Case III: Five terminal MVDC network connected in the PTP configuration

This case study is similar to that of the case study of the five terminal MVDC network of Table 3.4. The specified quantities for the sequential power-flow are identical to those in columns 1-3 of Table 3.4 and are detailed again in columns 1-3 of Table 3.7. The power flow solution is shown in row 3 and columns 4-5 of Table 3.7. The convergence characteristic for this case study is shown in Fig. 3.26. From Fig. 3.26, it can again be observed that the quadratic convergence of the unified Newton-Raphson algorithm is lost due to the adoption of the sequential power-flow method employed in this case. The bus voltage profile for the study of Table 3.7 is shown in Fig. 3.27. From Fig. 3.27, it is again observed that the bus voltage profile does not change much except at the AC terminal buses to which the converters are connected.

Table 3.7  
Study of IEEE 300 bus system with five terminal VSC HVDC network

HVDC link		HVDC link specifications	Power flow solution	
			Base case power flow converged in six iterations (NI=6) with CT=0.56 sec; $V_i = 1.011\angle -11.24$ ; $V_j = 1.011\angle -11.32$ ; $V_k = 0.998\angle -17.67$ ; $V_l = 0.981\angle -19.46$ ; $V_m = 1.006\angle -17.47$ ;	
Master Converter	Slave Converters	Master Converter	AC terminal buses	HVDC variables
i	j, k, l, m	$V_{DCi} = 3$ ; $V_i = 1.02$ ;	$\theta_i = -11.5055$ ; $\theta_j = -11.5252$ ; $\theta_k = -5.1646$ ; $\theta_l = -3.5273$ ; $\theta_m = -6.5236$ ; $V_j = 1.0206$ ; $V_k = 1.0085$ ;	Master Converter $V_{shi} = 1.0616\angle -17.7394$ ; $m_i = 1.008$ ; $P_{DCi} = 1.1497$ ; $P_{lossi}(\%) = 2.09$ ;
		Slave Converters $P_{shj} = 0.3$ ; $V_l = 0.99$ ; $P_{shk} = 0.2$ ; $V_m = 1.01$ ; $P_{shl} = 0.3$ ; $P_{shm} = 0.3$ ; $Q_{shj} = 0.2$ ; $Q_{shk} = 0.05$ ;		Slave Converters $V_{shj} = 1.0409\angle -9.9176$ ; $V_{shk} = 1.0139\angle -4.0466$ ; $V_{shl} = 0.9831\angle -1.7564$ ; $V_{shm} = 1.0090\angle -4.8358$ ; $V_{DCj} = 2.999$ ; $V_{DCk} = 2.9991$ ; $V_{DCl} = 2.999$ ; $V_{DCm} = 2.999$ ; $m_j = 0.9817$ ; $m_k = 0.9562$ ; $m_l = 0.9272$ ; $m_m = 0.9516$ ; $P_{DCj} = -0.3127$ ; $P_{DCk} = -0.2118$ ; $P_{DCl} = -0.3125$ ; $P_{DCm} = -0.3124$ ; $P_{lossj}(\%) = 1.26$ ; $P_{lossk}(\%) = 1.18$ ; $P_{lossl}(\%) = 1.24$ ; $P_{lossm}(\%) = 1.23$ ; NI=11; CT= 2.16;
Note: For the above study, i=266, j=270, k=271, l=272 and m=273; Values of voltage magnitudes, active and reactive powers are in p.u. Phase angles of voltages are in degrees.				



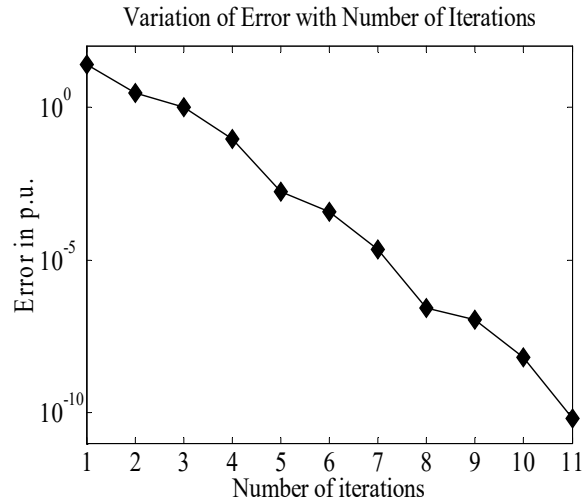


Fig. 3.26: Convergence characteristic for the study of Table 3.7

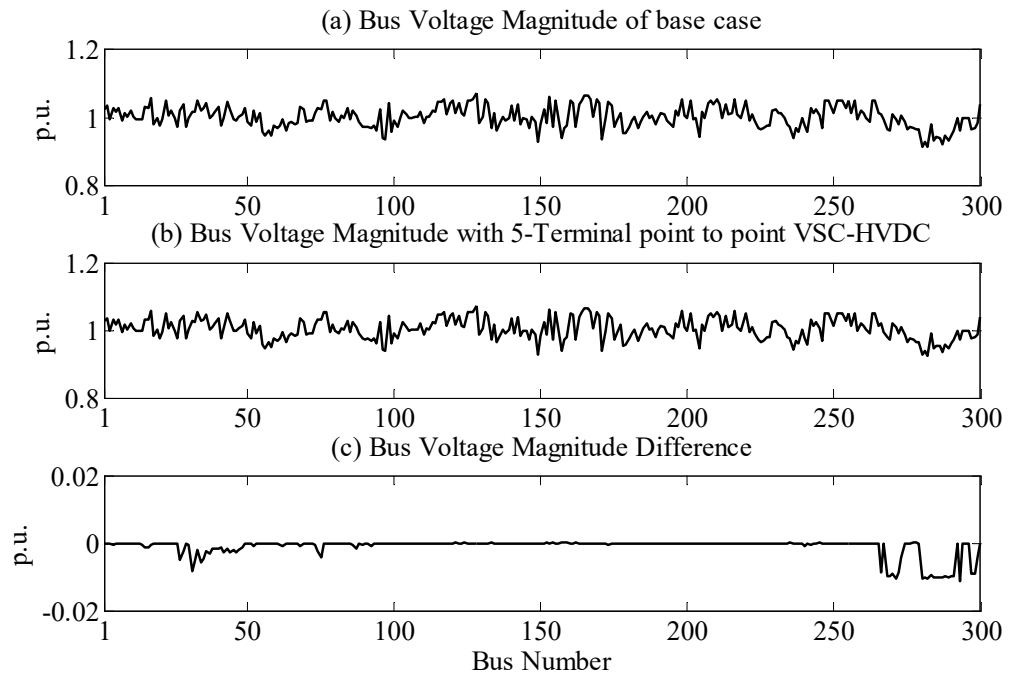


Fig. 3.27: Bus voltage profile for the study of Table 3.7

**Case IV: Five terminal MVDC network connected in the PTP configuration**

This case study is carried out on the five terminal MVDC network of Table 3.7 to investigate the effect of the operating conditions on the convergence characteristics of

both the unified and the sequential Newton AC-DC power-flow algorithms. The specified value of the active power-flow ' $P_{sh3}$ ' in line 3 is gradually increased and its effect on 'NI' is investigated. All the other electrical quantities are maintained constant at their respective values as detailed in Tables 3.4 and 3.7. The results are shown in Table 3.8.

From Table 3.8, it is observed that 'NI' with the unified AC-DC power-flow algorithm is independent of the variation of ' $P_{sh}$ '. However, for the sequential AC-DC power-flow algorithm, 'NI' gradually increases with increasing values of ' $P_{sh3}$ '.

From Tables 3.5, 3.6 and 3.7, it can be observed that with the sequential AC-DC power-flow algorithm, the values of both 'CT' and 'NI' are increased than those of the corresponding case studies employing the unified AC-DC power-flow algorithm (Tables 3.2, 3.3 and 3.4, respectively). From Tables 3.5 and 3.8, it is also observed that 'NI' is dependent on both the VSC control strategy employed and the operating point specifications.

Table 3.8

A comparison of the convergence characteristics of the unified and the sequential AC-DC power-flow algorithms

Variation of 'NI' with varying values of ' $P_{sh3}$ '					
Algorithm employed	$P_{sh3}$ (p.u)				
	0.2	0.25	0.3	0.35	0.4
Unified	6	6	6	6	6
Sequential	11	12	12	13	14

A comparison of the convergence features of the proposed model vis-à-vis existing models in the literature is shown in Table 3.9.

Table 3.9  
A comparison of convergence features with existing models

Reference no.	Tolerance (p.u.)	No. of buses in the system		NI	CT (in seconds)		
		AC	DC				
[82]	$10^{-8}$	29	5	Min: 3; Max: 15 (depending on wind power generation)	Min: 0.37 (for weak wind) Max: 1.99 (for strong wind)		
[78]	$10^{-6}$	9	4	6	0.2		
		32	4	7	0.45		
Proposed model	$10^{-10}$	300	NIL (Base)	6	0.56		
Unified	$10^{-10}$	300	BTB	6	1.77		
			3	6	PQ control	PV control	
			4	6	1.75	1.88	
			5	6	1.77	2.33	
Sequential	$10^{-10}$	300	3	PQ control	PV control	PQ control	PV control
				11	10	2.05	1.91
			4	11		2.04	
	5	11		2.16			

### 3.5 Conclusions

In this chapter, both unified and sequential Newton Power-Flow models of hybrid AC-DC systems have been developed. Unlike existing models, the modulation indices of the VSCs can be expressed as unknowns in both the models. Both the algorithms are implemented by employing diverse control strategies in different topologies of multi-terminal DC networks incorporated in the IEEE 300-bus test system. It is observed that the unified method possesses the quadratic convergence characteristics as in the base case power-flow. Further, the number of iterations taken by the unified Newton-Raphson Power-Flow algorithm for convergence is independent of the MTDC topology, the MTDC control strategies employed and the operating point

specifications. On the other hand, the quadratic convergence characteristics of the Newton-Raphson method is lost if the sequential AC-DC power-flow algorithm is adopted. Also, the number of iterations taken by the unified Newton Power-Flow algorithm for convergence is dependent on both the operating point specifications and the MTDC control strategies employed.

# Chapter 4

## Newton Power Flow Modeling of Voltage Source Converter (VSC) Based Hybrid AC-DC Systems Employing DC Voltage Droop Control

### 4.1 Introduction

The Newton power-flow modeling of voltage sourced converter-based hybrid AC-DC systems employing DC slack bus control (also known as master-slave control) was presented in Chapter 3. As already discussed in Chapter 3, the main disadvantage of this control scheme is the DC grid instability following a failure of the master converter. This problem can be tackled by ensuring that individual converters take part in the DC voltage regulation scheme by adjusting their active power flow in response to changes in the DC voltage with the operating point, known as DC voltage droop control [12], [20]. For MTDC systems, different types of DC voltage droop control have been envisaged to ensure proper sharing based on the converter ratings. These include Voltage Margin (VM) control, Voltage-Power (V-P) droop, Voltage-Current (V-I) droop and Voltage-Power (V-P) droop with Dead-Band (DB) [12], [24], [31], [37].

For planning, operation and control of hybrid AC-MVDC systems employing DC voltage droop control, their power flow solution is an essential requirement. In this respect, [81]-[84] present some comprehensive research works on the development of efficient Newton power-flow algorithms of hybrid AC-MVDC systems employing DC voltage droop control.

However, the above research works do not address the following issues:

- [1] Development of a unified Newton power-flow model of hybrid AC-MVDC systems employing DC voltage droop control. In this respect, [81] and [82] have presented sequential Newton power-flow models of hybrid AC-MVDC systems incorporating DC voltage droop control. However, the quadratic convergence characteristic of the unified AC/DC Newton-Raphson algorithm is lost in [81] and [82] due to the adoption of the sequential AC-DC power-flow algorithm,.
- [2] The VSC modulation index ‘ $m$ ’ has not been considered as an unknown in any of the above models. For VSC applications, ‘ $m$ ’ is a crucial parameter. Typically,  $0 < m \leq 1$ . Some of the factors that put a cap on the lower and upper bounds of ‘ $m$ ’ have been reported in [11].

This chapter presents a generalized approach to both the unified and the sequential Newton power-flow modeling of hybrid AC-MVDC grids employing DC voltage droop control. Unlike most of the research works published in this area, in the proposed model, ‘ $m$ ’ is considered as an unknown and can be obtained directly from the power-flow solution. The proposed work also includes the converter losses.

## **4.2 Modeling of Hybrid AC-MVDC Systems Employing DC Voltage Droop Control**

For modeling of hybrid AC-MVDC systems employing DC voltage droop control, the generalized AC-DC network shown in Fig. 3.1 (Chapter 3) comprising a ‘ $n$ ’ bus AC power system network integrated with a MVDC grid using ‘ $q$ ’ VSCs and their respective converter transformers, is again considered and is shown in Fig. 4.1 below. The assumptions adopted for the modeling are also identical to those in Chapter 3. As shown in Fig. 4.1, the AC buses connected to the ‘ $q$ ’ VSCs are numbered as ‘ $i$ ’, ‘ $(i+1)$ ’, and so on, up to ‘ $(i+q-1)$ ’, while the ‘ $q$ ’ VSCs are connected

in the PTP configuration on their DC sides. The PTP connection is considered, being more prevalent in practical HVDC installations over the world. Fig. 4.2 shows the equivalent circuit of the network shown in Fig. 4.1 with  $q$  fundamental frequency, positive sequence voltage sources pertaining to the ' $q$ ' VSCs.  $V_{sha}$  represents the voltage phasor pertaining to the  $a^{\text{th}}$  ( $1 \leq a \leq q$ ) VSC. The  $a^{\text{th}}$  ( $1 \leq a \leq q$ ) VSC is connected to AC terminal bus ' $(i+a-1)$ ' whose voltage is represented by the phasor  $V_{i+a-1} = V_{i+a-1} \angle \theta_{i+a-1}$ .

From Fig. 4.2, the current in the link (not shown) connecting the  $a^{\text{th}}$  VSC and its AC terminal bus is

$$I_{sha} = y_{sha}(V_{sha} - V_{i+a-1}) \quad (4.1)$$

where  $V_{sha} = V_{sha} \angle \theta_{sha} = m_a c V_{DCa} \angle \theta_{sha}$ ,  $y_{sha} = 1/Z_{sha}$ ,  $Z_{sha} = R_{sha} + jX_{sha}$ ,  $R_{sha}$  and  $X_{sha}$  are the resistance and the leakage reactance of the  $a^{\text{th}}$  converter transformer, respectively, ' $m_a$ ' is the VSC modulation index and the constant ' $c$ ' is representative of the VSC architecture [11].

As already detailed in Chapter 3 and from Figures 4.1 and 4.2, the net current injection at the AC bus ' $(i+a-1)$ ' connected to the  $a^{\text{th}}$  ( $1 \leq a \leq p$ ) converter can be

$$\text{written as } I_{i+a-1} = \sum_{k=1}^n Y_{(i+a-1)k} V_k - y_{sha} V_{sha} \quad (4.2)$$

In the above equation,  $Y_{(i+a-1)(i+a-1)} = Y_{(i+a-1)(i+a-1)}^{\text{old}} + y_{sha}$  and  $Y_{(i+a-1)(i+a-1)}^{\text{old}} = y_{(i+a-1)0} + \sum_{k=1, k \neq i+a-1}^n Y_{(i+a-1)k}$  are the values of the self admittances of bus ' $(i+a-1)$ ' with the  $a^{\text{th}}$  VSC connected and in the original ' $n$ ' bus AC system without any VSC, respectively. Similarly, ' $y_{(i+a-1)0}$ ' accounts for the shunt capacitances of all the transmission lines connected to bus ' $(i+a-1)$ '.

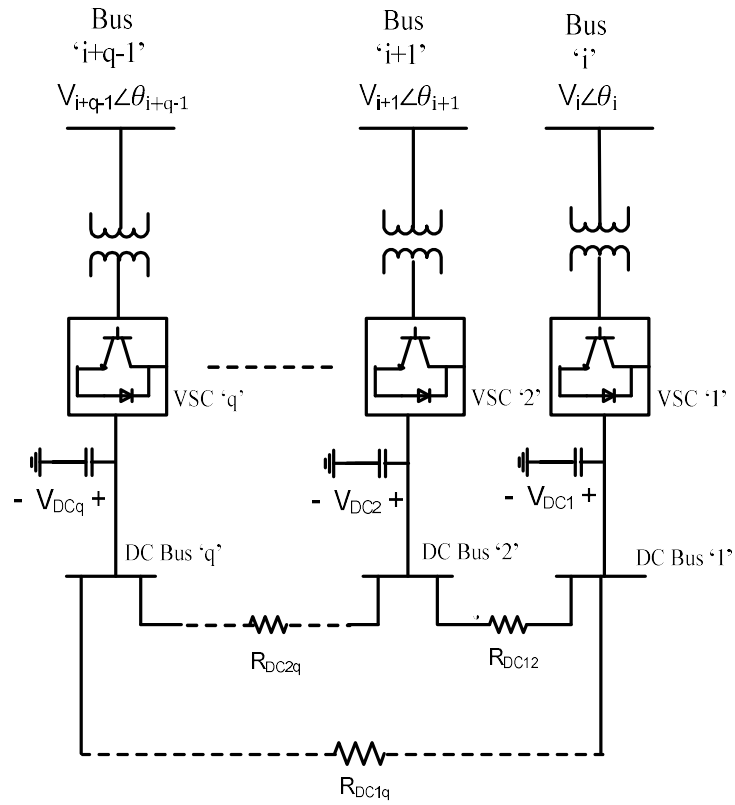


Fig. 4.1: Schematic diagram of an integrated AC-MTDC system

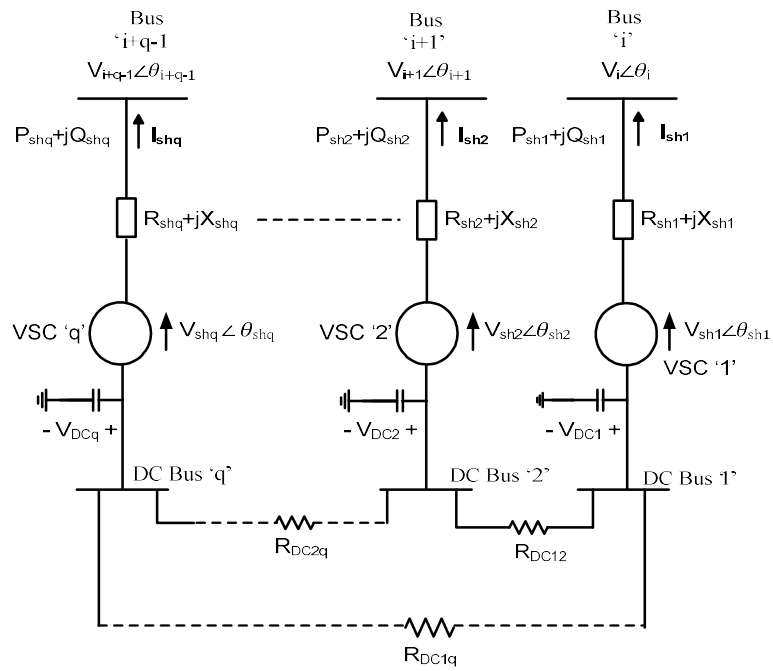


Fig. 4.2: Equivalent circuit of Fig. 4.1



### 4.3 Power Flow Equations of Hybrid AC-MVDC systems with DC Voltage Droop Control

From Fig. 4.2, the net active and reactive power injections at the AC bus '(i+a-1)' are

$$P_{i+a-1} = \sum_{k=1}^n V_{i+a-1} V_k Y_{(i+a-1)k} \cos \left[ \theta_{i+a-1} - \theta_k - \phi_{(i+a-1)k} \right] - m_a c V_{DCa} V_{i+a-1} Y_{sha} \cos(\theta_{i+a-1} - \theta_{sha} - \phi_{sha}) \quad (4.3)$$

$$Q_{i+a-1} = \sum_{k=1}^n V_{i+a-1} V_k Y_{(i+a-1)k} \sin \left[ \theta_{i+a-1} - \theta_k - \phi_{(i+a-1)k} \right] - m_a c V_{DCa} V_{i+a-1} Y_{sha} \sin(\theta_{i+a-1} - \theta_{sha} - \phi_{sha}) \quad (4.4)$$

Also, from Fig. 4.2, the active and reactive power flows at the terminal end of the line connecting the a<sup>th</sup> VSC to the AC bus '(i+a-1)' are

$$P_{sha} = \text{Re} \left[ \mathbf{V}_{i+a-1} \mathbf{I}_{sha}^* \right] = m_a c V_{DCa} V_{i+a-1} Y_{sha} \cos(\theta_{i+a-1} - \theta_{sha} - \phi_{sha}) - V_{i+a-1}^2 Y_{sha} \cos \phi_{sha} \quad (4.5)$$

$$\text{and } Q_{sha} = m_a c V_{DCa} V_{i+a-1} Y_{sha} \sin(\theta_{i+a-1} - \theta_{sha} - \phi_{sha}) + V_{i+a-1}^2 Y_{sha} \sin \phi_{sha} \quad (4.6)$$

Also, from Fig. 4.2, by virtue of the power balance on the AC and DC sides of the a<sup>th</sup> VSC,

$$\text{Re}(\mathbf{V}_{sha} \mathbf{I}_{sha}^*) + \sum_{v=1}^q V_{DCa} V_{DCv} Y_{DCav} = -P_{lossa} \quad (4.7)$$

Substitution of eqn. (4.1) in eqn. (4.7) gives

$$(m_a c V_{DCa})^2 y_{sha} \cos \phi_{sha} - m_a c V_{DCa} V_{i+a-1} Y_{sha} \cos(\theta_{sha} - \theta_{i+a-1} - \phi_{sha}) + \sum_{v=1}^q V_{DCa} V_{DCv} Y_{DCav} + P_{lossa} = 0$$

$$\text{or, } f_{1a} = 0 \quad \forall 1 \leq a \leq q \quad (4.8)$$

Thus, for 'q' VSCs, 'q' independent equations are obtained.

In eqns. (4.7) and (4.8),  $Y_{DCav} = -\frac{1}{R_{DCav}}$ , where ‘ $R_{DCav}$ ’ is the resistance of the DC link between DC buses ‘a’ and ‘v’. Also, ‘ $P_{lossa}$ ’ represents the losses [18], [92] of the a<sup>th</sup> VSC as already detailed in Chapter 3 and is again given below.

$$P_{lossa} = a_1 + b_1 I_{sha} + c_1 I_{sha}^2 \quad (4.9)$$

where ‘ $a_1$ ’, ‘ $b_1$ ’ and ‘ $c_1$ ’ are loss factors [18], [92] and

$$I_{sha} = y_{sha} [V_{i+a-1}^2 + (m_a c V_{DCa})^2 - 2 V_{i+a-1} m_a c V_{DCa} \cos(\theta_{i+a-1} - \theta_{sha})]^{1/2} \quad (4.10)$$

The derivation of eqn. (4.10) is given in Appendix A.

Now, in the AC-MTDC system (Fig. 4.2) with ‘q’ VSCs, if it is assumed that the r<sup>th</sup> ( $1 \leq r \leq q$ ) VSC is used for voltage control of its corresponding AC bus, we have

$$V_{i+a-1}^{sp} - V_{i+a-1}^{cal} = 0 \quad \forall a, 1 \leq a \leq q, a = r \quad (4.11)$$

Also, not more than ‘(q-1)’ line active and reactive power flows {eqn. (4.5) and (4.6)} can be specified, which give us ‘(2q-2)’ independent equations given as

$$P_{sha}^{sp} - P_{sha}^{cal} = 0 \quad (4.12)$$

$$Q_{sha}^{sp} - Q_{sha}^{cal} = 0 \quad (4.13)$$

$\forall a, 1 \leq a \leq q, a \neq r.$

Instead of PQ control mode, if a VSC operates in the PV one, eqn. (4.13) changes to

$$V_{i+a-1}^{sp} - V_{i+a-1}^{cal} = 0 \quad \forall a, 1 \leq a \leq q, a \neq r \quad (4.14)$$

Further, the net reactive power injection at AC bus ‘(i+r-1)’ can be specified as its voltage is controlled by the r<sup>th</sup> VSC. Thus, we get

$$Q_{i+a-1}^{sp} - Q_{i+a-1}^{cal} = 0 \quad \forall a, 1 \leq a \leq q, a = r \quad (4.15)$$

In eqns. (4.11)-(4.15),  $V_{i+a-1}^{sp}$ ,  $Q_{i+a-1}^{sp}$ ,  $P_{sha}^{sp}$  and  $Q_{sha}^{sp}$  are specified values while  $V_{i+a-1}^{cal}$ ,  $Q_{i+a-1}^{cal}$ ,  $P_{sha}^{cal}$  and  $Q_{sha}^{cal}$  are calculated values {using eqns. (4.4), (4.5) and (4.6)}.

#### 4.4 DC Voltage droop control in MVDC Systems

In DC voltage droop control [12], [20], [24]-[31], [37], multiple converters participate in the DC voltage control scheme. Droop control comprises both linear and nonlinear voltage droop characteristics. Among the linear ones, Voltage-Power (V-P) and Voltage-Current (V-I) droops have been the two most popular and widely used strategies for DC voltage droop control. Nonlinear voltage droop control characteristics include dead-bands and limits. Among the nonlinear ones, Voltage Margin, V-P droop with power Dead-Band and V-P droop with voltage limits are some of the more widely used characteristics. Some of these are elaborated below.

##### 1. Voltage-Power (V-P) Droop

If the  $a^{\text{th}}$  VSC follows a linear V-P droop characteristic, its rectifying power can be expressed as

$$P_{DCa} = R_a(V_{DCa}^* - V_{DCa}) + P_{DCa}^* \quad (4.16)$$

where ' $V_{DCa}^*$ ' and ' $P_{DCa}^*$ ' represent the DC voltage and power references of its droop characteristics and ' $R_a$ ' is the droop control gain.

##### 2. Voltage-Current (V-I) Droop

If the  $a^{\text{th}}$  VSC follows a linear V-I droop characteristic; the net DC current injection at its terminal can be expressed as

$$I_{DCa} = R_a(V_{DCa}^* - V_{DCa}) + I_{DCa}^* \quad (4.17)$$

where ' $I_{DCa}^*$ ' and ' $V_{DCa}^*$ ' are the DC current and voltage references of its droop line and ' $R_a$ ' is the droop control gain.

Thus, the rectifying power of the VSC can be expressed as

$$P_{DCa} = V_{DCa} [R_a(V_{DCa}^* - V_{DCa}) + I_{DCa}^*] \quad (4.18)$$

Fig. 4.3 depicts the linear V-P and V-I droop characteristics for any arbitrary VSC 'a'.

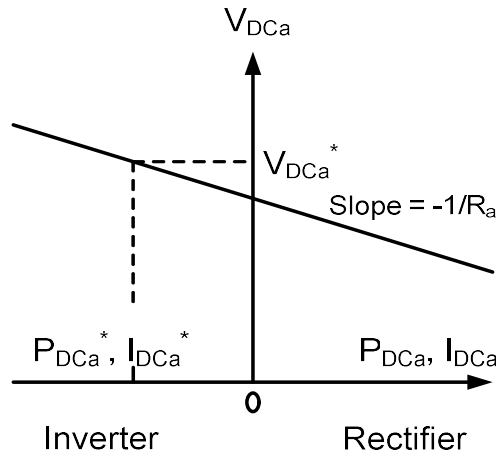


Fig. 4.3: Linear Voltage Droop Characteristic of the  $a^{\text{th}}$  VSC

#### Computation of ' $V_{DCa}^*$ ' and ' $P_{DCa}^*$ '

The values of the DC voltage and power references ' $V_{DCa}^*$ ', ' $P_{DCa}^*$ ' and ' $I_{DCa}^*$ ' in eqns. 4.16 - 4.18 for all the 'q' converters are either pre specified or obtained from a DC power-flow. While carrying out the DC power-flow, if DC slack bus control is assumed, then, by convention, the voltage ' $V_{DC1}^*$ ' (of DC terminal 1) is specified and it does not operate on droop control. This problem can be circumvented if the average voltage of all the 'q' DC terminals ' $V_{DCav}^*$ ' is specified instead of ' $V_{DC1}^*$ ' [82]. In that case, the DC power-flow equations are

Solve  $\mathbf{V}_{DC}^*$  specified  $\mathbf{P}_{DC}^*$  and  $V_{DCav}^*$

$$\text{where } \mathbf{V}_{DC}^* = [V_{DC}^* \dots V_{DCq}^*]^T, \mathbf{P}_{DC}^* = [P_{DC2}^* \dots P_{DCq}^*]^T$$

Subsequently,  $P_{DC}^*$  and ' $I_{DCa}^*$ ' ( $1 \leq a \leq q$ ) can be computed.

### 3. Voltage-Power (V-P) Droop with dead-band

In practical DC grids, the droop characteristics can be a combination of multiple linear or nonlinear functions of the DC voltage. Fig. 4.4 shows the voltage droop characteristics with dead-band and voltage limits. If the  $a^{\text{th}}$  VSC follows a nonlinear droop characteristic as shown in Fig. 4.4, the converters operate in constant power control mode when DC voltage is maintained between ' $V_{DCa\text{ high}}^*$ ' and ' $V_{DCa\text{ low}}^*$ '. When the DC voltage lies outside the dead-band zone, the DC terminal follows the linear V-P characteristic. Again, beyond a threshold DC voltage, the droop control gain increases ( $R_{a\text{ max}}$ ) to maintain the DC voltage within an acceptable limit for the stability of the DC grid.

The composite droop characteristic is shown in Fig. 4.4 and can be expressed as

$$P_{DCa} = R_{a\text{ max}}(V_{DCa\text{ max}} - V_{DCa}) + [R_a (V_{DCa\text{ high}}^* - V_{DCa\text{ max}}) + P_{DCa}^*] \text{ for } V_{DCa} \geq V_{DCa\text{ max}} \quad (4.19)$$

$$= R_a (V_{DCa\text{ high}}^* - V_{DCa}) + P_{DCa}^* \quad \text{for } V_{DCa\text{ high}}^* < V_{DCa} < V_{DCa\text{ max}} \quad (4.20)$$

$$= 0 \cdot (V_{DCa\text{ high}}^* - V_{DCa}) + P_{DCa}^* \quad \text{for } V_{DCa\text{ low}}^* \leq V_{DCa} \leq V_{DCa\text{ high}}^* \quad (4.21)$$

$$= R_a (V_{DCa\text{ low}}^* - V_{DCa}) + P_{DCa}^* \quad \text{for } V_{DCa\text{ min}}^* < V_{DCa} < V_{DCa\text{ low}}^* \quad (4.22)$$

$$= R_{a\text{ max}}(V_{DCa\text{ min}} - V_{DCa}) + [R_a (V_{DCa\text{ low}}^* - V_{DCa\text{ min}}) + P_{DCa}^*] \text{ for } V_{DCa} \leq V_{DCa\text{ min}} \quad (4.23)$$

In this scheme, the droop control gains can be specified according to the rating of the converters to share the additional power.

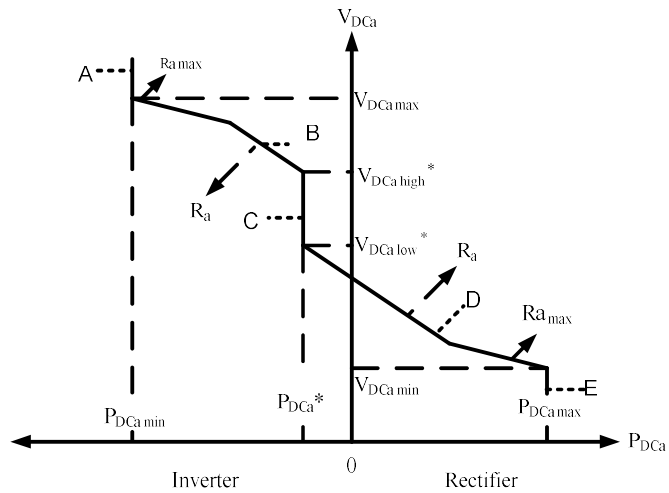


Fig. 4.4: Nonlinear Voltage Droop Characteristic of the  $a^{\text{th}}$  VSC

#### 4. DC voltage margin control

In this mode of DC voltage control, each VSC regulates the DC voltage as long as its DC power is within the minimum and maximum power limits and the reference DC voltages of the different VSCs are offset from one another by a voltage margin [82]. The V-P characteristic corresponding to this scheme is shown in Fig. 4.5.

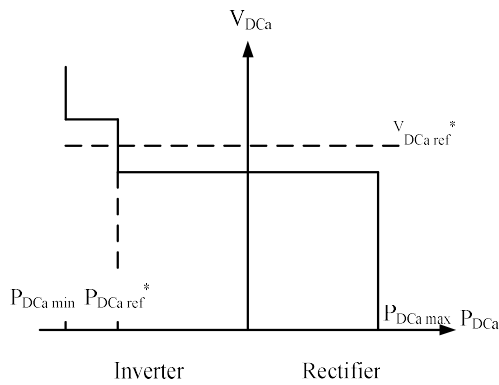


Fig. 4.5: Voltage Margin Characteristic of the  $a^{\text{th}}$  VSC

## 4.5 MODELING OF AC-MTDC SYSTEMS WITH DC VOLTAGE DROOP

### CONTROL

Let us assume now that all the ‘q’ VSCs in the AC-MTDC system shown in Fig. 4.1 operate on droop control. To simplify matters, let all the ‘q’ VSCs follow linear V-P droops. Then, for the a<sup>th</sup> VSC ( $1 \leq a \leq q$ ), from eqns. (4.16), we have

$$P_{DCa} = V_{DCa} I_{DCa} = \sum_{v=1}^q V_{DCa} V_{DCv} Y_{DCav} = R_a (V_{DCa}^* - V_{DCa}) + P_{DCa}^*$$

$$\text{or, } \sum_{v=1}^q V_{DCa} V_{DCv} Y_{DCav} + R_a V_{DCa} - R_a V_{DCa}^* - P_{DCa}^* = 0 \quad (4.24)$$

$$\text{or, } f_{2a} = 0 \quad \forall a, \quad 1 \leq a \leq q \quad (4.25)$$

eqn. (4.25) represents ‘q’ independent equations.

As already mentioned earlier in Section 4.4, in eqn. (4.24), the values of the DC voltage and power references ‘ $V_{DCa}^*$ ’ and ‘ $P_{DCa}^*$ ’ for all the ‘q’ converters are either pre specified or obtained from a DC power-flow. Now, two distinctly different models can be realized depending on whether the values of ‘ $V_{DCa}^*$ ’ and ‘ $P_{DCa}^*$ ’ are specified or not. These are elaborated below.

*Model ‘A’: Values of ‘ $V_{DCa}^*$ ’ and ‘ $P_{DCa}^*$ ’ are known apriori*

In some models [82], the values of ‘ $V_{DCa}^*$ ’ and ‘ $P_{DCa}^*$ ’ for all the ‘q’ converters are pre-specified or obtained by carrying out a DC power-flow. In such cases, the ‘q’ independent droop equations represented by eqn. (4.24) are sufficient to compute the values of the DC bus voltages ‘ $V_{DCa}$ ’ directly, and subsequently, the DC bus power injections ‘ $P_{DCa}$ ’ ( $1 \leq a \leq q$ ). Once ‘ $P_{DCa}$ ’ are known, for the AC-MTDC power-flow, the active powers ‘ $P_{sha}$ ’ {eqn. (4.5)} in the lines joining the ‘(q-1)’ VSCs to their corresponding AC buses cannot be specified, as this would be tantamount to knowing

the losses in the converter transformers and the VSC, prior to the power-flow. This is detailed in Fig. 4.6. This is not in line with practical considerations which are targeted to maintain a specified ' $P_{sha}$ '. This is a major drawback of the model.

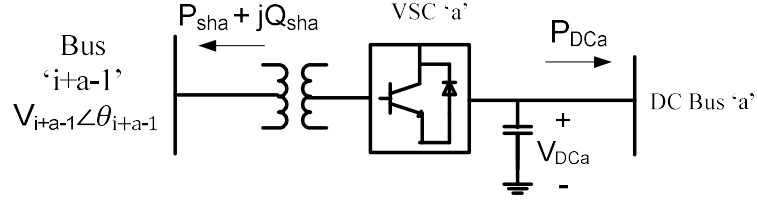


Fig. 4.6: Power flows for the  $a^{\text{th}}$  VSC connected to its AC bus '(i+a-1)'

Now, under the assumption that there are ' $g$ ' generators connected at the first ' $g$ ' buses of the ' $n$ ' bus AC system with bus 1 being the slack bus, the unified AC-MTDC power-flow problem corresponding to model 'A' is of the form

Compute:  $\theta, V, X$

Given:  $P, Q, R$

with

$$\theta = [\theta_2 \dots \theta_n]^T, \quad V = [V_{g+1} \dots V_n]^T, \quad \theta_{sh} = [\theta_{sh} \dots \theta_{shq}]^T, \quad m = [m_1 \dots m_q]^T,$$

$$X = [\theta_{sh}^T \quad m^T]^T$$

$$P = [P_2 \dots P_n]^T, \quad Q = [Q_{g+1} \dots Q_n]^T, \quad Q_{sh} = [Q_{sh2} \dots Q_{shq}],$$

$$f_1 = [f_{11} \dots f_{1q}], \quad R = [Q_{sh} \quad V_{i+r-1} \quad f_1]^T$$

For this model, it is presumed that VSC ' $r$ ' is employed for the voltage control of the AC bus '(i+r-1)' unlike the other '(q-1)' VSCs, which control the line reactive power flows.



The Newton power flow equation is

$$\mathbf{J}[\Delta\boldsymbol{\theta}^T \Delta\mathbf{V}^T \Delta\boldsymbol{\theta}_{sh}^T \Delta\mathbf{m}^T]^T = [\Delta\mathbf{P}^T \Delta\mathbf{Q}^T \Delta\mathbf{R}^T]^T \quad (4.26)$$

where,  $\mathbf{J}$  is the power-flow Jacobian.

In eqn. (4.26), ' $\Delta\mathbf{P}$ ', ' $\Delta\mathbf{Q}$ ' and ' $\Delta\mathbf{R}$ ' represent the mismatch vectors while  $\Delta\boldsymbol{\theta}$ ,  $\Delta\mathbf{V}$ ,  $\Delta\boldsymbol{\theta}_{sh}$  and  $\Delta\mathbf{m}$  represent the correction vectors. The elements of ' $\mathbf{J}$ ' can be obtained very easily from eqn. (4.26).

It can be observed that ' $V_{DCa}$ ' ( $1 \leq a \leq q$ ) can be solved using eqn. (4.24), independent of the AC-MTDC power-flow {eqn. (4.26)}, if ' $V_{DCa}^*$ ' and ' $P_{DCa}^*$ ' are known.

After all the unknowns are solved, the line active power-flows ' $P_{sha}$ ' can be computed {using eqn. (4.5)}.

Thus, to summarize, Model 'A' addresses the problem "given the DC voltage and power (or current) references of the VSC droop lines and the target line reactive power flows, what should be the line active power flow values?"

*Model 'B': Values of ' $V_{DCa}^*$ ' and ' $P_{DCa}^*$ ' are not known a priori*

If the DC voltage (' $V_{DCa}^*$ ') and power (' $P_{DCa}^*$ ') reference values of the 'q' VSCs are not known, the DC bus voltages ' $V_{DCa}$ ' and hence the DC bus power injections ' $P_{DCa}$ ' ( $1 \leq a \leq q$ ) cannot be computed independently {using eqn. (4.24)}. This enables the line active power-flow values ' $P_{sha}$ ' to be specified control objectives {Fig. 4.6}, which is in line with practical MTDC control. This is an advantage over model 'A'.

For the above modeling strategy, the unified AC-MTDC power-flow problem is of the form

Compute:  $\boldsymbol{\theta}$ ,  $\mathbf{V}$ ,  $\mathbf{X}$

Given:  $\mathbf{P}$ ,  $\mathbf{Q}$ ,  $\mathbf{R}$

with

$$\boldsymbol{\theta} = [\theta_2 \dots \theta_n]^T, \mathbf{V} = [V_{g+1} \dots V_n]^T, \boldsymbol{\theta}_{sh} = [\theta_{sh1} \dots \theta_{shq}]^T, \mathbf{m} = [m_1 \dots m_q]^T, \mathbf{V}_{DC} = [V_{DC1} \dots V_{DCq}]^T$$

$$\mathbf{X} = [\boldsymbol{\theta}_{sh}^T \mathbf{m}^T \mathbf{V}_{DC}^T]^T$$

$$\mathbf{P} = [P_2 \dots P_n]^T, \mathbf{Q} = [Q_{g+1} \dots Q_n]^T, \mathbf{P}_{sh} = [P_{sh2} \dots P_{shq}], \mathbf{Q}_{sh} = [Q_{sh2} \dots Q_{shq}], \mathbf{f}_1 = [f_{11} \dots f_{1q}]$$

$$\text{and } \mathbf{R} = [\mathbf{P}_{sh} \ \mathbf{Q}_{sh} \ V_{i+r-1} \ V_{DCav} \ \mathbf{f}_1]^T$$

For this model too, it is presumed that VSC ‘r’ is employed for the control of voltage magnitude of the AC bus ‘(i+r-1)’ unlike the other ‘(q-1)’ VSCs, which control the line active as well as reactive power flows.

The unified AC-MTDC power flow equation is

$$\mathbf{J}[\Delta\boldsymbol{\theta}^T \ \Delta\mathbf{V}^T \ \Delta\boldsymbol{\theta}_{sh}^T \ \Delta\mathbf{m}^T \ \Delta\mathbf{V}_{DC}^T]^T = [\Delta\mathbf{P}^T \ \Delta\mathbf{Q}^T \ \Delta\mathbf{R}^T]^T \quad (4.27)$$

where  $\mathbf{J}$  is the power-flow Jacobian.

Fig. 4.7 and 4.8 depict the flow charts of the proposed approach for droop control models ‘A’ and ‘B’ respectively.

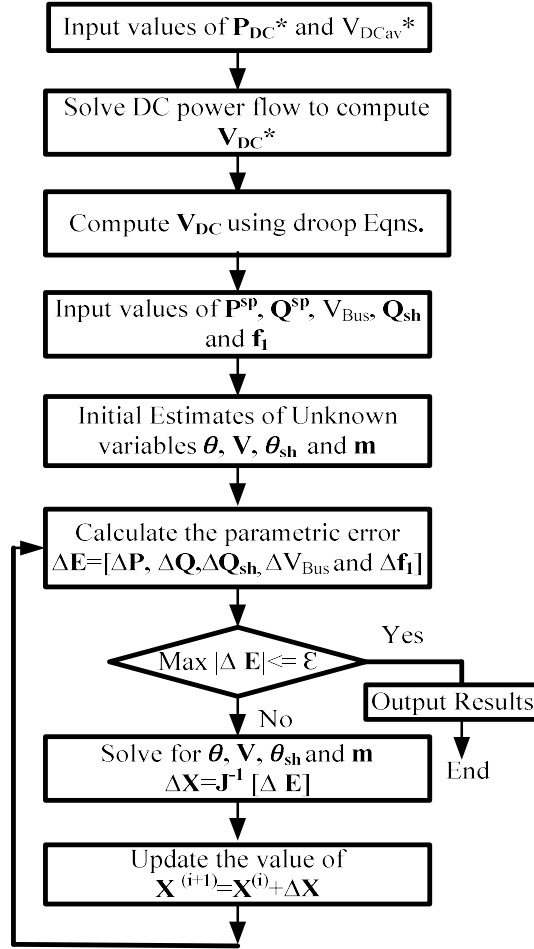


Fig. 4.7: Flow chart of the proposed approach (Model A)

It is important to note that for Model ‘B’, after ‘ $V_{DCa}$ ’ ( $1 \leq a \leq q$ ) is obtained from the AC-MTDC power-flow {eqn. (4.27)}, ‘ $P_{DCa}$ ’ ( $1 \leq a \leq q$ ) is computed.

Subsequently, to compute the DC voltage (‘ $V_{DCa}^*$ ’), power (‘ $P_{DCa}^*$ ’) or the current (‘ $I_{DCa}^*$ ’) references of the ‘ $q$ ’ VSC droop lines, we proceed as follows.

Substituting  $P_{DCa}^* = V_{DCa}^* I_{DCa}^* = \sum_{v=1}^q V_{DCa}^* V_{DCv}^* Y_{DCav}$  in eqn. (4.16), we get

$$\sum_{v=1}^q V_{DCa}^* V_{DCv}^* Y_{DCav} + R_a V_{DCa}^* - R_a V_{DCa} - P_{DCa} = 0 \quad \forall a, \quad 1 \leq a \leq q \quad (4.28)$$

From eqn. (4.28), it can be observed that since ' $V_{DCa}$ ' ( $1 \leq a \leq q$ ) is already known from the AC-MTDC power-flow solution, ' $P_{DCa}$ ' can be computed as well, and hence, (' $V_{DCa}^*$ ') can be solved. After ' $V_{DCa}^*$ ' ( $1 \leq a \leq q$ ) is obtained {from eqn. (4.28)}, the power (' $P_{DCa}^*$ ') or the current (' $I_{DCa}^*$ ') references are also computed.

Thus, to summarize, Model 'B' addresses the problem "given the target line active and reactive power flows, what should be the voltage and power references of the VSC droop lines?"

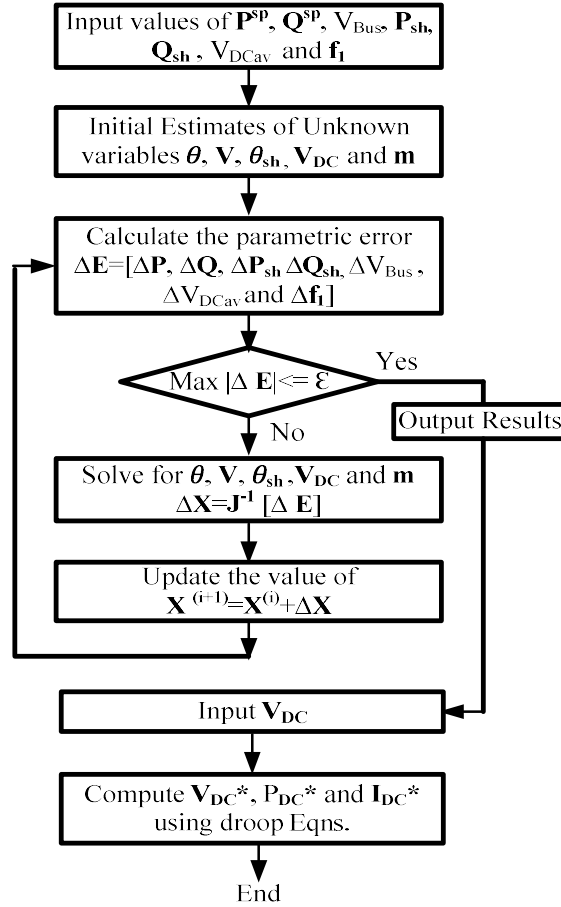


Fig. 4.8: Flow chart of the proposed approach (Model B)

It may be noted that the above analysis was done considering that the 'q' VSCs follow linear V-P voltage droop characteristics. In a similar manner, if all the 'q' VSCs

follow linear V-I droop characteristics, substituting  $I_{DCa}^* = \sum_{v=1}^q V_{DCv}^* Y_{DCav}$  in eqn. (4.17), we get

$$I_{DCa} = R_a(V_{DCa}^* - V_{DCa}) + \sum_{v=1}^q V_{DCv}^* Y_{DCav}$$

$$\text{or, } \sum_{v=1}^q V_{DCv}^* Y_{DCav} + R_a V_{DCa}^* - R_a V_{DCa} - I_{DCa} = 0 \quad (4.29)$$

Thus, for Model ‘B’, subsequent to ‘ $V_{DCa}$ ’ ( $1 \leq a \leq q$ ) being obtained from the AC-MTDC power-flow {eqn. (4.27)}, ‘ $I_{DCa}$ ’ ( $1 \leq a \leq q$ ) is computed. Then, the DC voltage (‘ $V_{DCa}^*$ ’) references of the ‘ $q$ ’ VSC droop lines can be solved from the ‘ $q$ ’ droop equations given in eqn. (4.29) above. After ‘ $V_{DCa}^*$ ’ ( $1 \leq a \leq q$ ) are computed, the current (‘ $I_{DCa}^*$ ’) or the power (‘ $P_{DCa}^*$ ’) references can also be computed.

Similarly, if the  $a^{\text{th}}$  VSC follows a nonlinear voltage droop characteristic as shown in Fig. 4.4 and operates at point ‘A’ of the characteristic, we have,

$$P_{DCa} = R_{a \max}(V_{DCa \max} - V_{DCa}) + [R_a(V_{DCa \text{ high}}^* - V_{DCa \max}) + P_{DCa}^*]$$

$$\text{or, } \sum_{v=1}^q V_{DCa}^* V_{DCv}^* Y_{DCav} + R_a(V_{DCa \text{ high}}^* - V_{DCa \max}) + R_{a \max}(V_{DCa \max} - V_{DCa}) - P_{DCa} = 0 \quad (4.30)$$

In a similar manner, the equations corresponding to other operating points (‘B’, ‘C’, ‘D’ and ‘E’) of the non-linear voltage droop characteristics shown in Fig. 4.4 can also be derived very easily.

## 4.6 Case Studies and Results

For validation of the above models, a large number of studies were carried out by employing diverse DC voltage droop control strategies on MTDC grids embedded within the IEEE 300-bus network [104]. In all the occurrences, the VSC constant was selected as  $c = \frac{1}{2\sqrt{2}}$  [11]. Also, for all the VSC coupling transformers,  $R_{\text{sha}} = 0.001$

p.u. and  $X_{sha} = 0.1$  p.u. ( $\forall a, 1 \leq a \leq q$ ). The converter loss constants ‘ $a_1$ ’, ‘ $b_1$ ’ and ‘ $c_1$ ’ were chosen as 0.011, 0.003 and 0.0043, respectively [18], [95]. For interconnections between DC terminals,  $R_{DCuv} = 0.01$  p.u. ( $\forall u, v, 1 \leq u \leq q, 1 \leq v \leq q, u \neq v$ ), throughout the chapter [83]. In all occurrences, a termination error tolerance of  $10^{-10}$  p.u. was selected. ‘NI’ and ‘CT’ denote the number of iterations and the computational time in seconds, pertaining to a 1.99 GHz Dell PC. In all the results given in Tables 4.1- 4.8, values of bus voltage magnitudes, current magnitudes, active and reactive powers and droop control gains are denoted in p.u. while phase angles of voltage phasors are denoted in degrees.

#### **4.6.1 Studies of three terminal VSC-HVDC network incorporated in the IEEE 300 bus system**

##### **Case I: Model-A employing Linear V-P and V-I droop characteristics**

For this case study, at the outset, the base case power-flow (in the absence of any MTDC grid) is carried out. The results are given in row 1 of Table 4.1. Then a 3-terminal MTDC grid ( $q = 3$ ) is integrated with the IEEE 300-bus test system at AC buses ‘268’, ‘272’ and ‘273’. While the VSCs connected to AC buses ‘268’ and ‘272’ follow linear V-P droop characteristics, the VSC connected to AC bus ‘273’ operates on a linear V-I droop characteristic. The droop control gains of VSCs 1, 2 and 3 are set to 20, 15 and 10, respectively [24], [28], [29] and [82].

Next, a DC power-flow is carried out to obtain the voltage (‘ $V_{Dca}^*$ ’), power (‘ $P_{Dca}^*$ ’) and current (‘ $I_{Dca}^*$ ’) references ( $1 \leq a \leq 3$ ) for the droop lines of the VSCs. The results are given in row 4 of Table 4.1.

Thereafter, the DC voltages  $\{V_{DCa}^* (1 \leq a \leq 3)\}$  are computed from the voltage ( $V_{DCa}^*$ ), power ( $P_{DCa}^*$ ) and current ( $I_{DCa}^*$ ) references using the droop eqn. (4.24). The results are given in rows 7 of Table 4.1.

Table 4.1

Study of IEEE 300 bus system with three terminal VSC HVDC network incorporating linear DC voltage droop characteristics (Model A)

Base case power-flow (NI=6 and CT=0.56); $V_{268} = 0.9684 \angle -21.01$ ; $V_{272} = 0.9811 \angle -19.46$ ; $V_{273} = 1.0058 \angle -17.47$ ;		
DC (3-terminal) power-flow		
Specified quantities	Solution	
$V_{DCav}^*=3$ ; $P_{DC2}^* = 0.5$ ; $P_{DC3}^* = 0.4$ ;	DC power-flow converged in three iterations $V_{DC1}^* = 2.9990$ ; $V_{DC2}^* = 3.0006$ ; $V_{DC3}^* = 3.0004$ ; $P_{DC1}^* = -0.8995$ ; $I_{DC3}^* = 0.1333$ ; NI=3; CT=0.11;	
Computation of $V_{DC}$ from droop eqns.		
Specified quantities	Solution	
$V_{DC1}^* = 2.9990$ ; $V_{DC2}^* = 3.0006$ ; $V_{DC}^* = 3.0004$ ; $P_{DC}^* = -0.8995$ ; $P_{DC2}^* = 0.5$ ; $I_{DC3}^* = 0.1333$ ; $R_1 = 20$ ; $R_2 = 15$ ; $R_3 = 10$ ;	$V_{DC1} = 2.9990$ ; $V_{DC2} = 3.0006$ ; $V_{DC3} = 3.0004$ ; NI=4; CT=0.07;	
AC-MTDC power-flow with linear voltage droop control (VSCs connected to AC buses 268, 272 and 273)		
Specified quantities	Solution	
	AC buses	VSC
$V_{DC1} = 2.9990$ ; $V_{DC} = 3.0006$ ; $V_{DC} = 3.0004$ ; $V_{268} = 0.98$ ; $Q_{sh2} = -0.05$ ; $Q_{sh3} = -0.05$ ;	$\theta_{268} = -2.8508$ ; $V_{272} = 0.9527 \angle -9.7288$ ; $V_{273} = 0.9514 \angle -35.3471$ ; $P_{sh2} = -0.5142$ ; $P_{sh3} = -0.4133$ ;	$\theta_{sh1} = 2.3580$ ; $m_1 = 0.9339$ ; $\theta_{sh} = -12.9877$ ; $m_2 = 0.8941$ ; $\theta_{sh3} = -37.9739$ ; $m_3 = 0.8925$ ;
	DC Power	Converter loss (%)
	$P_{DC1} = -0.8995$ ; $P_{DC2} = 0.50$ ; $P_{DC3} = 0.40$ ;	$P_{loss1} = 1.72$ ; $P_{loss2} = 1.39$ ; $P_{loss3} = 1.31$ ;
	NI=6; CT=1.34;	

After obtaining  $V_{DCa}^*$ , the AC-MTDC power-flow is executed. The results are given in row 10 of Table 4.1. The computed values of the active power flows in the (two) lines ( $P_{sh2}$  and  $P_{sh3}$ ) are shown in bold in row 10 of Table 4.1. Thus, the line

active power-flows are not controllable, unlike the line reactive powers (which are specified). This is a major drawback of model ‘A’.

Table 4.1 shows that for both the base case and the AC-MTDC power-flow with droop model ‘A’, ‘NI’ remains same. But ‘CT’ is more in the latter case as the number of variables increase.

### **Case II: Model-B employing Linear V-P and V-I droop characteristics**

This case study is similar to the previous study of Table 4.1. The 3-terminal MTDC grid is again integrated with the AC system at buses ‘268’, ‘272’ and ‘273’. However, the specified line reactive power-flows are modified from their values in Table 4.1. The results of the AC-MTDC power-flow are given in rows 3-9 of Table 4.2. It may be noted that unlike the previous study of Table 4.1, now the line active power flows can also be specified. This is an advantage of model ‘B’.

From the AC-MTDC power-flow, using the values of ‘ $V_{DCa}$ ’ obtained (and hence, ‘ $P_{DCa}$ ’ and ‘ $I_{DCa}$ ’), the DC voltage (‘ $V_{DCa}^*$ ’) and thereafter, the power (‘ $P_{DCa}^*$ ’) and current (‘ $I_{DCa}^*$ ’) references for the droop lines of the VSCs are computed using the droop eqns. {eqns. (4.28) and (4.29)}. The results are given in row 11 of Table 4.2.

From Tables 4.1 and 4.2, it can be observed that both in droop models ‘A’ and ‘B’, ‘NI’ remains same. But ‘CT’ is slightly more in the latter as the number of variables increase { $V_{DCa}$  ( $1 \leq a \leq 3$ ) are now included}.

The convergence characteristics corresponding to the case studies of base case, Table 4.1 and Table 4.2 are shown in Figures 4.9 - 4.11, respectively. From Figures 4.9 - 4.11, it is observed that the developed algorithm demonstrates excellent



convergence characteristics, similar to the base case and converging in six iterations. The bus voltage profiles of Table 4.1 and Table 4.2 are shown in Figures 4.12 and 4.13, respectively. From Figures 4.12 and 4.13, it can be observed that the bus voltage profiles do not change much except at the AC terminal buses to which the converters are connected.

Table 4.2

Study of IEEE 300 bus system with three terminal VSC HVDC network incorporating linear DC voltage droop characteristics (Model B)

Base case power-flow (NI=6 and CT=0.56); $V_{268} = 0.9684\angle -21.01$ ; $V_{272} = 0.9811\angle -19.46$ ; $V_{273} = 1.0058\angle -17.47$ ;		
(VSCs connected to AC buses 268, 272 and 273) AC-MTDC power-flow with linear voltage droop control		
Specified quantities		Solution
		AC buses
$V_{DCav}$	3.0	$\theta_{268} = -39.1737$ ; $\theta_{272} = -31.2288$ ; $\theta_{273} = -6.7581$ ; $V_{272} = 1.0086$ ; $V_{273} = 1.0366$ ; $\theta_{sh1} = -43.2335$ ; $m_1 = 0.9347$ ; $V_{DC} = 3.0008$ ; $\theta_{sh} = -29.2837$ ; $m_2 = 0.931$ ; $V_{DC} = 2.9996$ ; $\theta_{sh} = -5.1792$ ; $m_3 = 0.9604$ ; $V_{DC3} = 2.9997$ ; NI=6; CT=1.54;
$V_{268}$	0.98	
$P_{sh2}$	0.35	
$Q_{sh2}$	0.1	
$P_{sh3}$	0.3	
$Q_{sh3}$	0.1	
Computation of references $V_{DC}^*$ from droop eqns.		
$V_{DC} = 3.0008$ ; $V_{DC} = 2.9996$ ; $V_{DC} = 2.9997$ ; $R_1 = 20$ ; $R_2 = 15$ ; $R_3 = 10$ ;		$V_{DC1}^* = 3.0008$ ; $V_{DC2}^* = 2.9996$ ; $V_{DC3}^* = 2.9997$ ; DC Power $P_{DC1} = 0.6754$ ; $P_{DC2} = -0.3628$ ; $P_{DC3} = -0.3124$ ; Converter loss (%) $P_{loss1} = 1.54$ ; $P_{loss} = 1.26$ ; $P_{loss3} = 1.23$ ;
		NI=4; CT=0.05;

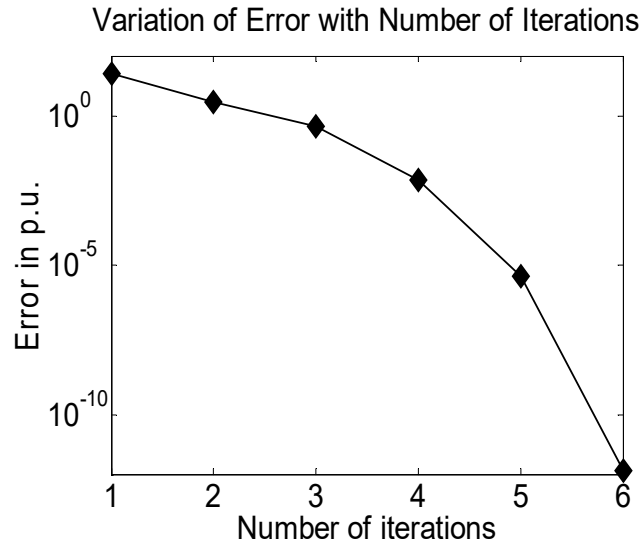


Fig. 4.9: Convergence characteristic for the base case power flow in IEEE-300 bus system

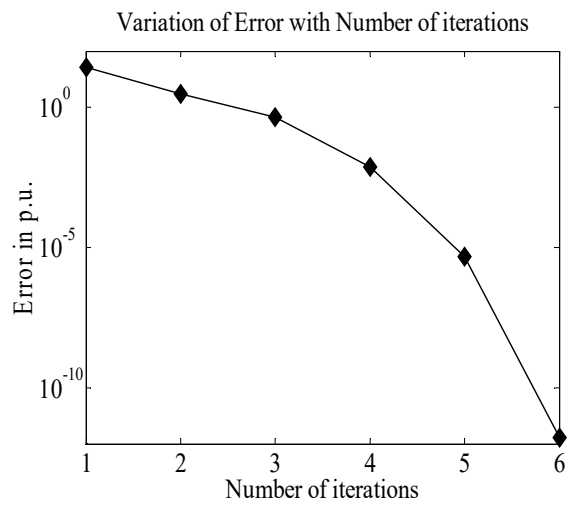


Fig. 4.10: Convergence characteristic for the case study of Table 4.1

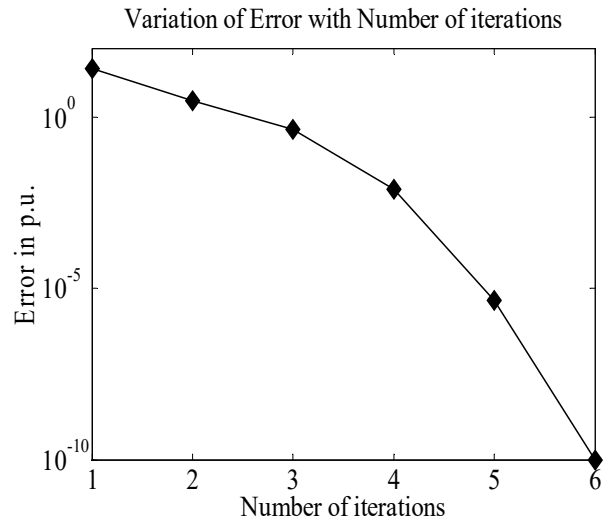


Fig. 4.11: Convergence characteristic for the study of Table 4.2

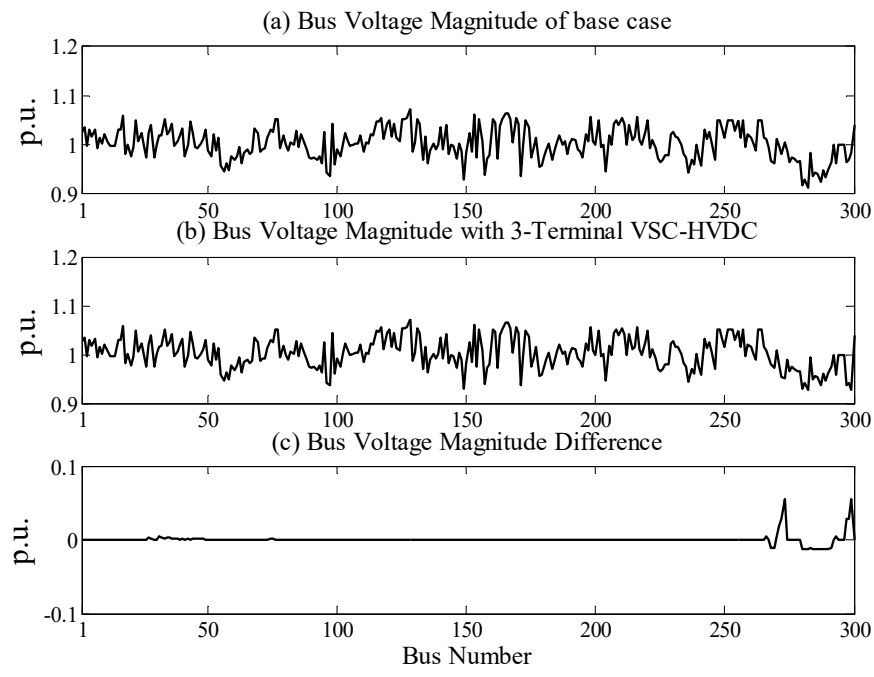


Fig. 4.12: Bus voltage profile for the study of Table 4.1

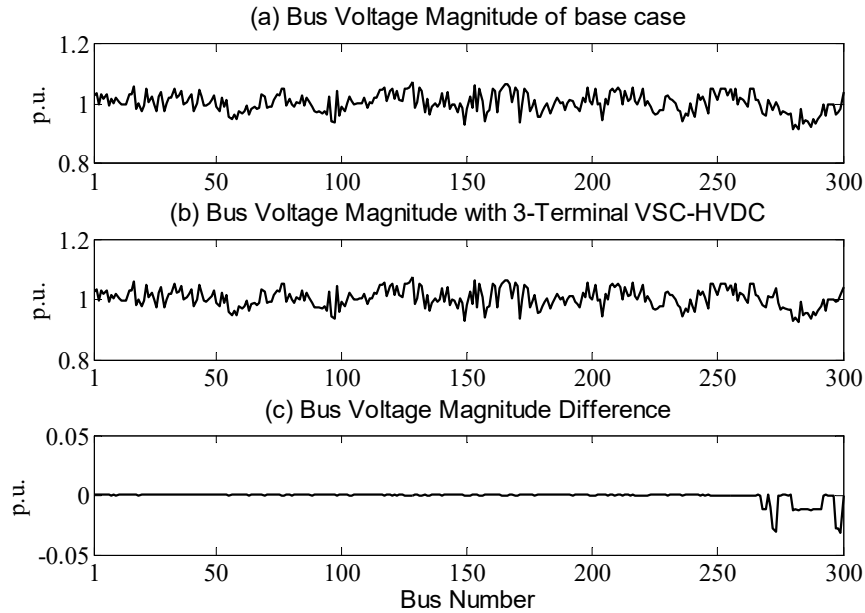


Fig. 4.13: Bus voltage profile for the study of Table 4.2

**Case III Model-B employing nonlinear V-P droop with Dead-Band**

This case study is similar to the previous study of Table 4.2, except VSC 2 which follows a nonlinear V-P droop characteristic with dead-band. The droop control gains are identical to the previous study of Table 4.2. First, a separate DC power-flow is carried out to calculate the reference values for the droop control lines. The results are shown in row 4 of Table 4.3. Next, the AC-MTDC power flow is carried out. The power flow solution is shown in rows 5-13 of Table 4.3. From the power flow solution, it is observed that VSC-2 (connected to AC bus 272) operates at the point ‘A’ as shown in Fig. 4.4.

Table 4.3

Study of IEEE 300 bus system with three terminal VSC HVDC network  
incorporating nonlinear DC voltage droop characteristics with dead-band

Base case power-flow (NI=6 and CT=0.652); $V_{268} = 0.9684\angle - 21.01$ ; $V_{272} = 0.9811\angle - 19.46$ ; $V_{273} = 1.0058\angle - 17.47$ ;	
DC power-flow to calculate DC reference values	
Specified Quantities	Power flow solution
$V_{DCav}^* = 3.02$ ; $P_{DC2}^* = - 0.5$ ; $P_{DC3}^* = - 0.4$ ;	$V_{DC1}^* = 3.0206$ ; $V_{DC2}^* = 3.0197$ ; $V_{DC3}^* = 3.0197$ ; $P_{DC1}^* = 0.9003$ ; $I_{DC3}^* = -0.1325$ ;
	NI=3; CT=0.02;
AC-MTDC power-flow with linear voltage droop and nonlinear droop with dead-band (VSCs connected to AC buses 268, 272, 273)	
Specified Quantities	Power flow solution
Control parameters	DC terminal buses
$V_{DCmax} = 3.014$ ; $V_{DChigh}^* = 3.013$ ; $V_{DClow}^* = 3.012$ ; $V_{DCmin} = 3.009$ ; $R_1 = 20$ ; $R_2 = 15$ ; $R_3 = 10$ ; $R_{max} = 30$ ;	$V_{DC1} = 3.0183$ ; $V_{DC2} = 3.0173$ ; $V_{DC3} = 3.0175$ ;
Converter	Control Mode
1	V-P droop
2	V-P droop with dead-band
3	V-I droop
VSCs	
$\theta_{sh1} = -48.7989$ ; $\theta_{sh2} = -28.8620$ ; $\theta_{sh3} = -4.4850$ ; $m_1 = 0.9491$ ; $m_2 = 0.9584$ ; $m_3 = 0.9810$ ;	
AC terminal buses	
$\theta_{268} = \angle - 43.2010$ ; $V_{272} = 1.0102\angle - 32.1815$ ; $V_{273} = 1.0362\angle - 6.1658$ ;	
$V_{268} = 0.98$ ; $Q_{sh2} = 0.1$ ; $Q_{sh} = 0.1$ ;	DC Power
	Converter loss (%)
	$P_{DC} = 0.9457$ ; $P_{DC2} = - 0.6138$ ; $P_{DC3} = - 0.3316$ ;
	$P_{loss} = 1.86$ ; $P_{loss} = 1.44$ ; $P_{loss3} = 1.24$ ;
NI=6; CT=1.49;	

#### Case IV Model-B employing Voltage Margin control

This case study is carried out on the same AC-MTDC system but the VSC connected to AC bus 272 employs voltage margin control. The droop control gains of the converters connected to AC buses 268 and 273 are similar to the studies of Table 4.1-4.3. The droop control gain of the converter connected to AC bus '272' is set to a value of 1000 corresponding to the operation of voltage margin control. For voltage

margin control characteristic, the maximum and the minimum DC powers are set to values of 1.0 and -1.0 p.u, respectively. The power flow solution is shown in rows 5-13 of Table 4.4.

Table 4.4

Study of IEEE 300 bus system with three terminal VSC HVDC network employing voltage margin control

Specified Quantities		Power flow solution	
Base case power-flow (NI=6 and CT=0.56); $V_{268} = 0.9684\angle - 21.01$ ; $V_{272} = 0.9811\angle - 19.46$ ; $V_{273} = 1.0058\angle - 17.47$ ;			
DC power-flow to calculate DC reference values			
Specified Quantities		Power flow solution	
$V_{DCav}^* = 3.03$ ; $P_{DC}^* = - 0.5$ ; $P_{DC3}^* = - 0.4$ ;		$V_{DC1}^* = 3.0310$ ; $V_{DC2}^* = 3.0294$ ; $V_{DC3}^* = 3.0296$ ; $P_{DC1}^* = 0.9004$ ; $I_{DC3}^* = -0.1320$ ;	
		NI=4; CT=0.02;	
AC-MTDC power-flow with linear voltage droop and nonlinear voltage margin (VSCs connected to AC buses 268, 272, 273)			
Specified Quantities		Power flow solution	
Control parameters		DC terminal buses	
$V_{DCmax} = 3.01$ ; $V_{DChigh}^* = 3$ ; $V_{DClow}^* = 2.99$ ; $V_{DCmin} = 2.98$ ; $R_1 = 20$ ; $R_2 = 1000$ ; $R_3 = 10$ ;		$V_{DC1} = 3.0210$ ; $V_{DC2} = 3.0187$ ; $V_{DC3} = 3.0197$ ;	
Converter	Control Mode	VSCs	
1	V-P droop	$\theta_{sh1} = -43.3748$ ; $\theta_{sh2} = -18.1817$ ; $\theta_{sh3} = -14.1289$ ; $m_1 = 0.95$ ; $m_2 = 0.9714$ ; $m_3 = 0.9784$ ;	
2	Voltage Margin		
3	V-I droop		
$V_{268} = 0.98$ ; $Q_{sh2} = 0.1$ ; $Q_{sh3} = 0.05$ ;		AC terminal buses $\theta_{268} = -36.8764$ ; $V_{272} = 1.0215\angle - 23.4921$ ; $V_{273} = 1.0348\angle - 14.5915$ ;	
		DC Power $P_{DC} = 1.1006$ ; $P_{DC2} = -1.0000$ ; $P_{DC3} = -0.0997$ ;	Converter loss % $P_{loss} = 2.06$ ; $P_{loss2} = 1.79$ ; $P_{loss3} = 1.15$ ;
NI=6; CT=1.46;			

The convergence characteristics of Table 4.3 and 4.4 are shown in Figures 4.14 and 4.15, respectively. From Figures 4.14 and 4.15, it is observed that the developed algorithm demonstrates excellent convergence characteristics, again converging in six

iterations. The bus voltage profiles of Table 4.3 and 4.4 are shown in Figures 4.16 and 4.17, respectively. Again, from Figures 4.16 and 4.17, it is observed that the bus voltage profiles do not alter much from the base case except the AC buses at which the converters are connected.

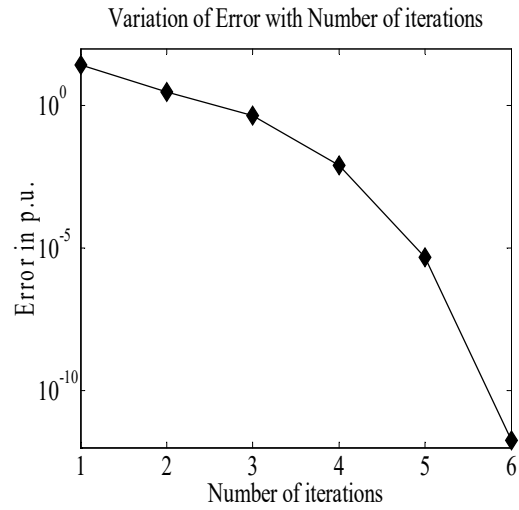


Fig. 4.14: Convergence characteristic for the case study of Table 4.3

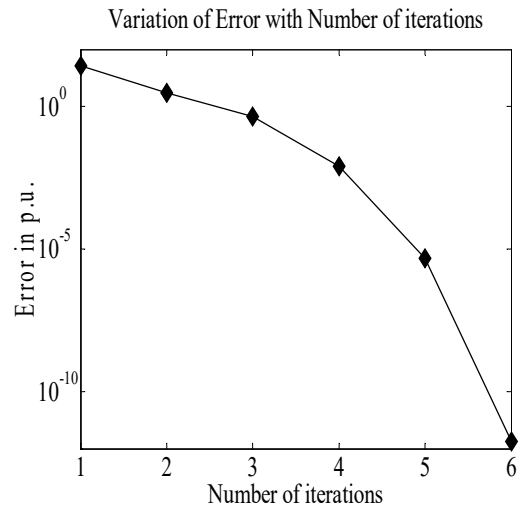


Fig. 4.15: Convergence characteristic for the case study of Table 4.4

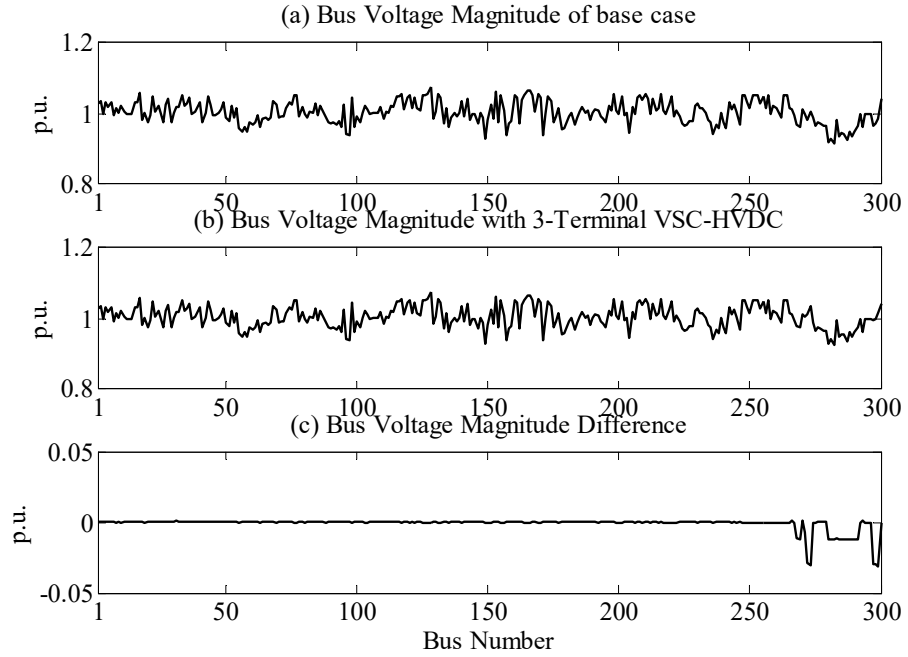


Fig. 4.16: Bus voltage profile for the study of Table 4.3

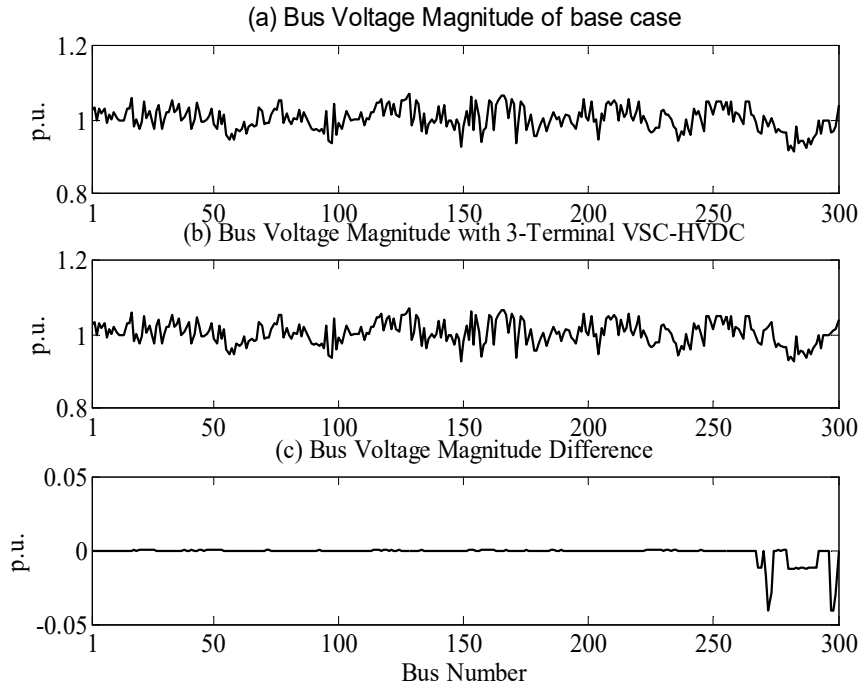


Fig. 4.17: Bus voltage profile for the study of Table 4.4



## 4.6.2 Studies of five terminal VSC-HVDC network incorporated in the IEEE 300 bus system

### Case I: Model-A employing Linear V-P and V-I droop characteristics

This case study is similar to that of Table 4.1 except with five DC terminals. For this study, at the outset, the base case power-flow (in the absence of any MTDC grid) is carried out. The results are given in row 1 of Table 4.5. Then a 5-terminal MTDC grid is integrated with the IEEE 300-bus test system at AC buses ‘266’, ‘270’, ‘271’, ‘272’ and ‘273’. While the VSCs connected to AC buses ‘266’ and ‘270’ follow linear V-P droop characteristics, the VSCs connected to AC buses ‘271’, ‘272’ and ‘273’ operate on linear V-I droop characteristics. The droop control gains of VSCs 1 and 2 are set to 20 and 15, respectively [24], [82]. The droop control gains of VSCs 3, 4 and 5 are all set to a value of 10.

Next, a DC power-flow is carried out to obtain the voltage ( $V_{DCa}^*$ ), power ( $P_{DCa}^*$ ) and current ( $I_{DCa}^*$ ) references ( $1 \leq a \leq 5$ ) for the droop lines of the VSCs. The results are given in row 4 of Table 4.5.

Thereafter, the DC voltages  $\{V_{DCa}\}$  ( $1 \leq a \leq 5$ ) are computed from the voltage ( $V_{DCa}^*$ ), power ( $P_{DCa}^*$ ) and current ( $I_{DCa}^*$ ) references using droop eqn. (4.24). The results are given in row 7 of Table 4.5.

After obtaining  $V_{DCa}$ , the AC-MTDC power-flow is carried out. The results are given in row 10 of Table 4.5. The computed values of the active power flows in lines ( $P_{sh2}$ ,  $P_{sh3}$ ,  $P_{sh}$  and  $P_{sh}$ ) are shown in bold in row 10 of Table 4.5.

Table 4.5 shows that for both the base case and the AC-MTDC power-flow with droop model ‘A’, ‘NI’ remains same. But ‘CT’ is more in the latter case as the

number of variables increase. It is also observed that CT is more with the five terminal MTDC network than the three terminal one.

Table 4.5

Study of IEEE 300 bus system with five terminal VSC HVDC network employing linear DC voltage droop characteristics (Model A)

Base case power flow (NI=6 and CT=0.56)		
$V_{266} = 1.011 \angle -11.24$ ; $V_{270} = 1.011 \angle -11.32$ ; $V_{271} = 0.998 \angle -17.67$ ; $V_{272} = 0.981 \angle -19.46$ ; $V_{273} = 1.006 \angle -17.47$ ;		
DC (5-terminal) power-flow		
Given quantities	Solution	
$V_{DCav}^* = 3$ ; $P_{DC2}^* = 0.35$ ; $P_{DC3}^* = 0.3$ ; $P_{DC4}^* = 0.3$ ; $P_{DC5}^* = 0.4$ ;	DC power-flow converged in three iterations $V_{DC1}^* = 2.9991$ ; $V_{DC}^* = 3.0002$ ; $V_{DC3}^* = 3.0002$ ; $V_{DC4}^* = 3.0002$ ; $V_{DC5}^* = 3.0003$ ; $P_{DC1}^* = -1.3495$ ; $I_{DC3}^* = 0.1$ ; $I_{DC4}^* = 0.1$ ; $I_{DC5}^* = 0.1333$ ; NI=3; CT=0.02;	
Computation of $V_{DC}$ from droop eqns.		
Given quantities	Solution	
$V_{DC1}^* = 2.9991$ ; $V_{DC2}^* = 3.0002$ ; $V_{DC3}^* = 3.0002$ ; $V_{DC4}^* = 3.0002$ ; $V_{DC5}^* = 3.0003$ ; $P_{DC1}^* = -1.3495$ ; $P_{DC}^* = 0.35$ ; $I_{DC3}^* = 0.1$ $I_{DC4}^* = 0.1$ ; $I_{DC5}^* = 0.1333$ ; $R_1 = 20$ ; $R_2 = 15$ ; $R_3 = 10$ ; $R_4 = 10$ ; $R_5 = 10$ ;	$V_{DC1} = 2.9991$ ; $V_{DC2} = 3.0002$ ; $V_{DC3} = 3.0002$ ; $V_{DC4} = 3.0002$ ; $V_{DC5} = 3.0003$ ; NI=4; CT=0.07;	
AC-MTDC power-flow with linear voltage droop control		
Given quantities	Solution	
	AC buses	VSC
$V_{DC} = 2.9991$ ; $V_{DC2} = 3.0002$ ; $V_{DC} = 3.0002$ ; $V_{DC} = 3.0002$ ; $V_{DC} = 3.0003$ ; $V_{266} = 1.02$ ; $Q_{sh2} = 0.2$ ; $Q_{sh3} = 0.15$ ; $Q_{sh4} = 0.12$ ; $Q_{sh5} = 0.1$ ;	$\theta_{266} = -11.6616$ ; $V_{270} = 1.0201 \angle -11.8087$ ; $V_{271} = 1.022 \angle -34.5310$ ; $V_{272} = 1.0118 \angle -39.7253$ ; $V_{273} = 1.0014 \angle -33.9952$ ; $P_{sh1} = 1.3239$ ; $P_{sh} = -0.3631$ ; $P_{sh3} = -0.3126$ ; $P_{sh4} = -0.3126$ ; $P_{sh5} = -0.4132$ ;	$\theta_{sh1} = -4.7995$ ; $m_1 = 1.0203$ ; $\theta_{sh} = -13.7810$ ; $m_2 = 0.9804$ ; $\theta_{sh} = -36.2298$ ; $m_3 = 0.9775$ ; $\theta_{sh} = -41.4609$ ; $\theta_{sh5} = -36.3384$ ; $m_4 = 0.9652$ ; $m_5 = 0.9538$ ;
	DC Power	Converter loss (%)
	$P_{DC} = -1.3495$ ; $P_{DC} = 0.3500$ ; $P_{DC3} = 0.3000$ ; $P_{DC4} = 0.3000$ ; $P_{DC5} = 0.4000$ ;	$P_{loss1} = 2.37$ ; $P_{lo} = 1.29$ ; $P_{loss3} = 1.25$ ; $P_{loss4} = 1.25$ ; $P_{loss5} = 1.31$ ;
NI=6; CT=1.44;		

## Case II: Model-B employing Linear V-P and V-I droop characteristics

In this case study, the 5-terminal MTDC grid is again integrated with the AC system at AC buses ‘266’, ‘270’, ‘271’, ‘272’ and ‘273’. But the line reactive power values are modified. The results of the AC-MTDC power-flow are given in rows 4-13 of Table 4.6. It may be noted that unlike the previous study of Table 4.5, now the line active power flows can also be specified. This is an advantage of model ‘B’.

Table 4.6

Study of IEEE 300 bus system with five terminal VSC HVDC network  
incorporating linear DC voltage droop characteristics (Model B)

Base case power flow (NI=6 and CT=0.56)			
$V_{266} = 1.011 \angle -11.24$ ; $V_{270} = 1.011 \angle -11.32$ ; $V_{271} = 0.998 \angle -17.67$ ; $V_{272} = 0.981 \angle -19.46$ ; $V_{273} = 1.006 \angle -17.47$ ;			
AC-MTDC power-flow with linear voltage droop control (VSCs connected to AC buses 266, 270, 271, 272 and 273)			
Given quantities		Solution	
		AC buses	VSC
$V_{DCav}$	3.0	$\theta_{266} = -11.5227$ ; $\theta_{270} = -11.5210$ ; $\theta_{271} = -4.4870$ ; $\theta_{272} = -3.8018$ ; $\theta_{273} = -3.1837$ ; $V_{270} = 1.0205$ ; $V_{271} = 1.0695$ ; $V_{272} = 1.0730$ ; $V_{273} = 1.0387$ ;	$\theta_{sh1} = -19.1658$ ; $m_1 = 0.9933$ ; $V_{DC1} = 3.0009$ ; $\theta_{sh} = -9.3615$ ; $m_2 = 0.9771$ ; $V_{DC2} = 2.9997$ ; $\theta_{sh3} = -2.9940$ ; $m_3 = 1.0134$ ; $\theta_{sh4} = -2.5661$ ; $m_4 = 1.0166$ ; $\theta_{sh} = -1.0859$ ; $m_5 = 0.9895$ ; $V_{DC3} = 2.9998$ ; $V_{DC4} = 2.9998$ ; $V_{DC5} = 2.9997$ ;
$V_{266}$	0.98		
$P_{sh2}$	0.4		
$Q_{sh2}$	0.15		
$P_{sh3}$	0.3		
$Q_{sh3}$	0.05		
$P_{sh4}$	0.25		
$Q_{sh4}$	0.05		
$P_{sh5}$	0.4		
$Q_{sh5}$	0.1		
NI=6; CT=1.57;			
Computation of references $V_{DC}^*$ from droop eqns.			
$V_{DC1} = 3.0009$ ; $V_{DC2} = 2.9997$ ; $V_{DC3} = 2.9998$ ; $V_{DC4} = 2.9998$ ; $V_{DC5} = 2.9997$ ; $R_1 = 20$ ; $R_2 = 15$ ; $R_3 = 10$ ; $R_4 = 10$ ; $R_5 = 10$ ;		$V_{DC1} = 3.0009$ ; $V_{DC2} = 2.9997$ ; $V_{DC3} = 2.9998$ ; $V_{DC4} = 2.9998$ ; $V_{DC5} = 2.9997$ ;	
		DC Power	Converter loss (%)
		$P_{DC1} = 1.4011$ ; $P_{DC2} = -0.4132$ ; $P_{DC3} = -0.3123$ ; $P_{DC} = -0.2620$ ; $P_{DC5} = -0.4130$ ;	$P_{loss1} = 2.39$ ; $P_{loss2} = 1.30$ ; $P_{loss} = 1.22$ ; $P_{loss} = 1.19$ ; $P_{loss5} = 1.29$ ;
NI=4; CT=0.05;			

Subsequent to the AC-MTDC power-flow, using the values of ' $V_{DCa}$ ' obtained (and hence, ' $P_{DCa}$ ' and ' $I_{DCa}$ '), the DC voltage (' $V_{DCa}^*$ ') and thereafter, the power (' $P_{DCa}^*$ ') and current (' $I_{DCa}^*$ ') references for the droop lines of the VSCs are computed using the droop eqns. {eqns. (4.28) and (4.29)}. The results are given in row 15 of Table 4.6.

From Tables 4.5 and 4.6, it is observed that both in droop models 'A' and 'B', 'NI' remains same. But 'CT' is slightly more in the latter as the number of variables rise (all  $V_{DCs}$  are now included).

The convergence characteristics of Table 4.5 and 4.6 are shown in Fig. 4.18 and 4.19, respectively. From Figures 4.18 and 4.19, it is observed that the power flow algorithm demonstrates convergence characteristics similar to the base case, converging in six iterations. The bus voltage profiles corresponding to Tables 4.5 and 4.6 are shown in Figures 4.20 and 4.21, respectively. Again, from Figures 4.20 and 4.21, it is observed that the bus voltage profiles do not change much from the base case except the buses at which the converters are connected.

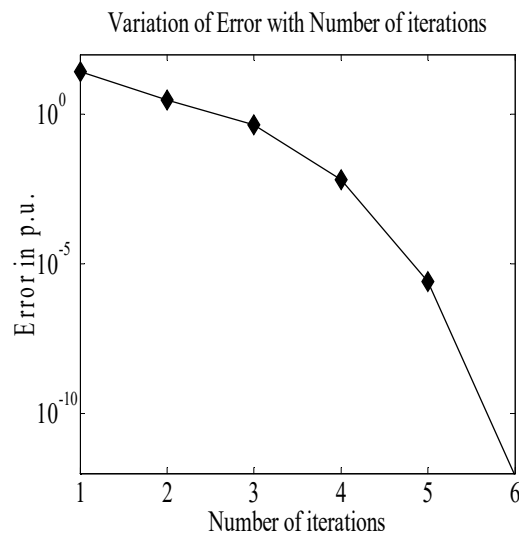


Fig. 4.18: Convergence characteristic for the study of Table 4.5

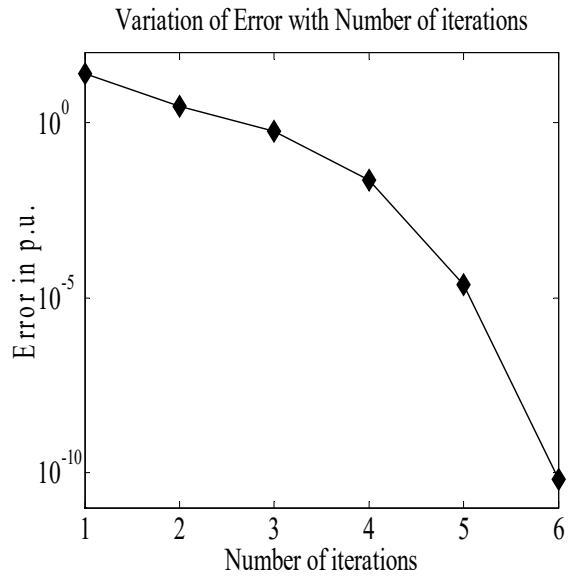


Fig. 4.19: Convergence characteristic for the study of Table 4.6

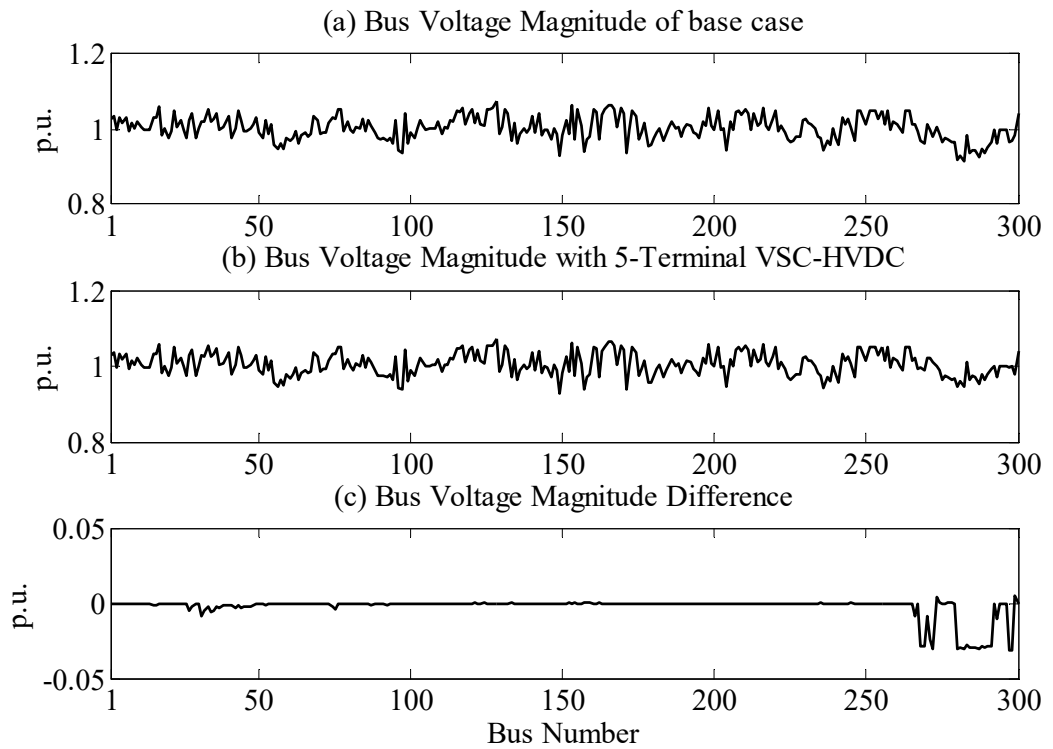


Fig. 4.20: Bus voltage profile for the study of Table 4.5

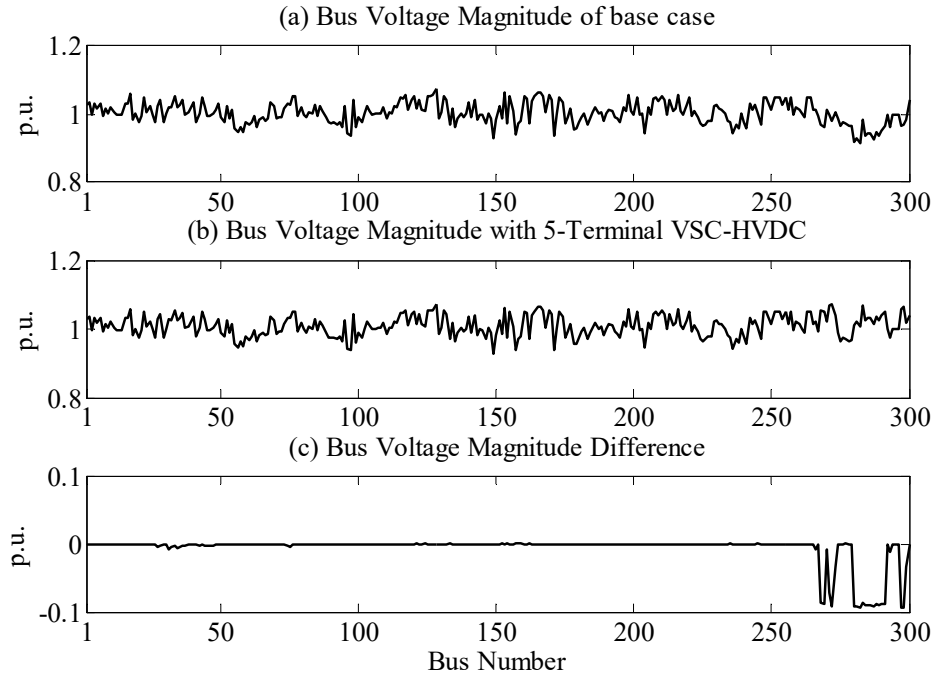


Fig. 4.21: Bus voltage profile for the study of Table 4.6

### Case III Model-B employing nonlinear V-P droop with dead-band

This case study is similar to the previous study of Table 4.6 except VSC 2 which employs a nonlinear V-P droop with dead-band. The droop control gains are identical to that of the study of Table 4.6. First, a separate DC power-flow is carried out to calculate the reference values for the droop control lines. The results are shown in row 4 of Table 4.7. Subsequently, the AC-MTDC power flow is carried out. The results are shown in rows 5-13 of Table 4.7.

From the power flow solution, it is observed that the converter connected at AC bus 272 operates at the point 'A' as shown in Fig. 4.4.

Table 4.7

Study of IEEE 300 bus system with five terminal VSC HVDC network  
incorporating non-linear voltage droop characteristics with dead-band

Base case power flow (NI=6 and CT=0.56)	
$V_{266} = 1.011 \angle -11.24$ ; $V_{270} = 1.011 \angle -11.32$ ; $V_{271} = 0.998 \angle -17.67$ ; $V_{272} = 0.981 \angle -19.46$ ; $V_{273} = 1.006 \angle -17.47$ ;	
DC power-flow to calculate DC reference values	
Specified Quantities	Power flow solution
$V_{DCav}^* = 3.02$ ; $P_{DC}^* = -0.5$ ; $P_{DC3}^* = -0.4$ ; $P_{DC4}^* = -0.3$ ; $P_{DC5}^* = -0.4$ ;	$V_{DC1}^* = 3.0211$ ; $V_{DC2}^* = 3.0197$ ; $V_{DC3}^* = 3.0197$ ; $V_{DC4}^* = 3.0198$ ; $V_{DC5}^* = 3.0197$ ; $P_{DC1}^* = 1.6007$ ; $I_{DC3}^* = -0.1325$ ; $I_{DC4}^* = -0.0993$ ; $I_{DC5}^* = -0.1325$ ;
	NI=3; CT=0.02;
AC-MTDC power-flow with linear voltage droop and nonlinear droop with dead-band (VSCs connected to AC buses 266, 270, 271, 272 and 273)	
Specified Quantities	Power flow solution
Control parameters	DC terminal buses
$V_{DCmax} = 3.014$ ; $V_{DChigh}^* = 3.013$ ; $V_{DClow}^* = 3.012$ ; $V_{DCmin} = 3.009$ ; $R_1 = 20$ ; $R_2 = 15$ ; $R_3 = 10$ ; $R_4 = 10$ ; $R_5 = 10$ ; $R_{max} = 30$ ;	$V_{DC1} = 3.0198$ ; $V_{DC2} = 3.0183$ ; $V_{DC} = 3.0184$ ; $V_{DC} = 3.0185$ ; $V_{DC} = 3.0184$ ;
Converter	Control Mode
1	V-P droop
2	V-P droop with dead-band
3	V-I droop
VSCs	
$\theta_{sh1} = -20.3526$ ; $\theta_{sh2} = -8.0873$ ; $\theta_{sh} = -1.5592$ ; $\theta_{sh} = -1.3553$ ; $\theta_{sh} = -3.2532$ ; $m_1 = 0.9958$ ; $m_2 = 0.9678$ ; $m_3 = 1.0016$ ; $m_4 = 1.0020$ ; $m_5 = 0.9840$ ;	
AC terminal buses	
$\theta_{266} = -20.3526$ ; $V_{270} = 1.0102 \angle -8.0873$ ; $V_{271} = 1.0362 \angle -1.5592$ ; $V_{272} = 1.0362 \angle -1.3553$ ; $V_{273} = 1.0362 \angle -3.2532$ ;	
DC Power	
$P_{DC1} = 1.6266$ ; $P_{DC} = -0.6428$ ; $P_{DC} = -0.3610$ ; $P_{DC4} = -0.2610$ ; $P_{DC5} = -0.3610$ ;	Converter loss (%)
	$P_{loss1} = 2.78$ ; $P_{loss2} = 1.45$ ; $P_{lo} = 1.25$ ; $P_{loss4} = 1.19$ ; $P_{loss5} = 1.26$ ;
NI=6; CT=1.51;	
$V_{268} = 0.98$ ; $Q_{sh} = 0.1$ ; $Q_{sh3} = 0.05$ ; $Q_{sh} = 0.04$ ; $Q_{sh} = 0.1$ ;	

#### **Case IV Model employing Voltage Margin control**

This case study is conducted on the same AC-MTDC system of Table 4.7 but the VSC connected to AC bus 270 employs voltage margin control. The droop control gains of the VSCs are identical to that of Table 4.7, except VSC 2, which operates in voltage margin control. The droop gain for voltage margin control is set to a value of 1000. For voltage margin control characteristic, the maximum and minimum DC powers are set to 1.0 and -1.0 p.u, respectively. The power flow solution is shown in rows 5-13 of Table 4.8.

The convergence characteristics of Table 4.7 and 4.8 are shown in Figures 4.22 and 4.23, respectively. From Figures 4.22 and 4.23, it is observed that the proposed algorithm demonstrates excellent convergence characteristics, converging in six iterations. The bus voltage profiles for the studies of Table 4.7 and 4.8 are shown in Figures 4.24 and 4.25, respectively. From Figures 4.24 and 4.25, it can be observed that the bus voltage profiles do not change much except at the AC terminal buses to which the converters are connected.



Table 4.8

Study of IEEE 300 bus system with five terminal VSC HVDC network  
incorporating non-linear DC voltage droop characteristics (Voltage Margin)

Specified Quantities		Power flow solution
Base case power flow (NI=6 and CT=0.56) $V_{266} = 1.011 \angle -11.24$ ; $V_{270} = 1.011 \angle -11.32$ ; $V_{271} = 0.998 \angle -17.67$ ; $V_{272} = 0.981 \angle -19.46$ ; $V_{273} = 1.006 \angle -17.47$ ;		
DC power-flow to calculate DC reference values		
Specified Quantities		Power flow solution
$V_{DCav}^* = 3.03$ ; $P_{DC2}^* = -0.5$ ; $P_{DC3}^* = -0.45$ ; $P_{DC4}^* = -0.35$ ; $P_{DC5}^* = -0.3$ ;		$V_{DC1}^* = 3.0311$ ; $V_{DC2}^* = 3.0297$ ; $V_{DC}^* = 3.0297$ ; $V_{DC}^* = 3.0298$ ; $V_{DC5}^* = 3.0298$ ; $P_{DC1}^* = 1.6007$ ; $I_{DC3}^* = -0.1485$ ; $I_{DC4}^* = -0.1155$ ; $I_{DC5}^* = -0.0990$ ; NI=4; CT=0.02;
AC-MTDC power-flow with linear voltage droop and nonlinear voltage margin (VSCs connected to AC buses 266, 270, 271, 272 and 273)		
Specified Quantities		Power flow solution
Control parameters		DC terminal buses
$V_{DCmax} = 3.01$ ; $V_{DChigh}^* = 3$ ; $V_{DClow}^* = 2.99$ ; $V_{DCmin} = 2.98$ ; $R_1 = 20$ ; $R_2 = 1000$ ; $R_3 = 10$ ; $R_4 = 10$ ; $R_5 = 10$ ;		$V_{DC1} = 3.0265$ ; $V_{DC2} = 3.0248$ ; $V_{DC} = 3.0252$ ; $V_{DC4} = 3.0253$ ; $V_{DC5} = 3.0253$ ;
Converter	Control Mode	VSCs
1	V-P droop	
2	Voltage Margin	
3	V-I droop	$\theta_{sh1} = -20.7095$ ; $\theta_{sh2} = -6.1022$ ; $\theta_{sh3} = -4.1554$ ; $\theta_{sh4} = -4.3862$ ; $\theta_{sh5} = -11.2625$ ; $m_1 = 0.9934$ ; $m_2 = 0.9669$ ; $m_3 = 1.0072$ ; $m_4 = 1.0052$ ; $m_5 = 0.9648$ ;
$V_{266} = 1.02$ ; $Q_{sh2} = 0.08$ ; $Q_{sh3} = 0.06$ ; $Q_{sh4} = 0.04$ ; $Q_{sh5} = 0.05$ ;		AC terminal buses $\theta_{266} = -11.5486$ ; $V_{270} = 1.0207 \angle -11.4324$ ; $V_{271} = 1.0710 \angle -5.6475$ ; $V_{272} = 1.0711 \angle -5.3878$ ; $V_{273} = 1.0268 \angle -12.0814$ ;
		DC Power $P_{DC1} = 1.6912$ ; $P_{DC} = -1.0000$ ; $P_{DC3} = -0.3133$ ; $P_{DC4} = -0.2135$ ; $P_{DC5} = -0.1635$ ;
		Converter loss $P_{loss1} = 2.88$ ; $P_{loss2} = 1.79$ ; $P_{loss3} = 1.22$ ; $P_{loss4} = 1.17$ ; $P_{loss5} = 1.16$ ;
NI=6; CT=1.54;		

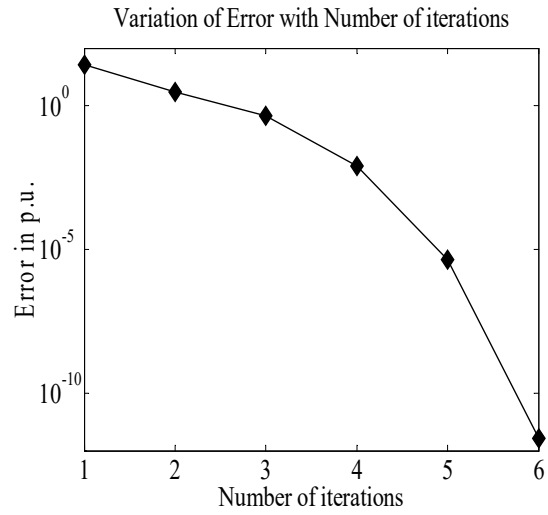


Fig. 4.22: Convergence characteristic for the study of Table 4.7

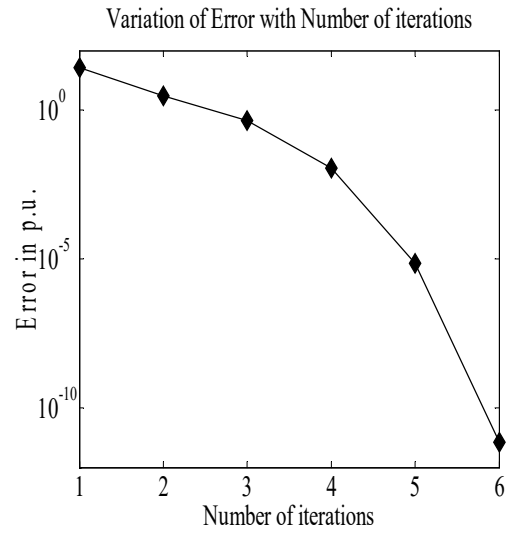


Fig. 4.23: Convergence characteristic for the study of Table 4.8

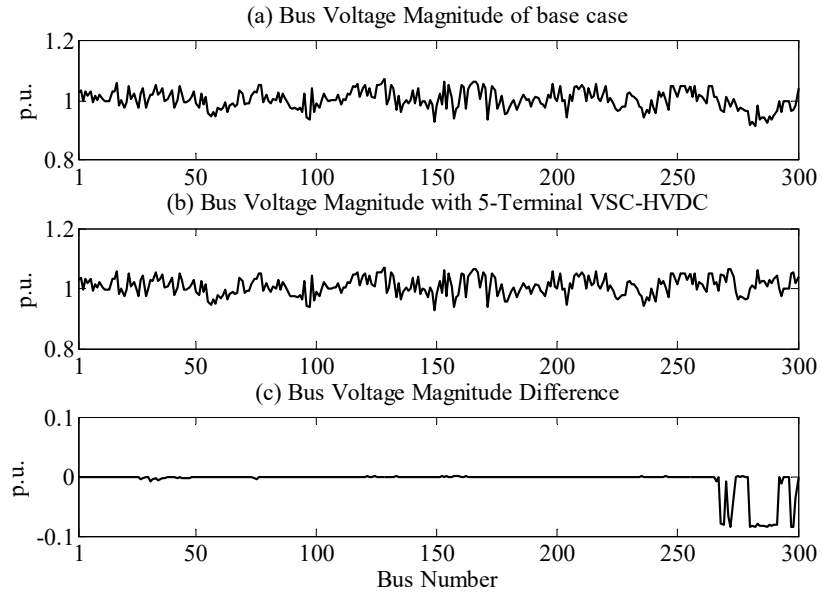


Fig. 4.24: Bus voltage profile for the study of Table 4.7

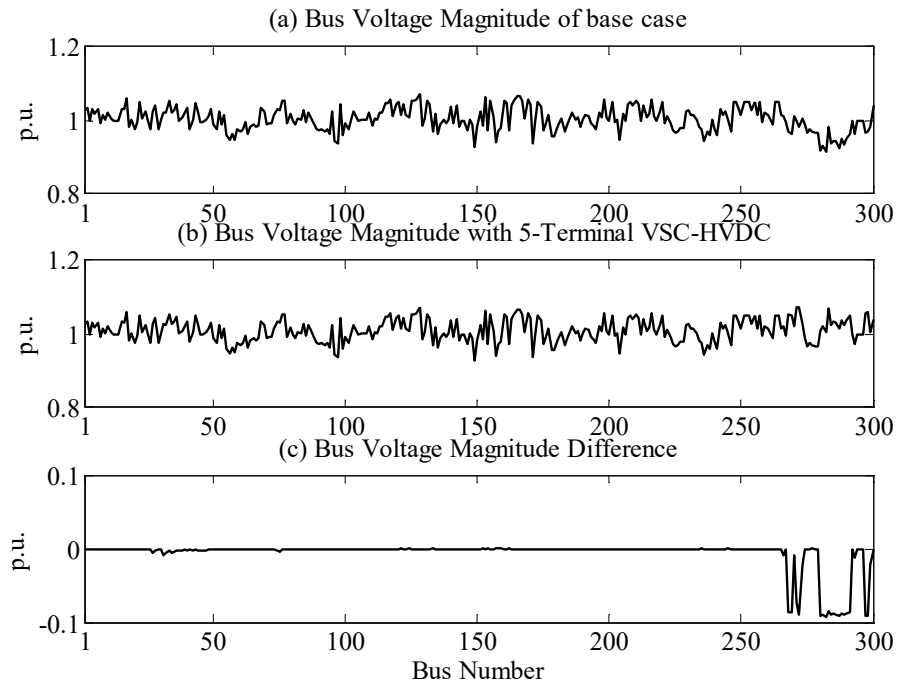


Fig. 4.25: Bus voltage profile for the study of Table 4.8

## 4.7 Conclusions

In this chapter, a generalized approach for the development of Newton power-flow models of hybrid AC-MTDC systems employing DC voltage droop control is presented. In the proposed model, the modulation indices of the VSCs are obtained directly from the power-flow solution. Diverse MTDC grid control techniques including linear and nonlinear DC voltage droop control have been employed. It is observed that unlike droop model 'A', model 'B' facilitates the specification of both line end active and reactive power-flows. The model displays excellent convergence characteristics, independent of the DC grid topology and the MTDC grid control technique employed. This validates the model.

# Chapter 5

## Newton Power Flow Modeling of Voltage Source Converter (VSC) Based Hybrid AC-DC Systems Incorporated with Interline DC Power Flow Controller (IDCPFC)

### 5.1 Introduction

One of the main challenges in VSC based hybrid AC-DC systems is the management of DC power flow within the DC grids. Although the VSCs control the power injections into a DC grid, the power flows within the DC grid depend upon the resistances of the DC Links or cables. In this respect, DC power-flow control devices [39]-[44] have been conceptualized and developed, similar to Flexible AC Transmission Systems (FACTS) Controllers developed for AC grids. The Interline DC Power Flow Controller (IDCPFC) reported in [43], [44] is a DC power-flow controller which has been implemented for the power-flow management of MTDC grids. It is similar to the Interline Power Flow Controller (IPFC) [45]-[47], which is a FACTS Controller [13].

Now, for planning, operation and control of VSC based hybrid AC-DC systems, their power-flow models are required. [76]-[98] present some comprehensive Newton power-flow models of VSC based hybrid AC-DC systems. However, none of these research works address the power-flow modeling of hybrid AC-DC systems incorporating the IDCPFC.

This chapter presents the Newton power-flow modeling of VSC based hybrid AC-DC systems employing IDCPFCs for power-flow management. Similar to

Chapters 3 and 4, the VSC modulation index ‘m’ is considered as an unknown and can be obtained directly, from the power-flow solution. VSC losses are included in this model.

## 5.2 Modeling of AC-MVDC systems incorporating IDCPFCs

The basic assumptions adopted for this chapter are similar to those available in section 3.2 (Chapter-3) of this thesis. Fig. 5.1 shows a ‘n’ bus AC power system network integrated with a ‘q’ terminal VSC-MTDC grid. ‘q’ VSCs are used for integrating the VSC-MTDC grid with the AC network at AC buses ‘i’, ‘(i+1)’, and so on, up to bus ‘(i+q-1)’, through their respective converter transformers. Fig. 5.1 also shows an IDCPFC incorporated within the MTDC grid for its power-flow management. The IDCPFC comprises ‘z’ ( $z \leq q-1$ ) variable DC voltage sources interconnected between DC bus ‘1’ and ‘z’ other DC buses numbered as ‘2’, ‘3’ and so on, upto ‘(z+1)’. The equivalent circuit of Fig. 5.1 is shown in Fig. 5.2.

In Fig. 5.2, the ‘q’ VSCs are represented by ‘q’ fundamental frequency, positive sequence voltage sources. The  $a^{\text{th}}$  ( $1 \leq a \leq q$ ) VSC is connected to AC terminal bus ‘(i+a-1)’ whose voltage is represented by the phasor  $\mathbf{V}_{i+a-1} = V_{i+a-1} \angle \theta_{i+a-1}$ .

From Fig. 5.2, the current in the link (not shown) connecting the  $a^{\text{th}}$  VSC and its AC terminal bus is

$$\mathbf{I}_{\text{sha}} = \mathbf{y}_{\text{sha}}(\mathbf{V}_{\text{sha}} - \mathbf{V}_{i+a-1}) \quad (5.1)$$

where  $\mathbf{V}_{\text{sha}} = V_{\text{sha}} \angle \theta_{\text{sha}} = m_a c V_{\text{DCa}} \angle \theta_{\text{sha}}$ ,  $\mathbf{y}_{\text{sha}} = 1/\mathbf{Z}_{\text{sha}}$ ,  $\mathbf{Z}_{\text{sha}} = R_{\text{sha}} + jX_{\text{sha}}$ ,  $R_{\text{sha}}$  and  $X_{\text{sha}}$  are the resistance and the leakage reactance of the  $a^{\text{th}}$  converter transformer,

respectively, ' $m_a$ ' is the VSC modulation index and the constant ' $c$ ' is representative of the VSC architecture [11].

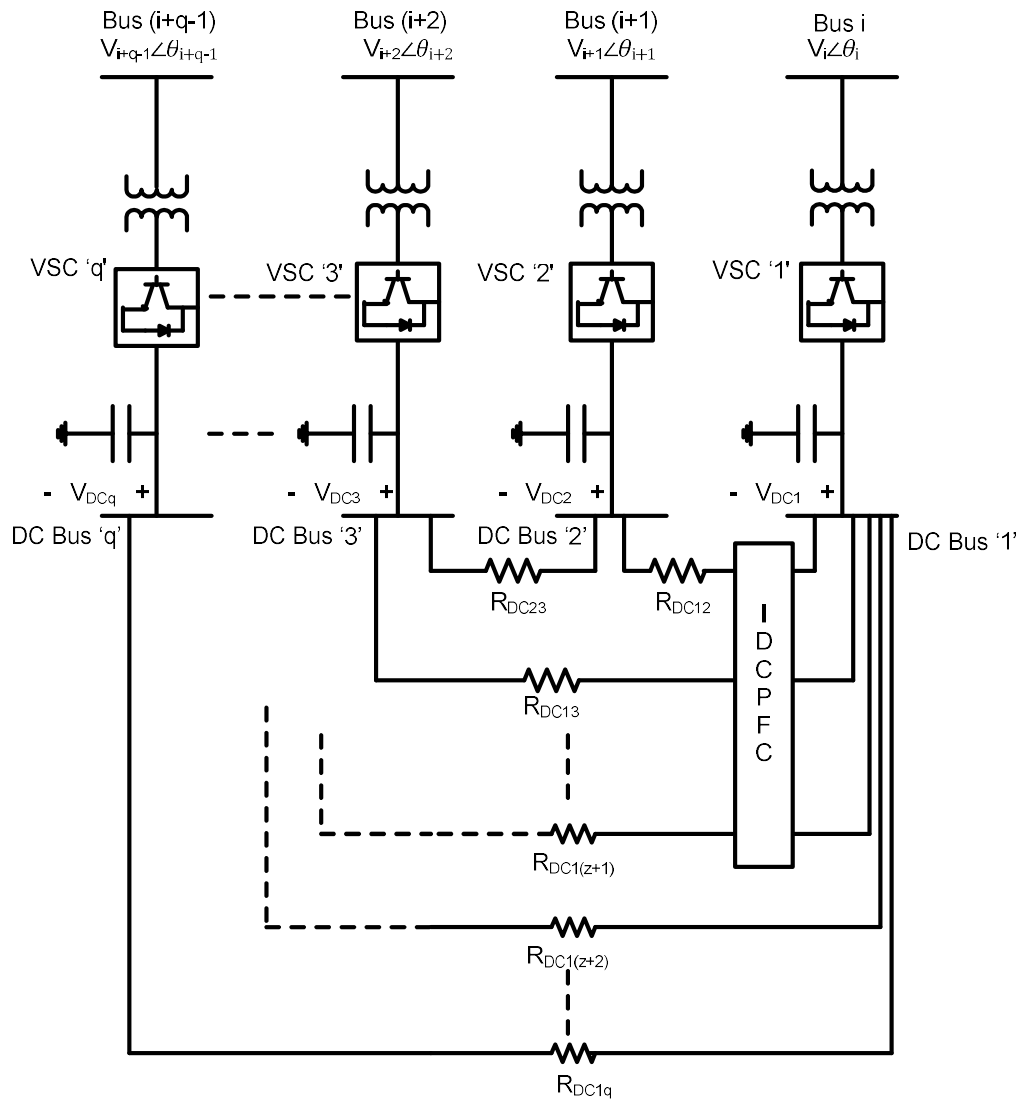


Fig. 5.1: Schematic diagram of an AC-MTDC system incorporating an IDC-PFC

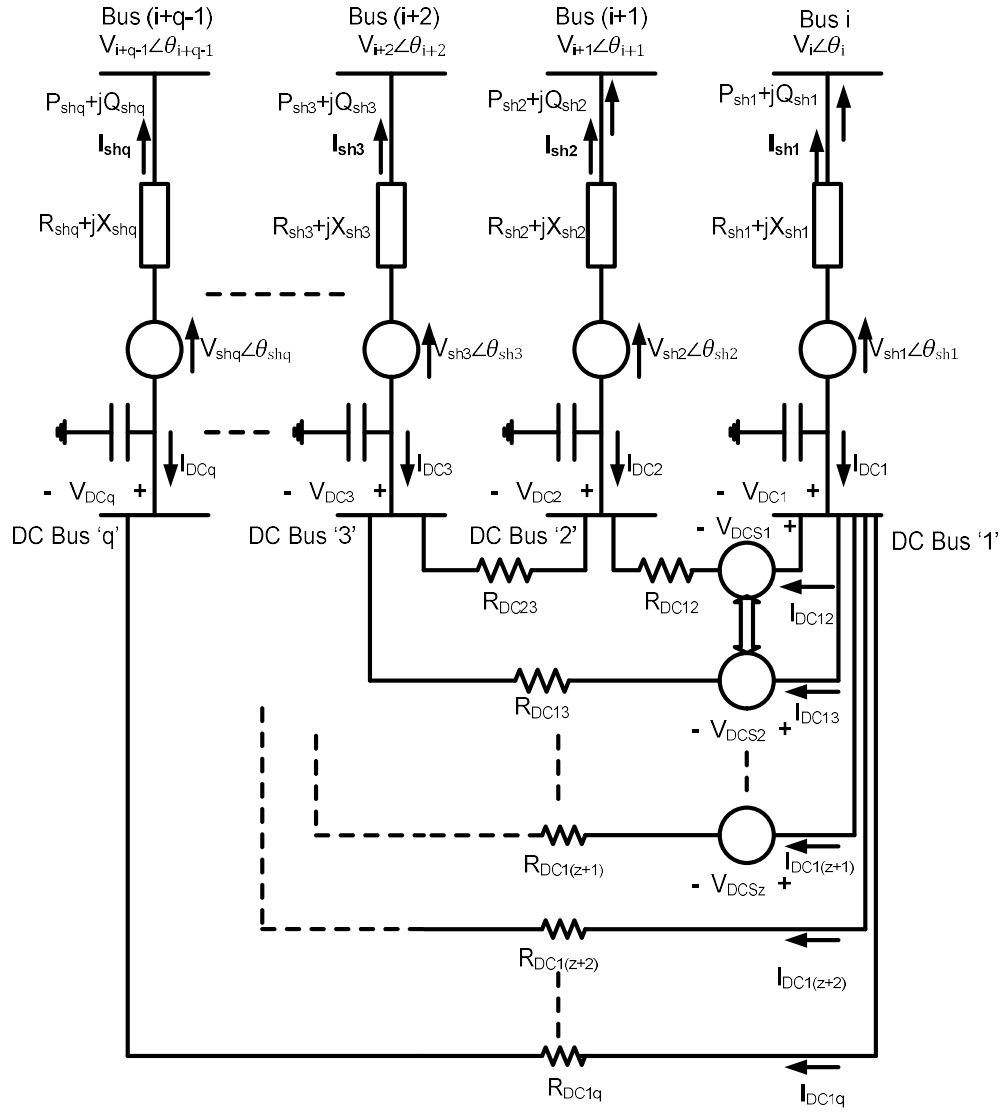


Fig. 5.2: Equivalent circuit of AC-MTDC system incorporating an IDCPFCS

Also, as already detailed in Chapter 3, from Figures 5.1 and 5.2, the net current injection at the AC bus '(i+a-1)' connected to the a<sup>th</sup> ( $1 \leq a \leq p$ ) converter can be written as

$$I_{i+a-1} = \sum_{k=1}^n Y_{(i+a-1)k} V_k - y_{sha} V_{sha} \quad (5.2)$$



where  $Y_{(i+a-1)(i+a-1)} = Y_{(i+a-1)(i+a-1)}^{\text{old}} + y_{\text{sha}}$  and

$Y_{(i+a-1)(i+a-1)}^{\text{old}} = y_{(i+a-1)0} + \sum_{k=1, k \neq i+a-1}^n Y_{(i+a-1)k}$  are the values of self admittances of bus '(i+a-1)' with the  $a^{\text{th}}$  VSC connected and the original 'n' bus AC system without any VSC, respectively. Similarly, ' $y_{(i+a-1)0}$ ' accounts for the shunt capacitances of all the transmission lines connected to bus '(i+a-1)'.

Now, in Fig. 5.2, the IDCPFC comprises 'z' ( $z \leq q-1$ ) variable DC voltage sources and it is assumed, without any loss of generality, that the  $w^{\text{th}}$  variable DC voltage source ' $V_{\text{DCsw}}$ ' ( $1 \leq w \leq z$ ) is connected in series with the link interconnecting the DC buses '1' and '(1+w)' ( $1 \leq w \leq z, \forall z \leq q-1$ ). Then, from Fig. 5.2, the current and power in this link (connected between DC buses '1' and 'w+1') is

$$I_{\text{DC1}(w+1)} = Y_{\text{DC1}(w+1)} [V_{\text{DCw+1}} - V_{\text{DC}} + V_{\text{DCsw}}] \quad (5.3)$$

$$P_{\text{DC1}(w+1)} = V_{\text{DC}} I_{\text{DC1}(w+1)} \quad (5.4)$$

Further, with the IDCPFC, the net DC current injection at the 1<sup>st</sup> DC bus can be written as

$$I_{\text{DC1}} = \sum_{u=1, u \neq 1}^{z+1} I_{\text{DC1u}} + \sum_{u=z+2, u \neq 1}^q I_{\text{DC1u}} \quad (5.5)$$

Writing  $I_{\text{DC1u}}$  in the form of eqn. (5.3) and substituting in eqn. (5.5), we get

$$I_{\text{DC1}} = \sum_{u=1}^q Y_{\text{DC1u}} V_{\text{DCu}} + \sum_{u=1, u \neq 1}^{z+1} Y_{\text{DC1u}} V_{\text{DCs}(u-1)} \quad (5.6)$$

In a similar manner, the net DC current injections at the other DC buses can also be written very easily. It can be shown that the net DC current injection at any arbitrary DC node 'u' ( $1 \leq u \leq q$ ) can be generalized as

$$\begin{aligned}
I_{DCu} &= \sum_{v=1}^q Y_{DCuv} V_{DCv} + \sum_{v=1, v \neq 1}^{z+1} Y_{DCuv} V_{DCs(v-1)} && \text{if } u = 1 \\
&= \sum_{v=1}^q Y_{DCuv} V_{DCv} - Y_{DCu1} V_{DCs(u-1)} && \text{if } 2 \leq u \leq z + 1 \\
&= \sum_{v=1}^q Y_{DCuv} V_{DCv} && \text{if } z + 2 \leq u \leq q
\end{aligned} \tag{5.7}$$

### 5.3 Power Flow Equations of hybrid AC-MVDC systems incorporating IDCPFC

From Fig. 5.2, at the AC bus ‘(i+a-1)’ pertaining to the a<sup>th</sup> VSC, it can be shown that the net active and reactive power injections are

$$P_{i+a-1} = \sum_{k=1}^n V_{i+a-1} V_k Y_{(i+a-1)k} \cos[\theta_{i+a-1} - \theta_k - \phi_{(i+a-1)k}] - m_a c V_{DCa} V_{i+a-1} Y_{sha} \cos(\theta_{i+a-1} - \theta_{sha} - \phi_{sha}) \tag{5.8}$$

$$Q_{i+a-1} = \sum_{k=1}^n V_{i+a-1} V_k Y_{(i+a-1)k} \sin[\theta_{i+a-1} - \theta_k - \phi_{(i+a-1)k}] - m_a c V_{DCa} V_{i+a-1} Y_{sha} \sin(\theta_{i+a-1} - \theta_{sha} - \phi_{sha}) \tag{5.9}$$

where ‘ $\phi_{sha}$ ’ is the phase angle of  $y_{sha}$ .

In addition, from Fig. 5.2, it can be shown that the active and reactive power flows at the terminal end of the link interconnecting the a<sup>th</sup> VSC to the AC bus ‘(i+a-1)’ are

$$P_{sha} = m_a c V_{DCa} V_{i+a-1} Y_{sha} \cos(\theta_{i+a-1} - \theta_{sha} - \phi_{sha}) - V_{i+a-1}^2 Y_{sha} \cos \phi_{sha} \tag{5.10}$$

$$Q_{sha} = m_a c V_{DCa} V_{i+a-1} Y_{sha} \sin(\theta_{i+a-1} - \theta_{sha} - \phi_{sha}) + V_{i+a-1}^2 Y_{sha} \sin \phi_{sha} \tag{5.11}$$

Now, if all the VSCs as well as the IDCPFC are lossless, the AC-DC power balance equation for the a<sup>th</sup> ( $1 \leq a \leq q$ ) VSC can be written using eqn. (5.7) as

$$\begin{aligned}
& (m_a c V_{DCa})^2 y_{sha} \cos \phi_{sha} - m_a c V_{DCa} V_{i+a-1} y_{sha} \cos(\theta_{sha} - \theta_{i+a-1} - \phi_{sha}) \\
&= - \sum_{v=1}^q V_{DCa} V_{DCv} Y_{DCav} \quad \text{if } z+2 \leq a \leq q \\
&= - \sum_{v=1}^q V_{DCa} V_{DCv} Y_{DCav} + V_{DCa} V_{DCs(a-1)} Y_{DCa1} \quad \text{if } 2 \leq a \leq z+1 \\
&= - \sum_{v=1}^q V_{DCa} V_{DCv} Y_{DCav} - \sum_{v=1, v \neq 1}^{z+1} V_{DCa} V_{DCs(v-1)} Y_{DCav} \quad \text{if } a = 1
\end{aligned}$$

If VSC losses are considered, the above equation for the  $a^{\text{th}}$  ( $1 \leq a \leq q$ ) VSC becomes

$$\begin{aligned}
& (m_a c V_{DCa})^2 y_{sha} \cos \phi_{sha} - m_a c V_{DCa} V_{i+a-1} y_{sha} \cos(\theta_{sha} - \theta_{i+a-1} - \phi_{sha}) \\
&= - \sum_{v=1}^q V_{DCa} V_{DCv} Y_{DCav} - P_{lossa} \quad \text{if } (z+2) \leq a \leq q \\
&= - \sum_{v=1}^q V_{DCa} V_{DCv} Y_{DCav} + V_{DCa} V_{DCs(a-1)} Y_{DCa1} - P_{lossa} \quad \text{if } 2 \leq a \leq z+1 \\
&= - \sum_{v=1}^q V_{DCa} V_{DCv} Y_{DCav} - \sum_{v=1, v \neq 1}^{z+1} V_{DCa} V_{DCs(v-1)} Y_{DCav} - P_{lossa} \quad \text{if } a = 1
\end{aligned}$$

or,  $f_{1a} = 0 \quad \forall a, 1 \leq a \leq q$  (5.12)

where,  $P_{lossa}$  represents the losses [18], [92] of the  $a^{\text{th}}$  VSC as already detailed in Chapter 3 {eqn. (3.10)}.

eqn. (5.12) represents ‘q’ independent equations. The detailed derivation of eqn. (5.12) is shown in Appendix A.

Now, in the AC-MTDC system (Fig. 5.1) with ‘q’ VSCs, if it is assumed that the  $r^{\text{th}}$  ( $1 \leq r \leq q$ ) VSC is used for voltage control of its corresponding AC bus, we have

$$V_{i+a-1}^{\text{sp}} - V_{i+a-1}^{\text{cal}} = 0 \quad \forall a, 1 \leq a \leq q, a = r \quad (5.13)$$

Also, not more than ‘(q-1)’ line active and reactive power flows {eqn. (5.10) and (5.11)} can be specified, which give us ‘(2q-2)’ independent equations given as

$$P_{sha}^{sp} - P_{sha}^{cal} = 0 \quad (5.14)$$

$$Q_{sha}^{sp} - Q_{sha}^{cal} = 0 \quad (5.15)$$

$\forall a, 1 \leq a \leq q, a \neq r.$

Instead of PQ control mode, if a VSC operates in the PV one, eqn. (5.15) changes to

$$V_{i+a-1}^{sp} - V_{i+a-1}^{cal} = 0 \quad \forall a, 1 \leq a \leq q, a \neq r \quad (5.16)$$

Further, the net reactive power injection at AC bus ‘(i+r-1)’ can be specified as its voltage is controlled by the r<sup>th</sup> VSC. Thus, we get

$$Q_{i+a-1}^{sp} - Q_{i+a-1}^{cal} = 0 \quad \forall a, 1 \leq a \leq q, a = r \quad (5.17)$$

In eqns. (5.13)-(5.17),  $V_{i+a-1}^{sp}$ ,  $Q_{i+a-1}^{sp}$ ,  $P_{sha}^{sp}$  and  $Q_{sha}^{sp}$  are specified values while  $V_{i+a-1}^{cal}$ ,  $Q_{i+a-1}^{cal}$ ,  $P_{sha}^{cal}$  and  $Q_{sha}^{cal}$  are calculated values {using eqns. (5.9), (5.10) and (5.11)}.

Now, in the DC network as shown in Fig. 5.2, the IDCPFC is represented by ‘z’ variable DC voltage sources (incorporated in series with ‘z’ DC links). Hence, the inclusion of the IDCPFC in the hybrid AC-MTDC system introduces ‘z’ additional unknowns. To solve them would require ‘z’ specified or known quantities. It is important to note that if the IDCPFC is considered lossless, from Fig. 5.2, the power delivered by the IDCPFC is

$$P_{IDCPFC} = [V_{DCs1}\{-I_{DC12}\} + V_{DCs2}\{-I_{DC13}\} + \dots + V_{DCsz}\{-I_{DC1(z+1)}\}] = 0 \quad (5.18)$$

eqn. (5.18) represents a single, independent equation. Thus, additional ‘(z-1)’ equations are required for a complete solution of the IDCPFC variables, which is similar to the degree of freedom of an IPFC [45]-[47]. These ‘(z-1)’ equations are obtained from the control objectives of the IDCPFC. [43] has implemented DC link power-flow control with an IDCPFC. In this chapter, both current and power-flow controls of the DC link(s) have been considered.

With DC link current control, the line currents in all the ‘z’ DC links (containing the ‘z’ variable DC voltage sources of the IDCPFC) except one, can be controlled. If it is presumed that the line current in the DC link containing the  $y^{\text{th}}$  ( $1 \leq y \leq z$ ) variable DC voltage source ‘ $V_{DCsy}$ ’ is not being controlled by the IDCPFC, the control equations for the rest of the ‘(z-1)’ DC links are

$$I_{DC1(w+1)}^{\text{sp}} - I_{DC1(w+1)}^{\text{cal}} = 0 \quad (5.19)$$

In a similar manner, the control equations for the power-flow in the ‘(z-1)’ DC links are

$$P_{DC1(w+1)}^{\text{sp}} - P_{DC (w+1)}^{\text{cal}} = 0 \quad (5.20)$$

eqns. (5.19) and (5.20) can be generalized as

$$f_{2w} = 0 \quad \forall \quad w, \quad 1 \leq w \leq z - 1, \quad w \neq y, \quad z \leq q - 1 \quad (5.21)$$

It may be noted that if the IDCPFC employs current control for some of the DC links and power-flow control for the rest, eqn. (5.21) would comprise both eqn. (5.19) and (5.20).

In the above equations,  $I_{DC (w+1)}^{\text{sp}}$  and  $P_{DC (w+1)}^{\text{sp}}$  are the specified value of the current and power-flow in the DC link between the DC buses ‘1’ and ‘(1+w)’ (and containing

the variable DC voltage source ‘ $V_{DCsw}$ ’), respectively, while  $I_{DC1(w+1)}^{cal}$  and  $P_{DC(w+1)}^{cal}$  are their calculated value obtained using eqn. (5.3) and (5.4), respectively.

## 5.4 Implementation in Newton Power Flow Analysis

If it is assumed that there are ‘ $g$ ’ generators connected at the first ‘ $g$ ’ buses of the ‘ $n$ ’ bus AC system with bus 1 being the slack bus, then, for the AC-MTDC system incorporating an IDCPFC with ‘ $z$ ’ variable DC voltage sources and following DC slack bus control, the unified AC-MTDC power-flow problem is of the form

Compute:  $\theta, V, X$

Given:  $P, Q, R$

with

$$\theta = [\theta_2 \dots \theta_n]^T, V = [V_{g+1} \dots V_n]^T, \theta_{sh} = [\theta_{sh1} \dots \theta_{shq}]^T, m = [m_1 \dots m_q]^T,$$

$$V_{DC} = [V_{DC2} \dots V_{DCq}]^T$$

$$V_{DCs} = [V_{DCs1} \dots V_{DCsz}]^T \text{ and } X = [\theta_{sh}^T \ m^T \ V_{DC}^T \ V_{DCs}^T]^T$$

$$P = [P_2 \dots P_n]^T, Q = [Q_{g+1} \dots Q_n]^T, P_{sh} = [P_{sh2} \dots P_{shq}], Q_{sh} = [Q_{sh} \dots Q_{shq}]$$

$$f_1 = [f_{11} \dots f_{1q}], f_2 = [f_{21} \dots f_{2(z-1)}]$$

$$\text{and } R = [P_{sh} \ Q_{sh} \ V_{i+r-1} \ P_{IDCPFC} \ f_1 \ f_2]^T$$

It is presumed that in this model, DC slack bus control (master slave control) is adopted ( $V_{DC}$  is specified). Also, the master VSC ‘ $r$ ’ controls the voltage magnitude

of the AC bus ‘(i+r-1)’ unlike the other ‘(q-1)’ slave VSCs, which control the line active as well as reactive power flows.

The Newton power flow equation can be written as

$$\mathbf{J}[\Delta\boldsymbol{\theta}^T \Delta\mathbf{V}^T \Delta\boldsymbol{\theta}_{sh}^T \Delta\mathbf{m}^T \Delta\mathbf{V}_{DC}^T \Delta\mathbf{V}_{DCs}^T]^T = [\Delta\mathbf{P}^T \Delta\mathbf{Q}^T \Delta\mathbf{R}^T]^T \quad (5.22)$$

where  $\mathbf{J}$  is the power-flow Jacobian.

It may be noted that instead of the DC slack bus voltage ‘ $V_{DC1}$ ’, if the average voltage of all the DC terminals ‘ $V_{DCav}$ ’ is specified, the following modifications are required.

$$\mathbf{V}_{DC} = [V_{DC} \dots V_{DCq}]^T, \mathbf{R} = [\mathbf{P}_{sh} \mathbf{Q}_{sh} V_{i+r-1} V_{DCav} P_{IDCPF} \mathbf{f}_1 \mathbf{f}_2]^T.$$

The individual elements of  $\mathbf{J}$  have to be appropriately modified for the above case.

If ‘x’ IDCPFcs are present, ‘ $\mathbf{V}_{DCs}$ ’ gets enlarged (with ‘xz’ elements) and ‘ $P_{IDCPF}$ ’ is replaced by a vector ‘ $\mathbf{P}_{IDCPF}$ ’ having ‘x’ elements, each governed by an equation similar to eqn. (5.18). Also, the individual elements of  $\mathbf{J}$  are appropriately modified.

Fig. 5.3 depicts the flow chart of the proposed approach with IDCPF.

## 5.5 Case Studies and Results

For validation of the above model, a large number of studies were carried out by employing diverse DC voltage control strategies on MTDC grids integrated with the IEEE 300-bus test system [104]. For all the VSC coupling transformers,  $R_{sha} = 0.001$  p.u. and  $X_{sha} = 0.1$  p.u. ( $\forall a, 1 \leq a \leq q$ ). For interconnections between DC terminals,  $R_{DCuv} = 0.01$  p.u. ( $\forall u, v, 1 \leq u \leq q, 1 \leq v \leq q, u \neq v$ ), throughout

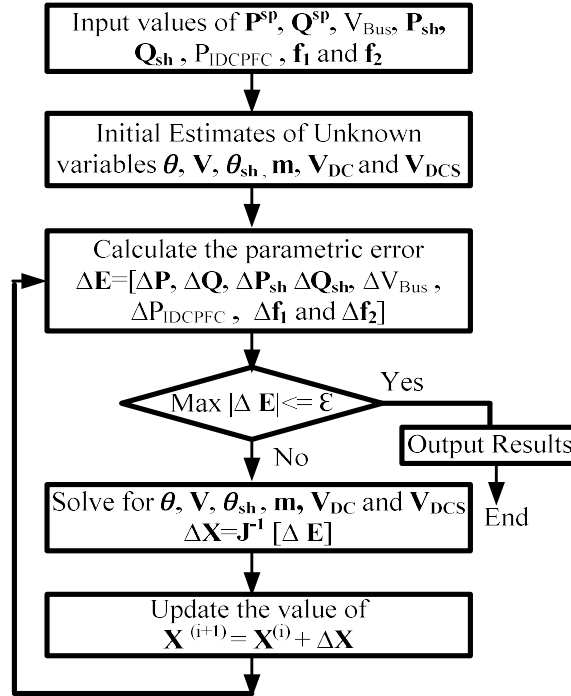


Fig. 5.3: Flow chart of the proposed approach with IDCPFC

the chapter [83]. The converter loss constants ‘a<sub>1</sub>’, ‘b<sub>1</sub>’ and ‘c<sub>1</sub>’ are chosen to be 0.011, 0.003 and 0.0043, respectively [18], [92], [95]. The initial values of all the variable DC voltage sources ( $V_{DCsy} \forall y, 1 \leq y \leq z$ ) were chosen as 0.001 p.u. In all occurrences, a termination error tolerance of  $10^{-10}$  p.u. was selected. ‘NI’ and ‘CT’ denote the number of iterations and the computational time in seconds, pertaining to a 1.99 GHz Dell PC. In all the results given in Tables 5.1 - 5.6, the values of bus voltage magnitudes, current magnitudes, active and reactive powers and droop control gains are denoted in p.u. while phase angles of voltage phasors are denoted in degrees.

## 5.5.1 Study of three terminal VSC-HVDC network incorporating IDCPFC

### Case I: DC link current control using IDCPFC



In this study, at first, a three terminal VSC-MTDC grid is integrated with the IEEE-300 bus test system at buses 266, 270 and 271 and the AC-MTDC power-flow is carried out. For this analysis, DC slack bus control is assumed ( $V_{DC1}$  is specified). The power-flow solution is shown in the first row of Table 5.1, with the line current in the DC link between DC buses 1 and 2 computed to be 0.093 p.u. Subsequently, a IDCPFC (having two variable DC voltage sources) is incorporated in the 3-terminal VSC-MTDC grid integrated with the IEEE 300-bus test network and the AC-MTDC power-flow is again carried out. The IDCPFC is used to control the line current in the DC link between DC buses 1 and 2 to a specified value of 0.12 p.u. (the DC link current without any IDCPFC is 0.093 p.u.). The specified quantities for this study are shown in the rows 3-11 and columns 1-2 of Table 5.1. The power flow solution with the IDCPFC is shown in the rows 3-11 and columns 3-4 of Table 5.1.

Table 5.1

Study of IEEE 300 bus system with three terminal VSC HVDC network incorporating IDCPFC in DC current control mode

AC-MTDC power-flow without any IDCPFC (VSCs connected to AC buses 266, 270 and 271)			
$P_{sh2} = 0.3; Q_{sh2} = 0.1; P_{sh3} = 0.2; Q_{sh3} = 0.09; V_{DC1} = 3.0; V_{DC2} = 2.9991;$ $V_{DC3} = 2.9992; I_{DC12} = 0.093; NI=6; CT=1.45;$			
AC-MTDC power-flow with IDCPFC			
Given quantities		Solution	
		AC buses	VSCs
$V_{266}$	1.02	$V_{270} = 1.0202;$ $V_{271} = 1.0619;$ $\theta_{266} = -11.3851;$ $\theta_{270} = -11.4005;$ $\theta_{271} = -12.6900;$	$\theta_{sh1} = -14.2881; \theta_{sh2} = -9.7713;$ $\theta_{sh3} = -11.6866; V_{DC2} = 2.9991;$ $V_{DC3} = 2.9989; m_1 = 0.9894;$ $m_2 = 0.9721; m_3 = 1.0099;$
$V_{DC1}$	3.0		
$P_{sh2}$	0.3		
$Q_{sh2}$	0.1		
$P_{sh3}$	0.2		
$Q_{sh3}$	0.09		
IDCPFC		IDCPFC	
$I_{DC12}$	0.12	DC power $P_{DC1} = 0.5245;$ $P_{DC2} = -0.3124;$ $P_{DC3} = -0.2118;$	Converter Loss (%) $P_{loss1} = 1.44;$ $P_{loss2} = 1.23;$ $P_{loss3} = 1.18;$
$NI=6; CT=1.52;$			

Subsequently, a study is conducted on the same AC-MTDC network but with the VSCs now connected to AC buses 268, 272 and 273. The AC-MTDC power-flow solution without any IDCPF is shown in the first row of Table 5.2, with the current in the DC link between the DC buses 1 and 3 computed to be 0.1098 p.u. Subsequently, a IDCPF (having two variable DC voltage sources) is again incorporated in the 3-terminal VSC-MTDC grid integrated with the IEEE 300-bus test network and the AC-MTDC power-flow is again carried out. The IDCPF maintains the DC current between DC buses 1 and 3 to a value of 0.12 p.u (the DC link current without any IDCPF is 0.1098 p.u.). The specified quantities for this study are shown in the rows 3-11 and columns 1-2 of Table 5.2. The AC-MTDC power flow solution with the IDCPF is shown in the rows 3-11 and columns 3-4 of Table 5.2.

Table 5.2

Study of IEEE 300 bus system with three terminal VSC HVDC network incorporating IDCPF in DC current control mode

AC-MTDC power-flow without any IDCPF (VSCs connected to AC buses 268, 272 and 273)		AC-MTDC power-flow with IDCPF	
$P_{sh2} = 0.35; Q_{sh2} = 0.1; P_{sh3} = 0.3; Q_{sh3} = 0.1; V_{DC1} = 3.0; V_{DC2} = 2.9988; V_{268} = 0.98;$ $V_{DC3} = 2.9989; I_{DC13} = 0.1098; NI=6; CT=1.45;$		Solution	
Given quantities		AC buses	VSCs
$V_{268}$	0.98	$V_{272} = 1.0086;$ $V_{273} = 1.0366;$ $\theta_{268} = -39.1739;$ $\theta_{272} = -31.2289;$ $\theta_{273} = -6.7581;$	$\theta_{sh1} = -43.2336; \theta_{sh2} = -29.2839;$ $\theta_{sh} = -5.1793; V_{DC} = 2.9988;$ $V_{DC3} = 2.9989; m_1 = 0.9418;$ $m_2 = 0.9615; m_3 = 0.9874;$
$V_{DC1}$	3.0		
$P_{sh2}$	0.35		
$Q_{sh2}$	0.1		
$P_{sh3}$	0.3		
$Q_{sh3}$	0.1		
IDCPF			IDCPF
$I_{DC13}$	0.12	$V_{DCs1} = 0.00016; V_{DCs2} = -0.00014;$ $I_{DC12} = 0.0815; I_{DC13} = 0.0933; P_{DC12} = 0.2444;$ DC power $P_{DC1} = 0.6754;$ $P_{DC2} = -0.3628;$ $P_{DC3} = -0.3124;$ Converter Loss (%) $P_{loss} = 1.54;$ $P_{loss2} = 1.26;$ $P_{loss3} = 1.23;$	
		NI=6; CT=1.51;	

The convergence characteristics corresponding to the base case, study of row 1 of Table 5.1 (without IDCPFC) and rows 3-5 of Table 5.1 (with IDCPFC) are shown in Figures 5.4, 5.5 and 5.6 respectively.

Similarly, the convergence characteristic plots for the study of row 1 of Table 5.2 (without IDCPFC) and rows 3-5 of Table 5.2 (with IDCPFC) are shown in Figures 5.7 and 5.8 respectively. From Figures 5.4-5.8, it is observed that the AC-MTDC power-flow solutions with the IDCPFC demonstrate quadratic convergence characteristics, similar to the base case power-flow. Also, the convergence pattern is independent of the MTDC grid location and the IDCPFC operating point specifications.

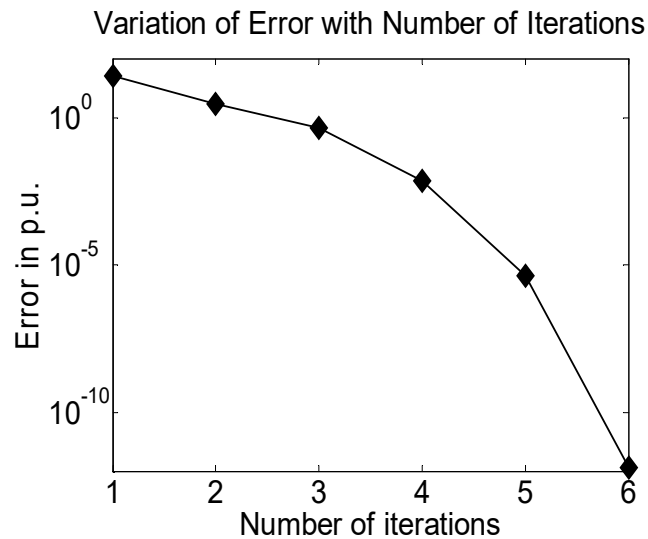


Fig. 5.4: Convergence characteristic for the base case power flow in IEEE-300 bus system

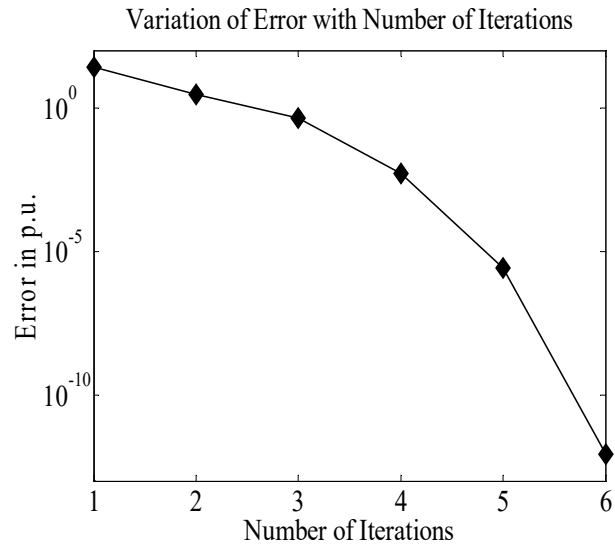


Fig. 5.5: Convergence characteristic for the case study of row 1 in Table 5.1

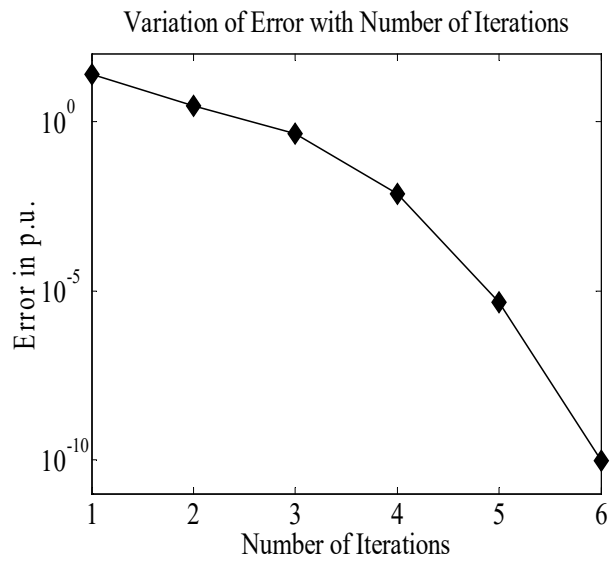


Fig. 5.6: Convergence characteristic for the case study of rows 3-11 in Table 5.1

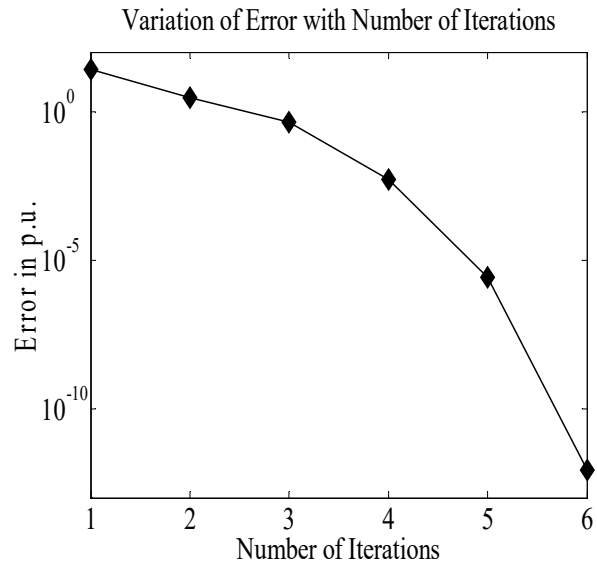


Fig. 5.7: Convergence characteristic for the case study of row 1 in Table 5.2

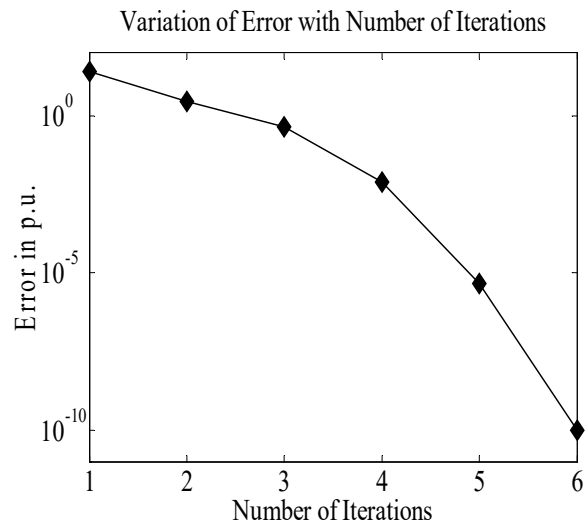


Fig. 5.8: Convergence characteristic for the case study of rows 3-11 in Table 5.2

The bus voltage profiles for the studies of Table 5.1 and Table 5.2 are depicted in Figures 5.9 and 5.10, respectively. From Figures 5.9 and 5.10, it is observed that the

bus voltage profiles of the AC-MTDC system including IDCPFC do not alter much from that of the base case except the AC buses at which the VSCs are connected.

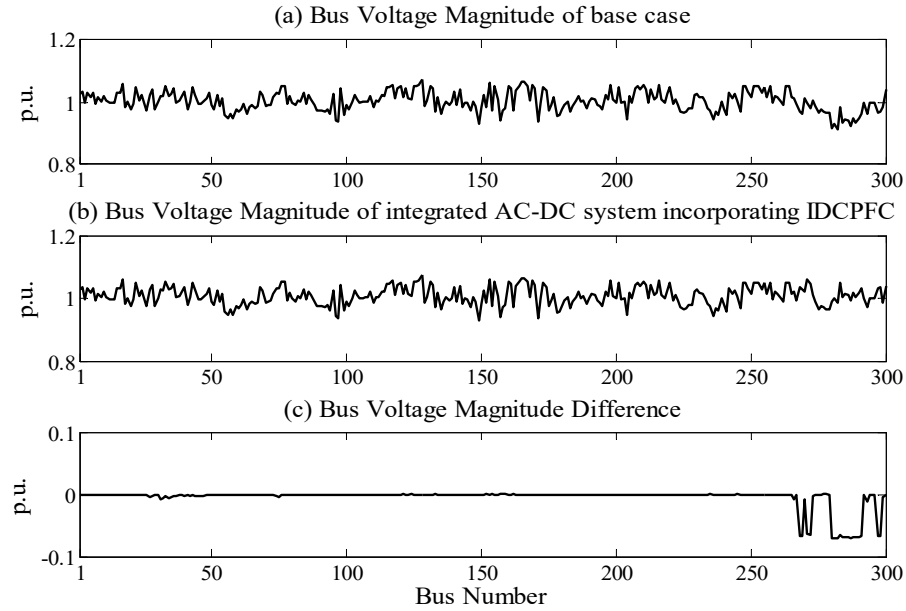


Fig. 5.9: Bus voltage profile for the study of Table 5.1

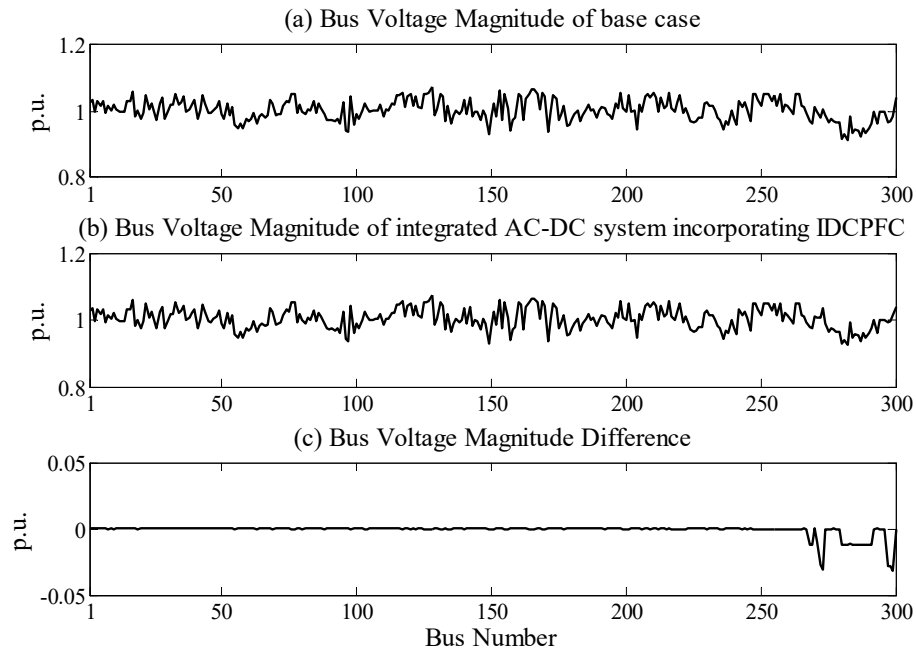


Fig. 5.10: Bus voltage profile for the study of Table 5.2

## Case II: DC link power control using IDCPFC

In this study, at first, a three terminal VSC-MTDC grid is integrated with the IEEE-300 bus test system at buses 266, 270 and 271 and the AC-MTDC power-flow is carried out. For this analysis, DC slack bus control is assumed ( $V_{DC1}$  is specified). The power-flow solution is shown in the first row of Table 5.3, with the sending end line power in the DC link between DC buses 1 and 3 computed to be 0.2454 p.u. Subsequently, a IDCPFC (having two variable DC voltage sources) is incorporated in the 3-terminal VSC-MTDC grid integrated with the IEEE 300-bus test network and the AC-MTDC power-flow is again carried out. The IDCPFC is used to control the sending end power in the DC link between DC buses 1 and 3 to a specified value of 0.28 p.u. (the sending end DC link power without any IDCPFC is 0.2454 p.u.). The specified quantities are shown in rows 3-11 and columns 1-2 of Table 5.3. The AC-MTDC power flow solution with the IDCPFC is shown in the rows 3-11 and columns 3-4 of Table 5.3.

Subsequently, a study is executed on the same three terminal AC-MTDC network but with the three VSCs connected to AC buses 268, 272 and 273. The AC-MTDC power-flow solution without any IDCPFC is shown in the first row of Table 5.4, with the sending end power flow in the DC link between the DC buses 1 and 2 computed to be 0.3461 p.u. Subsequently, a IDCPFC (having two variable DC voltage sources) is incorporated in the 3-terminal VSC-MTDC grid integrated with the IEEE 300-bus test network and the AC-MTDC power-flow is again carried out. The IDCPFC is used to control the sending end power in the DC link between DC buses 1 and 2 to a specified value of 0.36 p.u. (the sending end DC link power without any IDCPFC is 0.3461 p.u.). The specified quantities are shown in the rows 3-11 and

columns 1-2 of Table 5.4. The AC-MTDC power flow solution with the IDCPFC is shown in the rows 3-11 and columns 3-4 of Table 5.4.

Table 5.3

Study of IEEE 300 bus system with three terminal VSC HVDC network incorporating IDCPFC in DC power control mode

AC-MTDC power-flow without any IDCPFC (VSCs connected to AC buses 266, 270 and 271)					
$P_{sh2} = 0.3; Q_{sh2} = 0.1; P_{sh3} = 0.2; Q_{sh3} = 0.09; V_{DC1} = 3.0; V_{DC2} = 2.9991;$ $V_{DC3} = 2.9992; P_{DC13} = 0.2454; NI=6; CT=1.45;$					
AC-MTDC power-flow with IDCPFC					
Given quantities		Solution			
		AC buses	VSCs		
$V_{266}$	1.02	$V_{270} = 1.0202;$ $V_{271} = 1.0619;$ $\theta_{266} = -11.3850;$ $\theta_{270} = -11.4005;$ $\theta_{271} = -12.6899;$	$\theta_{sh1} = -14.2879; \theta_{sh2} = -9.7712;$ $\theta_{sh3} = -11.6866; V_{DC} = 2.9990;$ $V_{DC3} = 2.9992; m_1 = 0.9894;$ $m_2 = 0.9721; m_3 = 1.0097;$		
$V_{DC1}$	3.0		<b>IDCPFC</b> $V_{DCs1} = 0.00018; V_{DCs2} = -0.00016;$ $I_{DC12} = 0.116; I_{DC13} = 0.0933; P_{DC12} = 0.3481;$		
$P_{sh2}$	0.3			<b>DC power</b> $P_{DC1} = 0.5244;$ $P_{DC2} = -0.3124;$ $P_{DC3} = -0.2118;$	
$Q_{sh2}$	0.1				<b>Converter Loss (%)</b> $P_{loss1} = 1.44;$ $P_{loss2} = 1.23;$ $P_{loss3} = 1.18;$
$P_{sh3}$	0.2				
$Q_{sh3}$	0.09				
<b>IDCPFC</b>					
$P_{DC13}$	0.28	$NI=6; CT=1.53;$			

Table 5.4

Study of IEEE 300 bus system with three terminal VSC HVDC network incorporating IDCPFC in DC power control mode

AC-MTDC power-flow without any IDCPFC (VSCs connected to AC buses 268, 272 and 273)					
$P_{sh2} = 0.35; Q_{sh2} = 0.1; P_{sh3} = 0.3; Q_{sh3} = 0.1; V_{DC1} = 3.0; V_{DC2} = 2.9988; V_{268} = 0.98;$ $V_{DC3} = 2.9989; P_{DC12} = 0.3461; NI=6; CT=1.45;$					
AC-MTDC power-flow with IDCPFC					
Given quantities		Solution			
		AC buses	VSCs		
$V_{268}$	0.98	$V_{272} = 1.0086;$ $V_{273} = 1.0366;$ $\theta_{268} = -39.1738;$ $\theta_{272} = -31.2288;$ $\theta_{273} = -6.7581;$	$\theta_{sh1} = -43.2335; \theta_{sh2} = -29.2837;$ $\theta_{sh3} = -5.1792; V_{DC2} = 2.9989;$ $V_{DC3} = 2.9989; m_1 = 0.9418;$ $m_2 = 0.9615; m_3 = 0.9874;$		
$V_{DC1}$	3.0		<b>IDCPFC</b> $V_{DCs1} = -0.000064; V_{DCs2} = 0.000074;$ $I_{DC12} = 0.12; P_{DC13} = 0.3571; I_{DC13} = 0.119;$		
$P_{sh2}$	0.35			<b>DC power</b> $P_{DC1} = 0.6754;$ $P_{DC2} = -0.3628;$ $P_{DC3} = -0.3124;$	
$Q_{sh2}$	0.1				<b>Converter Loss (%)</b> $P_{loss1} = 1.54;$ $P_{loss2} = 1.26;$ $P_{loss3} = 1.23;$
$P_{sh3}$	0.3				
$Q_{sh3}$	0.1				
<b>IDCPFC</b>					
$P_{DC12}$	0.36	$NI=6; CT=1.52;$			



The convergence characteristics corresponding to the studies of rows 3-11 of Table 5.3 (with IDCPFC) and rows 3-11 of Table 5.4 (with IDCPFC), are shown in Figures 5.11 and 5.12, respectively. From Figures, 5.11 and 5.12, it is observed that the AC-MTDC power-flow solutions with the IDCPFC demonstrate quadratic convergence characteristics, similar to the base case power flow.

The bus voltage profiles for the studies of Table 5.3 and Table 5.4 are shown in Figures 5.13 and 5.14, respectively. Again, from Figures 5.13 and 5.14, it is observed that the bus voltage profiles do not change much from that of the base case except at the AC terminal buses to which the VSCs are connected.

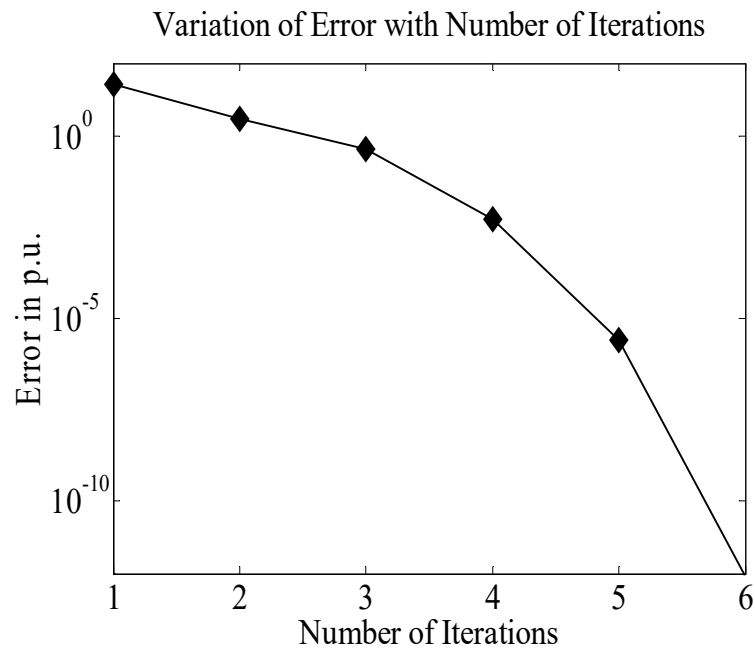


Fig. 5.11: Convergence characteristic for the case study of rows 3-11 in Table 5.3

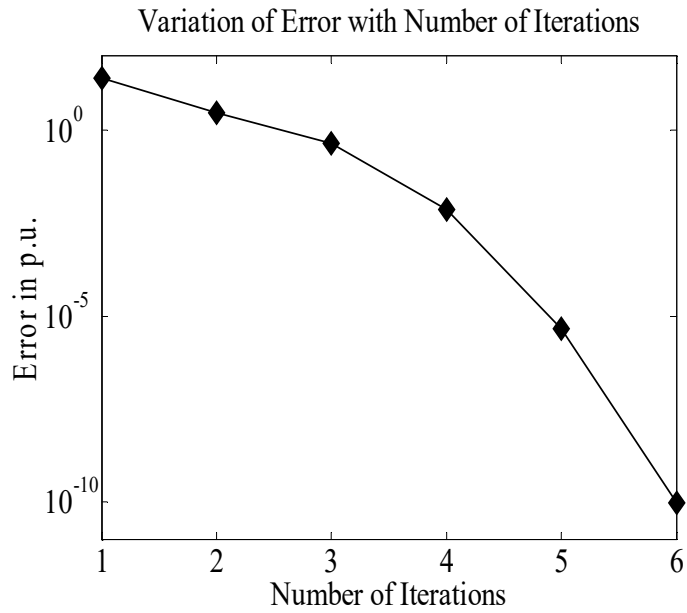


Fig. 5.12: Convergence characteristic for the case study of rows 3-11 in Table 5.4

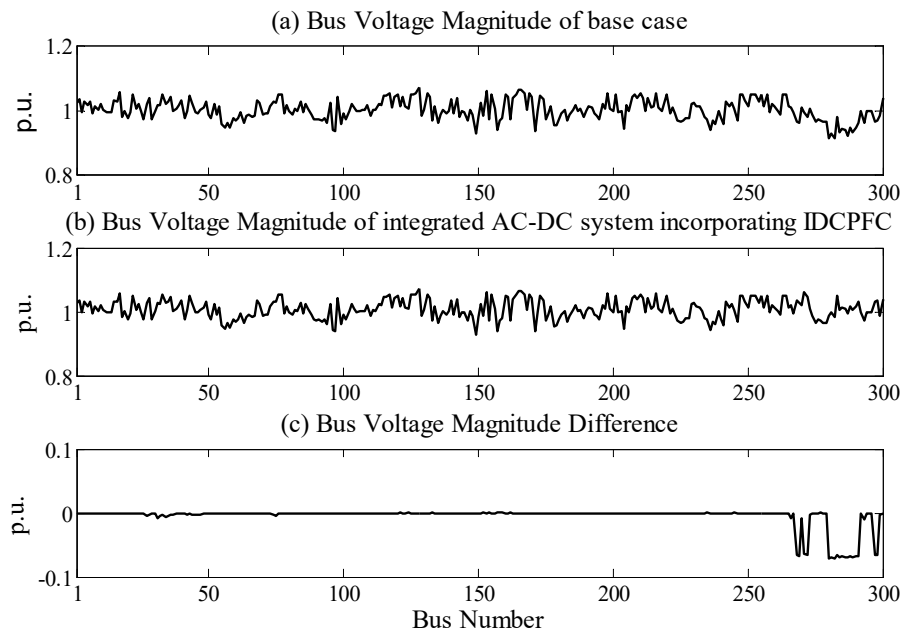


Fig. 5.13: Bus voltage profile for the study of Table 5.3

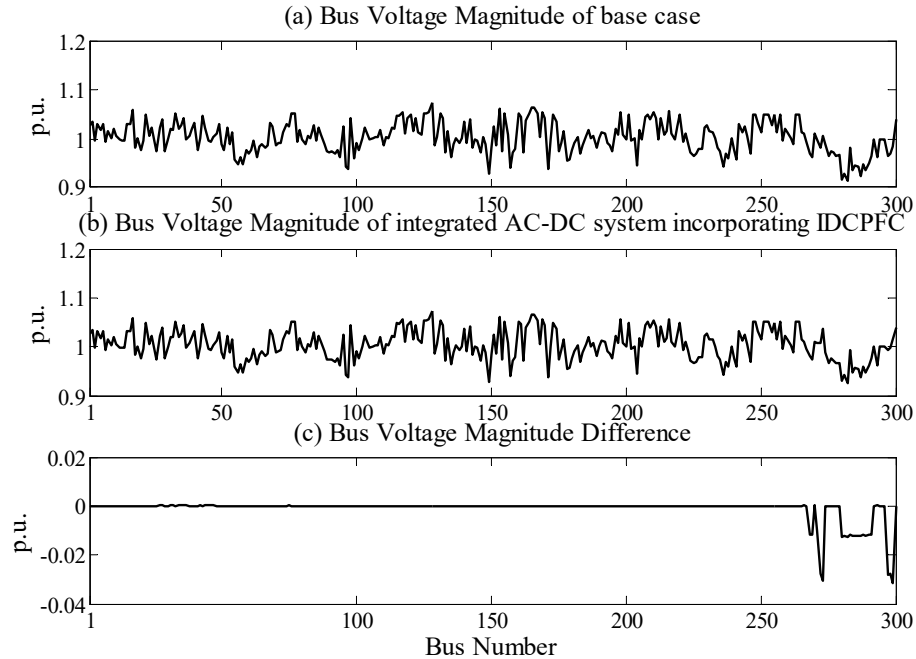


Fig. 5.14: Bus voltage profile for the study of Table 5.4

## 5.5.2 Study of five terminal VSC-MTDC network incorporating IDCPFC

### Case I: DC current control by using IDCPFC

In this study, at first, a five terminal VSC-MTDC grid is integrated with the IEEE-300 bus test system at buses 266, 270, 271, 272 and 273 and the AC-MTDC power-flow is carried out. DC slack bus control is assumed ( $V_{DC}$  is specified). The power-flow solution is shown in the first row of Table 5.5, with the line current in the DC link between DC buses 1 and 2 computed to be 0.111 p.u. Subsequently, a IDCPFC (having two variable DC voltage sources) is incorporated in the 5-terminal VSC-MTDC grid integrated with the IEEE 300-bus test network and the AC-MTDC power-flow is again carried out. The IDCPFC is used to control the current in the DC link between DC buses 1 and 2 to a specified value of 0.13 p.u. (the DC link current without any IDCPFC is 0.111 p.u.). The specified quantities are shown in rows 3-11

and columns 1-2 of Table 5.5. The AC-MTDC power flow solution with the IDCPFC is shown in the rows 3-11 and columns 3-4 of Table 5.5.

The convergence characteristic for the study of row 1 of Table 5.5 (without IDCPFC) and rows 3-11 of Table 5.5 (with IDCPFC), are shown in Figures 5.15 and 5.16, respectively. From Figures 5.15 and 5.16, it is observed that the proposed AC-MTDC model incorporating IDCPFC in line current control mode possesses quadratic convergence characteristics, similar to the base case power flow.

Table 5.5

Study of IEEE 300 bus system with five terminal VSC HVDC network incorporating IDCPFC in DC current control mode

Given quantities		Solution												
		AC buses	VSCs											
AC-MTDC power-flow without any IDCPFC $P_{sh2} = 0.3; Q_{sh} = 0.2; P_{sh3} = 0.2; Q_{sh3} = 0.09; P_{sh4} = 0.3; P_{sh5} = 0.5;$ $V_{266} = 1.02; V_{272} = 0.99; V_{273} = 1.01; V_{DC1} = 3.0; V_{DC2} = 2.9953; V_{DC3} = 2.9959;$ $I_{DC12} = 0.111; NI=6; CT=2.13;$														
AC-MTDC power-flow with IDCPFC (VSCs connected to AC buses 266, 270, 271, 272 and 273)														
$V_{266}$	1.02	$\theta_{266} = -11.5366;$ $\theta_{270} = -11.5562;$ $\theta_{271} = -5.2515;$ $\theta_{272} = -3.5532;$ $\theta_{273} = 0.8651;$ $V_{270} = 1.0206;$ $V_{271} = 1.0137;$	$\theta_{sh1} = -18.8296; \theta_{sh2} = -9.9487; \theta_{sh3} = -4.1515;$ $\theta_{sh4} = -1.7755; \theta_{sh5} = 3.6692;$ $V_{DC2} = 2.9982; V_{DC3} = 2.9979; V_{DC4} = 2.9983;$ $V_{DC5} = 2.9982; m_1 = 1.0059; m_2 = 0.9819;$ $m_3 = 0.9652; m_4 = 0.9247; m_5 = 0.9546;$											
$V_{272}$	0.99													
$V_{273}$	1.01													
$V_{DC1}$	3.0													
$P_{sh2}$	0.3													
$Q_{sh2}$	0.2		IDCPFC $V_{DCs1} = 0.0005; V_{DCs2} = 0.0023;$ $I_{DC13} = -0.0255; P_{DC12} = 0.39; P_{DC13} = -0.0766;$											
$P_{sh3}$	0.2													
$Q_{sh3}$	0.09													
$P_{sh4}$	0.3													
$P_{sh5}$	0.5													
IDCPFC			<table border="1" style="width: 100%;"> <thead> <tr> <th>DC power</th> <th>Converter Loss (%)</th> </tr> </thead> <tbody> <tr> <td><math>P_{DC1} = 1.3517;</math></td> <td><math>P_{loss} = 2.37;</math></td> </tr> <tr> <td><math>P_{DC} = -0.3127;</math></td> <td><math>P_{loss2} = 1.26;</math></td> </tr> <tr> <td><math>P_{DC3} = -0.2119;</math></td> <td><math>P_{loss3} = 1.19;</math></td> </tr> <tr> <td><math>P_{DC} = -0.3125;</math></td> <td><math>P_{loss4} = 1.24;</math></td> </tr> <tr> <td><math>P_{DC5} = -0.5138;</math></td> <td><math>P_{loss5} = 1.35;</math></td> </tr> </tbody> </table>	DC power	Converter Loss (%)	$P_{DC1} = 1.3517;$	$P_{loss} = 2.37;$	$P_{DC} = -0.3127;$	$P_{loss2} = 1.26;$	$P_{DC3} = -0.2119;$	$P_{loss3} = 1.19;$	$P_{DC} = -0.3125;$	$P_{loss4} = 1.24;$	$P_{DC5} = -0.5138;$
DC power	Converter Loss (%)													
$P_{DC1} = 1.3517;$	$P_{loss} = 2.37;$													
$P_{DC} = -0.3127;$	$P_{loss2} = 1.26;$													
$P_{DC3} = -0.2119;$	$P_{loss3} = 1.19;$													
$P_{DC} = -0.3125;$	$P_{loss4} = 1.24;$													
$P_{DC5} = -0.5138;$	$P_{loss5} = 1.35;$													
$I_{DC12}$	0.13	NI=6; CT=2.19;												

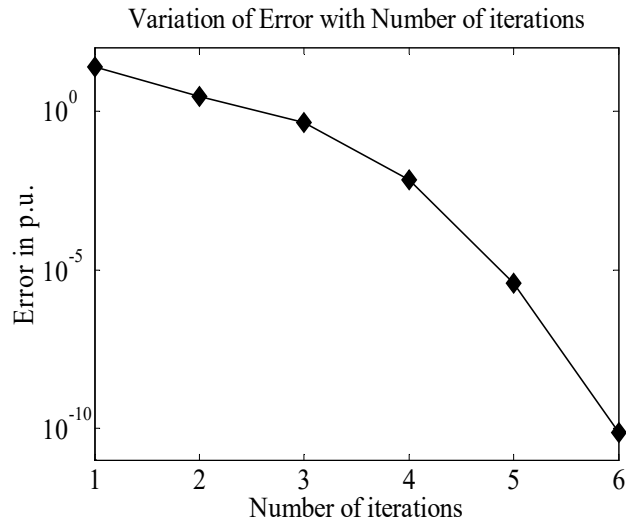


Fig. 5.15: Convergence characteristic for the case study of row 1 of Table 5.5

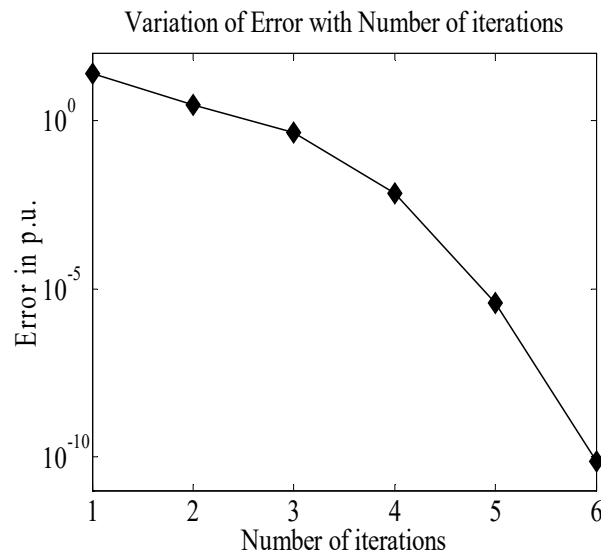


Fig. 5.16: Convergence characteristic for the case study of rows 3-15 in Table 5.5

The bus voltage profile for the study corresponding to rows 3-11 of Table 5.5 is shown in Fig. 5.17. Again, from Fig. 5.17, it is observed that the bus voltage profile does not alter much from that of the base case study except at the AC terminal buses connected to the VSCs.

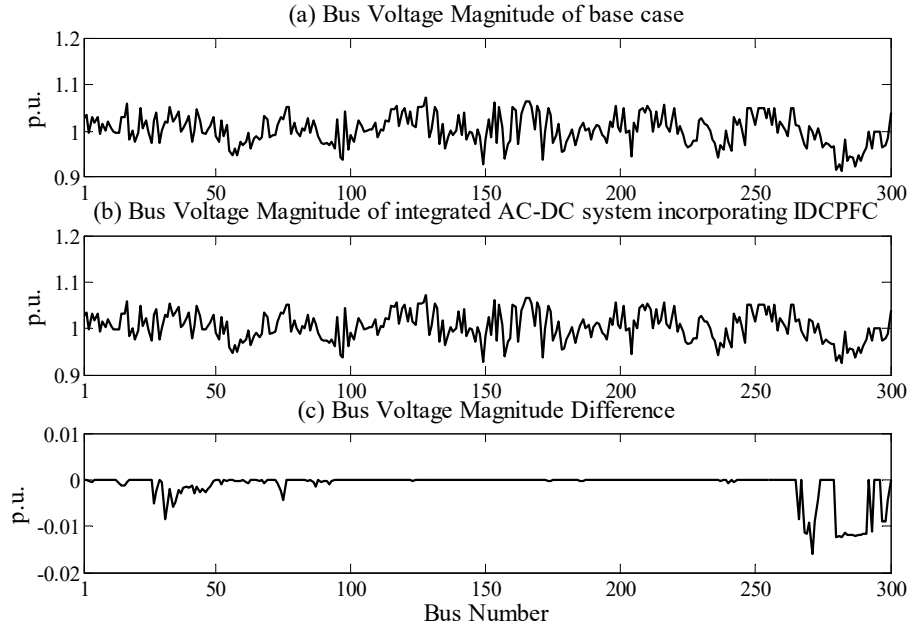


Fig. 5.17: Bus voltage profile for the study of Table 5.5

### Case II: DC link power control using IDCPFC

In this study, at first, a five terminal VSC-MTDC grid is integrated with the IEEE-300 bus test system at buses 266, 270, 271, 272 and 273 and the AC-MTDC power-flow is carried out. DC slack bus control is assumed ( $V_{DC}$  is specified). The power-flow solution is shown in the first row of Table 5.6, with the sending end line power in the DC link between DC buses 1 and 3 computed to be 0.3127 p.u. Subsequently, a IDCPFC (having two variable DC voltage sources) is incorporated in the 5-terminal VSC-MTDC grid integrated with the IEEE 300-bus test network and the AC-MTDC power-flow is again carried out. The IDCPFC is used to enhance the sending end power-flow in the DC link between DC buses 1 and 3 to a specified value of 0.35 p.u. (the sending end DC link power without any IDCPFC is 0.3127 p.u.). The specified quantities are shown in rows 3-11 and columns 1-2 of Table 5.6. The AC-MTDC power flow solution with the IDCPFC is shown in the rows 3-11 and columns 3-4 of Table 5.6.

The convergence characteristic plot for the study of rows 3-11 of Table 5.6 (with IDCPF) is shown in Fig. 5.18. From Fig. 5.18, it is observed that the proposed AC-MTDC model including IDCPF employing DC link current control possesses quadratic convergence characteristics, similar to the base case power flow. The bus voltage profile for the study of rows 3-11 of Table 5.6 is shown in Fig. 5.19. From Fig. 5.19, it is observed that the bus voltage profile with the IDCPF does not change much from that of the base case power-flow, except at the AC terminal buses connected to the VSCs.

Table 5.6

Study of IEEE 300 bus system with five terminal VSC HVDC network incorporating IDCPF in DC power control mode

Given quantities		Solution		
		AC buses	VSCs	
AC-MTDC power-flow without any IDCPF $P_{sh2} = 0.3; Q_{sh2} = 0.2; P_{sh3} = 0.2; Q_{sh} = 0.09; P_{sh4} = 0.3; P_{sh} = 0.5;$ $V_{266} = 1.02; V_{272} = 0.99; V_{273} = 1.01; V_{DC1} = 3.0; V_{DC2} = 2.9953; V_{DC3} = 2.9959;$ $P_{DC13} = 0.3127; NI=6; CT=2.13;$				
AC-MTDC power-flow with IDCPF (VSCs connected to AC buses 266, 270, 271, 272 and 273)				
$V_{266}$	1.02	$\theta_{266} = -11.5366;$ $\theta_{270} = -11.5564;$ $\theta_{271} = -5.2517;$ $\theta_{272} = -3.5534;$ $\theta_{273} = 0.8649;$ $V_{270} = 1.0206;$ $V_{271} = 1.0137;$	$\theta_{sh1} = -18.8301; \theta_{sh2} = -9.9489;$ $\theta_{sh3} = -4.1517;$ $\theta_{sh4} = -1.7757; \theta_{sh5} = 3.6690;$ $V_{DC2} = 2.9977; V_{DC} = 2.9982; V_{DC4} = 2.9983;$ $V_{DC5} = 2.9981; m_1 = 1.0059; m_2 = 0.9821;$ $m_3 = 0.9651; m_4 = 0.9247; m_5 = 0.9546;$	
$V_{272}$	0.99		IDCPF $V_{DCs1} = 0.0026; V_{DCs2} = 0.0006;$ $I_{DC12} = -0.0294; I_{DC13} = 0.1167; P_{DC12}$ $= -0.0883;$	
$V_{273}$	1.01			
$V_{DC1}$	3.0		DC power $P_{DC1} = 1.3518;$ $P_{DC} = -0.3127;$ $P_{DC3} = -0.2119;$ $P_{DC} = -0.3125;$ $P_{DC5} = -0.5138;$	Converter Loss (%) $P_{loss1} = 2.37;$ $P_{loss} = 1.26;$ $P_{loss} = 1.19;$ $P_{loss} = 1.24;$ $P_{loss5} = 1.35;$
$P_{sh2}$	0.3			
$Q_{sh2}$	0.2			
$P_{sh3}$	0.2			
$Q_{sh3}$	0.09			
$P_{sh4}$	0.3			
$P_{sh5}$	0.5			
IDCPF				
$P_{DC13}$	0.35			
NI=6; CT=2.17;				

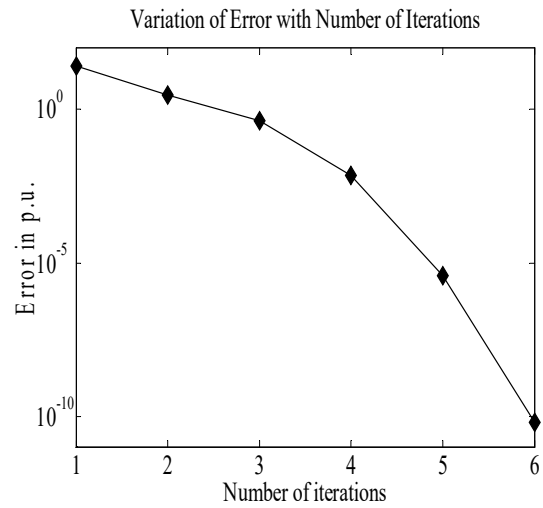


Fig. 5.18: Convergence characteristic for the case study of rows 3-15 in Table 5.6

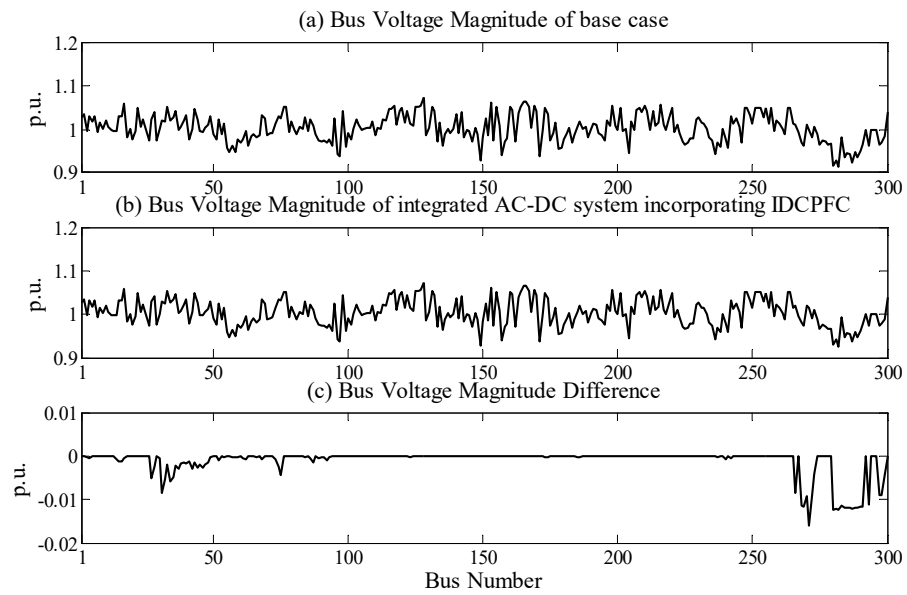


Fig. 5.19: Bus voltage profile for the study of Table 5.6

## 5.6 Conclusions

This chapter presents a generalized approach to the development of unified Newton power-flow models of VSC based hybrid AC-DC systems incorporating IDCPFCs.



The IDCPFC is a DC power-flow controller used for the power-flow management of DC grids. The proposed model has been implemented with IDCPFC in three and five terminal MTDC grids integrated with the IEEE 300-bus test network. The convergence characteristics validate the model.

# Chapter 6

## Newton Power Flow Modeling of Voltage Source Converter (VSC) Based Hybrid AC-DC Systems with Renewable Energy Sources

### 6.1 Introduction

Due to the ever increasing demand of electrical energy and environmental concerns, both the industry and the academia have been focusing on the harnessing of renewable energy sources, particularly the integration of offshore renewable energy sources [19]-[21]. In order to integrate such remotely located energy sources with the AC grid, multi-terminal VSC based HVDC (MVDC) systems have been proposed over conventional HVDC which can connect different offshore stations at the same voltage or at different voltages.

Now, for planning, operation and control of AC-MVDC systems integrated with renewable energy sources, their Newton power-flow models are required. As already discussed in the previous chapters, MVDC systems can employ DC slack bus control or DC voltage droop control for operation. A power-flow model should include both these control strategies for completeness.

### 6.2 Modeling of AC-MVDC systems incorporating renewable energy sources

The assumptions adopted for modeling are similar to those in Chapter-3 of this thesis. Fig. 6.1 shows a 'p' bus HVDC grid integrated with a 'n' bus AC power system network. The interfacing of the HVDC grid with the AC network takes place at 'q' (q

$\leq p$ ) AC buses through ‘q’ VSCs and their respective converter transformers. The DC sides of these ‘q’ VSCs are connected in the PTP configuration and constitute part of the larger ‘p’ bus DC grid. The rest of the ‘(p-q)’ DC buses are appropriately interfaced (through AC/DC converters) with offshore wind farms (OWFs). Without loss of generality, it is assumed that the ‘q’ VSCs are connected to AC buses ‘i’, ‘(i+1)’, and so on, up to bus ‘(i+q-1)’, through ‘q’ converter transformers and the ‘(p-q)’ OWFs are interfaced with DC buses ‘(q+1)’, ‘(q+2)’ and so on, up to DC bus ‘p’.

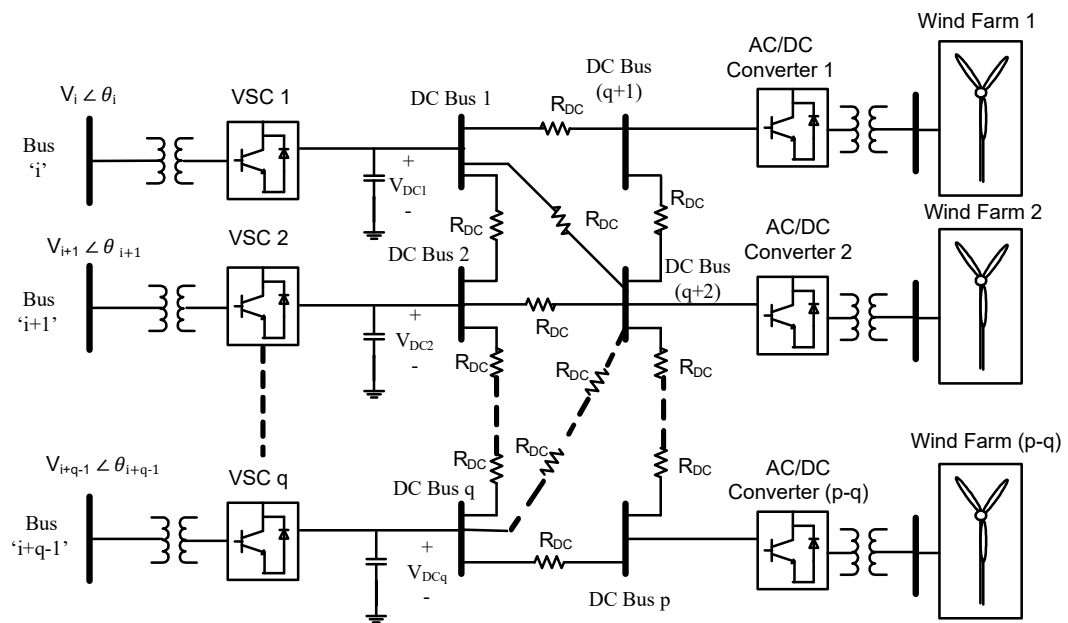


Fig. 6.1: Schematic diagram of hybrid AC-MVDC system with offshore wind farms

Fig. 6.2 shows the equivalent circuit for the network shown in Fig. 6.1. In Fig. 6.2, each of the ‘q’ VSCs is represented as a fundamental frequency, positive sequence voltage source. Thus,  $\mathbf{V}_{sha}$  represents the voltage phasor pertaining to the  $a^{\text{th}}$  ( $1 \leq a \leq q$ ) VSC. Each converter transformer is represented by its leakage impedance. The  $a^{\text{th}}$  ( $1 \leq a \leq q$ ) VSC is connected to AC bus ‘(i+a-1)’ whose voltage is represented by the

phasor  $\mathbf{V}_{i+a-1} = V_{i+a-1} \angle \theta_{i+a-1}$ , through the  $a^{\text{th}}$  converter transformer. All the ‘(p-q)’ DC buses with renewable energy sources are represented as DC power injections.

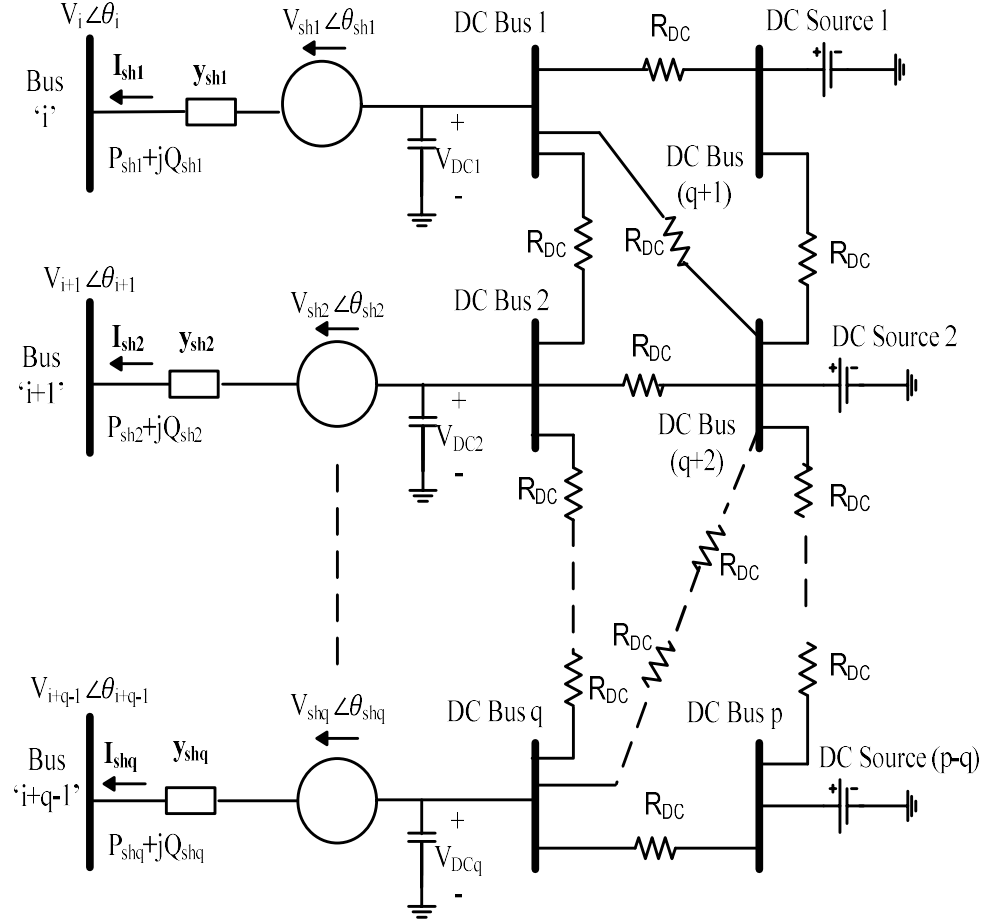


Fig. 6.2: Equivalent circuit of hybrid AC-MVDC system with offshore wind farms

In Fig. 6.2, let  $R_{sha}$  and  $X_{sha}$  be the resistance and the leakage reactance of the converter transformer of the  $a^{\text{th}}$  ( $1 \leq a \leq q$ ) VSC, respectively. Also, let  $y_{sha} = 1/Z_{sha}$ , where  $Z_{sha} = R_{sha} + jX_{sha}$ . Then, from Fig. 6.2, the current in the link (not shown) connecting the  $a^{\text{th}}$  VSC to its AC terminal bus ‘(i+a-1)’ is

$$\mathbf{I}_{sha} = y_{sha}(\mathbf{V}_{sha} - \mathbf{V}_{i+a-1}) \quad (6.1)$$

where  $V_{sha} = V_{sha} \angle \theta_{sha} = m_a c V_{DCa} \angle \theta_{sha}$ . In the above equation, ‘ $m_a$ ’ and ‘ $V_{DCa}$ ’ are the modulation index and the DC side voltage of the  $a^{th}$  VSC, respectively, while ‘ $\theta_{sha}$ ’ is the phase angle of  $V_{sha}$ . ‘ $c$ ’ is a constant which depends on the VSC architecture [11].

Again, from Fig. 6.2, the net current injection at the AC bus ‘ $(i+a-1)$ ’ connected to the  $a^{th}$  ( $1 \leq a \leq q$ ) VSC can be written as

$$I_{i+a-1} = \sum_{k=1}^n Y_{(i+a-1)k} V_k - y_{sha} V_{sha} \quad (6.2)$$

Where  $Y_{(i+a-1)(i+a-1)} = Y_{(i+a-1)(i+a-1)}^{old} + y_{sha}$  and

$Y_{(i+a-1)(i+a-1)}^{old} = y_{(i+a-1)0} + \sum_{k=1, k \neq i+a-1}^n Y_{(i+a-1)k}$  are the values of self admittances for the bus ‘ $(i+a-1)$ ’ with the  $a^{th}$  VSC connected and in the original ‘ $n$ ’ bus AC system without any VSC, respectively.

### 6.3 Power flow equations in the proposed model of hybrid VSC-HVDC System with Renewable Energy Sources

Now, from Fig. 6.2, at the AC bus ‘ $(i+a-1)$ ’ pertaining to the  $a^{th}$  VSC, it can be shown that the net active and reactive power injections are

$$P_{i+a-1} = \sum_{k=1}^n V_{i+a-1} V_k Y_{(i+a-1)k} \cos [\theta_{i+a-1} - \theta_k - \phi_{(i+a-1)k}] - m_a c V_{DCa} V_{i+a-1} y_{sha} \cos(\theta_{i+a-1} - \theta_{sha} - \phi_{sha}) \quad (6.3)$$

$$Q_{i+a-1} = \sum_{k=1}^n V_{i+a-1} V_k Y_{(i+a-1)k} \sin [\theta_{i+a-1} - \theta_k - \phi_{(i+a-1)k}] - m_a c V_{DCa} V_{i+a-1} y_{sha} \sin(\theta_{i+a-1} - \theta_{sha} - \phi_{sha}) \quad (6.4)$$

where ‘ $\phi_{sha}$ ’ is the phase angle of  $y_{sha}$ .

In addition, from Fig. 6.2, it can be shown using eqn. (6.2) that the active and reactive power flows at the terminal end of the link interconnecting the  $a^{\text{th}}$  VSC to the AC bus ‘ $(i+a-1)$ ’ are

$$P_{\text{sha}} = m_a c V_{\text{DCa}} V_{i+a-1} Y_{\text{sha}} \cos(\theta_{i+a-1} - \theta_{\text{sha}} - \phi_{\text{sha}}) - V_{i+a-1}^2 Y_{\text{sha}} \cos \phi_{\text{sha}} \quad (6.5)$$

$$Q_{\text{sha}} = m_a c V_{\text{DCa}} V_{i+a-1} Y_{\text{sha}} \sin(\theta_{i+a-1} - \theta_{\text{sha}} - \phi_{\text{sha}}) + V_{i+a-1}^2 Y_{\text{sha}} \sin \phi_{\text{sha}} \quad (6.6)$$

Also, from Fig. 6.2, by virtue of the power balance on the AC and DC sides of the  $a^{\text{th}}$  VSC,

$$\text{Re}(\mathbf{V}_{\text{sha}} \mathbf{I}_{\text{sha}}^*) + \sum_{v=1}^p V_{\text{DCa}} V_{\text{DCv}} Y_{\text{DCav}} = -P_{\text{lossa}} \quad (6.7)$$

Substitution of eqn. (6.1) in eqn. (4.7) gives

$$(m_a c V_{\text{DCa}})^2 y_{\text{sha}} \cos \phi_{\text{sha}} - m_a c V_{\text{DCa}} V_{i+a-1} Y_{\text{sha}} \cos(\theta_{\text{sha}} - \theta_{i+a-1} - \phi_{\text{sha}}) + \sum_{v=1}^p V_{\text{DCa}} V_{\text{DCv}} Y_{\text{DCav}} + P_{\text{lossa}} = 0$$

$$\text{or, } f_{1a} = 0 \quad \forall 1 \leq a \leq q \quad (6.8)$$

Thus, for ‘ $q$ ’ VSCs, ‘ $q$ ’ independent equations are obtained.

In eqns. (6.7) and (6.8),  $Y_{\text{DCav}} = -\frac{1}{R_{\text{DCav}}}$ , where ‘ $R_{\text{DCav}}$ ’ is the resistance of the DC link between DC buses ‘ $a$ ’ and ‘ $v$ ’. Also, ‘ $P_{\text{lossa}}$ ’ represents the losses of the  $a^{\text{th}}$  VSC as already detailed in Chapter 3 and is again given below.

$$P_{\text{lossa}} = a_1 + b_1 I_{\text{sha}} + c_1 I_{\text{sha}}^2 \quad (6.9)$$

where ‘ $a_1$ ’, ‘ $b_1$ ’ and ‘ $c_1$ ’ are loss factors [18], [92] and

$$I_{\text{sha}} = y_{\text{sha}} [V_{i+a-1}^2 + (m_a c V_{\text{DCa}})^2 - 2 V_{i+a-1} m_a c V_{\text{DCa}} \cos(\theta_{i+a-1} - \theta_{\text{sha}})]^{1/2} \quad (6.10)$$

The derivation of eqn. (6.10) is given in Appendix A.

Now, in the AC-MTDC system (Fig. 6.2) with ‘q’ VSCs, if it is assumed that the  $r^{\text{th}}$  ( $1 \leq r \leq q$ ) VSC is used for voltage control of its corresponding AC bus, we have

$$V_{i+a-1}^{\text{sp}} - V_{i+a-1}^{\text{cal}} = 0 \quad \forall a, 1 \leq a \leq q, a = r \quad (6.11)$$

Also, not more than ‘(q-1)’ line active and reactive power flows {eqn. (6.5) and (6.6)} can be specified, which give us ‘(2q-2)’ independent equations given as

$$P_{\text{sha}}^{\text{sp}} - P_{\text{sha}}^{\text{cal}} = 0 \quad (6.12)$$

$$Q_{\text{sha}}^{\text{sp}} - Q_{\text{sha}}^{\text{cal}} = 0 \quad (6.13)$$

$\forall a, 1 \leq a \leq q, a \neq r.$

Instead of PQ control mode, if a VSC operates in the PV one, eqn. (6.13) changes to

$$V_{i+a-1}^{\text{sp}} - V_{i+a-1}^{\text{cal}} = 0 \quad \forall a, 1 \leq a \leq q, a \neq r \quad (6.14)$$

Further, the net reactive power injection at AC bus ‘(i+r-1)’ can be specified as its voltage is controlled by the  $r^{\text{th}}$  VSC. Thus, we get

$$Q_{i+a-1}^{\text{sp}} - Q_{i+a-1}^{\text{cal}} = 0 \quad \forall a, 1 \leq a \leq q, a = r \quad (6.15)$$

In eqns. (6.11)-(6.15),  $V_{i+a-1}^{\text{sp}}$ ,  $Q_{i+a-1}^{\text{sp}}$ ,  $P_{\text{sha}}^{\text{sp}}$  and  $Q_{\text{sha}}^{\text{sp}}$  are specified values while  $V_{i+a-1}^{\text{cal}}$ ,  $Q_{i+a-1}^{\text{cal}}$ ,  $P_{\text{sha}}^{\text{cal}}$  and  $Q_{\text{sha}}^{\text{cal}}$  are calculated values {using eqns. (6.4), (6.5) and (6.6)}.

#### 6.4 Modeling of AC-MTDC systems employing DC slack bus control

In Fig. 6.1, if it is assumed that ‘g’ generators are connected at the first ‘g’ buses of the ‘n’ bus AC system with bus 1 being the slack bus, then the Newton-Raphson

power flow model of the ‘n’ bus AC system integrated with a ‘p’ terminal DC network with ‘(p-q)’ offshore wind farms is written as

Compute:  $\boldsymbol{\theta}$ ,  $\mathbf{V}$ ,  $\mathbf{X}$

Given:  $\mathbf{P}$ ,  $\mathbf{Q}$ ,  $\mathbf{R}$

with

$$\boldsymbol{\theta} = [\theta_2 \dots \theta_n]^T, \mathbf{V} = [V_{g+1} \dots V_n]^T, \boldsymbol{\theta}_{sh} = [\theta_{sh1} \dots \theta_{shq}]^T, \mathbf{m} = [m_1 \dots m_q]^T, \mathbf{V}_{DC} = [V_{DC2} \dots V_{DCp}]^T$$

$$\mathbf{X} = [\boldsymbol{\theta}_{sh}^T \quad \mathbf{m}^T \quad \mathbf{V}_{DC}^T]^T$$

$$\mathbf{P} = [P_2 \dots P_n]^T, \mathbf{Q} = [Q_{g+1} \dots Q_n]^T, \mathbf{P}_{sh} = [P_{sh} \dots P_{shq}], \mathbf{Q}_{sh} = [Q_{sh2} \dots Q_{shq}]$$

$$\mathbf{f}_1 = [f_{11} \dots f_{1q}], \mathbf{P}_{DCWF} = [P_{DCWF1} \dots P_{DCWF(p-q)}], \mathbf{R} = [\mathbf{P}_{sh} \quad \mathbf{Q}_{sh} \quad V_{i+r-1} \quad \mathbf{f}_1 \quad \mathbf{P}_{DCWF}]^T$$

In this model, DC slack bus control is assumed with the master VSC ‘r’ controlling the voltage magnitude of its AC terminal bus ‘(i+r-1)’ unlike the other ‘(q-1)’ slave VSCs which control the line active and reactive power flows.

The Newton power flow equation is

$$\mathbf{J}[\Delta\boldsymbol{\theta}^T \quad \Delta\mathbf{V}^T \quad \Delta\boldsymbol{\theta}_{sh}^T \quad \Delta\mathbf{m}^T \quad \Delta\mathbf{V}_{DC}^T]^T = [\Delta\mathbf{P}^T \quad \Delta\mathbf{Q}^T \quad \Delta\mathbf{R}^T]^T \quad (6.16)$$

where  $\mathbf{J}$  is the power-flow Jacobian.

In eqn. (6.16), ‘ $\Delta\mathbf{P}$ ’, ‘ $\Delta\mathbf{Q}$ ’ and ‘ $\Delta\mathbf{R}$ ’ represent the mismatch vectors while  $\Delta\boldsymbol{\theta}$ ,  $\Delta\mathbf{V}$ ,  $\Delta\boldsymbol{\theta}_{sh}$ ,  $\Delta\mathbf{m}$  and  $\Delta\mathbf{V}_{DC}$  represent the correction vectors.

## 6.5 Modeling of AC-MTDC Systems with DC Voltage Droop Control



### 6.5.1 Types of DC voltage droop control

As already mentioned in Chapter 4, in DC voltage droop control [24]-[29], multiple converters participate in the DC voltage control scheme. Droop control comprises either linear voltage droop characteristics like voltage-power (V-P) or voltage-current (V-I) droops or nonlinear voltage droop characteristics with dead-bands and limits.

#### 1. Voltage-Power (V-P) Droop

If the  $a^{\text{th}}$  VSC follows a linear V-P droop characteristic, its rectifying power can be expressed as

$$P_{\text{DCa}} = R_a(V_{\text{DCa}}^* - V_{\text{DCa}}) + P_{\text{DCa}}^* \quad (6.17)$$

#### 2. Voltage-Current (V-I) Droop

If the  $a^{\text{th}}$  VSC follows a linear V-I droop characteristic; the net DC current injection at its terminal can be expressed as

$$I_{\text{DCa}} = R_a(V_{\text{DCa}}^* - V_{\text{DCa}}) + I_{\text{DCa}}^* \quad (6.18)$$

Thus, the rectifying power of the VSC can be expressed as

$$P_{\text{DC}} = V_{\text{DCa}} [R_a(V_{\text{DCa}}^* - V_{\text{DCa}}) + I_{\text{DCa}}^*] \quad (6.19)$$

In eqns. (6.17), (6.18) and (6.19), ' $V_{\text{DCa}}^*$ ', ' $P_{\text{DCa}}^*$ ' and ' $I_{\text{DCa}}^*$ ' represent the DC voltage, power and current references of the droop characteristics, respectively while ' $R_a$ ' is the droop control gain.

*Computation of ' $V_{\text{DCa}}^*$ ' and ' $P_{\text{DCa}}^*$ '*

As already mentioned in Section 4.4 of Chapter 4, the values of the DC power and current references ' $P_{DCa}^*$ ' and ' $I_{DCa}^*$ ' in eqns. (6.17) and (6.18) for all the 'q' converters are either pre specified or obtained from a DC power-flow.

### 3. Voltage-Power (V-P) Droop with dead-band

As already described in Chapter 4, if the  $a^{\text{th}}$  VSC ( $1 \leq a \leq q$ ) follows a nonlinear voltage droop characteristics with dead-band and voltage limits as shown in Fig. 6.3, the droop characteristic can be expressed as

$$P_{DCa} = R_{a \max}(V_{DCa \max} - V_{DCa}) + [R_a (V_{DCa \text{ high}}^* - V_{DCa \max}) + P_{DCa}^*] \text{ for } V_{DCa} \geq V_{DCa \max} \quad (6.20)$$

$$= R_a (V_{DCa \text{ high}}^* - V_{DCa}) + P_{DCa}^* \quad \text{for } V_{DCa \text{ high}}^* < V_{DCa} < V_{DCa \max} \quad (6.21)$$

$$= 0 \cdot (V_{DCa \text{ high}}^* - V_{DCa}) + P_{DCa}^* \quad \text{for } V_{DCa \text{ low}}^* \leq V_{DCa} \leq V_{DCa \text{ high}}^* \quad (6.22)$$

$$= R_a (V_{DCa \text{ low}}^* - V_{DCa}) + P_{DCa}^* \quad \text{for } V_{DCa \text{ min}}^* < V_{DCa} < V_{DCa \text{ low}}^* \quad (6.23)$$

$$= R_{a \max}(V_{DCa \text{ min}} - V_{DCa}) + [R_a (V_{DCa \text{ low}}^* - V_{DCa \text{ min}}) + P_{DCa}^*] \quad \text{for } V_{DCa} \leq V_{DCa \text{ min}} \quad (6.24)$$

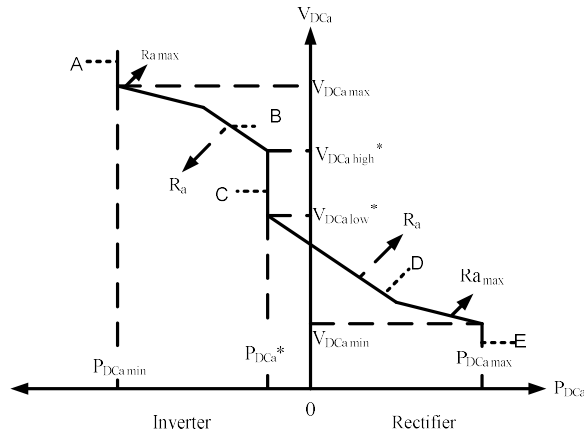


Fig. 6.3: Nonlinear Voltage Droop Characteristic of the  $a^{\text{th}}$  VSC

#### 4. DC voltage margin control

As already discussed in Chapter 4, the V-P characteristic pertaining to the DC voltage margin control is shown in Fig. 6.4.

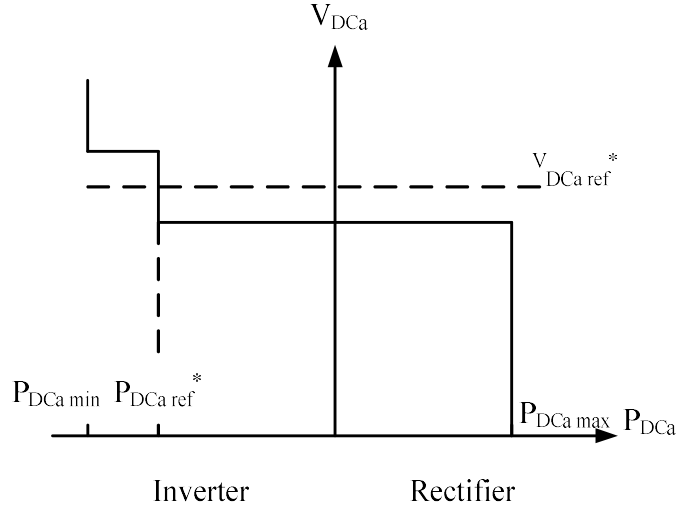


Fig. 6.4: Voltage Margin Characteristic of the  $a^{\text{th}}$  VSC

The inclusion of linear and nonlinear DC voltage droop control is accommodated in the AC-MTDC model with renewable energy sources as shown below.

### 6.5.2 Implementation of DC voltage droop control in AC-MTDC systems integrated with offshore wind farms

Let us assume now that all the 'q' VSCs in the AC-MTDC system shown in Fig. 6.1 and 6.2 operate on droop control. To simplify matters, let all the 'q' VSCs follow linear V-P droops. Then, for the  $a^{\text{th}}$  VSC ( $1 \leq a \leq q$ ), from eqns. (6.17), we have

$$P_{DCa} = V_{DCa} I_{DCa} = \sum_{v=1}^p V_{DCa} V_{DCv} Y_{DCav} = R_a (V_{DCa}^* - V_{DCa}) + P_{DCa}^*$$

$$\text{or, } \sum_{v=1}^p V_{DCa} V_{DCv} Y_{DCav} + R_a V_{DCa} - R_a V_{DCa}^* - P_{DCa}^* = 0 \quad (6.25)$$

$$\text{or, } f_{2a} = 0 \quad \forall a, \quad 1 \leq a \leq q \quad (6.26)$$

Eqn. (6.26) represents ‘q’ independent equations.

Now, two distinctly different models can be realized depending on whether the values of ‘ $V_{DCa}^*$ ’ and ‘ $P_{DCa}^*$ ’ are specified or not. These are elaborated below.

*Model ‘A’: Values of ‘ $V_{DCa}^*$ ’ and ‘ $P_{DCa}^*$ ’ are known a priori*

In some cases, the values of ‘ $V_{DCa}^*$ ’ and ‘ $P_{DCa}^*$ ’ for all the ‘q’ converters are pre-specified [82], having been obtained from a DC power-flow, or otherwise. In such cases, the ‘q’ independent droop equations represented by eqn. (6.26) along with ‘(p-q)’ specified values of rectified wind farm power injections ( $P_{DCWFS}$ ) are sufficient to compute the values of the DC bus voltages ‘ $V_{DCa}$ ’ directly, and subsequently, the DC bus power injections ‘ $P_{DCa}$ ’. Now, as already described in Section 4.5 of Chapter 4, once ‘ $P_{DCa}$ ’ are known, the active powers ‘ $P_{sha}$ ’ {eqn. (6.5)} in the lines joining the ‘(q-1)’ VSCs to their corresponding AC buses cannot be specified for the AC-MTDC power-flow. This is not in line with practical considerations which are targeted to maintain a specified ‘ $P_{sha}$ ’. This is a major drawback of the model.

Now, under the assumption that there are ‘g’ generators connected at the first ‘g’ buses of the ‘n’ bus AC system with bus 1 being the slack bus, the unified AC-MTDC power-flow problem corresponding to model ‘A’ is of the form

Compute:  $\theta, V, X$

Given:  $P, Q, R$

where

$$\theta = [\theta_2 \dots \theta_n]^T, \mathbf{V} = [V_{g+1} \dots V_n]^T, \theta_{sh} = [\theta_{sh} \dots \theta_{shq}]^T, \mathbf{m} = [m_1 \dots m_q]^T, \mathbf{X} = [\theta_{sh}^T \mathbf{m}^T]^T$$

$$\mathbf{P} = [P_2 \dots P_n]^T, \mathbf{Q} = [Q_{g+1} \dots Q_n]^T, \mathbf{Q}_{sh} = [Q_{sh} \dots Q_{shq}], \mathbf{f}_1 = [f_{11} \dots f_{1q}], \mathbf{R} = [Q_{sh} V_{i+r-1} \mathbf{f}_1]^T$$

For this model, it is presumed that VSC ‘r’ controls the voltage magnitude of the AC bus ‘(i+r-1)’ unlike the other ‘(q-1)’ VSCs, which control the line reactive power flows.

The Newton power flow equation is

$$\mathbf{J}[\Delta\theta^T \Delta\mathbf{V}^T \Delta\theta_{sh}^T \Delta\mathbf{m}^T]^T = [\Delta\mathbf{P}^T \Delta\mathbf{Q}^T \Delta\mathbf{R}^T]^T \quad (6.27)$$

where  $\mathbf{J}$  is the power-flow Jacobian.

In eqn. (6.27), ‘ $\Delta\mathbf{P}$ ’, ‘ $\Delta\mathbf{Q}$ ’ and ‘ $\Delta\mathbf{R}$ ’ represent the mismatch vectors while  $\Delta\theta$ ,  $\Delta\mathbf{V}$ ,  $\Delta\theta_{sh}$  and  $\Delta\mathbf{m}$  represent the correction vectors. The elements of ‘ $\mathbf{J}$ ’ can be obtained very easily from eqn. (6.27).

Thus, in Model ‘A’, if ‘ $V_{DCa}^*$ ’ and ‘ $P_{DCa}^*$ ’ are known, ‘ $V_{DCa}$ ’ ( $1 \leq a \leq p$ ) can be solved using eqn. (6.25) and ‘(p-q)’ specified values of rectified wind farm power injections (‘ $P_{DCWFs}$ ’), independent of the AC-MTDC power-flow {eqn. (6.27)}. Subsequent to the AC-MTDC power-flow, the rest of the unknowns are also solved and the line active power-flows ‘ $P_{sha}$ ’ can be computed {using eqn. (6.5)}.

To summarize, Model ‘A’ addresses the problem “given the DC voltage and power (or current) references of the VSC droop lines and the target line reactive power flows, what should be the line active power flow values?”

*Model ‘B’: Values of ‘ $V_{DC}^*$ ’ and ‘ $P_{DC}^*$ ’ are not known a priori*

If the DC voltage (‘ $V_{DC}^*$ ’) and power (‘ $P_{DC}^*$ ’) reference values of the ‘q’ VSCs are not known, the DC bus voltages ‘ $V_{DCa}$ ’ ( $1 \leq a \leq p$ ) and hence the DC bus power injections ‘ $P_{DCa}$ ’ cannot be computed from the ‘(p-q)’ specified values of rectified wind farm power injections (‘ $P_{DCWFs}$ ’) only (it is assumed that  $q \neq 0$ ). This enables

the line active power-flow values ‘ $P_{sh}$ ’ to be specified control objectives, which is in line with practical MTDC control. This is an advantage over model ‘A’.

For the above modeling strategy, the unified AC-MTDC power-flow problem is of the form

Compute:  $\theta, V, X$

Given:  $P, Q, R$

with

$$\theta = [\theta_2 \dots \theta_n]^T, V = [V_{g+1} \dots V_n]^T, \theta_{sh} = [\theta_{sh1} \dots \theta_{shq}]^T, m = [m_1 \dots m_q]^T, V_{DC} = [V_{DC} \dots V_{DCp}]^T$$

$$X = [\theta_{sh}^T \ m^T \ V_{DC}^T]^T$$

$$P = [P_2 \dots P_n]^T, Q = [Q_{g+1} \dots Q_n]^T, P_{sh} = [P_{sh} \dots P_{shq}], Q_{sh} = [Q_{sh2} \dots Q_{shq}],$$

$$f_1 = [f_{11} \dots f_{1q}], P_{DCWF} = [P_{DCWF} \dots P_{DCWF(p-q)}]$$

$$\text{and } R = [P_{sh} \ Q_{sh} \ V_{i+r-1} \ V_{DCav} \ f_1 \ P_{DCWF}]^T$$

For this model too, it is presumed that VSC ‘r’ is employed for the control of the voltage magnitude of the AC bus ‘(i+r-1)’ unlike the other ‘(q-1)’ VSCs, which control the line active as well as reactive power flows.

The unified AC-MTDC power flow equation is

$$J[\Delta\theta^T \ \Delta V^T \ \Delta\theta_{sh}^T \ \Delta m^T \ \Delta V_{DC}^T]^T = [\Delta P^T \ \Delta Q^T \ \Delta R^T]^T \quad (6.28)$$

where  $J$  is the power-flow Jacobian.

The values of ‘ $V_{DCa}$ ’ ( $1 \leq a \leq p$ ) are now obtained from the AC-MTDC power-flow {eqn. (6.28)} and the DC bus power injections ‘ $P_{DCa}$ ’ are computed.

Thereafter, the DC voltage ( $V_{DCa}^*$ ) and power ( $P_{DCa}^*$ ) references of the droop lines of the 'q' VSCs can be computed from the 'q' droop equations along with the '(p-q)' specified values of rectified wind farm power injections ( $P_{DCWFS}$ ), as elaborated below.

From eqn. (6.19),

$$P_{DCa}^* + R_a V_{DCa}^* - R_a V_{DCa} - P_{DCa} = 0$$

$$\text{or, } \sum_{v=1}^p V_{DCa}^* V_{DCv}^* Y_{DCav} + R_a V_{DCa}^* - R_a V_{DCa} - P_{DCa} = 0 \quad (6.29)$$

The values of ' $V_{DCa}$ ' ( $1 \leq a \leq p$ ) and hence, ' $P_{DCa}$ ' obtained from the AC-MTDC power-flow {eqn. (6.28)} are substituted in eqn. (6.29) above and the 'p' voltages ' $V_{DCa}^*$ ' are solved using eqn. (6.29) along with the '(p-q)' specified values of rectified wind farm power injections ( $P_{DCWFS}$ ). The voltages ( $V_{DCa}^*$ ) corresponding to the 'q' VSCs are taken as their DC voltage references. From the values of ' $V_{DCa}^*$ ', the power references ' $P_{DCa}^*$ ' are computed.

Figures 6.5 and 6.6 depict the flow charts of the proposed approach for droop control models A and Model B, respectively.

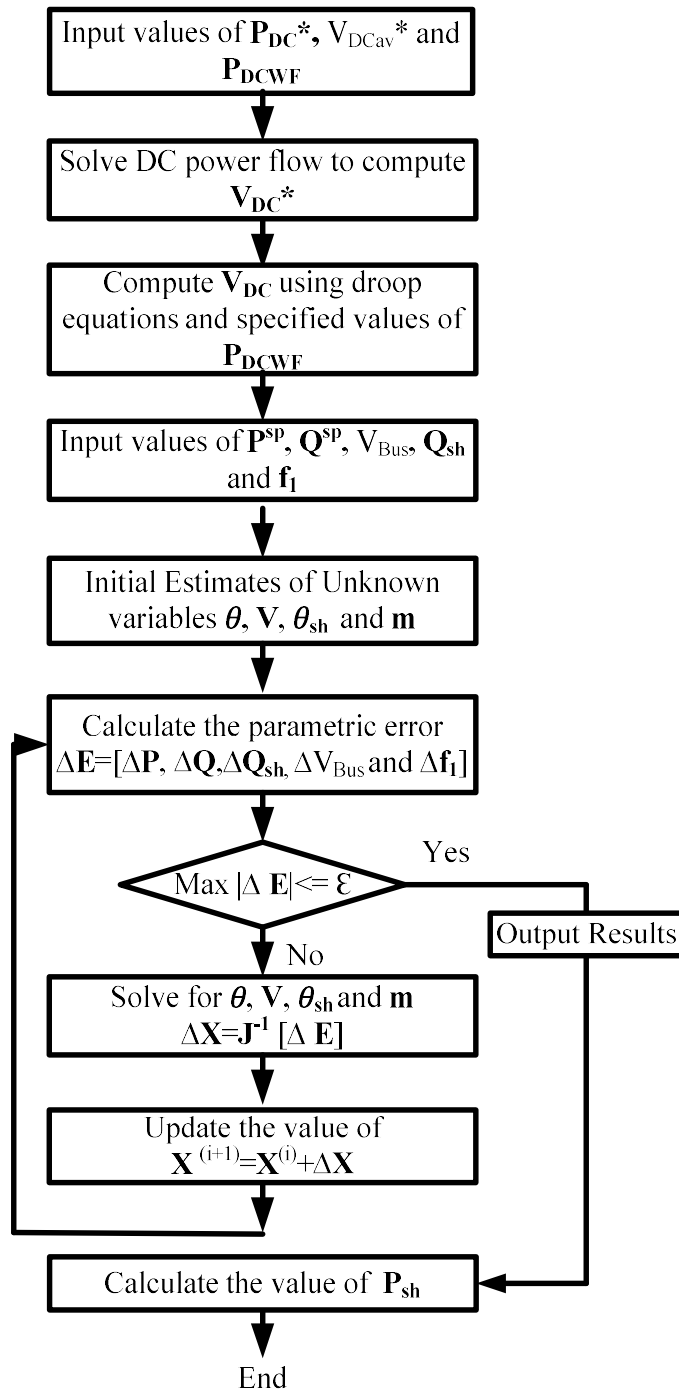


Fig. 6.5: Flow chart of the proposed approach (Model A)



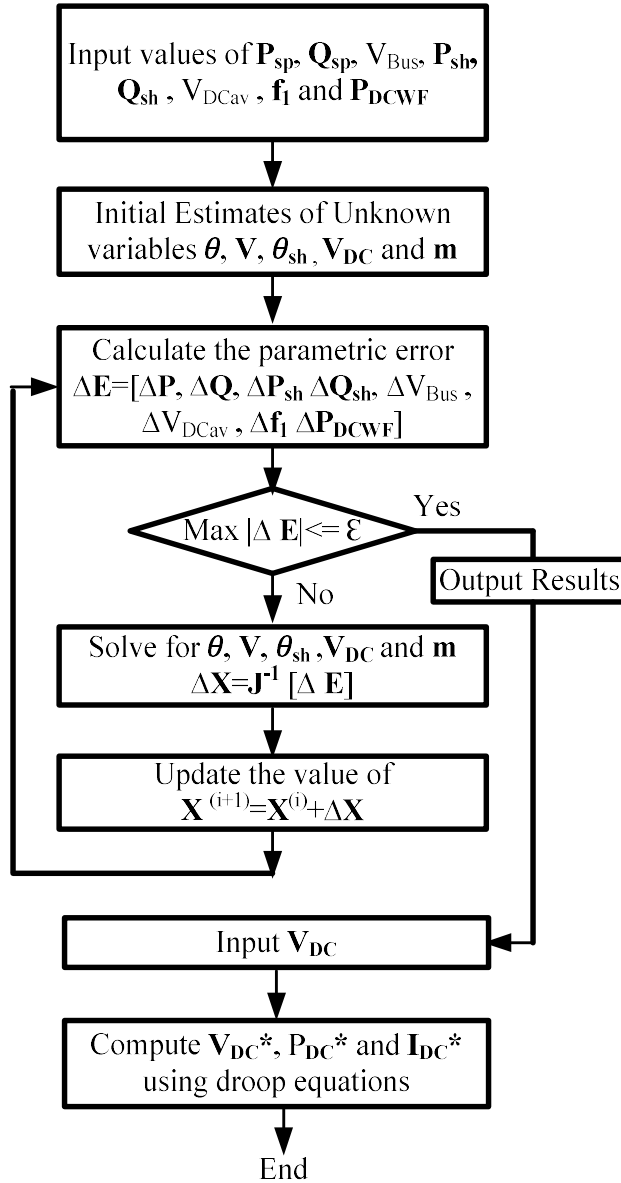


Fig. 6.6: Flow chart of the proposed approach (Model B)

## 6.6 Case Studies and Results

For validation of the above models, a large number of studies were carried out by employing diverse DC voltage droop control strategies on MTDC grids embedded within the IEEE 300-bus network [104]. In all the occurrences, the VSC constant was

selected as  $c = \frac{1}{2\sqrt{2}}$  [11]. Also, for all the VSC coupling transformers,  $R_{sha} = 0.001$  p.u. and  $X_{sha} = 0.1$  p.u. ( $\forall a, 1 \leq a \leq q$ ). The converter loss constants ‘ $a_1$ ’, ‘ $b_1$ ’ and ‘ $c_1$ ’ were chosen as 0.011, 0.003 and 0.0043, respectively [18], [95]. For interconnections between DC terminals,  $R_{DCuv} = 0.01$  p.u. ( $\forall u, v, 1 \leq u \leq q, 1 \leq v \leq q, u \neq v$ ), has been selected throughout the chapter [83]. In all occurrences, a termination error tolerance of  $10^{-10}$  p.u. was selected. ‘NI’ and ‘CT’ denote the number of iterations and the computational time in seconds, pertaining to a 1.99 GHz Dell PC. In all the results given in Tables 4.1- 4.8, values of bus voltage magnitudes, current magnitudes, active and reactive powers and droop control gains are denoted in p.u. while phase angles of voltage phasors are denoted in degrees.

### **6.6.1 Study of five terminal MVDC network with offshore wind farms employing DC slack bus control**

In this study, at first, a base case power flow (without any MTDC network connected) was carried out. The results are shown in row 1 of Table 6.1. Subsequently, a five terminal VSC-HVDC network with DC slack bus control is integrated with the IEEE-300 bus system at AC buses 266, 270 and 292. Two offshore wind farms are connected with DC buses ‘4’ and ‘5’ of the five terminal HVDC network. The master converter is connected to bus no. 266 and operates in bus voltage control mode. The slave converters are connected to AC buses 270 and 292 and operate in the PQ control mode. The specified quantities are shown in rows 2-5 and column 1 of Table 6.1. The power-flow solution is shown in rows 2-5 and column 2 of Table 6.1.

The convergence characteristic plots for the studies corresponding to row 1 of Table 6.1 (base case) and rows 2-5 of Table 6.1 are shown in Figures 6.7 and 6.8,

respectively. From Figures 6.7 and 6.8, it can be observed that the proposed AC-MTDC model with offshore wind farms demonstrates quadratic convergence characteristics, similar to the base case power-flow. The voltage profile corresponding to this study is shown in Fig. 6.9. From Fig. 6.9, it is observed that the bus voltage profile for the AC-MTDC power-flow is similar to the base case except at the terminals at which the VSCs are connected.

Table 6.1

Study of IEEE 300 bus system with five terminal VSC HVDC network incorporating OWFs (Slack control)

Base case power-flow (NI=6 and CT=0.56); $V_{266} = 1.011 \angle -11.24$ ; $V_{270} = 1.011 \angle -11.32$ ; $V_{292} = 1 \angle -18.74$		
AC-MTDC power-flow with OWFs (Slack bus control)		
Given quantities	Power Flow Solution	
	Master Converter	
	$\theta_{sh1} = -9.0873$ ; $m_1 = 0.9766$ ;	
Master Converter $V_{266} = 1.02$ ; $V_{DC1} = 3.0$ ;	Slave Converters $V_{DC2} = 2.9996$ ; $V_{DC} = 2.9995$ ; $m_2 = 0.9692$ ; $m_3 = 0.9477$ ; $\theta_{sh2} = -5.7444$ ; $\theta_{sh3} = -1.2441$ ;	
Slave converters $P_{sh2} = 0.45$ ; $Q_{sh2} = 0.06$ ; $P_{sh3} = 0.55$ ; $Q_{sh3} = 0.03$ ;	AC terminal buses $\theta_{266} = -8.3208$ ; $V_{270} = 1.0206 \angle -8.1996$ ; $V_{292} = 1.00 \angle -4.3794$ ;	Wind farm terminals $V_{DC4} = 3.0002$ ; $V_{DC5} = 3.0002$ ;
Rectifying power of offshore wind farms $P_{DCWF} = 0.5$ ; $P_{DCWF2} = 0.4$ ;	DC power $P_{DC1} = 0.1279$ ; $P_{DC2} = -0.4634$ ; $P_{DC3} = -0.5643$ ;	Converter Loss (%) $P_{loss1} = 1.18$ ; $P_{loss2} = 1.32$ ; $P_{loss3} = 1.4$ ;
NI=6; CT=1.24;		

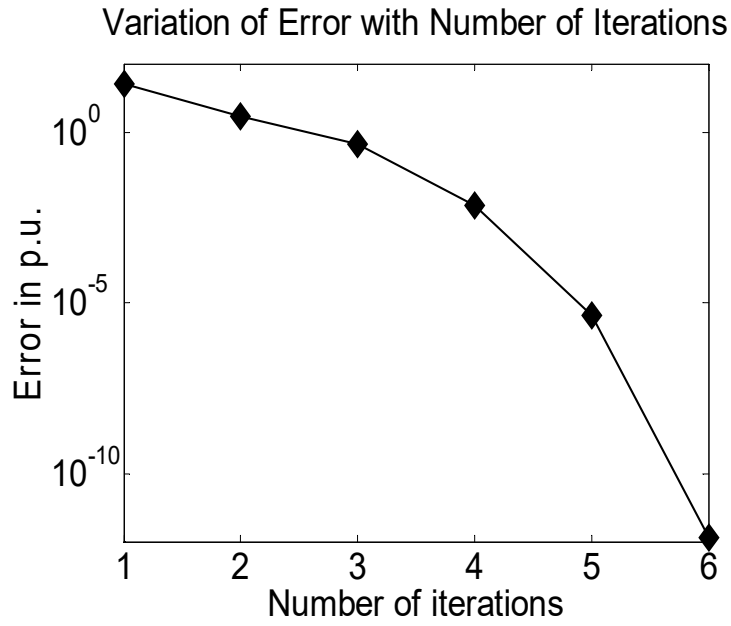


Fig. 6.7: Convergence characteristic of row in Table 6.1

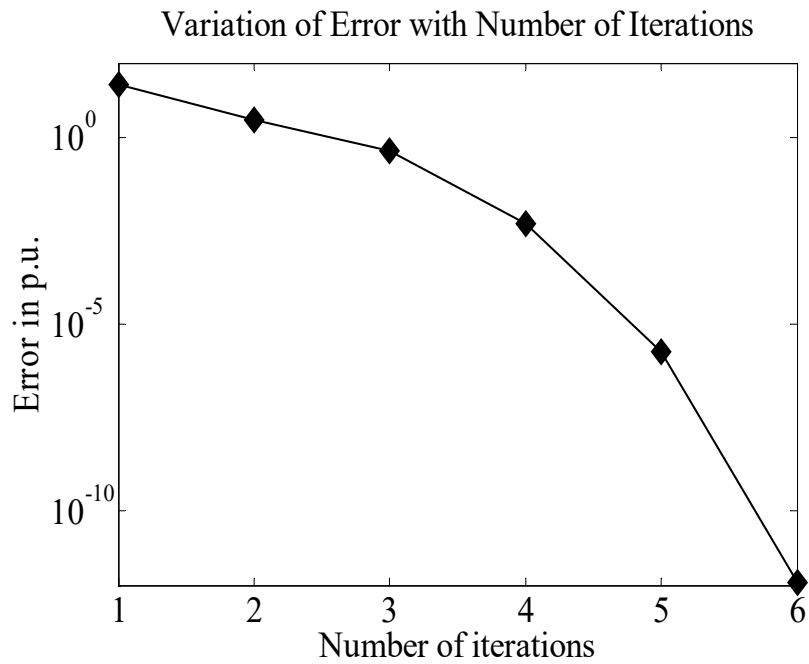


Fig. 6.8: Convergence characteristic of rows 2-6 in Table 6.1

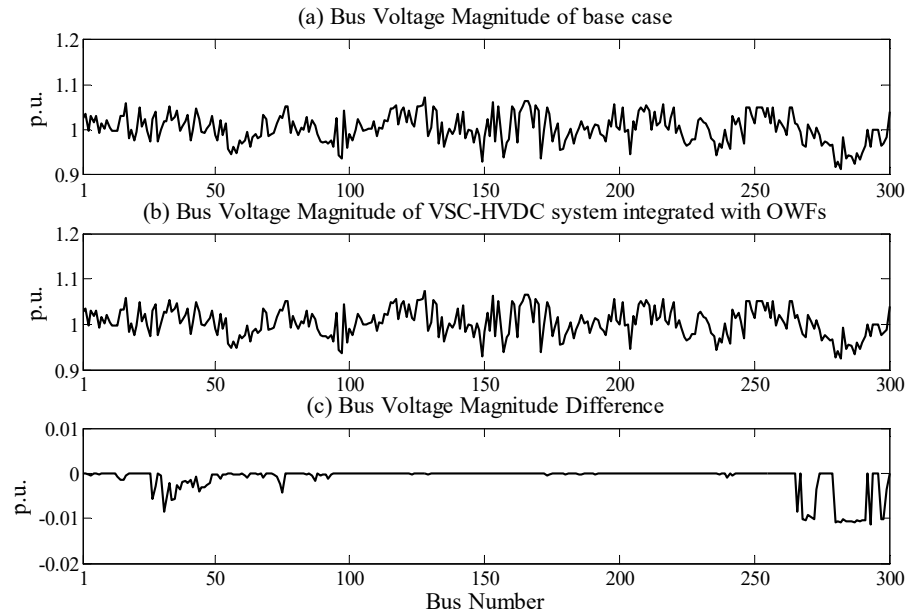


Fig. 6.9: Bus voltage profile for the study of Table 6.1

## 6.6.2 Study of five terminal MVDC network with offshore wind farms employing DC voltage droop control

Based on the quantities specified, two AC-MTDC power-flow models have been developed. These models are named as ‘Model A’ and ‘Model B’ and have been described in Chapter 4 of this thesis.

### Case I: Model-A employing Linear V-P and V-I droop characteristics with offshore wind farms

This study is similar to the study of Table 6.1 except that the VSCs are operated in the linear DC voltage droop control mode. The VSCs connected to AC buses 266 and 270 are operated in V-P droop while the VSC connected to AC bus 292 operates in the V-I droop. Two offshore wind farms with rectifying powers  $P_{DCWF1} = 0.4$  p.u. and

$P_{DCWF2} = 0.3$  p.u. are injected into the DC grid at terminals 4 and 5, respectively. The droop control gains of VSCs 1, 2 and 3 are set to 20, 15 and 10, respectively [24].

At first, a DC load flow is carried out to calculate the reference values of the droop lines of the three VSCs. The results are shown in rows 2-4 of Table 6.2. Subsequently, the DC grid bus voltages are computed by using the three droop equations and two values of offshore wind farm power injections ( $P_{DCWF}$  and  $P_{DCW}$ ). The results are given in rows 5-7 of Table 6.2. Finally, an AC-MTDC load flow is carried out. The power-flow solution is shown in rows 8-10 of Table 6.2.

The convergence characteristic corresponding to the study of Table 6.2 is shown in Fig. 6.10. From Fig. 6.10, it is observed that the AC-MTDC power-flow model with offshore wind farms demonstrates a quadratic convergence characteristic, similar to the base case. The bus voltage profile for this study is shown in Fig. 6.11. From Fig. 6.11, it is observed that the bus voltage profile hardly changes except at the AC buses connected to the VSCs.

Subsequently, another case study is conducted on the same AC-MTDC system by varying the rectifying power of the OWF connected at DC terminal 5 while maintaining the rectifying power of the OWF connected at DC terminal 4 at a value of 0.4 p.u. The droop control gains of the VSCs are maintained identical to the previous study of Table 6.2. Fig. 6.12 shows the variation of the voltage of the DC terminal-5 with the variation of the rectifying power of OWF ( $P_{DCWF2}$ ) connected to it. It is also observed that the number of iterations 'NI' is independent of the variation of the injected value of  $P_{DCWF2}$  as shown in Fig. 6.13.

Table 6.2

Study of IEEE 300 bus system with five terminal VSC HVDC network  
incorporating OWFs (Model A)

Base case power-flow (NI=6 and CT=0.56); $V_{266} = 1.011 \angle -11.24$ ; $V_{270} = 1.011 \angle -11.32$ ; $V_{292} = 1.00 \angle -18.74$ ;		
DC power-flow		
Given quantities	Solution	
$V_{DCav}^* = 3$ ; $P_{DC2}^* = 0.5$ ; $P_{DC3}^* = 0.4$ ;	DC power-flow converged in three iterations $V_{DC1}^* = 3.0006$ ; $V_{DC2}^* = 2.9997$ ; $V_{DC3}^* = 2.9997$ ; $P_{DC1}^* = 0.9003$ ; $I_{DC3}^* = -0.1333$ ;	
	NI=3; CT=0.02;	
Computation of $V_{DC}$ from droop eqns.		
Given quantities	Solution	
$V_{DC1}^* = 3.0006$ ; $V_{DC2}^* = 2.9997$ ; $V_{DC3}^* = 2.9997$ ; $P_{DC1}^* = 0.9003$ ; $P_{DC2}^* = -0.5$ ; $I_{DC3}^* = -0.1333$ ; $R_1 = 20$ ; $R_2 = 15$ ; $R_3 = 10$ ; $P_{DCWF1} = 0.4$ ; $P_{DCWF2} = 0.3$ ;	$V_{DC1} = 3.0114$ ; $V_{DC2} = 3.0105$ ; $V_{DC3} = 3.0104$ ; $V_{DC4} = 3.0112$ ; $V_{DC5} = 3.0111$ ;	
	NI=4; CT=0.08;	
AC-MTDC power-flow with linear voltage droop control (VSCs connected to AC buses 266, 270 and 292)		
Given quantities	Solution	
	AC buses	VSC
$V_{DC1} = 3.0114$ ; $V_{DC2} = 3.0105$ ; $V_{DC3} = 3.0104$ ; $V_{DC4} = 3.0112$ ; $V_{DC5} = 3.0111$ ; $V_{266} = 1.02$ ; $Q_{sh} = 0.1$ ; $Q_{sh3} = 0.05$ ;	$\theta_{266} = -9.0287$ ; $V_{270} = 1.0209 \angle -8.8407$ ; $V_{292} = 1.00 \angle -1.8436$ ; $P_{sh2} = -0.6472$ ; $P_{sh3} = -0.7077$ ;	$\theta_{sh1} = -12.8198$ ; $\theta_{sh} = -5.3314$ ; $\theta_{sh3} = 2.1761$ ; $m_1 = 0.9795$ ; $m_2 = 0.9708$ ; $m_3 = 0.9472$ ;
	DC Power $P_{DC1} = 0.6852$ ; $P_{DC2} = -0.6619$ ; $P_{DC3} = -0.7230$ ;	Converter loss (%) $P_{loss1} = 1.54$ ; $P_{loss2} = 1.47$ ; $P_{loss3} = 1.53$ ;
	NI=6; CT=1.12;	

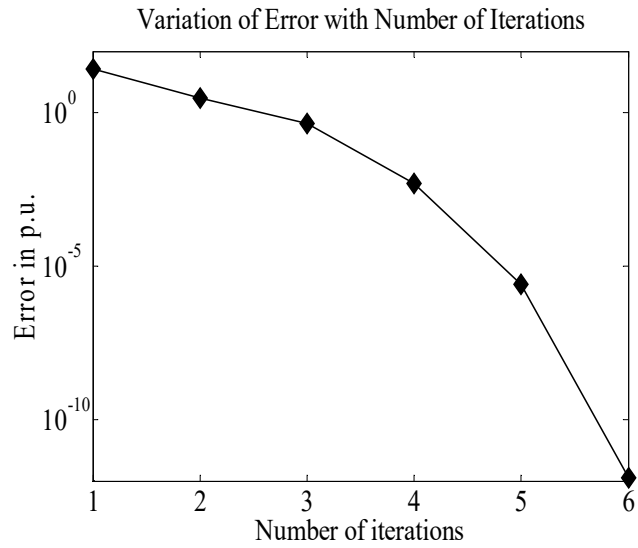


Fig. 6.10: Convergence characteristic of rows 8-10 in Table 6.2

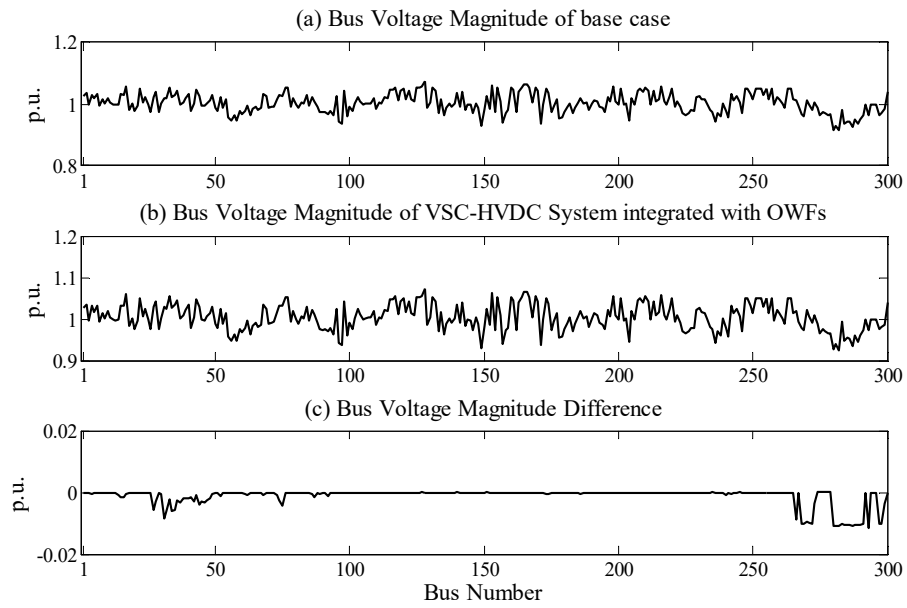


Fig. 6.11: Bus voltage profile for the study of Table 6.2



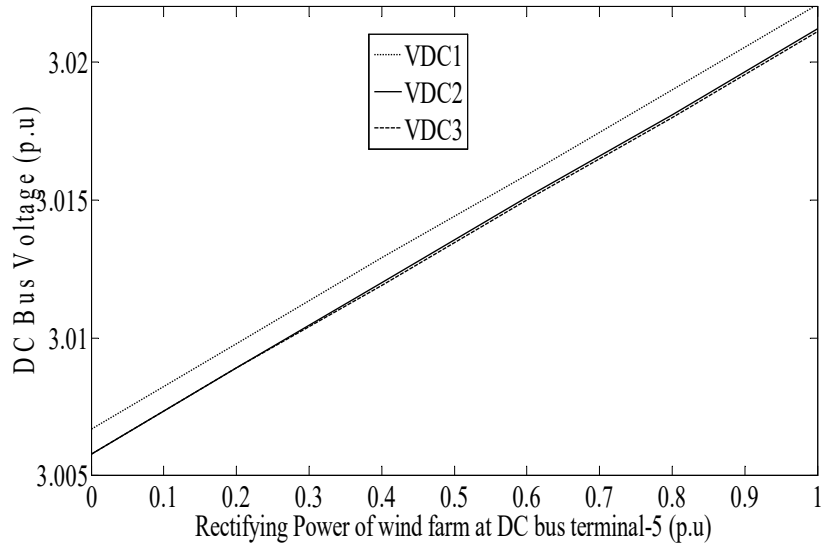


Fig. 6.12: Variation of the power generation of the OWF connected at bus 5 and the DC voltage

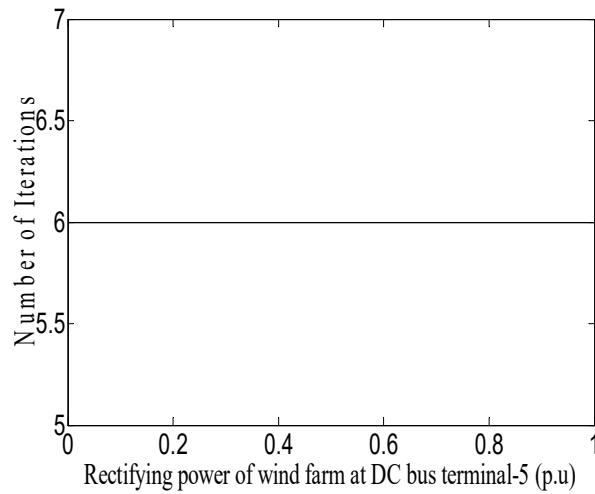


Fig. 6.13: Variation of NI with the variation of  $P_{DCWF2}$

**Case II: Model-B employing Linear V-P and V-I droop characteristics with offshore wind farms**

This study is similar to the study of Table 6.2 except that the VSC terminal end line active powers  $P_{sh2}$  and  $P_{sh}$  are specified in this study. At first, an AC-MTDC power-flow is carried out with two OWFs connected at the terminals ‘4’ and ‘5’ of the DC

grid. The powers specified for these two OWFs at terminals ‘4’ and ‘5’ are 0.5 and 0.4, respectively. The other specified quantities are given in rows 3-9 and column 1-2 of Table 6.3. The power flow solution is shown in rows 3-9 and columns 3-4 of Table 6.3. Subsequent to the AC-MTDC power flow, the VSC droop equations are solved to calculate the reference values of droop lines.

Table 6.3  
Study of IEEE 300 bus system with five terminal VSC HVDC network  
incorporating OWFs (Model B)

Base case power-flow (NI=6 and CT=0.56); $V_{268} = 0.9684\angle -21.01$ ; $V_{272} = 0.9811\angle -19.46$ ; $V_{273} = 1.0058\angle -17.47$ ;			
(VSCs connected to AC buses 268, 272 and 273) Power flow of AC-MTDC system with OWFs			
Given quantities		Solution	
		AC buses	VSCs
$V_{DCav}$	3.0	$\theta_{268} = -39.1737$ ; $\theta_{272} = -31.2288$ ; $\theta_{273} = -6.7581$ ; $V_{272} = 1.0086$ ; $V_{273} = 1.0366$ ; 	$\theta_{sh1} = -43.2335$ ; $\theta_{sh2} = -29.2837$ ; $\theta_{sh} = -5.1792$ ; $m_1 = 0.9347$ ; $m_2 = 0.931$ ; $m_3 = 0.9604$ ; $V_{DC} = 3.0008$ ; $V_{DC2} = 2.9996$ ; $V_{DC} = 2.9997$ ; Wind farm terminals $V_{DC4} = 2.9996$ ; $V_{DC5} = 2.9997$ ; 
$V_{268}$	0.98		
$P_{sh2}$	0.35		
$Q_{sh2}$	0.1		
$P_{sh3}$	0.3		
$Q_{sh3}$	0.1		
Rectifying power of offshore wind farms $P_{DCWF1} = 0.5$ ; $P_{DCWF2} = 0.4$ ;		DC Power	Converter loss (%)
		$P_{DC1} = 0.6754$ ; $P_{DC2} = -0.3628$ ; $P_{DC3} = -0.3124$ ;	$P_{loss1} = 1.5445$ ; $P_{loss2} = 1.2643$ ; $P_{loss3} = 1.2315$ ;
NI=6; CT=1.22;			
Computation of references $V_{DC}^*$ from droop eqns.			
$V_{DC1} = 3.0008$ ; $V_{DC2} = 2.9996$ ; $V_{DC} = 2.9997$ ; $R_1 = 20$ ; $R_2 = 15$ ; $R_3 = 10$ ;		$V_{DC}^* = 3.0008$ ; $V_{DC}^* = 2.9996$ ; $V_{DC3}^* = 2.9997$ ;	
NI=4; CT=0.08;			

The convergence characteristic corresponding to the study of rows 3-10 of Table 6.3 is shown in Fig. 6.14. From Fig. 6.14, it is observed that the proposed model demonstrates the quadratic convergence characteristics, similar to the base case.

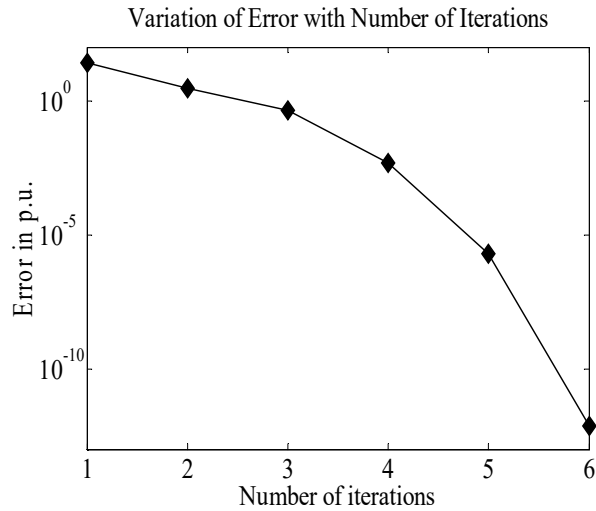


Fig. 6.14: Convergence characteristic of rows 2-10 in Table 6.3

The bus voltage profile of the study corresponding to rows 3-10 of Table 6.3 is shown in Fig. 6.15. From Figure 6.15, it is observed that by incorporating OWFs in the DC grid of the integrated AC-DC system, the bus voltage profile of the AC system does not change except at the AC buses connected to the VSCs.

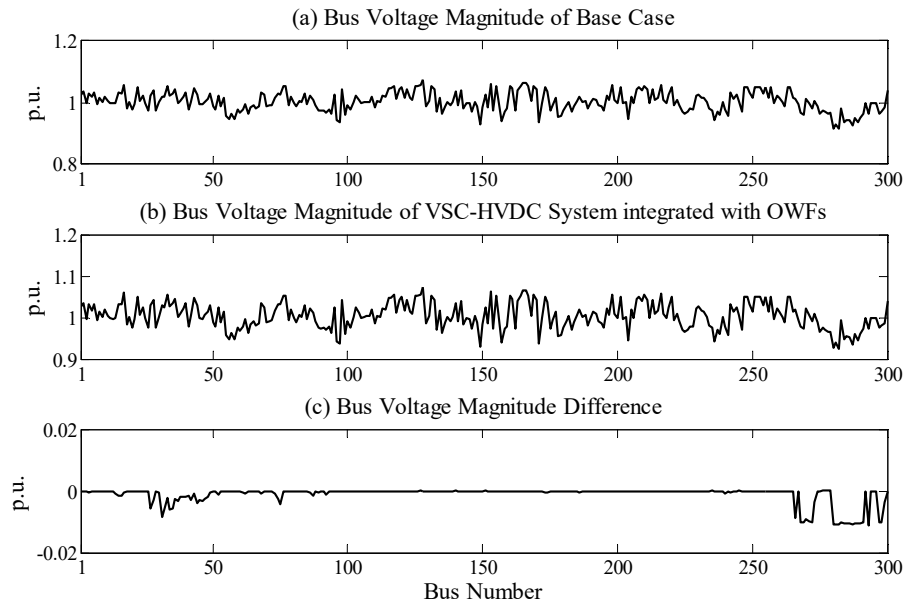


Fig. 6.15: Bus voltage profile for the study of Table 6.3

Table 6.4

Study of IEEE 300 bus system with five terminal VSC HVDC network incorporating OWFs with Droop Control and Dead-band at Operating Point A

Base case power-flow (NI=6 and CT=0.56); $V_{266}^* = 1.011 \angle -11.24$ ; $V_{270} = 1.011 \angle -11.32$ ; $V_{292} = 1.00 \angle -18.74$ ;	
DC power-flow to calculate DC reference values	
Specified Quantities	Power flow solution
$V_{DCav}^* = 3$ ; $P_{DC2}^* = -0.5$ ; $P_{DC3}^* = -0.4$ ;	$V_{DC1}^* = 3.0006$ ; $V_{DC2}^* = 2.9997$ ; $V_{DC3}^* = 2.9997$ ; $P_{DC1}^* = 0.9003$ ; $I_{DC3}^* = -0.1333$ ;
	NI=3; CT=0.02;
AC-MTDC power-flow with linear voltage droop and nonlinear droop with dead-band (VSCs connected to AC buses 266,270,292)	
Specified Quantities	Power flow solution
Control parameters	DC terminal buses
$V_{DCmax} = 3.014$ ; $V_{DChigh}^* = 3.013$ ; $V_{DClow}^* = 3.012$ ; $V_{DCmin} = 3.009$ ; $R_1 = 20$ ; $R_2 = 15$ ; $R_3 = 10$ ; $R_{max} = 30$ ;	$V_{DC1} = 3.0182$ ; $V_{DC2} = 3.0174$ ; $V_{DC3} = 3.0172$ ; $V_{DC4} = 3.0182$ ; $V_{DC} = 3.0181$ ; $P_{DC1} = 0.5483$ ; $P_{DC2} = -0.6178$ ; $P_{DC3} = -0.9300$ ;
	DC Power $P_{DC1} = 0.5483$ ; $P_{DC2} = -0.6178$ ; $P_{DC3} = -0.93$ ;
Converter	Control Mode
1	V-P droop
2	V-P droop with dead-band
3	V-I droop
$V_{266} = 1.02$ ; $Q_{sh2} = 0.08$ ; $Q_{sh3} = 0.06$ ; $P_{DCWF} = 0.55$ ; $P_{DCW} = 0.45$ ;	VSCs $\theta_{sh1} = -11.0806$ ; $\theta_{sh2} = -4.5244$ ; $\theta_{sh3} = 8.5203$ ; $m_1 = 0.9736$ ; $m_2 = 0.9664$ ; $m_3 = 0.9478$ ;
	AC terminal buses $\theta_{266} = -8.0264$ ; $V_{270} = 1.0209 \angle -7.8054$ ; $V_{292} = 1.00 \angle 3.3494$ ;
NI=6; CT=1.15;	

**Case III: Study of non-linear droop characteristics with offshore wind farms**

This study is similar to the study carried out in Table 6.2 except that VSC 2 now employs a nonlinear V-P droop with dead-band. The droop control gains are kept identical to the studies of Table 6.2. At first, the reference values for the droop lines are computed by solving the droop equations. The results are shown in rows 2-4 and column 2 of Table 6.4. Subsequently, an AC-MTDC power flow is conducted. The

results are shown in rows 5-9 and column 2 of Table 6.4. From the power flow results shown in Table 6.4, it is observed that the VSC connected at AC bus 270 operates at point 'A' of the characteristic (Fig. 6.3). The VSC connected to AC bus 270 is made to operate at different operating points of non-linear droop characteristic (Fig. 6.3) by varying the rectifying power of the OWFs. The results corresponding to the different operating points of the non-linear droop characteristic (Fig. 6.3) are shown in Table 6.5.

Table 6.5

Different operating points for nonlinear V-P droop with dead band

$P_{DCWF1}$ (p.u)	$P_{DCWF2}$ (p.u)	$V_{DC2}$ (p.u)	$\theta_{shi}$ (deg.)	$\theta_{shj}$ (deg.)	$\theta_{shk}$ (deg.)	Operating point
0.55	0.45	3.0174	-11.0806	-4.5244	8.5203	A
0.4	0.3	3.0136	-12.4818	-6.1537	4.5117	B
0.35	0.3	3.0128	-12.7342	-6.3796	3.7126	C
0.25	0.3	3.0119	-13.2508	-6.8028	2.0315	D
0.2	0.2	3.0088	-13.9909	-7.5283	0.2422	E

The convergence characteristic corresponding to the study of rows 5-13 of Table 6.4 is shown in Fig. 6.16. From Fig. 6.16, it is observed that the proposed model demonstrates excellent convergence characteristics, converging in six iterations. The bus voltage profile for the studies of Table 6.4 is shown in Fig. 6.17. From Fig. 6.17, it is again observed that in the presence of MTDC grid with OWFs, the bus voltage profile do not alter much except at the AC buses at which the VSCs are connected.

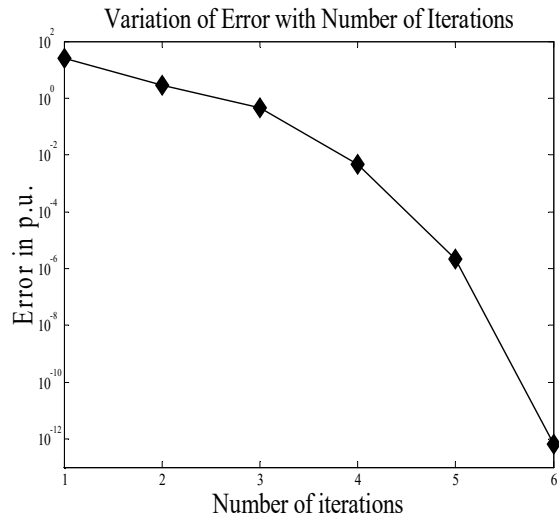


Fig. 6.16: Convergence characteristic of rows 5-13 in Table 6.4

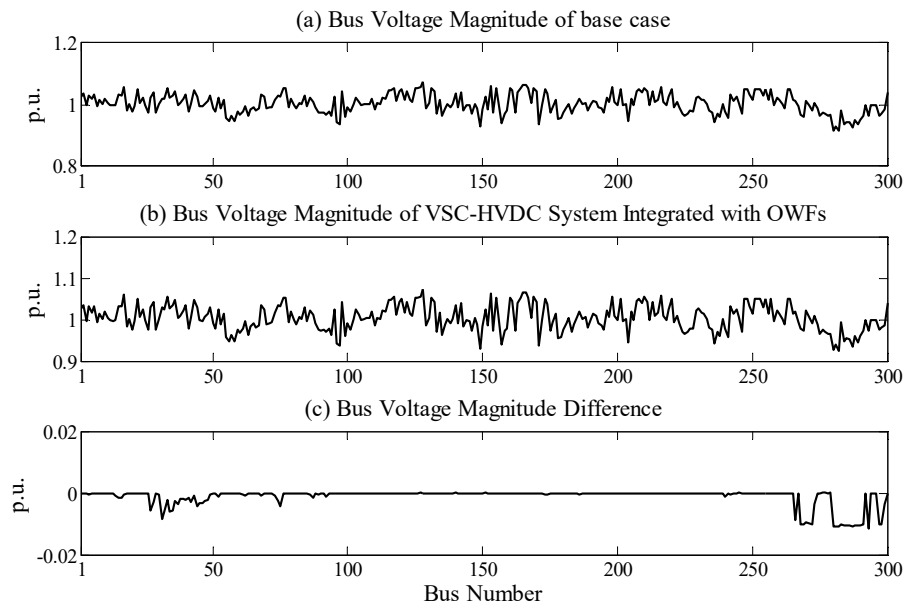


Fig. 6.17: Bus voltage profile for the study of Table 6.4

Subsequently, another study is carried out on the same AC-MTDC system but with the VSC connected at bus 270 operated in the DC voltage margin control mode. The droop control gains of the converters connected to 266 and 292 are maintained

identical to their values in Table 6.4. The droop gain of the converter connected to AC bus 270 is set to a value of 1000 for voltage margin control. For voltage margin control, the maximum and minimum DC powers are set to values of 1.0 and -1.0 p.u, respectively. The power flow solution is shown in Table 6.6. From Table 6.6, it is observed that the convergence characteristic of the proposed model is independent of the power injections from the OWFs and the location of the MTDC grid in the AC system.

Table 6.6

Study of IEEE 300 bus system with five terminal VSC HVDC network incorporating OWFs with Droop Control and Voltage Margin

Specified Quantities		Power flow solution	
Base case power-flow (NI=6 and CT=0.56); $V_{266} = 1.011 \angle -11.24$ ; $V_{270} = 1.011 \angle -11.32$ ; $V_{292} = 1.00 \angle -18.74$ ;			
DC power-flow to calculate DC reference values			
Specified Quantities		Power flow solution	
$V_{DCav}^* = 3$ ; $P_{DC2}^* = -0.5$ ; $P_{DC3}^* = -0.4$ ;		$V_{DC1}^* = 3.0006$ ; $V_{DC2}^* = 2.9997$ ; $V_{DC3}^* = 2.9997$ ; $P_{DC1} = 0.9003$ ; $I_{DC3} = -0.1333$ ; NI=3; CT=0.02;	
AC-MTDC power-flow with linear voltage droop and nonlinear voltage margin (VSCs connected to AC buses 266, 270, 292)			
Specified Quantities		Power flow solution	
Control parameters		DC terminal buses	
$V_{DCmax} = 3.014$ ; $V_{DChigh}^* = 3.013$ ; $V_{DClow}^* = 3.012$ ; $V_{DCmin} = 3.009$ ; $R_1 = 20$ ; $R_2 = 1000$ ; $R_3 = 10$ ;		$V_{DC1} = 3.0166$ ; $V_{DC2} = 3.0155$ ; $V_{DC3} = 3.0156$ ; $V_{DC4} = 3.0166$ ; $V_{DC5} = 3.0166$ ; $P_{DC1} = 0.5810$ ; $P_{DC2} = -1.00$ ; $P_{DC3} = -0.8804$ ;	
		DC Power	Converter loss (%)
		$P_{DC} = 0.5810$ ; $P_{DC2} = -1.00$ ; $P_{DC3} = -0.8804$ ;	$P_{loss} = 1.43$ ; $P_{loss2} = 1.79$ ; $P_{loss3} = 1.68$ ;
Converter	Control Mode	VSCs	
1	V-P droop	$\theta_{sh1} = -10.2907$ ; $\theta_{sh2} = -1.4338$ ;	
2	V-P droop with VM	$\theta_{sh3} = 8.3060$ ; $m_1 = 0.9638$ ;	
3	V-I droop	$m_2 = 0.9721$ ; $m_3 = 0.9469$ ;	
		AC terminal buses	
$V_{266} = 1.02$ ; $Q_{sh2} = 0.1$ ; $Q_{sh3} = 0.05$ ; $P_{DCWF1} = 0.7$ ; $P_{DCWF2} = 0.6$ ;		$\theta_{266} = \angle -7.0303$ ; $V_{270} = 1.0212 \angle -6.7475$ ; $V_{292} = 1.00 \angle 3.4060$ ;	
NI=6; CT=1.13;			

The convergence characteristics of rows 5-13 of Table 6.6 is shown in Fig. 6.18. From Fig. 6.18, it is observed that the proposed algorithm demonstrates excellent convergence characteristics, converging in six iterations. The bus voltage profile for the study of Table 6.6 is shown in Fig. 6.19. From Fig. 6.19, it is again observed that in the presence of MTDC grid with OWFs, the bus voltage profile do not alter much except at the buses at which the VSCs are connected.

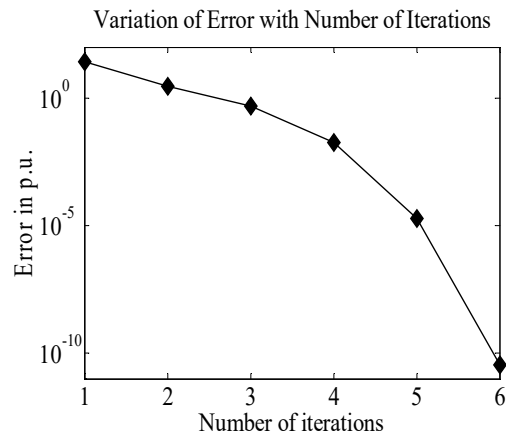


Fig. 6.18: Convergence characteristic of rows 5-13 in Table 6.5

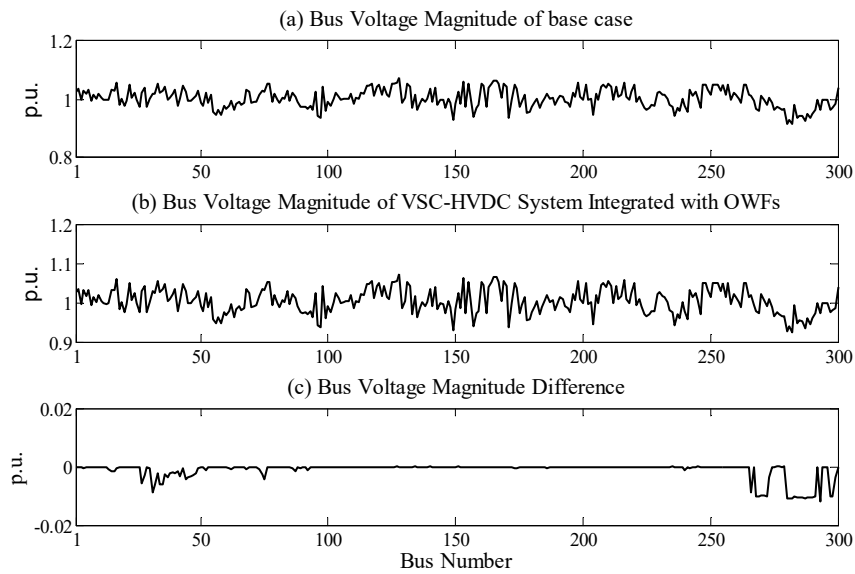


Fig. 6.19: Bus voltage profile for the study of Table 6.5



In addition, the proposed model has also been compared with some other existing models and a comparison of the convergence features is shown in Table 6.7.

Table 6.7

A comparison of convergence features with existing models

Ref No.	Tolerance (p.u)	No. of buses		NI	CT	
		AC	DC			
[82]	$10^{-8}$	29	5	Min:3 Max:15	Min:0.37 Max:0.99	
[78]	$10^{-6}$	9	4	6	0.2	
		32	4	7	0.45	
Proposed Model	$10^{-10}$	300	NIL	6	0.56	
			5 (slack)	6	1.24	
			5 Linear droop	6	Model A 1.12	Model B 1.22
			5 Droop- DB	6	1.15	
			5 Droop- VM	6	1.13	

## 6.7 Conclusions

In this chapter, a Newton Raphson power flow model of hybrid AC-MTDC systems integrated with offshore wind farms has been developed. The proposed model was investigated by including OWFs to different topologies of multi-terminal VSC-MTDC grids and integrating them with the IEEE 300-bus test network. Diverse MTDC grid control techniques including linear and nonlinear DC voltage droop control have been employed. Both models ‘A’ and ‘B’ were implemented for droop control. Droop Model ‘B’ facilitates the specification of both line end active and reactive power-flows. The model displays excellent convergence characteristics independent of the DC grid topology, the DC voltage droop control employed, the location of the MTDC grid and the OWF power injections. This validates the model.

# Chapter 7

## Conclusions and scope of further work

### 7.1 Conclusions

The following conclusions are drawn based on the work reported in this thesis:

- In the present thesis, an attempt has been made to develop Newton power-flow models of both LCC and VSC based hybrid AC-DC systems.
- For LCC based hybrid AC-DC systems, both unified and sequential Newton power-flow models were developed. It is observed that based on the selection of the base quantities, different per-unit AC-DC system models can be developed. Different per-unit AC-DC system models affect the power-flow convergence in minor ways.
- For LCC based hybrid AC-DC systems, it is also observed that different DC link control strategies affect the power-flow convergence in different ways. Nine different DC link control strategies were considered for a three-terminal HVDC network. It is observed that the power-flow convergence is affected by the location of the DC network and the operating point specifications.
- For VSC based hybrid AC-DC systems employing DC slack bus control, both unified and sequential Newton power-flow models were developed. In both the models, the modulation indices of the VSCs are obtained directly from the power-flow solution. It is observed that unlike the sequential AC-DC power-flow model, the convergence characteristic of the unified AC-DC power-flow

model is independent of location of the MTDC grid, the MTDC grid topology, the MTDC control strategy employed and the operating point specifications.

- For VSC based hybrid AC-DC systems employing DC voltage droop control, two different AC-MTDC models were developed, depending upon the terminal end power specifications. It is observed that unlike droop model ‘A’, model ‘B’ facilitates the specification of both line end active and reactive power-flows. It is observed that both the proposed models demonstrate quadratic convergence characteristics.
- A unified Newton power-flow model of VSC based hybrid AC-DC systems employing IDCPFCs was also developed. The IDCPFC is a DC power-flow controller used for power-flow management of DC grids.
- A unified Newton power flow model of hybrid AC-DC systems integrated with offshore wind farms was developed. Both linear as well as nonlinear voltage droop control of the DC grid can be accommodated in the model. The convergence characteristic of the proposed model is independent of the DC grid topology, the DC voltage droop control employed, the location of the MTDC grid and the OWF power injections.
- The VSC station losses and the losses in the converter transformers have been considered in all the models.
- Feasibility studies of all the models have been carried out on the IEEE 300-bus test system to validate their convergence characteristics.

## **7.2 Some suggestions for further work**

The work reported in this thesis has been mainly concerned with the development of Newton power-flow models of both LCC and VSC based hybrid AC-DC systems.

However, during the course of the work reported in the thesis, it was realized that the work could open up further possibilities in the area, which can be taken up in the future. Some suggestions for further work are as follows:

- Inertial support from wind turbine generators (WTGs) connected to AC grids through HVDC links is an important issue which needs to be addressed. This support is usually provided by controlling the power references of the WTGs. Incorporating this aspect in the power-flow modeling appears to be challenging.
- For modeling of offshore wind farms integrated with the DC grid, their detailed power-flow modeling needs to be carried out. In addition, other sources of renewable energy can also be modelled in the existing AC-DC power-flow algorithm.
- Power-flow modeling of AC-DC systems involving multiple AC grids interconnected through multi-terminal DC grids.

# Bibliography

- [1] J. Arrillaga and N.R Watson, *Computer Modelling of Electrical Power Systems*, 2<sup>nd</sup> ed., John Wiley & Sons Ltd, 2003.
- [2] P. Kundur, *Power System Stability and Control*, Tata McGraw-Hill Publishing Co. Ltd., 2007.
- [3] K.R. Padiyar, *HVDC Power Transmission Systems*, 2<sup>nd</sup> edn., New Age International Publishers, 2012.
- [4] V. K. Sood, *HVDC and FACTS Controllers – Applications of Static Converters in Power Systems*, Kluwer, 2004.
- [5] C. K. Kim, V. K. Sood, G. S. Jang, S. J. Lim and S. J. Lee, *HVDC TRANSMISSION: Power Conversion Applications in Power Systems*, John Wiley & Sons Ltd, 2009.
- [6] X.F. Wang, Y.H. Song and Malcolm Irving, *Modern Power Systems Analysis*, Springer, Berlin, Germany, 2008.
- [7] J. Arrillaga, Y. H. Liu and N.R Watson, *Flexible Power Transmission: The HVDC Options*, John Wiley & Sons Ltd, 2007.
- [8] E. Acha, V.G.Agelidis, O. Anaya Lara and T.J.E. Miller, *Power Electronic Control in Electrical Systems*, Newnes, Butterworth, Oxford, 2002.
- [9] E. Acha, C.R Fuerte-Esquivel, H.A. Perez and C.A. Camacho, *FACTS modelling and Simulation in Power Networks*, John Wiley, 2004.
- [10] X.P. Zhang, C. Rehtanz and B. Pal, *Flexible AC Transmission Systems: Modelling and Control*, Springer, 2006.
- [11] A. Yazdani and R. Iravani, *Voltage-Sourced Converters in Power Systems: Modeling, Control and Applications*, Wiley-IEEE Press, 2010, pp. 171.

- [12] N.R Chaudhuri, B. Chaudhuri, R. Majumdar and A. Yazdani, *Multi-terminal Direct Current Grids: Modelling, Analysis and Control*, IEEE Press, Wiley, 2014.
- [13] N.G. Hingorani and L. Gyugyi, *Understanding FACTS: Concept and Technology of Flexible AC Transmission Systems*, IEEE Press, New York, 2000.
- [14] D.P. Kothari and I.J Nagrath, *Modern Power System Analysis*, 3<sup>rd</sup> ed., Tata McGraw Hill, New Delhi, 2003.
- [15] Gunnar Asplund, “Application of HVDC Light to Power System Enhancement”, *IEEE Proc. PES Winter Meeting*, January 2000.
- [16] N. Flourentzou, V.G. Agelidis and G.D. Demetriades, “VSC-Based HVDC power Transmission Systems: An Overview”, *IEEE Trans. Power Electronics*, vol. 24, no. 3, pp. 592-602, March 2009.
- [17] C. Dierckxsens, “VSC MTDC Systems with Distributed Slack Bus,” M.S. thesis, Katholieke Universiteit, Leuven, Belgium, 2010.
- [18] G. Daelemans, “VSC HVDC in Meshed Networks”, Katholieke Universiteit Leuven, Belgium, Master’s Thesis, pp. 11, 2008.
- [19] J. Blau, “Europe plans a North Sea grid”, *IEEE Spectr.*, vol. 47, issue 3, March 2010, pp. 12–13.
- [20] Temesgen M. Haileselassie, Kjetil Uhlen, “Power System Security in a Meshed North Sea HVDC Grid”, *IEEE Proc., Invited Paper*, vol. 101, no. 4, April 2013, pp. 978-990.
- [21] S.K. Chaudhary, R. Teodorescu and P. Rodriguez, “Wind Farm Grid Integration Using VSC Based HVDC Transmission: An Overview”, *IEEE Conf. ENERGY 2030*, Nov. 2008, pp.1-7.

- [22] R.T. Pinto, P. Bauer, S. Rodrigues, E. Wiggelinkhuizen, J. Pierik and B. Ferreira, “A novel distributed direct voltage control strategy for grid integration of offshore wind energy systems through MTDC network”, *IEEE Trans. Industrial Electronics*, vol. 60, pp. 2429-2441, June 2013.
- [23] S. Cole, J. Beerten and R. Belmans, “Generalized Dynamic VSC MTDC Model for Power System Stability Studies”, *IEEE Trans. Power Systems*, vol. 25, no. 3, pp. 1655-1662, Aug. 2010.
- [24] E.P Arauzo, F.D. Bianchi, A. Ferre and O. G. Bellmunt, “Methodology for Droop Control Dynamic Analysis of Multiterminal VSC-HVDC Grids for Offshore Wind Farms”, *IEEE Trans. Power Del.*, vol. 26, no. 4, pp. 2476-2485, Oct. 2011.
- [25] M. A. Penalba, A. E. Alvarez, O. G. Bellmunt and A. Sumper, “Optimum voltage control for loss minimization in HVDC multi-terminal transmission systems for large offshore wind farms”, *Electrical Power Systems Research*, vol. 89, pp. 54-63, Aug. 2012.
- [26] O. G. Bellmunt, J. Liang, J. Ekanayake and N. Jenkins, “Voltage Current Characteristics of Multiterminal HVDC VSC for Offshore Wind Farms”, *Electrical Power Systems Research*, vol 81, pp. 440-450, Feb. 2011.
- [27] K. Rouzbehi, A. Miranian, J.I Candela, A. Luna and P. Rodriguez, “A Generalised Voltage Droop Strategy for Control of Multi-terminal DC Grids”, *IEEE Trans. Industry Applications*, vol. 51, no. 1, pp. 607-618, Feb. 2015.
- [28] A. S. A. Khalik, A. M. Massoud, A. A. Elserougi and S. Ahmed, “Optimum Power Transmission Based Droop Control Design for Multi-terminal HVDC of Offshore Wind Farms”, *IEEE Trans. Power Syst.*, vol. 28 no. 3, pp. 3401-3409, Aug. 2013.

- [29] X. Zhao and K. Li, "Droop Setting Design for Multi-terminal HVDC Grids Considering Voltage Deviation Impacts", *Electric Power Systems Research*, vol., 123, pp. 67-75, Feb. 2015.
- [30] L. Xu, B.W. Williams, and L. Yao, "Multi-terminal DC Transmission Systems for Connecting Large Offshore Wind Farms", *IEEE Proc. PES General Meeting- Conversion and Delivery of Electrical Energy, 21<sup>st</sup> Century*, July 2008, pp. 1-7.
- [31] R. da Silva, R. Teodorescu and Rodriguez, "Power Delivery in MTDC Transmission System for Offshore Wind Power Applications", *IEEE Proc. PES ISGT Europe*, Oct. 2010, pp. 1-8.
- [32] P. Mitra, L. Zhang and L. Harnefors, "Offshore Wind Integration to a Weak Grid by VSC-HVDC Links Using Power Synchronization Control: A Case Study", *IEEE Trans. Power Del.*, vol 29, no. 1, pp. 453-461, Feb., 2014.
- [33] L. Zhang, L.Harnefors and H. P. Nee, "Interconnection of Two Very Weak AC Systems by VSC HVDC Links Using Power Synchronization Control", *IEEE Trans. Power Syst.*, vol. 26, no. 1, pp. 344-355, Feb. 2011.
- [34] L. Zhang, L. Harnefors and H. P. Nee, "Modeling and Control of VSC HVDC Links Connected to Island Systems", *IEEE Trans. Power Syst.*, vol. 26, no. 2, pp. 783-793, May 2011.
- [35] A. E. Alvarez, J. Beerten, D. V. Hertem and O. G. Bellmund, "Hierarchical Power Control of Multi-terminal HVDC Grids", *Electrical Power Systems Research*, vol. 21, pp. 207-215, April 2015.
- [36] A. Moawwad, M.S El Moursi, W. Xiao and J. L. Kirtley Jr., "Novel Configuration and Transient Management Control Strategy for VSC-HVDC", *IEEE Trans. Power Syst.*, vol. 29, no. 5, pp. 2478-2488, Sep. 2014.



- [37] J. Beerten and R. Belmans, "Analysis of power sharing and voltage deviations in droop controlled DC grids", *IEEE Trans. Power syst.*, vol. 28, no. 4, pp. 4588-4597, Nov. 2013.
- [38] T.M. Haileselassie and K. Uhlen, "Impact of DC line Voltage Drops on Power Flow of MTDC Using Droop Control", *IEEE Trans. on Power Syst.*, vol. 27, no. 3, pp. 1441-1449, 2012.
- [39] D. Jovicic and B. T. Ooi, "Developing DC Transmission Networks Using DC Transformers", *IEEE Trans. on Power Del.*, vol. 25, no. 4, pp. 2535-2543, Oct. 2010.
- [40] Q. Mu, J. Liang, Y. Li and X. Zhou, "Power Flow Control Devices in DC Grids", *IEEE Power and Energy Society General Meeting*, 2012, pp. 1-7.
- [41] C. Barker and R. Whitehouse, "A Current Flow Controller for use in HVDC grids", *Proc. IET Int. Conf. AC DC Power Transm.*, 2012, pp. 1-5.
- [42] E. Veilleux and B. Ooi, "Multiterminal HVDC With Thyristor Power-Flow Controller", *IEEE Trans. Power Del.*, vol. 27, no. 3, pp. 1205-1212, July 2012.
- [43] W. Chen, X. Zhu, L. Yao, X. Ruan, Z. Wang and Y. Cao, "An Interline DC Power-Flow Controller (IDCPFC) for Multiterminal HVDC System", *IEEE Trans. Power Del.*, vol. 30, no. 4, pp. 2027-2036, Aug. 2015.
- [44] W. Chen, X. Zhu, L. Yao, G. Ning, Y. Li, Z. Wang, W. Gu and X. Qu, "A Novel Interline DC Power Flow Controller (IDCPFC) for Meshed HVDC Grids", *IEEE Trans. Power Del.*, vol. 31, no. 4, pp. 2027-2036, pp. 1719-1727, Aug. 2016.
- [45] L. Gyugyi, K. K. Sen, and C. D. Schauder, "The Interline Power Flow Controller concept: A new approach to power flow management in transmission systems", *IEEE Trans. Power Del.*, vol. 14, no. 3, pp. 1115-1123, July 1999.

- [46] Y. Zhang, Y. Zhang, and C. Chen, “A novel power injection model of IPFC for power flow analysis inclusive of practical constraints”, *IEEE Trans. Power Syst.*, vol. 21, no. 4, pp. 1550–1556, Nov. 2006.
- [47] S. Bhowmick, B. Das and N. Kumar, “An Advanced IPFC Model to Reuse Newton Power Flow Codes”, *IEEE Trans. Power Syst.*, vol. 24, no. 2, pp. 525-532, May 2009.
- [48] W. F. Tinney and C. E. Hart, “Power-Flow Solution by Newton’s Method”, *IEEE Trans. Power Apparatus and Syst.*, vol. PAS-86, no. 11, pp. 1449–1460, Nov. 1967.
- [49] B. Stott and O. Alsac, “Fast Decoupled Load Flow”, *IEEE Trans. Power Apparatus and Systems*, vol. PAS-93, no. 3, pp. 859–869, May/June 1974.
- [50] J. Arrillaga, B.J. Harker and K.S Turner, “Clarifying an ambiguity in recent AC-DC load flow formulations”, *IEE Proc. C* 127, 1980, pp. 324-325.
- [51] J. Arrillaga, P. Bodger, “Integration of HVDC Links with Fast Decoupled Load Flow Solutions”, *IEEE Proc.*, vol. 124, no. 5, May 1977, pp. 463-468.
- [52] Y. K. Fan, D. Niebur, C.O. Nwankpa, H. Kwanyu and R. Fischl, “Multiple Power Flow Solutions of Small Integrated AC-DC Power Systems”, *IEEE Proc. Int. Symp. Circuits and Systems, Geneva, Switzerland*, May 2000, pp. 224-227.
- [53] H. A. Perez, E. Acha and C.R.F. Esquivel, “High Voltage Direct Current Modelling in Optimal Power Flows”, *Electrical Power and Energy Syst.*, pp. 157-168, March 2008.
- [54] S. Messalti, S. Belkhiat, S. Saadate and D. Flieller, “A new Approach for Load Flow Analysis Integrated AC-DC Power Systems using Sequential Modified

- Gauss Seidel Methods”, *European Trans. Electrical Power*, vol. 22, issue 4, pp. 421-432, May 2012.
- [55] J. Yu, W. Yan, W. Y. Li, C.Y Chung and K.P Wong, “An Unfixed Piecewise Optimal Reactive Power Flow Model and its Algorithms for AC-DC Systems”, *IEEE Trans. Power Syst.*, vol. 23, no. 1, pp. 170-176, Feb. 2008.
- [56] U. Kilic and K. Ayan, “Optimal Power Flow Solution of Two Terminal HVDC Systems Using Genetic Algorithm”, *Electrical Engg.*, pp. 65-77, 2014.
- [57] U. Kilic and Kursat Ayan, “Optimizing Power Flow of AC-DC Power Systems using Artificial Bee Colony Algorithms”, *Electrical Power and Energy Syst.*, vol. 53, pp. 592-602, Dec. 2013.
- [58] U. Kilic, K. Ayan and U. Arifoglu, “Optimizing Reactive Power Flow of HVDC Systems Using Genetic Algorithms”, *Electrical Power and Energy Syst.*, vol., 55, pp. 1-12, Feb. 2014.
- [59] M. M. DJesus, D. S. Martin, S. Arnaltes and E. D. Castronuovo, “Optimal Reactive Power Allocation in an Offshore Wind Farm with LCC HVDC Link Connection”, *Renewable Energy*, vol. 40, pp. 157-166, April 2012.
- [60] H.N.P. Srivastava, A.K. Sinha and L. Roy, “Fast Second order AC-DC Load Flow”, *Electrical Machines and Power Systems*, pp. 233-247, 1995.
- [61] J. Arrillaga and P.S. Bodger, “AC – DC Load Flows with Realistic Representation of the Converter Plant”, *Proc. Inst. Elect. Eng.*, vol. 125, pp. 41-46, Jan. 1978.
- [62] Duane A. Braunagel, Leonard A. Kraft, Jewel L. Whysong, “Inclusion of DC Converter and Transmission Equations Directly in A Newton Power Flow”, *IEEE Trans. Power Apparatus and Syst.*, PAS-95, pp. 76-87, Feb. 1976.

- [63] M.M .El-Marsafawy, R.M Mathur, “A New, Fast Technique for Load Flow Solution of Integrated Multi terminal DC/ AC Systems”, *IEEE Trans. Power Apparatus and Syst.*, PAS-99, pp. 246-255, Feb. 1980.
- [64] T Smed, G Andersson, G.B. Sheble and L.L. Grigsby, “A New Approach to AC/ DC Power Flow”, *IEEE Trans. Power Syst.*, vol. 6, no. 3, pp. 1238-1244, Aug. 1991.
- [65] C.M. Ong, A. H. Nejad, “A General Purpose Multi-terminal DC Load Flow”, *IEEE Trans. Power Apparatus and Syst.*, vol. PAS 100, no. 7, pp. 3166-3174, July 1981.
- [66] J. Reeve, G. Fahmy and B. Stott, “Versatile load flow method for multi terminal HVDC systems”, *IEEE Trans. Power Appar. Syst.* PAS-96, pp. 925-933, June 1977.
- [67] J. Mahseredjian, S. Lefebvre and D. Mukhedkar, “A Multiterminal HVDC Load Flow with Flexible Control Specifications”, *IEEE Trans. Power Syst.*, vol. PWRD-1, no. 2, pp. 272-282, April 1986.
- [68] Q. Ding, T.S. Chung and B. Zhang, “An Improved Sequential Method for AC/MTDC Power System State Estimation”, *IEEE Trans. Power Syst.*, vol. 16, no. 3, pp. 506-512, Aug. 2001.
- [69] Chongru Liu, Boming Zhang, Yunhe Hou, Felix F. Wu and Yingshang Liu, “An Improved Approach for AC-DC Power flow Calculation with Multi Infeed DC Systems”, *IEEE Trans. Power Syst.*, vol. 26, no. 2, pp. 862-869, May 2011.
- [70] K. R. Padiyar and V. K. Raman, “A General Method for Power Flow Analysis in MTDC Systems”, *ACE 90 Proceedings of XVI Annual Convention and Exhibition of the IEEE in India*, 1990, pp. 146-150.

- [71] Congru Liu, Anjan Bose and Yunhe Hou, "Discussion of the Solvability of HVDC Power Flow with a Sequential method", *Electric Power Systems Research*, vol. 92, pp. 155-161, Nov. 2012.
- [72] Q.F. Ding and B.M. Zhang, "A New Approach to AC/MTDC Power Flow", *APSCOM IEEE*, vol. 2, 1997, pp. 689-694.
- [73] Padiyar, K.R., Kalyanaraman, "Power Flow Analysis in MTDC-AC Systems- A New Approach", *Electric Machines and Power Systems*, vol. 23, pp. 37-54, 1995.
- [74] H. Fudeh and C.M. Ong, "A Simple and Efficient AC-DC Load Flow Method for Multiterminal DC systems", *IEEE Trans. Power Apparatus and Systems*, vol. PAS-100, no. 11, pp. 4389-4396, Nov. 1981.
- [75] M.E. El-Hawary, S.T Ibrahim, "A new Approach to AC –DC load flow Analysis", *Electric Power Systems Research*, vol. 33, pp. 193-200, 1995.
- [76] C. Angeles-Camacho, O.L Tortelli, E. Acha, and C.R Fuerte-Esquivel, "Inclusion of a high voltage DC-voltage source converter model in a Newton Raphson power flow algorithm", *Proc. Inst. Elect. Eng., Gen., Transm., Distrib.*, vol 150. no. 6, Nov. 2003, pp. 691-696.
- [77] X.P. Zhang, "Multiterminal voltage-sourced converter-based HVDC models for power flow analysis", *IEEE Trans. Power Syst.*, vol. 19, no. 4 , pp. 1877-1884, Nov. 2004.
- [78] M. Baradar and M. Ghandhari, "A Multi-Option Unified Power Flow Approach for Hybrid AC/DC Grids Incorporating Multi-Terminal VSC-HVDC", *IEEE Trans. Power Syst.*, vol. 28, no. 3, pp. 2376-2383, Aug. 2013.

- [79] R. Z. Chai, B.H. Zhang, Z.Q. Bo and J.M. Dou, “A Generalized Unified Power Flow Algorithm for AC/DC Networks Containing VSC Based Multi-terminal DC Grid”, *POWERCON, CP2771*, 2014, pp. 2361-2366.
- [80] L. Gengyin, Z.Ming, H. Jie, L. Guangkai, and L. Haifeng, “Power flow calculation of power systems incorporating VSC-HVDC”, *Proc. Int. Conf. Power System Technology (PowerCon)*, vol. 2, pp. 1562–1566, Nov. 2004.
- [81] J. Beerten, D. V. Hertem and R. Belmans, “VSC MTDC Systems with a Distributed DC Voltage Control- A Power Flow Approach”, *IEEE Trondheim Power Tech*, 2011, pp. 1-6.
- [82] W. Wang, Mike Barnes, “Power Flow Algorithms for Multi-Terminal VSC-HVDC With Droop Control”, *IEEE Trans. Power Syst.*, vol. 29, no. 4, pp. 1721-1730, July 2014.
- [83] J. Cao, W. Du and H.F. Wang, “Minimization of Transmission Loss in Meshed AC/DC Grids with VSC-MTDC Networks”, *IEEE Tran. Power Syst.*, vol. 28, no. 3, pp. 3047-3055, Aug. 2013.
- [84] L. Xiao, Z. Xu, T. An and Z. Bian, “Improved Analytical Model for the Study of Steady State Performance of Droop-controlled VSC-MTDC Systems”, *IEEE Trans. Power Syst., Early Access*, 2016.
- [85] E. Acha, B. Kazemtabrizi and L. M. Castro, “A New VSC-HVDC Model for Power Flows Using the Newton-Raphson Method”, *IEEE Trans. Power Syst.*, vol. 28, no. 3 , pp. 2602-2612, Aug. 2013.
- [86] A. P. Martinez, C. Esquivel, and C. Camacho, “Voltage Source Converter Based High Voltage DC System Modelling for Optimal Power Flow Studies,” *Electric Power Components and Systems*, vol. 40, issue 3, pp. 312-320, Jan. 2012.

- [87] R. Wiget, G. Anderson, “DC Optimal Power Flow Including HVDC Grids”, *IEEE Electrical Power and Energy Conference*, 2013 pp. 1-6.
- [88] M. Baradar, M. Ghandhari and D.V. Hertem, “The modeling of multi-terminal VSC-HVDC in power flow calculation using unified methodology”, *Proc. IEEE PES Int. Conf. Exhib. Innovative Smart Grid Technology. (ISGT Europe)*, Dec. 2011, pp. 1-6.
- [89] J. Lei, T. An, Z. Du and Z. Yuan, “A General Unified AC/DC Power Flow Algorithm with MTDC”, *IEEE Trans. Power Syst., Early Access*, 2016.
- [90] E. Acha and L. M. Castro, “A generalised frame of reference for the incorporation of, multi-terminal VSC HVDC systems in Power Flow Solutions”, *Electrical Power Systems Research*, vol. 136, pp. 415-424, July 2016,.
- [91] Temesgen M. Haileselassie, Kjetil Uhlen, “Power flow analysis of multi-terminal HVDC networks”, in *Proc. Power Tech*, Trondheim, Norway, 2011, pp.1-6.
- [92] J. Beerten, S. Cole and R. Belmans, “Generalized Steady-State VSC MTDC Model for Sequential AC/DC Power Flow Algorithms”, *IEEE Trans. Power Syst.*, vol. 27, no. 2, pp. 821-829, May 2012.
- [93] J. Beerten, S. Cole and R. Belmans, “Implementation Aspects of a sequential AC/DC power flow computation algorithm for multi-terminal VSC HVDC systems,” *IET International conference*, 2010, pp. 1-6.
- [94] J. Beerten, S. Cole and R. Belmans, “A sequential AC/DC power flow algorithm for networks containing multi-terminal VSC-HVDC systems”, *Proc. IEEE PES General General Meeting*, July 2010, pp. 1-7.

- [95] G. Daelemans, K. Srivastava, M.Reza, S.Cole and Belmans, “Minimization of Steady State Losses in Meshed Networks using VSC HVDC”, *IEEE Power and Energy Society General Meeting*, 2009, pp. 1-5.
- [96] E. B. Melendrez, L.E. U. Caballero and E.L. M. Goytia, “Sequential algorithm based model for the study of AC/DC power flow in VSC-MTDC systems”, *IEEE International Autumn Meeting on Power Electronics and computing, ROPEC*, 2015, pp. 1-5.
- [97] N. Narayanan and P. Mitra, “A Comparative study of a sequential and simultaneous AC-DC Power flow algorithms for a multi-terminal VSC-HVDC system”, *IEEE ISGT*, 2013, pp.1-6.
- [98] G. Zeng, T. Hennig and K. Rohrig, “Multi-terminal HVDC Modelling in Power Flow Analysis Considering Converter Station Topologies and Losses”, *Energy Procedia, Elsevier*, vol 80, 2015, pp. 123-130.
- [99] W. Feng, L. A. Tuan, L. B. Tjernberg, A. Mannikoff and A. Bergman, “A New Approach for Benefit Evaluation of Multiterminal VSC–HVDC Using A Proposed Mixed AC/DC Optimal Power Flow”, *IEEE Trans. Power Del.*, vol. 29, no. 1, pp. 432-443, Feb. 2014.
- [100] A. Martinez, C. Esquivel, H. Perez and E. Acha, “Modeling of VSC-Based HVDC Systems for a Newton Raphson OPF Algorithm”, *IEEE Trans. Power Syst.*, vol. 22, no. 4, pp. 1794-1799, Nov. 2007.
- [101] J. Cao, W. Du, and H. F. Wang, “An Improved Corrective Security Constrained OPF for Meshed AC/DC Grids with Multi-Terminal VSC-HVDC”, *IEEE Trans. Power Syst.*, Early Access Articles, pp. 1-11, 2016.
- [102] K. Rouzbehi, A. Miranian, A. Luna and P. Rodriguez, “DC voltage control and power sharing in multi-terminal DC grids based on optimal dc power flow and



voltage droop strategy”, *IEEE Journal of Emerging and selected topics in power electronics*, vol. 02, no. 4, pp. 1171-1180, Dec. 2014.

[103] M. J. Carrizosa, F.D. Navas and Gilney Damm, “Optimal Power Flow in Multi-terminal HVDC Grids with Offshore Wind Farms and Storage Devices”, *Electrical Power and Energy Systems*, vol. 65, pp. 291-298, 2015.

[104] <http://www.ee.washington.edu/research/pstca/>

## Appendix A

### A.1 Expression for the net active and reactive power injections by incorporating three terminals LCC HVDC system in an existing AC system by using Unified method

For AC buses ‘i’, ‘j’ and ‘k’, the rectifier is connected at bus ‘i’. Two inverters ‘1’ and ‘2’ are connected at buses ‘j’ and ‘k’ respectively.

For control strategy ‘1’ and ‘5’

$$P_i = \sum_{p=1}^n V_i V_p Y_{ip} \cos(\theta_i - \theta_p - \phi_{ip}) + V_{DCR} \left( \frac{2 V_{DCR} - V_{DCI1} - V_{DCI2}}{R_{DC}} \right) \quad (A.1)$$

$$Q_i = \sum_{p=1}^n V_i V_p Y_{ip} \sin(\theta_i - \theta_p - \phi_{ip}) + V_{DCR} \left( \frac{2 V_{DCR} - V_{DCI1} - V_{DCI2}}{R_{DC}} \right) \tan\Phi_R \quad (A.2)$$

$$P_j = \sum_{p=1}^n V_j V_p Y_{jp} \cos(\theta_j - \theta_p - \phi_{jp}) - P_{DCI1} \quad (A.3)$$

$$Q_j = \sum_{p=1}^n V_j V_p Y_{jp} \sin(\theta_j - \theta_p - \phi_{jp}) + P_{DCI1} \tan\Phi_{I1} \quad (A.4)$$

$$P_k = \sum_{p=1}^n V_k V_p Y_{kp} \cos(\theta_k - \theta_p - \phi_{kp}) - P_{DCI2} \quad (A.5)$$

$$Q_k = \sum_{p=1}^n V_k V_p Y_{kp} \sin(\theta_k - \theta_p - \phi_{kp}) + P_{DCI2} \tan\Phi_{I2} \quad (A.6)$$

### A.1.2 Some typical elements and sub-matrices of Jacobian in eqn. (2.21) for control strategies ‘1’ and ‘5’ (Unified method)

$$\frac{\partial P_i}{\partial V_{DCI1}} = -\frac{V_{DCR}}{R_{DC}}, \quad \frac{\partial P_i}{\partial V_{DCI2}} = -\frac{V_{DCR}}{R_{DC}}, \quad \frac{\partial Q_i}{\partial V_{DCI1}} = -\frac{V_{DCR}}{R_{DC}} \tan\Phi_R, \quad \frac{\partial Q_i}{\partial V_{DCI2}} = -\frac{V_{DCR}}{R_{DC}} \tan\Phi_R;$$

$$\frac{\partial Q_i}{\partial \Phi_R} = V_{DCR} \left[ \frac{2V_{DCR} - V_{DCI1} - V_{DCI2}}{R_{DC}} \right] \sec^2 \Phi_R; \quad \frac{\partial Q_i}{\partial \Phi_{11}} = P_{DCI1} \sec^2 \Phi_{11}; \quad \frac{\partial Q_k}{\partial \Phi_{12}} = P_{DCI2} \sec^2 \Phi_{12};$$

Sub-matrix of control strategy '1' for Model '1' is given below

$$\frac{\partial f}{\partial \mathbf{X}} = \begin{bmatrix} -kk_1 & -kk_1 & -V_i \cos \alpha_R & 0 & 0 & 0 & 0 & 0 & 0 \\ 1 - kk_1 & 0 & 0 & -V_j \cos \gamma_{11} & 0 & 0 & 0 & 0 & 0 \\ 0 & 1 - kk_1 & 0 & 0 & -V_k \cos \gamma_{12} & 0 & 0 & 0 & 0 \\ 0 & 0 & -V_i \cos \Phi_R & 0 & 0 & a_R V_i \sin \Phi_R & 0 & 0 & 0 \\ 1 & 0 & 0 & -V_j \cos \Phi_{11} & 0 & 0 & a_{11} V_j \sin \Phi_{11} & 0 & 0 \\ 0 & 1 & 0 & 0 & -V_k \cos \Phi_{12} & 0 & 0 & a_{12} V_k \sin \Phi_{12} & 0 \\ kk_2 & 0 & 0 & 0 & 0 & 0 & 0 & 0 & 0 \\ 0 & kk_2 & 0 & 0 & 0 & 0 & 0 & 0 & 0 \end{bmatrix}$$

$$kk_1 = \frac{X_c}{R_{DC}}; \quad kk_2 = -V_{DCR} + 2V_{DCI1};$$

Sub-matrix of control strategy '1' for Model '2' is given below

$$\frac{\partial f}{\partial \mathbf{X}} = \begin{bmatrix} -k_1 & -k_1 & -k_2 V_i \cos \alpha_R & 0 & 0 & 0 & 0 & 0 & 0 \\ 1 - k_1 & 0 & 0 & -k_2 V_j \cos \gamma_{11} & 0 & 0 & 0 & 0 & 0 \\ 0 & 1 - k_1 & 0 & 0 & -k_2 V_k \cos \gamma_{12} & 0 & 0 & 0 & 0 \\ 0 & 0 & -k_2 V_i \cos \Phi_R & 0 & 0 & k_2 a_R V_i \sin \Phi_R & 0 & 0 & 0 \\ 1 & 0 & 0 & -k_2 V_j \cos \Phi_{11} & 0 & 0 & k_2 a_{11} V_j \sin \Phi_{11} & 0 & 0 \\ 0 & 1 & 0 & 0 & -k_2 V_k \cos \Phi_{12} & 0 & 0 & k_2 a_{12} V_k \sin \Phi_{12} & 0 \\ kk_2 & 0 & 0 & 0 & 0 & 0 & 0 & 0 & 0 \\ 0 & kk_2 & 0 & 0 & 0 & 0 & 0 & 0 & 0 \end{bmatrix}$$

$$\text{where } k_1 = 3 \frac{X_c n_b}{\pi R_{DC}}; \quad k_2 = \frac{3\sqrt{2} n_b}{\pi}; \quad kk_2 = -V_{DCR} + 2V_{DCI1};$$

Sub-matrix of control strategy '5' for Model '1'

$$\frac{\partial f}{\partial \mathbf{X}} = \begin{bmatrix} -kk_1 & -kk_1 & -a_R V_i & 0 & 0 & 0 & 0 & 0 & 0 \\ 1 - kk_1 & 0 & 0 & -a_{11} V_j & 0 & 0 & 0 & 0 & 0 \\ 0 & 1 - kk_1 & 0 & 0 & -a_{12} V_k & 0 & 0 & 0 & 0 \\ 0 & 0 & 0 & 0 & 0 & a_R V_i \sin \Phi_R & 0 & 0 & 0 \\ 1 & 0 & 0 & 0 & 0 & 0 & a_{11} V_j \sin \Phi_{11} & 0 & 0 \\ 0 & 1 & 0 & 0 & 0 & 0 & 0 & a_{12} V_k \sin \Phi_{12} & 0 \\ kk_2 & 0 & 0 & 0 & 0 & 0 & 0 & 0 & 0 \\ 0 & kk_2 & 0 & 0 & 0 & 0 & 0 & 0 & 0 \end{bmatrix}$$

$$\text{where, } kk_1 = \frac{X_c}{R_{DC}}; \quad kk_2 = -V_{DCR} + 2V_{DCI1};$$

Sub-matrix of control strategy '5' for Model '2'

$$\frac{\partial f}{\partial X}$$

$$= \begin{bmatrix} -k_1 & -k_1 & -k_2 a_R V_i & 0 & 0 & 0 & 0 & 0 \\ 1 - k_1 & 0 & 0 & -k_2 a_{i1} V_j & 0 & 0 & 0 & 0 \\ 0 & 1 - k_1 & 0 & 0 & -k_2 a_{i2} V_k & 0 & 0 & 0 \\ 0 & 0 & 0 & 0 & 0 & -k_2 a_R V_i \sin \Phi_R & 0 & 0 \\ 1 & 0 & 0 & 0 & 0 & 0 & -k_2 a_{i1} V_j \sin \Phi_{i1} & 0 \\ 0 & 1 & 0 & 0 & 0 & 0 & 0 & -k_2 a_{i2} V_k \sin \Phi_{i2} \\ k k_2 & 0 & 0 & 0 & 0 & 0 & 0 & 0 \\ 0 & k k_2 & 0 & 0 & 0 & 0 & 0 & 0 \end{bmatrix}$$

where  $k_1 = 3 \frac{X_c n_b}{\pi R_{DC}}$ ;  $k_2 = \frac{3\sqrt{2} n_b}{\pi}$ ;  $k k_2 = -V_{DCR} + 2V_{DCI1}$ ;

### A.1.3 Initial values of variables in LCC based HVDC systems

**Table A.1**

Variables in LCC HVDC system		Initial values
DC bus voltage	$V_{DC}^0$	1 p.u (Model 1); 2.3 p.u (Model 2)
Converter transformer tap ratios	$a_R^0, a_{i1}^0$ and $a_{i2}^0$	1
Firing angle of rectifier	$\alpha_R^0$	$\cos \alpha_R^0 = 1$
Extinction angles of inverters	$\gamma_{i1}^0$ and $\gamma_{i2}^0$	$\cos \gamma_{i1}^0 = 1$ ; $\cos \gamma_{i2}^0 = 1$
Power factors	$\cos \Phi_R^0, \cos \Phi_{i1}^0$ and $\cos \Phi_{i2}^0$	0.9

### A.2 Expression for the magnitude of converter current ( $I_{sha}$ ) for considering converter losses of a<sup>th</sup> VSC

From eqn. (3.1),

$$S_{sha} = V_{i+a-1} I_{sha}^* = V_{i+a-1} [Y_{sha}^* (V_{sha}^* - V_{i+a-1}^*)] \quad (A.7)$$

$$= V_{i+a-1} m_a c V_{DCa} Y_{sha} \angle (\theta_{i+a-1} - \theta_{sha} - \Phi_{sha}) - V_{i+a-1}^2 Y_{sha} \angle -\Phi_{sha}$$

$$= V_{i+a-1} m_a c V_{DCa} Y_{sha} \{ \cos(\theta_{i+a-1} - \theta_{sha} - \Phi_{sha}) + j \sin(\theta_{i+a-1} - \theta_{sha} - \Phi_{sha}) \}$$

$$- V_{i+a-1}^2 Y_{sha} \{ \cos \Phi_{sha} - j \sin \Phi_{sha} \}$$

$$= V_{i+a-1} m_a c V_{DCa} Y_{sha} \cos(\theta_{i+a-1} - \theta_{sha} - \Phi_{sha}) - V_{i+a-1}^2 Y_{sha} \cos \Phi_{sha}$$

$$+ j \{ V_{i+a-1} m_a c V_{DCa} Y_{sha} \sin(\theta_{i+a-1} - \theta_{sha} - \Phi_{sha}) + V_{i+a-1}^2 Y_{sha} \sin \Phi_{sha} \}$$

$$= \alpha + j \beta$$

where,  $\alpha = V_{i+a-1} m_a c V_{DCa} y_{sha} \cos(\theta_{i+a-1} - \theta_{sha} - \Phi_{sha}) - V_{i+a-1}^2 y_{sha} \cos \Phi_{sha}$

and  $\beta = V_{i+a-1} m_a c V_{DCa} y_{sha} \sin(\theta_{i+a-1} - \theta_{sha} - \Phi_{sha}) + V_{i+a-1}^2 y_{sha} \sin \Phi_{sha}$

$$S_{sha}^2 = \alpha^2 + \beta^2$$

$$= V_{i+a-1}^2 V_{sha}^2 y_{sha}^2 + V_{i+a-1}^4 y_{sha}^2 - 2 V_{i+a-1}^3 V_{sha} y_{sha}^2 \{ \cos \Phi_{sha} \cos(\theta_{i+a-1} - \theta_{sha} - \Phi_{sha}) - \sin \Phi_{sha} \sin(\theta_{i+a-1} - \theta_{sha} - \Phi_{sha}) \}$$

Now, using formula  $\cos A \cos B - \sin A \sin B = \cos(A+B)$

$$S_{sha}^2 = V_{i+a-1}^2 V_{sha}^2 y_{sha}^2 + V_{i+a-1}^4 y_{sha}^2 - 2 V_{i+a-1}^3 V_{sha} y_{sha}^2 \cos(\theta_{i+a-1} - \theta_{sha})$$

$$= y_{sha}^2 [V_{i+a-1}^4 + V_{i+a-1}^2 (m_a c V_{DCa})^2 - 2 V_{i+a-1}^3 m_a c V_{DCa} \cos(\theta_{i+a-1} - \theta_{sha})]$$

$$S_{sha} = y_{sha} [V_{i+a-1}^4 + V_{i+a-1}^2 (m_a c V_{DCa})^2 - 2 V_{i+a-1}^3 m_a c V_{DCa} \cos(\theta_{i+a-1} - \theta_{sha})]^{1/2}$$

$$I_{sha} = \frac{S_{sha}}{V_{i+a-1}}$$

$$I_{sha} = y_{sha} [V_{i+a-1}^2 + (m_a c V_{DCa})^2 - 2 V_{i+a-1} m_a c V_{DCa} \cos(\theta_{i+a-1} - \theta_{sha})]^{1/2} \quad (A.8)$$

## A.2.2 Expression of power balance equation with converter losses of a<sup>th</sup> VSC using unified method

From eqn. (3.14),

For master converter,

$$(m_a c V_{DCa})^2 y_{sha} \cos \Phi_{sha} - m_a c V_{DCa} V_{i+a-1} y_{sha} \cos(\theta_{sha} - \theta_{i+a-1} - \Phi_{sha}) + \sum_{v=1}^q V_{DCa} V_{DCv} Y_{DCav} + a_1 + b_1 d_1 + c_1 d_1^2 = 0 \quad (A.9)$$

$$\text{Where } d_1 = y_{sha} [V_{i+a-1}^2 + m_a^2 c^2 V_{DCa}^2 - 2 m_a c V_{DCa} V_{i+a-1} \cos(\theta_{i+a-1} - \theta_{sha})]^{1/2}$$

For slave converter,

$$\begin{aligned}
& (m_a c V_{DCa})^2 y_{sha} \cos \phi_{sha} - m_a c V_{DCa} V_{i+a-1} y_{sha} \cos(\theta_{sha} - \theta_{i+a-1} - \phi_{sha}) + \sum_{v=1}^q V_{DCa} V_{DCv} Y_{DCav} + a_1 \\
& + b_1 \frac{\sqrt{P_{sha}^{sp\ 2} + Q_{sha}^{sp\ 2}}}{V_{i+a-1}} + c_1 \left( \frac{\sqrt{P_{sha}^{sp\ 2} + Q_{sha}^{sp\ 2}}}{V_{i+a-1}} \right)^2 = 0 \tag{A.10}
\end{aligned}$$

### A.2.3 Typical elements in Jacobian sub-blocks of eqn. (3.23) using Unified method

For master converter,

$$\frac{\partial f_{1a}}{\partial \theta_{sha}} = m_a c V_{DCa} V_{i+a-1} y_{sha} \sin(\theta_{sha} - \theta_{i+a-1} - \phi_{sha}) + b_1 y_{sha} \frac{d_3}{2 d_2} + c_1 y_{sha}^2 d_3 \tag{A.11}$$

Where  $d_2 = [V_{i+a-1}^2 + m_a^2 c^2 V_{DCa}^2 - 2 m_a c V_{DCa} V_{i+a-1} \cos(\theta_{i+a-1} - \theta_{sha})]^{1/2}$

$$d_3 = -2 m_a c V_{DCa} V_{i+a-1} \sin(\theta_{i+a-1} - \theta_{sha})$$

$$\begin{aligned}
\frac{\partial f_{1a}}{\partial V_{DCa}} &= 2 m_a^2 c^2 V_{DCa} y_{sha} \cos \phi_{sha} - m_a c V_{i+a-1} y_{sha} \cos(\theta_{sha} - \theta_{i+a-1} - \phi_{sha}) + \sum_{v=1}^q V_{DCv} Y_{DCav} \\
&+ V_{DCa} Y_{DCaa} + b_1 y_{sha} \frac{d_4}{2 d_2} + c_1 y_{sha}^2 d_4 \tag{A.12}
\end{aligned}$$

Where  $d_4 = 2 V_{DCa} m_a^2 c^2 - 2 m_a c V_{i+a-1} \cos(\theta_{i+a-1} - \theta_{sha})$

$$\begin{aligned}
\frac{\partial f_{1a}}{\partial m_a} &= 2 m_a c^2 V_{DCa}^2 y_{sha} \cos \phi_{sha} - c V_{DCa} V_{i+a-1} y_{sha} \cos(\theta_{sha} - \theta_{i+a-1} - \phi_{sha}) \\
&+ b_1 y_{sha} \frac{d_5}{2 d_2} + c_1 y_{sha}^2 d_5 \tag{A.13}
\end{aligned}$$

$$d_5 = 2 V_{DCa}^2 m_a c^2 - 2 c V_{DCa} V_{i+a-1} \cos(\theta_{i+a-1} - \theta_{sha})$$

For slave converter in PQ control operation,

$$\frac{\partial f_{1a}}{\partial \theta_{sha}} = m_a c V_{DCa} V_{i+a-1} y_{sha} \sin(\theta_{sha} - \theta_{i+a-1} - \phi_{sha}) \tag{A.14}$$

$$\frac{\partial f_{1a}}{\partial V_{DCa}} = 2 m_a^2 c^2 V_{DCa} y_{sha} \cos \phi_{sha} - m_a c V_{i+a-1} y_{sha} \cos(\theta_{sha} - \theta_{i+a-1} - \phi_{sha}) + \sum_{v=1}^q V_{DCv} Y_{DCav} + V_{DCa} Y_{DCaa} \quad (A.15)$$

$$\frac{\partial f_{1a}}{\partial m_a} = 2 m_a c^2 V_{DCa}^2 y_{sha} \cos \phi_{sha} - c V_{DCa} V_{i+a-1} y_{sha} \cos(\theta_{sha} - \theta_{i+a-1} - \phi_{sha}) \quad (A.16)$$

#### A.2.4 Typical elements in Jacobian sub-blocks of eqn. (3.30) using Sequential method

From eqn. (3.27)

$$\frac{\partial f_{2a}}{\partial V_{i+a-1}} = -m_a c V_{DCa} y_{sha} \cos(\theta_{sha} - \theta_{i+a-1} - \phi_{sha}) - (P_{sha}^{sp^2} + Q_{sha}^{sp^2}) \left( \frac{-2 R_{sha}}{V_{i+a-1}^3} \right) \quad (A.17)$$

From eqn. (3.28)

$$\frac{\partial f_{3a}}{\partial V_{i+a-1}} = -m_a c V_{DCa} y_{sha} \sin(\theta_{sha} - \theta_{i+a-1} - \phi_{sha}) - (P_{sha}^{sp^2} + Q_{sha}^{sp^2}) \left( \frac{-2 X_{sha}}{V_{i+a-1}^3} \right) \quad (A.18)$$

#### A.2.5 Initial values of variables in VSC based HVDC systems

**Table A.2**

Variables in VSC HVDC system		Initial values
DC bus voltage	$V_{DCi}^0$	3 p.u
DC voltage reference for droop line of $i^{\text{th}}$ VSC	$(V_{DCi}^*)^0$	3 p.u
Modulation index of $i^{\text{th}}$ VSC	$m_i^0$	1.0
Magnitude of output voltage phasor of $i^{\text{th}}$ VSC	$V_{shi}^0$	1.0 p.u
Phase angle of output voltage phasor of $i^{\text{th}}$ VSC	$\theta_{shi}^0$	0 (degree)
Variable $i^{\text{th}}$ DC voltage source of IDCPFC	$V_{DCsi}^0$	0.001 p.u

#### A.3 Expression of power balance equation with converter losses of $a^{\text{th}}$ VSC considering as a master converter by incorporating IDCPFC

From eqn. (5.13)

$$\begin{aligned}
& (m_a c V_{DCa})^2 y_{sha} \cos \phi_{sha} - m_a c V_{DCa} V_{i+a-1} y_{sha} \cos(\theta_{sha} - \theta_{i+a-1} - \phi_{sha}) + \\
& \sum_{v=1}^q V_{DCa} V_{DCv} Y_{DCav} + \sum_{v=1, v \neq 1}^{z+1} V_{DCa} V_{DCs(v-1)} Y_{DCav} + a_1 + b_1 d_1 + c_1 d_1^2 = 0 \text{ if } a = \\
& 1, z = 2 \quad (\text{A. 19})
\end{aligned}$$

$$\begin{aligned}
\frac{\partial f_{1a}}{\partial V_{DCa}} &= 2 m_a^2 c^2 V_{DCa} y_{sha} \cos \phi_{sha} - m_a c V_{i+a-1} y_{sha} \cos(\theta_{sha} - \theta_{i+a-1} - \phi_{sha}) + \sum_{v=1}^q V_{DCv} Y_{DCav} \\
&+ V_{DCa} Y_{DCaa} + \sum_{v=1, v \neq 1}^{z+1} V_{DCs(v-1)} Y_{DCav} \\
&+ b_1 y_{sha} \frac{d_4}{2 d_2} + c_1 y_{sha}^2 d_4 \quad (\text{A. 20})
\end{aligned}$$

$$\frac{\partial f_{1a}}{\partial V_{DCs(v-1)}} = \sum_{v=1, v \neq 1}^{z+1} V_{DCa} Y_{DCav} \quad (\text{A. 21})$$

$$\frac{\partial P_{IDCPFC}}{\partial V_{DCsz}} = [V_{DC} - 2 V_{DCsz} - V_{DC(z+1)}] Y_{DC1(z+1)} \quad (\text{A. 22})$$

$$\frac{\partial P_{IDCPFC}}{\partial V_{DC(z+1)}} = - V_{DCsz} Y_{DC1(z+1)} \quad (\text{A. 23})$$



## **Appendix B**

### **Author's Brief Biography**

Shagufta Khan received her B.Tech degree in Electrical Engineering from College of Engineering and Technology, IILM Academy of Higher Learning, Gr. Noida, UPTU in 2009 and the M.Tech degree in Electrical Power System Management from the Jamia Millia Islamia, Delhi in 2012. She joined AAR VEE Controls Pvt. Ltd., Noida in 2009. She also joined the Jodhpur Vidyut Vitran Nigam Limited, Bikaner in 2012. Since 2012, she has been working as a Full time Research Scholar in the Department of Electrical Engineering, Delhi Technological University, Delhi, India.

Her research interest is in the area of Electrical Power Systems.

# Appendix C

## List of Publications

### International Journals

- [1] S. Khan and S. Bhowmick, "Generalised power flow models for VSC based multi-terminal HVDC systems," *IJEPES, Elsevier*, vol. 82, pp. 67-75, Nov. 2016.
- [2] S. Khan and S. Bhowmick, "A novel power flow model of multi-terminal VSC-HVDC systems," *EPSR Elsevier*, vol. 133, pp. 219-227, April 2016.
- [3] S. Khan and S. Bhowmick, "Impact of DC link control strategies on power flow convergence of integrated AC-DC systems," *AIN SHAMS Elsevier*, vol. 7, no. 1, pp. 249-264, March 2016.
- [4] S. Khan and S. Bhowmick, "Effect of DC link control strategies on multi-terminal AC-DC power flow," *Advance in Electrical Engineering, Hindawi*, pp. 1-15, 2015.
- [5] S. Khan and S. Bhowmick, "Impact of selection of DC base values and DC Link control strategies on sequential AC-DC power flow convergence," *Frontier in Energy, Springer*, vol. 9, no. 4, pp. 399-412, Aug., 2015.

### International Conferences

- [1] S. Khan and S. Bhowmick, "A Novel sequential power flow model for hybrid AC-DC systems," *IEEE INDICON*, pp. 1-6, 2015.